

# **Synthesis and Characterization of Recent Zeolites with Unusual Pore Architectures**

**Dissertation**

eingereicht am Fachbereich Chemie der Technischen Universität Kaiserslautern  
zur Verleihung des akademischen Grades “Doktor der Naturwissenschaften”

D 386



vorgelegt von

**M.Sc. Supak Tontisirin**

geboren in Rayong (Thailand)

Betreuer

**Prof. Dr.-Ing. Stefan Ernst**

Kaiserslautern, 2010



Die vorliegende Arbeit entstand zwischen August 2003 und März 2007 im Fachbereich Chemie, Fachrichtung Technische Chemie, der Technischen Universität Kaiserslautern.

Prüfungskommission:

Vorsitzender:	Prof. Dr. Werner Thiel
1. Berichterstatter:	Prof. Dr.-Ing. Stefan Ernst
2. Berichterstatter:	Prof. Dr. Helmut Sitzmann

Tag der mündlichen Prüfung: 13.07.2010

### Eidesstattliche Erklärung

Hiermit versichere ich, dass ich die vorliegende Arbeit eigenständig verfasst und keine anderen als die angegebenen Quellen und Hilfsmittel verwendet, sowie Literaturzitate kenntlich gemacht habe. Kooperationsprojekte sind ausdrücklich als solche gekennzeichnet. Ich erkläre außerdem, dass diese Arbeit weder in gleicher noch in ähnlicher Form bereits in einem anderen Prüfungsverfahren vorgelegen hat.

Kaiserslautern, den \_\_\_\_\_

\_\_\_\_\_  
Supak Tontisirin

## Acknowledgements

I wish to express my most sincere appreciation to my advisor, Prof. Dr.-Ing. Stefan Ernst, for giving me the opportunity to do an academic research work in his group and the valuable discussions throughout the academic years. I would like to thank Prof. Dr. Martin Hartmann for his valuable discussions and guidance in the first two and a half years of my research. I would like to thank Prof. Dr. Helmut Sitzmann for providing the special template for synthesizing of zeolite UTD-1. Moreover, I would like to thank the other member of my committee, Prof. Dr. Werner Thiel, for his time and interest.

Carlos López Monllor, Manuel Florian Seibel, Sawa Nordt, Xiao Juan Tang, Elena Bogdan and Carola Filß are thanked for their great contribution to my work via their diploma theses and “Forschungarbeiten”. I would like to thank all the lab colleagues, Silke Sauerbeck, Matthias Oberlinger, Helwig Thiel, Thomas Hecht, Stefan Ost, Carsten Streb, Sridhar Adapa, Alex Wagener, Markus Schindler and other colleagues for all discussions about small and big problems through my promotion time. In addition, I would like to acknowledge Ludvig Napast for his time of guidance in performing  $^1\text{H}$ - and  $^{13}\text{C}$ -NMR measurements and Heike Schramm for her kind administrative assistance.

Finally I would like to thank my family and my husband, Sitt Tontisirin. Without their encouragement and support, this work would not have been carried out.

## Summary

The main focus of this dissertation is the synthesis and characterization of more recent zeolites with different pore architectures. The unique shape-selective properties of the zeolites are important in various chemical processes and the new zeolites containing novel internal pore architectures are of high interest, since they could lead to further improvement of existing processes or open the way to new applications.

This dissertation is organized in the following way: The first part is focused on the synthesis of selected recent zeolites with different pore architectures and their modification to the acidic and bifunctional forms. The second part comprises the characterization of the physicochemical properties of the prepared zeolites by selected physicochemical methods, viz. powder X-ray diffractometry (XRD), N<sub>2</sub> adsorption, thermogravimetric analysis (TGA/DTA/MS), ultraviolet-visible (UV-Vis) spectroscopy, atomic absorption spectroscopy (AAS), infrared (IR) spectroscopy, scanning electron microscopy (SEM), <sup>27</sup>Al and <sup>29</sup>Si magic angle spinning nuclear magnetic resonance (MAS NMR) spectroscopy, temperature-programmed reduction (TPR), temperature-programmed desorption of pyridine (pyridine TPD) and adsorption experiments with hydrocarbon adsorptives. The third part of this work is devoted to the application of test reactions, i.e., the acid catalyzed disproportionation of ethylbenzene and the bifunctional hydroconversion of *n*-decane, to characterize the pore size and architecture of the prepared zeolites. They are known to be valuable tools for exploring the pore structure of zeolites. Finally, an additional test, viz. the competitive hydrogenation of 1-hexene and 2,4,4-trimethyl-1-pentene, has been applied to probe the location of noble metals in medium pore zeolite.

The synthesis of the following zeolite molecular sieves was successfully performed in the frame of this thesis (they are ranked according to the largest window size in the respective structure):

- 14-MR pores: UTD-1, CIT-5, SSZ-53 and IM-12
- 12-MR pores: ITQ-21 and MCM-68
- 10-MR pores: SSZ-35 and MCM-71

All of them were obtained as pure phase (except zeolite MCM-71 with a minor impurity phase that is hardly to avoid and also present in samples shown in the patent literature). The synthesis conditions are very critical with respect to the formation of the zeolite with a given structure. In this work, the recommended synthesis recipes are included. Among the 14-MR zeolites, the aluminosilicates UTD-1 ( $n_{\text{Si}}/n_{\text{Al}} = 28$ ), CIT-5 ( $n_{\text{Si}}/n_{\text{Al}} = 116$ ) and SSZ-53 ( $n_{\text{Si}}/n_{\text{Al}} = 55$ ) with unidimensional extra-large pore opening formed from 14-MR rings exhibit promising catalytic properties with high thermal stability and they possess strong Brønsted-acid sites. By contrast, the germanosilicate IM-12 with a structure containing 14-MR channels intersecting with 12-MR channels is unstable toward moisture. It was found that UTD-1 and SSZ-53 zeolites are highly active catalysts for the acid catalyzed disproportionation of ethylbenzene and *n*-decane hydroconversion due to their high Brønsted acidity. To explore their pore structures, the applied two test reactions suggest that UTD-1, CIT-5 and SSZ-53 zeolites contain a very open pore system (12-MR or larger pore systems) because the product distributions are not hampered by too small pores.

ITQ-21, a germanoaluminosilicate zeolite with a three-dimensional pore system and large spherical cages accessible through six 12-MR windows, can be synthesized with  $n_{\text{Si}}/n_{\text{Al}}$  ratios between 27 and >200. It possesses a large amount of Brønsted-acid sites. The aluminosilicate zeolite MCM-68 ( $n_{\text{Si}}/n_{\text{Al}} = 9$ ) is an extremely active catalyst in the disproportionation of

ethylbenzene and in the *n*-decane hydroconversion. This is due to the presence of a high density of strong Brønsted-acid sites in its structure. The disproportionation of ethylbenzene suggests that MCM-68 is a large pore (i.e., at least 12-MR) zeolite, in agreement with its crystallographic structure. In the hydroconversion of *n*-decane, the presence of tribranched and ethylbranched isomers and a high isopentane yield of 58 % in the hydrocracked products suggest the presence of large (12-MR) pores in its structure. By contrast, a relatively high value for  $CI^*$  (modified constraint index) of 2.9 suggests the presence of medium (10-MR) pores in its structure. As a whole, the results are in-line with the crystallographic structure of MCM-68.

SSZ-35, a 10-MR zeolite, can be synthesized in a broad range of  $n_{Si}/n_{Al}$  ratios between 11 and >500. This zeolite is interesting in terms of shape selectivity resulting from its unusual pore system having unidimensional channels alternating between 10-MR windows and large 18-MR cages. This thermally very stable zeolite contains both, strong Brønsted- and strong Lewis-acid sites. The disproportionation of ethylbenzene classifies SSZ-35 as a large pore zeolite. In the hydroconversion of *n*-decane, the suppression of bulky ethyloctanes and propylheptane clearly suggests the presence of 10-MR sections in the pore system. By contrast, the low  $CI^*$  values of 1.2-2.3 and the high isopentane yields of 56-60 % in the hydrocracked products suggest that SSZ-35 also possesses larger intracrystalline voids, i.e., the 18-MR cages. The results from the catalytic characterization are in good agreement with the crystallographic structure of zeolite SSZ-35. It was also found that the  $n_{Si}/n_{Al}$  ratio influences the crystallite size and therefore the external surface area. As a consequence, product selectivities are also influenced: The lowest  $n_{Si}/n_{Al}$  ratio or the smallest crystallite size sample produces larger amounts of the relatively bulky products. The formation of these products probably results from the higher conversion or they are preferentially formed on the external surface area of the catalyst.

Zeolite MCM-71 ( $n_{\text{Si}}/n_{\text{Al}} = 8$ ) possesses an extremely thermally stable structure and contains a high concentration of Brønsted-acid sites. Its structure allows for the separation of *n*-alkanes from branched alkanes by selective adsorption. MCM-71 exhibits unique shape-selective properties towards the product distribution in ethylbenzene disproportionation, which is different to those obtained in the medium pore SSZ-35 zeolite. All reaction parameters are fulfilled to classify MCM-71 as medium pore zeolite and this is in good agreement with its reported structure consisting of two-dimensional network of elliptical 10-MR channels and an orthogonal sinusoidal 8-MR channels.

The competitive hydrogenation of 1-hexene and 2,4,4-trimethyl-1-pentene was exploited to probe that the major part of the noble metal is located inside the intracrystalline void volume of the medium pore zeolite SSZ-35.



## Table of Contents

<b>1. Introduction.....</b>	<b>1</b>
<b>2. Literature review .....</b>	<b>3</b>
<b>2.1. Introduction to zeolites .....</b>	<b>3</b>
2.1.1. Structures of zeolites .....	3
2.1.2. Properties of zeolites .....	5
<b>2.2. Structures and properties of the zeolites investigated in this study .....</b>	<b>8</b>
2.2.1. Zeolite UTD-1 .....	8
2.2.2. Zeolite CIT-5.....	10
2.2.3. Zeolite SSZ-53 .....	11
2.2.4. Zeolite IM-12 .....	13
2.2.5. Zeolite ITQ-21 .....	14
2.2.6. Zeolite MCM-68 .....	16
2.2.7. Zeolite SSZ-35 .....	17
2.2.8. Zeolite MCM-71 .....	18
<b>2.3. Methods for characterizing the acidity of solid catalysts.....</b>	<b>20</b>
<b>2.4. Test reactions for characterizing the pore size and architecture of zeolites.....</b>	<b>21</b>
2.4.1. Ethylbenzene disproportionation as test reaction.....	22
2.4.1.1. Application to investigate pore size and architecture of zeolites.....	22
2.4.1.2. Mechanism of alkylbenzene disproportionation .....	24
2.4.1.3. Mechanism of dialkylbenzene isomerization.....	28
2.4.1.4. Thermodynamic equilibrium of the diethylbenzene isomers.....	29
2.4.2. <i>n</i> -Decane hydroconversion as test reaction.....	32
2.4.2.1. Application for characterizing the pore size and architecture of zeolites .....	32
2.4.2.2. Mechanistic concepts for the isomerization and hydrocracking of long chain <i>n</i> -alkanes .....	35
<b>2.5. Competitive hydrogenation of olefins for probing the location of noble metals         in zeolites .....</b>	<b>43</b>
<b>3. Experimental section .....</b>	<b>45</b>
<b>3.1. Synthesis and preparation of more recent zeolites with unusual pore         architectures .....</b>	<b>45</b>
3.1.1. Zeolites based on 14-membered ring pore openings.....	45

3.1.1.1. Zeolite UTD-1 .....	45
3.1.1.2. Zeolite CIT-5 .....	47
3.1.1.3. Zeolite SSZ-53 .....	49
3.1.1.4. Zeolite IM-12 .....	52
3.1.2. Zeolites based on 12-membered ring pore openings .....	54
3.1.2.1. Zeolite ITQ-21 .....	54
3.1.2.2. Zeolite MCM-68 .....	56
3.1.3. Zeolites based on 10-membered ring pore openings .....	60
3.1.3.1. Zeolite SSZ-35 .....	60
3.1.3.2. Zeolite MCM-71 .....	61
<b>3.2. Preparation of bifunctional catalysts .....</b>	<b>62</b>
<b>3.3. Physicochemical characterization .....</b>	<b>63</b>
3.3.1. Powder X-ray diffractometry (XRD) .....	63
3.3.2. Thermogravimetric analysis coupled to mass spectroscopy (TGA/DTA/MS) .....	63
3.3.3. N <sub>2</sub> adsorption .....	63
3.3.4. Infrared (IR) spectroscopy .....	63
3.3.5. Ultraviolet-visible (UV-Vis) spectroscopy .....	64
3.3.6. Scanning electron microscopy (SEM) .....	64
3.3.7. Atomic absorption spectroscopy (AAS) .....	64
3.3.8. Temperature-programmed desorption of pyridine (pyridine TPD) .....	65
3.3.8.1. Pyridine TPD in a flow-type apparatus .....	65
3.3.8.2. Pyridine TPD coupled with IR spectroscopy .....	65
3.3.9. <sup>27</sup> Al and <sup>29</sup> Si magic angle spinning nuclear magnetic resonance (MAS NMR) spectroscopy .....	66
3.3.10. Temperature-programmed reduction (TPR) .....	66
3.3.11. Characterization of the pore size by adsorption experiments .....	67
<b>3.4. Catalytic experiments .....</b>	<b>67</b>
3.4.1. Ethylbenzene disproportionation .....	67
3.4.1.1. Experimental setup .....	67
3.4.1.2. Catalytic evaluation .....	71
3.4.2. <i>n</i> -Decane hydroconversion .....	74
3.4.2.1. Experimental setup .....	74
3.4.2.2. Catalytic evaluation .....	77
3.4.3. Competitive hydrogenation of olefins .....	79

3.4.3.1. Experimental setup.....	79
3.4.3.2. Catalytic evaluation.....	83
<b>4. Results and discussions .....</b>	<b>85</b>
<b>4.1. Synthesis and characterization of zeolites based on 14-membered ring pore openings.....</b>	<b>85</b>
4.1.1. Zeolite UTD-1 .....	85
4.1.2. Zeolite CIT-5.....	96
4.1.3. Zeolite SSZ-53 .....	99
4.1.4. Zeolite IM-12 .....	103
<b>4.2. Synthesis and characterization of zeolites based on 12-membered ring pore openings.....</b>	<b>105</b>
4.2.1. Zeolite ITQ-21 .....	105
4.2.2. Zeolite MCM-68 .....	110
<b>4.3. Synthesis and characterization of zeolites based on 10-membered ring pore openings.....</b>	<b>116</b>
4.3.1. Zeolite SSZ-35 .....	116
4.3.2. Zeolite MCM-71 .....	126
<b>4.4. Characterization of the pore size of zeolites by hydrocarbon adsorption .....</b>	<b>136</b>
<b>4.5. Ethylbenzene disproportionation as test reaction.....</b>	<b>140</b>
4.5.1. Zeolites based on 14-membered ring pore openings.....	140
4.5.1.1. H-UTD-1 .....	140
4.5.1.2. H-CIT-5.....	142
4.5.1.3. H-SSZ-53 .....	144
4.5.2. Zeolites based on 12-membered ring pore openings.....	149
4.5.2.1. H-MCM-68 .....	149
4.5.3. Zeolites based on 10-membered ring pore openings.....	151
4.5.3.1. H-SSZ-35 .....	151
4.5.3.2. H-MCM-71 .....	156
<b>4.6. <i>n</i>-Decane hydroconversion as test reaction .....</b>	<b>160</b>
4.6.1. Zeolites based on 14-membered ring pore openings.....	160
4.6.1.1. 0.27Pd/HUTD-1 .....	160
4.6.1.2. 0.27Pd/HSSZ-53 .....	165
4.6.2. Zeolites based on 12-membered ring pore openings.....	168

4.6.2.1. 0.27Pd/HMCM-68 .....	168
4.6.3. Zeolites based on 10-membered ring pore openings .....	172
4.6.3.1. 0.27Pd/HSSZ-35 .....	172
<b>4.7. Competitive hydrogenation of olefins for probing the location of noble metals in zeolites .....</b>	<b>179</b>
<b>5. Conclusions.....</b>	<b>182</b>
<b>6. Appendices.....</b>	<b>187</b>
6.1. Appendix A: List of symbols and indices .....	187
6.2. Appendix B: List of abbreviations .....	189
<b>7. References.....</b>	<b>192</b>

## 1. Introduction

Zeolites are defined as crystalline microporous aluminosilicates with a three-dimensionally interconnected structure. The pore structure of zeolites consists of cavities and channels of molecular dimensions. Zeolites play an important role in diverse branches. Three classical properties which make them technologically important are: they are selective/strong adsorbents, selective ion exchangers, and catalytically active compounds [1]. Other new applications have emerged such as zeolites for hydrogen storage and optical information storage material [2]. In catalytic applications, one of the important features of zeolites is their ability to perform shape-selective reactions. The concept of shape selectivity describes the phenomena where the pore size of the zeolite limits the entrance of reactant molecules, the departure of product molecules or the formation of transition states within the zeolite pores [3, 4]. With this unique property, zeolites are now applied in numerous industrial processes, e.g., fluid catalytic cracking (FCC), hydrocracking, catalytic dewaxing, conversion of methanol to gasoline (MTG), ethylbenzene and cumene synthesis and xylene isomerization [5].

Even though commercially used zeolites are not more than twenty different types [6], many new zeolite structures have been disclosed because the new zeolites, containing novel internal pore architectures, could provide enhanced selectivities in certain processes. The shape selective property could determine the success or failure for those processes. Moreover, the novel internal pore architectures could provide improvements in existing chemical processes or open the way to new or specialty applications. From the past six years until January 2010, around 49 types of new zeolite structure frameworks have been registered by the International Zeolite Association (IZA) [7]. This confirms that the finding of new zeolite structures is still an on-going process.

Understanding or knowledge of the structure of a zeolite is a critical key to gain insight into its structure-property relationship. There are various methods in exploring the shape-selective properties of a zeolite, e.g., adsorption of a set of compounds with different molecular dimensions and catalytic test reactions for characterizing the effective pore width and pore architecture of the zeolite under catalytically relevant conditions. The catalytic tests offer the possibility to detect both, mass transfer effects (reactant and product shape selectivity) and chemical effects (restricted transition-state shape selectivity). Several catalytic test reactions have been suggested [8-13]. These model reactions are valuable tools for characterizing the pore structure of novel zeolites.

The goal of this work was to optimize the synthesis of various more recent zeolites with different pore sizes and architectures. Thereafter, the zeolites were modified via certain post-treatments in order to prepare the acidic and bifunctional forms. Various characterization methods were applied to explore the physicochemical properties of the prepared zeolites, i.e., powder X-ray diffractometry (XRD), N<sub>2</sub> adsorption, thermogravimetric analysis (TGA/DTA/MS), ultraviolet-visible (UV-Vis) spectroscopy, atomic absorption spectroscopy (AAS), infrared (IR) spectroscopy, scanning electron microscopy (SEM), <sup>27</sup>Al and <sup>29</sup>Si magic angle spinning nuclear magnetic resonance (MAS NMR) spectroscopy, temperature-programmed reduction (TPR), temperature-programmed desorption of pyridine (pyridine TPD) and adsorption experiments with different hydrocarbon adsorptives. Moreover, the pore size and architecture as well as the acidic properties of the prepared zeolites were characterized by selected catalytic test reactions, i.e., the acid-catalyzed disproportionation of ethylbenzene and the bifunctional hydroconversion of *n*-decane. Finally, to probe the location of active noble metals in the palladium-containing medium pore zeolites, an additional test, viz. competitive hydrogenation of olefins was carried out.

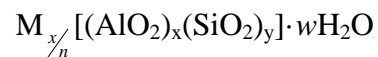
## 2. Literature review

### 2.1. Introduction to zeolites

Zeolites were first recognized by Axel F. Cronstedt [14] as a new group of minerals consisting of hydrated aluminosilicates of the alkali and alkaline earth, with his discovery of stilbite in 1756. Because the mineral swelled up when heated in a blowpipe flame, he called it zeolite which comes from two Greek words: “zein” = to boil and “lithos” = stone. From that time, studies of zeolite minerals have taken place over more than two centuries.

#### 2.1.1. Structures of zeolites

A zeolite is a crystalline, hydrated aluminosilicate of group I and group II elements, in particular sodium, potassium, magnesium and calcium [1]. Structurally, a zeolite is a framework aluminosilicate which is based on an infinitely extending three-dimensional network of  $\text{AlO}_4$  and  $\text{SiO}_4$  tetrahedra linked to each other by sharing all of the oxygens. The structure formula of a zeolite for a crystallographic unit cell is:



Where M represents the exchangeable cation of valence  $n$ ,  $w$  is the number of water molecules, the ratio  $y/x$  varies from 1 to  $\infty$  depending on the structure, the sum  $(x+y)$  is the total number of tetrahedra in the unit cell. The portion within the bracket represents the framework composition. The value of  $y/x$  must be equal or greater than one according to the empirical Löwenstein rule [15], because  $[\text{AlO}_4]^{5-}$  tetrahedral are joined only to  $[\text{SiO}_4]^{4-}$  tetrahedra.

The structure of zeolites is based on the primary tetrahedral building unit,  $\text{TO}_4$ , where the central tetrahedrally bonded (T) atom is usually either a silicon or aluminium atom surrounded by four oxygen atoms. By linking these tetrahedra together, it is possible to build

larger structures, so-called secondary building units (SBUs). The final framework structure consists of assemblages of the secondary building units which results in the zeolite framework. The primary building unit and the secondary building units known so far are demonstrated in Fig. 1.

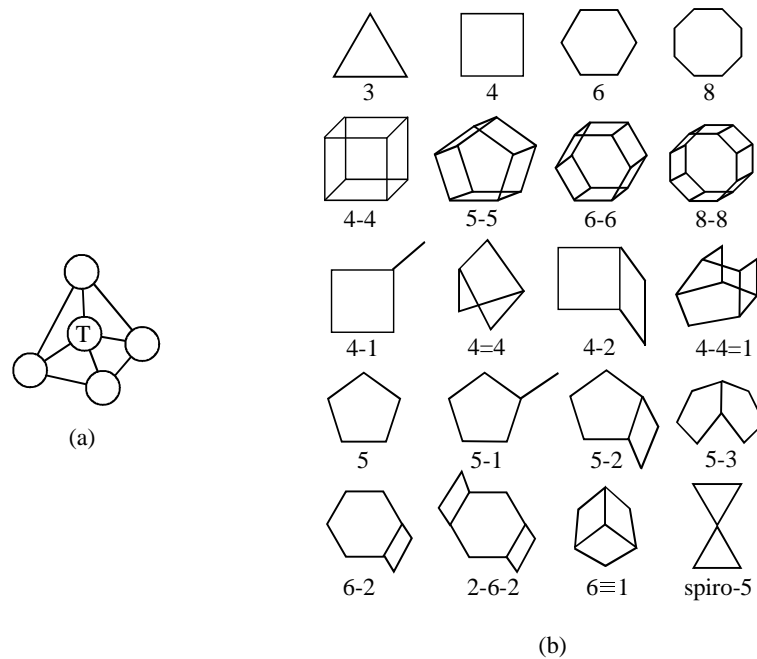


Fig. 1. (a) Primary building unit and (b) secondary building units (SBUs) (from ref. [16]).

The zeolite framework type describes the connectivity or topology of the framework tetrahedral atoms without reference to chemical composition, distribution of T-atoms, or observed symmetry. Each type defines the size and shape of pore opening size, dimensionality of channel system, volume, arrangement of cages, and types of cation sites.

A description of a zeolite structure always begins with a description of the framework type in terms of the size of the pore opening and the dimensionality of the channel system. The pore openings are characterized by size of the ring that defines the pore, designated an  $n$ -ring or  $n$ -membered ring (MR), where  $n$  is the number of T-atoms in the ring. An 8-ring is considered to be a small pore opening, a 10-ring a medium one, a 12-ring a large one with the free diameters of ca. 0.41, 0.55 and 0.74 nm, respectively. A zeolite with ring size above 12-ring

is termed “extra-large” pore zeolite as firstly proposed by Davis et al. in 1989 [17]. Fig. 2 shows examples of zeolite pore sizes illustrated with the oxygen packing model.

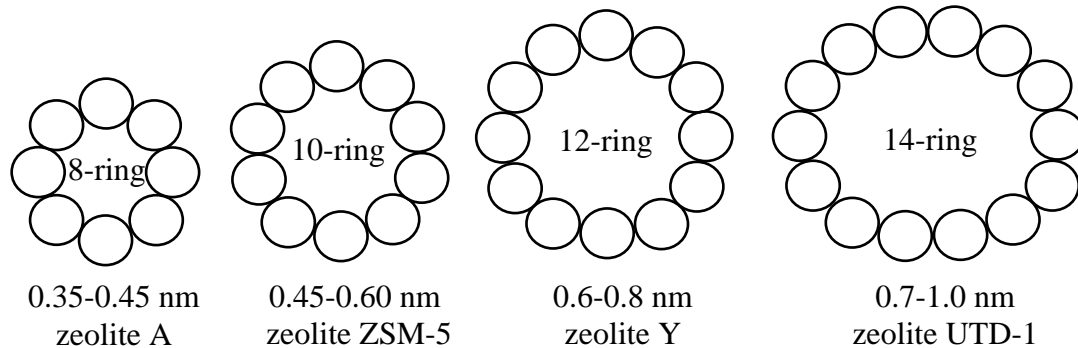


Fig. 2. Examples of zeolite pore sizes illustrated with the oxygen packing model (from ref. [18]).

Each confirmed zeolite framework type is assigned a three-letter code (e.g., **FAU** for the faujasite framework type) by the Structure Commission of the International Zeolite Association (IZA) according to rules set up by the IUPAC Commission on Zeolite Nomenclature [19], and details of these framework types are published in the Atlas of Zeolite Framework Types [20]. All framework types, including updates between printed editions of the Atlas, are also published in the internet [21].

### 2.1.2. Properties of zeolites

Zeolite structures exhibit five main properties which are the source of their catalytic activity. They possess molecular sieving ability, cation exchange, high surface area, variable acidity, and chemical and thermal stability [22]. Only two properties will be discussed as follow.

The *molecular sieving ability* of zeolites plays the major role in their unique shape-selective properties in catalysis, e.g., for hydrocarbon processing. The concept of shape selectivity was firstly recognized by Weisz and Frilette [3]. Later, three types of shape-selective catalytic behaviour have been classified by Csicsery [4] as:

- reactant shape selectivity
- product shape selectivity
- restricted transition-state shape selectivity

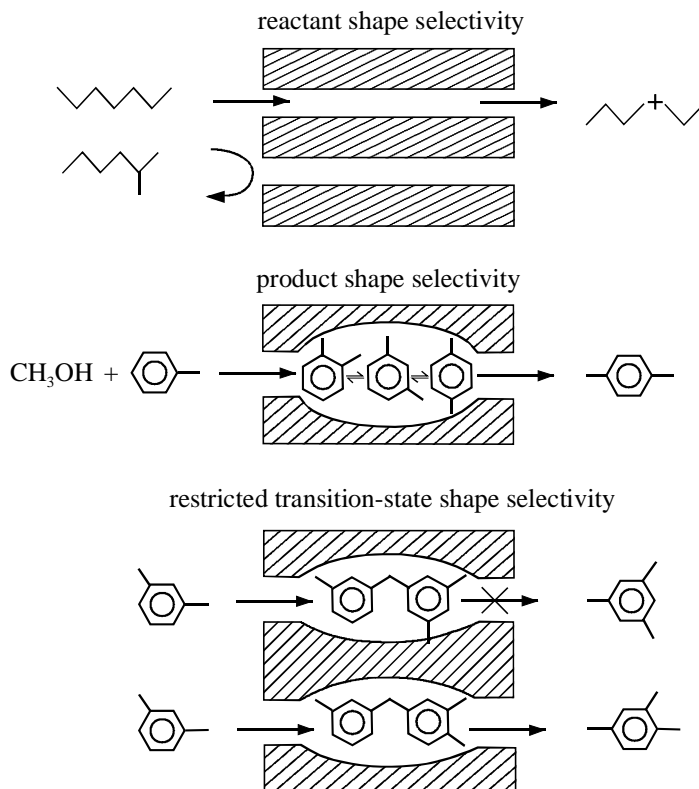


Fig. 3. Different types of shape selectivity (from ref. [4]).

The three different forms of shape selectivity are illustrated in Fig. 3. Reactant shape selectivity describes the case where reactant molecules may be too large to enter the pores and cavities of the zeolite. On the other hand, the product shape selectivity occurs when reaction products of different sizes are formed within the larger interior void spaces of the zeolite crystals and some of them are too bulky to diffuse out. The products, which can not escape from the cavities, may undergo secondary reactions to smaller molecules or may deactivate the catalyst by blocking the pores. A classic example for product shape selectivity is the considerably faster diffusion of *para*-xylene as compared to that of the *ortho*- and *meta*-xylene in the pores of zeolite ZSM-5. In restricted transition-state shape selectivity,

certain types of transition states or intermediates are too large to be accommodated within the pores or cavities of the zeolite. However, neither the reactants nor the products are restricted from diffusing through the pores of the zeolite. The transalkylation of dialkylbenzenes provides a good example of this type of shape selectivity.

In the property *variable acidity*, the “total” acidity depends on the amount, the strength, the nature and the accessibility of the acid sites in the zeolite. This property can be varied by controlling the  $n_{\text{Si}}/n_{\text{Al}}$  ratio during the zeolite synthesis or in post-treatments. Brønsted- and/or Lewis-type acid sites can be found in zeolites. Brønsted-acid sites are proton donors. Brønsted-acid sites in zeolites are developed when  $\text{Si}^{4+}$  is isomorphously substituted by a trivalent metal cation, e.g.,  $\text{Al}^{3+}$ , whereby a negative charge is created in the lattice, which is compensated by a proton. The proton is attached to the oxygen atom connected to neighbouring silicon and aluminium atoms resulting in a so-called “bridging hydroxyl group”. This site is responsible for the Brønsted acidity in zeolites. The first description of the chemical structure of bridging hydroxyl groups in zeolites has been proposed by Uytterhoeven et al. [23] who described it as a Si-OH group strongly influenced by a tricoordinated neighbouring  $\text{Al}^{3+}$ . Later on, this model was improved by Mortier et al. [24] by considering that the oxygen supporting the acidic hydrogen was chemically bonded to both  $\text{Al}^{3+}$  and  $\text{Si}^{4+}$  making a real bridge between them. The Brønsted-acid sites can be generated by ion-exchanging the zeolite with an acid solution or via thermal decomposition of previously introduced ammonium ions.

Lewis-acid sites show an ability of electron pair acceptor. This can be cations or aluminium defect centers, so-called true Lewis sites. A post-synthetic treatment of zeolites can change the aluminium coordination and create Lewis sites. The processes that can generate Lewis-acid sites are dehydroxylation of Brønsted-acid sites by thermal treatment [25] or the presence of  $\text{Al}^{3+}$  species or various other nonframework species, e.g.,  $\text{AlO}^+$ ,  $\text{Al}(\text{OH})^+$ ,

$\text{Al}(\text{OH})_2^+$ ,  $\text{Al}(\text{OH})_3$ ,  $\text{AlO}(\text{OH})$  and  $\text{Al}_2\text{O}_3$  created by leaching from the zeolite framework during chemical or thermal treatments [26-28]. Fig. 4 depicts schematically Brønsted-acid hydroxyl and Lewis-acid sites formed by dehydroxylation from Brønsted-acid sites.

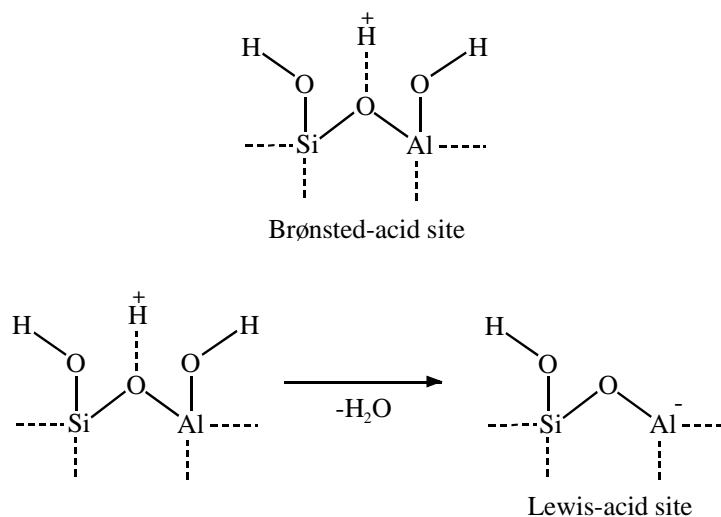


Fig. 4. Schematic representation of zeolitic Brønsted-acid hydroxyl groups and Lewis-acid sites derived by dehydroxylation from Brønsted-acid sites (from ref. [29]).

## 2.2. Structures and properties of the zeolites investigated in this study

### 2.2.1. Zeolite UTD-1

Zeolite UTD-1 (University of Texas at Dallas No. 1; framework-type code: **DON**) was first synthesized in the group of Kenneth Balkus, Jr. in 1995 by using the metallocene complex bis(pentamethylcyclopentadienyl) cobalt(III) hydroxide ( $\text{Cp}^*_2\text{CoOH}$ ) as a structure-directing agent (SDA) [30-33]. The smaller sized variant of this metallocene, viz. bis(tetramethylcyclopentadienyl) cobalt(III) hydroxide, was later reported to be also useful for the synthesis of UTD-1 [34]. Its structure contains unidimensional pores running down the b-axis with extra-large, elliptically-pore shapes circumscribed by 14-membered rings (14-MRs) with a diameter of ca.  $1 \times 0.75$  nm. Its main structural building unit consists of a double layer containing one 6-MRs surrounded by four 5-MRs. Within each layer, the building units

are linked via 4-MRs to form infinite two-dimensional layers parallel to the a-c plane [35, 36] (Fig. 5). The structural characterization of calcined UTD-1 indicates that it is disordered along the unidimensional 14-membered ring (14-MR) channels, but this does not affect the size of the pores, just the topology of the channel walls [36]. It was reported that UTD-1 is the first high-silica zeolite with extra-large pores. With this unusual large pore, combined with a high thermal stability and high acidity, it provides an opportunity to expand the range of industrial applications in the fine chemicals and pharmaceutical industries. For membrane applications, Si-UTD-1 has been successfully prepared as thin film growing onto polished silicon and on porous stainless steel discs by employing a pulse laser deposition technique [37]. These thin film, composed of crystalline zeolite, have attracted interest because of their potential application in the area of separations, catalysis and sensors. Moreover, Ti-UTD-1 (Ti incorporated into zeolite UTD-1) has been screened as catalyst for oxidation of alkanes, alkenes, cyclohexane, phenols and bulkier substrates such as 2,6-di-tertbutylphenol and stilbene using hydrogen peroxide as well as the larger oxidant t-butylhydroperoxide [38]. Recently, the successful preparation of single-walled carbon nanotubes (SWCNT) synthesized in zeolite UTD-1 via vacuum pyrolysis was reported [39]. This carbon nanotubes have shown promising electronic, mechanical, electromechanical and thermal properties.

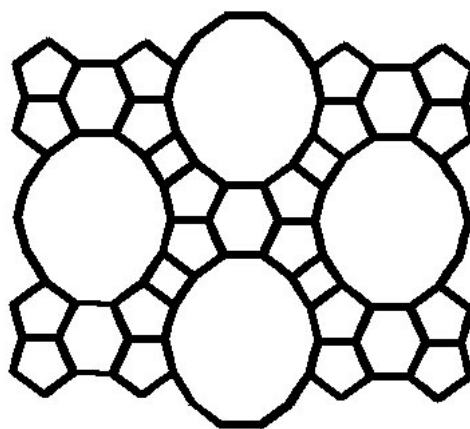


Fig. 5. UTD-1 framework structure viewed down the 14-MR channels.

### 2.2.2. Zeolite CIT-5

Zeolite CIT-5 (California Institute of Technology No. 5; framework-type code: **CFI**) was first synthesized by the group of Mark E. Davis in 1997 [40]. CIT-5 is synthesized in the presence of a bulky and rigid template, viz. N(16)-methylsparteinium and preferably lithium cations [40-43]. This template was used in the very first synthesis. Later, the N(1)-methyl- $\alpha$ -isosparteinium cation, which is a stereoisomer of the first template, has also been used [44]. Its structure is composed of unidimensional and extra-large pores of nearly circular cross section of ca. 0.73 nm circumscribed by 14-MRs. With small side pockets in the pores, a maximum free pore diameter of 1.07 nm is obtained. Its topology consists of zigzag ladders of 4-MRs with pendant 5-MRs. These units are interconnected through single zigzag chains to produce the pseudo body-centered structure [40, 41]. The crystal structure is neither faulted nor disordered. Although CIT-5 has 14-MR channels, its pore dimension is approximately the same as those of 12-MRs found in zeolite Y (ca. 0.75 nm) and zeolite Beta (ca. 0.73 x 0.71 nm). Up to the year of the publication in 1998 [41], UTD-1 and CIT-5 are the only high-silica molecular sieves that contain extra-large pores.

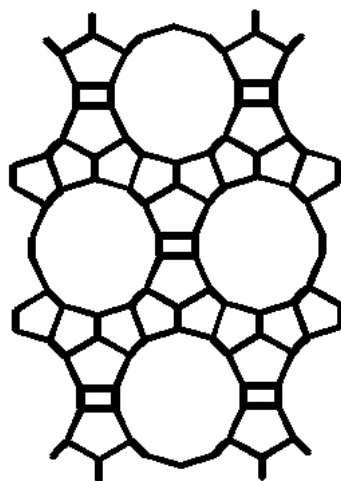


Fig. 6. CIT-5 framework structure viewed down the 14-MR channels.

### 2.2.3. Zeolite SSZ-53

Zeolite SSZ-53 (Socal Synthetic Zeolite No. 53; framework-type code: **SFH**) was patented by Saleh Elomari at Chevron in 2001 [45]. SSZ-53 possesses unidimensional, extra-large pores with an elliptical shape circumscribed by 14-MRs (ca. 0.85 x 0.65 nm) [46]. Like UTD-1, its structure is composed of  $[5^46^1]$  or butterfly building units with insertion of two pairs of 4-MRs between them. Differently, the pores of SSZ-53 are bound by the asymmetric 6-MR nets. This results in pores with a corrugated surface instead of the smooth one like in UTD-1. The pore corrugations are located on the major vertices of the elliptical pore where the curvature is at its maximum.

The structure-directing agent (SDA) for SSZ-53 has been carefully designed by tailoring the effect of template structure to the formed zeolite. As known, a polycyclic rigid template molecule tends to direct the synthesis toward cage-based zeolites, while freely rotating acyclic templates lead to unidimensional or multidimensional channel materials without cages. Therefore, the template has been designed between these two extremities of the rigidity and the flexibility in the following way: The cationic center is very open and accessible to the assembling silicate subunits, while the other portion of the template is fairly bulky with limited freedom of rotation [47]. This novel class of templates are derived from carbonitriles and it was the first time of using such nitriles as the precursors for the preparation of templates in zeolite synthesis [47]. Five types of phenylcycloalkyltrimethyl ammonium cations templates can be applied to synthesize SSZ-53. They are shown in Fig. 7 [45]:

-N,N,N-trimethyl-[1-(4-fluorophenyl)cyclopentyl]methyl ammonium hydroxide (template A)

-N,N,N-trimethyl-[1-(3-fluorophenyl)cyclopentyl]methyl ammonium hydroxide (template B)

-N,N,N-trimethyl-[1-(2-fluorophenyl)cyclopentyl]methyl ammonium hydroxide (template C)

-N,N,N-trimethyl-1-phenylcyclohexyl methyl ammonium hydroxide (template D)

-N,N,N-trimethyl-1-phenylcyclopentyl methyl ammonium hydroxide (template E)

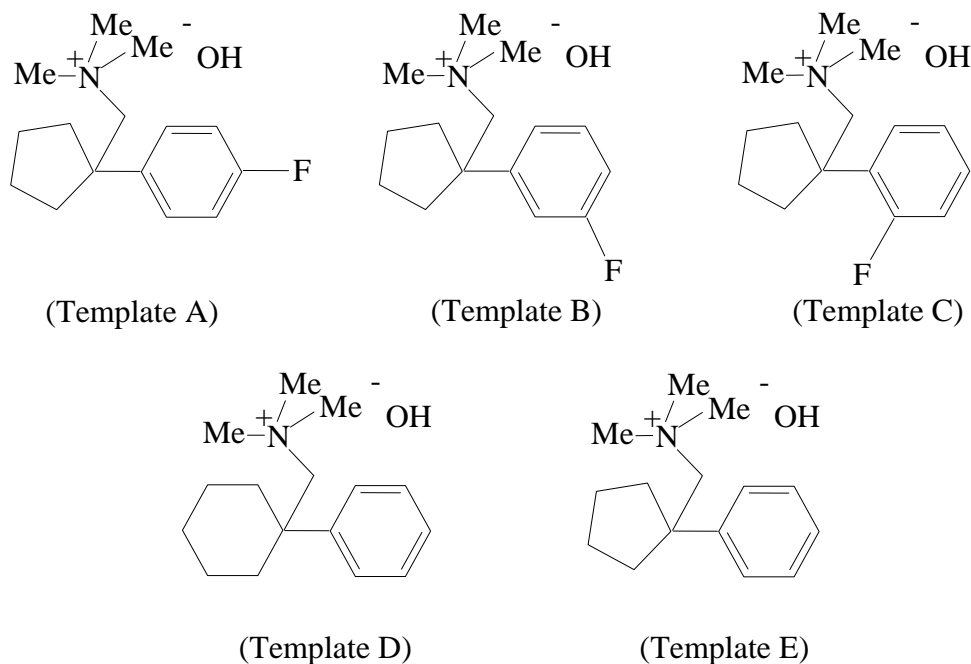


Fig. 7. Templates for the synthesis of zeolite SSZ-53 (from ref. [45]).

Adding different templates (A-D) to the synthesis gel, this sometimes causes a difference in crystallization time in order to achieve a fully crystalline SSZ-53 zeolite. Using template A, the synthesis of SSZ-53 is possible with molar ratios of  $n_{\text{SiO}_2}/n_{\text{B}_2\text{O}_3}$  from 23.5-94 by maintaining SSZ-53 as the majority phase. With higher  $n_{\text{SiO}_2}/n_{\text{B}_2\text{O}_3}$  ratios starting from 141, cristobalite was found as the majority phase together with SSZ-53. Template E is less selective to the formation of SSZ-53 in a narrow range of  $n_{\text{SiO}_2}/n_{\text{B}_2\text{O}_3}$  ratios. It was reported that SSZ-53 has a high cracking activity indicating strong acidic sites. Additionally, the catalyst exhibits good thermal stability. Zeolite SSZ-53 may also be used in other hydrocarbon conversion reactions [48] and the catalytic reduction of nitrogen oxides in a gas stream such as the exhaust gas from a combustion engine [49]. Up to the year of the

publication in 2003 [46], zeolites UTD-1, CIT-5, SSZ-53 and SSZ-59 are the only extra-large pore high-silica zeolites reported to that date.

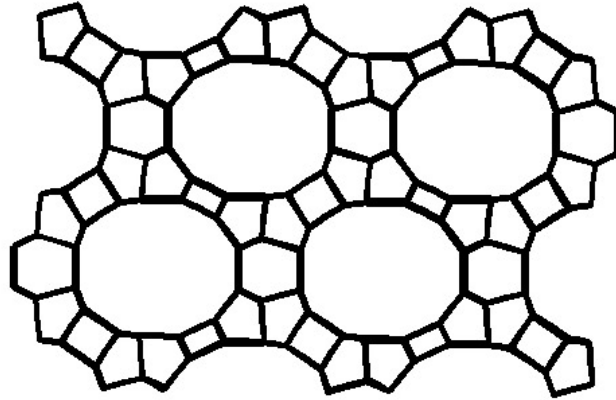


Fig. 8. SSZ-53 framework structure viewed down the 14-MR channels.

#### 2.2.4. Zeolite IM-12

Zeolite IM-12 (Institut Français du Pétrole and University of Mulhouse No. 12) was first synthesized in 2004 [50, 51]. It is a relatively new zeolite with the framework-type code **UTL**. It is synthesized in the presence of germanium and an organic template, viz. the (6R, 10S)-6,10-dimethyl-5-azoniaspiro [4, 5] decane cation. This germanosilicate zeolite contains an interconnected two-dimensional channel system. They are comprised of two types of straight channels defined by 14- and 12-MRs with free-pore diameters of ca. 0.95 x 0.71 nm and ca. 0.85 x 0.55 nm, respectively [50] (Fig. 9). The two-dimensional structure of IM-12 is described as layers stacked in the [100] direction, connected to each other by their 4-MRs and thereby forming double four ring (D4R) units. The germanium atoms can only be localized at T sites of the D4R units. Thus, each layer is essentially siliceous and constructed of fused small [4<sup>1</sup>5<sup>4</sup>6<sup>2</sup>] and [5<sup>2</sup>6<sup>2</sup>] cages. IM-12 displays a high thermal stability and high adsorption capacity.

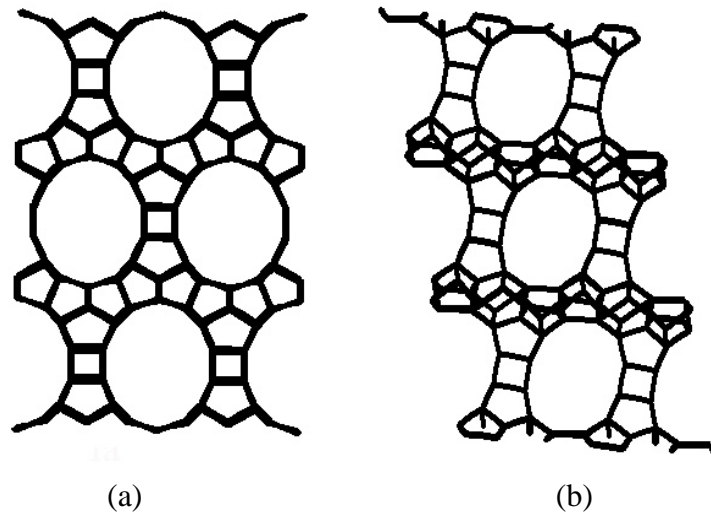


Fig. 9. IM-12 framework structure viewed along: (a) the 14-MR channels and (b) the 12-MR channels.

#### 2.2.5. Zeolite ITQ-21

Zeolite ITQ-21 (**I**nstituto de **T**ecnologia **Q**uimica Valencia No. **21**) was first synthesized in the group of Avelino Corma from Polytechnic University of Valencia in Spain [52-54]. The synthesis of ITQ-21 is achieved using N(16)-methylsparteinium hydroxide as structure-directing agent, either in the absence or in the presence of fluoride ions (i.e., OH<sup>-</sup> or F<sup>-</sup> media, respectively). The presence of germanium in the synthesis gel is also an important factor for the synthesis of this zeolite because the germanium directs towards the formation of structures containing D4Rs as secondary building units [55, 56]. Therefore, this zeolite structure is formed according to two structure-directing effects, viz. (1) the bulky and rigid SDA cations as pore-filling agent and (2) the directing effect of germanium. Another advantage of the germanium is to play an important role in the nucleation step and this leads to the crystallization of this zeolite [57]. As the early syntheses of this zeolite were using the fluoride route, it is believed that this way produces relatively defect-free zeolite crystals [58], with low framework density and quite large crystals [59, 60]. Its structure possesses a three-dimensional pore network containing cavities with a nearly spherical shape of ca. 1.18 nm in

diameter. Each of the cavities is accessible through six windows of ca. 0.74 nm in diameter [53]. The structure further contains  $4^6 6^{12}$  cages which are interconnected via D4R cages as shown in Fig. 10. As compared to zeolite faujasite, ITQ-21 possesses similar windows sizes but contains six windows leading to the large cavities instead of four. This makes the cavities of ITQ-21 much more accessible, hence, it allows for fast diffusion of reactants and products. According to this excellent structure, it makes zeolite ITQ-21 a prominent catalyst for crude oil conversion in the refining industry. ITQ-21 exhibits a high catalytic activity and selectivity for valuable products in preliminary oil refining tests. It was reported that the cracking activity of ITQ-21 is higher than that of ultrastable Y (USY) and much higher than that of zeolite beta. On the other hand, ITQ-21 produces a higher propylene yield than USY and a slightly higher yield than beta zeolites [53]. Recently, it was reported that ITQ-21 exhibits a higher selectivity to diesel-range products at high conversions as compared to USY- and Beta-type catalysts [61]. The results are affected by its particular topology that facilitates the diffusion of the intermediate diesel products by decreasing their re cracking into the lighter compounds.

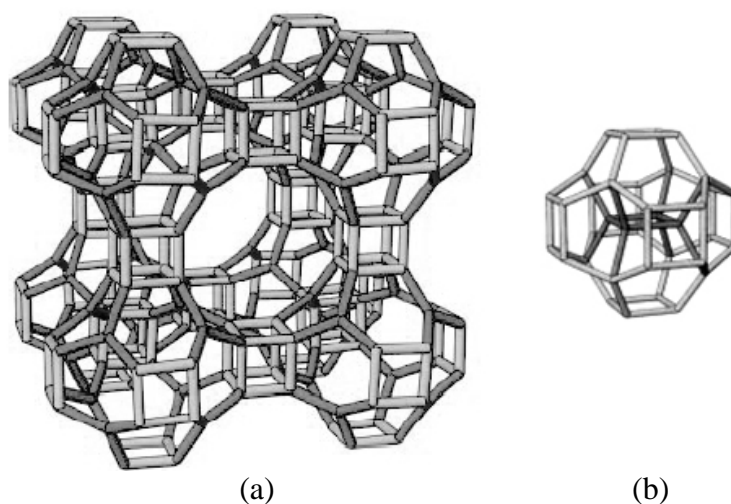


Fig. 10. (a) Perspective view of the unit cell of ITQ-21 and (b)  $[4^6 6^{12}]$  cage interconnected via double four ring units.

### 2.2.6. Zeolite MCM-68

Zeolite MCM-68 (Mobil Composition of Matter No. **68**; framework-type code: **MSE**) was patented in 2000 [62]. Its structure possesses a three-dimensional framework consisting of 12-MR channels (ca. 0.68 x 0.65 nm) intersecting with two orthogonal undulating 10-MR channels (ca. 0.55 x 0.51 nm) as shown in Fig. 11. The intersection of the two 10-MR channels creates an oval supercage with four 10-MR windows leading to the 12-MR channels. It is the first three-dimensional aluminosilicate with at least one 12-MR channel that does not represent a family where stacking faults occur as a prominent disorder [63]. Because of its high acidity and its particular structure, MCM-68 is useful in various industrial applications such as catalytic cracking [64], isomerization of paraffins [65], hydroalkylation of aromatic hydrocarbons [66], production of alkylaromatic compounds [67], production of arylsulfides and composites [68] and catalytic dewaxing [69]. Moreover, MCM-68 is found to be a highly active catalyst due to the presence of strong acid sites as deduced from the acid-catalyzed disproportionation of ethylbenzene as test reaction [70]. Recently, MCM-68 was also used to study hydrocarbon trap applications [71].

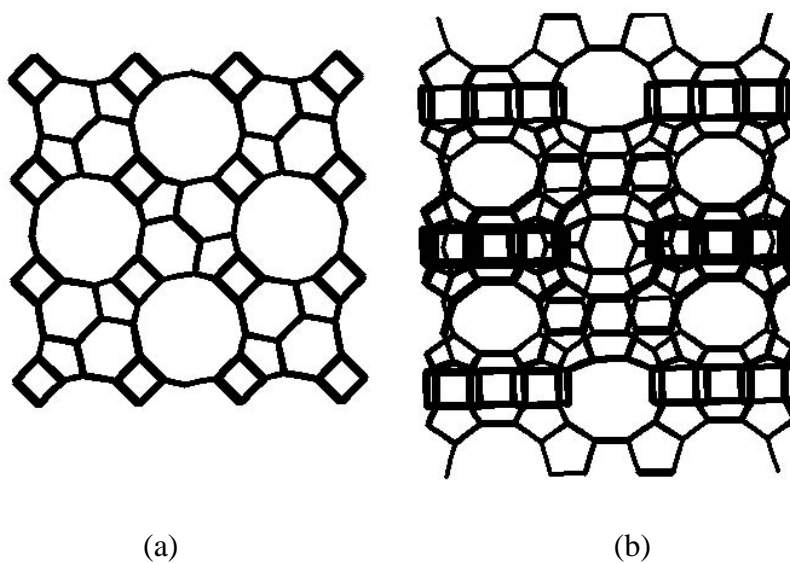


Fig. 11. MCM-68 framework structure viewed along: (a) the 12-MR channels and (b) the tortuous 10-MR channels.

### 2.2.7. Zeolite SSZ-35

Zeolite SSZ-35 (**S**ocal **S**ynthetic **Z**eilite No. **35**; framework-type code: **STF**) was patented by Yumi Nakagawa at Chevron in 1994 [72, 73]. Its structure contains unusual unidimensional straight channels which are circumscribed, in an alternating manner, by 10-MRs (ca. 0.61 x 0.55 nm) and contorted 18-MRs (ca. 1.25 x 0.9 nm) [74] (Fig. 12). This particular structure, viz. medium sized pores leading to a large cavity, makes this zeolite a promising shape-selective catalyst. It is the first high-silica zeolite that possesses pores with rings larger than 14-MR. Up to now, additional isostructural materials with the **STF** topology are ITQ-9 [75] and Mu-26 [76]. Zeolite SSZ-35 can be synthesized with a large number of templates, in particular with cyclic and polycyclic quaternized amine molecules. The template for SSZ-35 was discovered based on the design of organic molecules as structure-directing agents in order to synthesize large pore zeolites [77]. It was reported that the synthesis of SSZ-35 is also possible with a new template family of stereoisomers, e.g., N-methyl hexahydrojulolidinium salt [78].

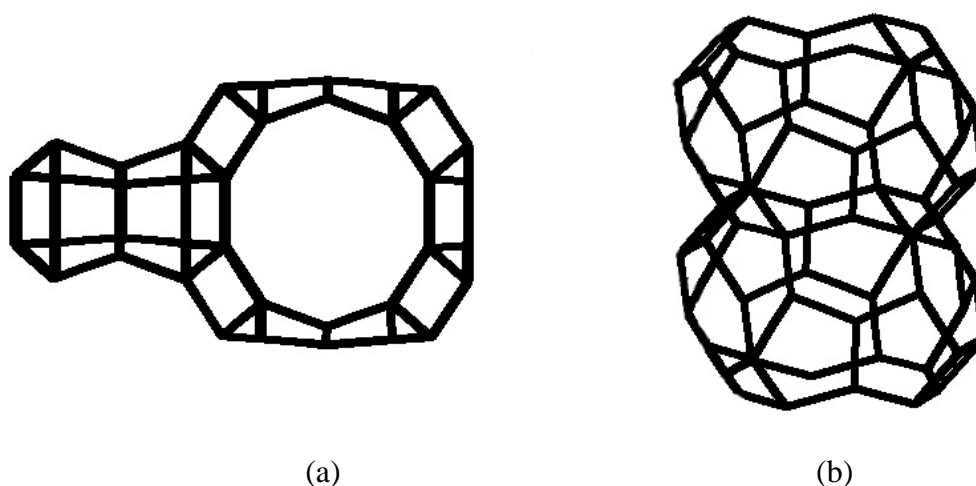


Fig. 12. SSZ-35 framework structure: (a) viewed along the 10-MR channel and (b) on the side view of interconnected staged cages.

### 2.2.8. Zeolite MCM-71

Zeolite MCM-71 (Mobil Composition of Matter No. **71**) was patented in 2002 [79]. It represents a new microporous material in the mordenite family [80]. This material possesses a two-dimensional network consisting of straight, highly elliptical 10-MR channels (ca. 0.65 x 0.43 nm) and orthogonal sinusoidal 8-MR channels (ca. 0.47 x 0.36 nm). The structure viewed along the 10-MR channels is shown in Fig. 13. The calcined form of MCM-71 has an X-ray diffraction pattern resembling that of DCM-2 [81]. This medium pore zeolite is useful for shape-selective acid catalysis such as dewaxing of the waxy feeds in preparation of lubricating oil basestocks [82-84].

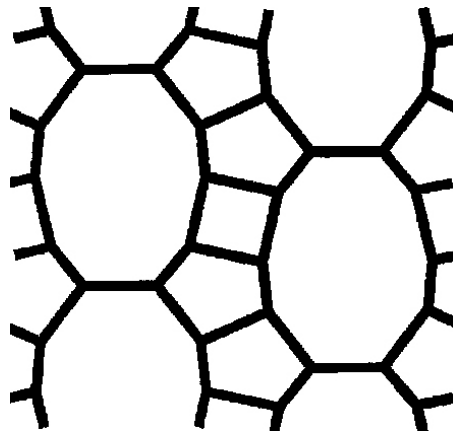


Fig. 13. MCM-71 framework structure viewed along the 10-MR channels.

The structural information of the zeolites selected for this study are summarized in Table 1.

Table 1. Structural data for the zeolites investigated in the present study.

Zeolite	Structure type	Pore structure	Ring size	Approximate pore size (nm)	Patent year and ref.	Ref. of structure
UTD-1	<b>DON</b>	unidimensional channels	14	1.0 x 0.75	1996 [33]	[35, 36]
CIT-5	<b>CFI</b>	unidimensional channels	14	0.73	2000 [42]	[40, 41]
SSZ-53	<b>SFH</b>	unidimensional channels	14	0.85 x 0.65	2001 [45]	[46]
IM-12	<b>UTL</b>	2D, intersection between 14- and 12-MR straight channels	14 12	0.95 x 0.71 0.85 x 0.55	2004 [51]	[50]
ITQ-21	-	3D, spherical cage (ca. 1.18 nm) with six 12-MR windows	12	0.74	2002 [52]	[53]
MCM-68	<b>MSE</b>	3D, intersection among straight 12-MR and two undulating 10-MR channels	12 10	0.68 x 0.65 0.55 x 0.51	2000 [62]	[63]
SSZ-35	<b>STF</b>	unidimensional channel with staged cages (18-MR: ca.1.25 x 0.9 nm)	10	0.61 x 0.55	1994 [72]	[74]
MCM-71	-	2D, intersection between straight 10-MR and undulating 8-MR channels	10 8	0.65 x 0.43 0.47 x 0.36	2002 [79]	[79, 80]

### 2.3. Methods for characterizing the acidity of solid catalysts

Infrared spectroscopy is one method of choice for a comprehensive examination of acid sites in zeolites. Both, (1) direct characterization of the protonated form of the zeolite in the hydroxyl stretching frequencies ( $3000\text{-}3800\text{ cm}^{-1}$ ) and (2) the spectroscopic changes observed when basic probe molecules are adsorbed ( $1400\text{-}1700\text{ cm}^{-1}$ ) give useful information about the nature of the acid sites. Pyridine is one of the most prominent basic probe molecules used in the IR spectroscopy for titration of the acid sites. This is useful because the assignment of the vibrations associated with pyridinium ions formed on Brønsted-acid sites and coordination complexes at Lewis-acid sites is established. The pioneering work in this respect has been done by Parry [85], Basila et al. [86] and Hughes and White [87]. Moreover, IR spectroscopy combined with temperature-programmed desorption can give an estimate of the acid strength distribution. Typical IR bands found on solid catalysts in the hydroxyl stretching and in the adsorbed pyridine region are summarized in Table 2.

The vibration region of the bridging hydroxyl groups varies for different zeolite structures, e.g., zeolite Y:  $3550$  and  $3650\text{ cm}^{-1}$  [87], ZSM-5:  $3600\text{ cm}^{-1}$  [90] and mordenite:  $3585$  and  $3612\text{ cm}^{-1}$  [91]. The given values are only guidelines.

Table 2. The assignment of the IR bands found on the acidic solid catalysts both in the hydroxyl stretching and the adsorbed pyridine region (the values taken from refs. [85-89]).

Vibration (cm <sup>-1</sup> )	Assigned group
3740-3750	external silanol (SiOH)
3550-3660	bridging hydroxyl (SiOHAl, Brønsted-acid site)
ca. 1640	pyridinium ions (PyH <sup>+</sup> , Brønsted-acid site)
1600-1633	coordinatively bonded pyridine (Lewis-acid site)
1580-1600	physisorbed pyridine
1540-1550	pyridinium ions (PyH <sup>+</sup> , Brønsted-acid site)
1485-1500	pyridinium ions/coordinatively bonded pyridine
1447-1460	coordinatively bonded pyridine (Lewis-acid site)
1440-1447	physisorbed pyridine

#### 2.4. Test reactions for characterizing the pore size and architecture of zeolites

Catalytic test reactions are valuable tools for characterizing the effective pore width and pore architecture of zeolites and related molecular sieves. Among these reactions are the competitive cracking of *n*-hexane and 3-methylpentane (determination of the constraint index, CI) [8], *m*-xylene conversion [9], ethylbenzene disproportionation [10], isomerization and hydrocracking of *n*-decane (the modified constraint index, CI<sup>\*</sup>) [11, 12] and hydrocracking of butylcyclohexane (the spaciousness index, SI) [13]. Applying such test reaction has some advantages with respect to physicochemical characterization such as

adsorption, viz. they are carried out under catalytically relevant conditions and offer the possibility to detect both, mass transfer effects (reactant and product shape selectivity) and chemical effects (restricted transition-state shape selectivity). The latter is not detectable by sorption techniques. For an ideal test reaction, the following holds: (1) it should supply the maximum information from a single measurement, (2) the experiment is easy to operate, (3) the disappearance of the reactants should not be diffusion controlled, (4) the test should be performed in non-deactivating condition and (5) the reaction mechanism should be relatively well understood.

In this work, ethylbenzene disproportionation over acidic catalysts and *n*-decane hydroconversion over bifunctional catalysts have been applied as tools to characterize the pore sizes and pore architectures of the prepared zeolites.

#### **2.4.1. Ethylbenzene disproportionation as test reaction**

##### *2.4.1.1. Application to investigate pore size and architecture of zeolites*

Initially, this test reaction was applied to characterize the acidity of zeolites. It was first applied by Karge et al. in 1981 to explore the conditions under which pure transalkylation of ethylbenzene occurs using hydrogen mordenite zeolites [92]. It was found that pure transalkylation took place at temperatures <200 °C and the catalyst did not exhibit substantial deactivation over 20 h time-on-stream. This suggested the possibility to apply the ethylbenzene disproportionation as a test reaction for characterizing the structure of zeolites without any complications due to the catalyst aging. In 1982, Karge et al. also studied various mordenite-type zeolites in the hydrogen, sodium, alkaline earth and lanthanum forms in this reaction in order to characterize their Brønsted-acid properties [93]. The results showed a linear relationship of the reaction rate and the density/number of Brønsted-acid sites as determined by infrared spectroscopy. Therefore, this reaction was proposed as a test reaction

for exploring the acidity of zeolites. Further results with faujasite-type zeolites also confirm this correlation [94]. Additionally, for faujasite-type zeolites, it was shown that only very strong Brønsted-acid sites ( $H_0 \leq -8.2$ , titration technique by Benesi [95]) are capable of catalyzing the disproportionation of ethylbenzene [94]. Acidic forms of pentasil zeolites such as ZSM-5 and ZSM-11 are active for this reaction [96]. In contrast to dealuminated mordenites, they show shape selectivity in that no ortho-isomer is formed and, at low aluminium content, the para-isomer occurs in excess over the meta-isomer. In 1986, Weitkamp et al. have applied this test reaction to various acidic zeolites with different pore sizes and shapes, viz. ZSM-5, ZSM-12, ZSM-22, ZSM-25, ZSM-34, ZSM-35, ZSM-48, ferrierite and FU-1. They have suggested ethylbenzene disproportionation reaction as a test reaction for the discrimination between large (12-MR) and medium (10-MR) pore zeolites for materials with unknown structure [10]. The classification is based on four parameters: (1) the presence of an induction period which typically occurs with large pore zeolites, (2) the rate of deactivation which is faster on medium pore zeolites, (3) the product ratio of diethylbenzene to benzene which is near-stoichiometric on large pore zeolites and (4) the equilibrium distribution of diethylbenzene isomers is observed on large pore zeolites. Moreover, the presence of large molecules like triethylbenzenes as products indicates that the zeolite contains large pores. Later on, this reaction has been proposed as standard reaction for zeolite characterization by the Catalysis Commission of the International Zeolite Association (IZA) [97].

Under appropriate conditions, pure disproportionation of ethylbenzene takes place. This means that two molecules of ethylbenzene (E-Bz) produce one molecule of benzene (Bz) and of diethylbenzene (DE-Bz). Thus, the molar yield of benzene to diethylbenzenes is 1:1. The possible diethylbenzene isomers are 1,2-(ortho-), 1,3-(meta-) and 1,4-(para-) diethylbenzene.

The theoretical product spectrum from pure ethylbenzene disproportionation is shown in Fig. 14.

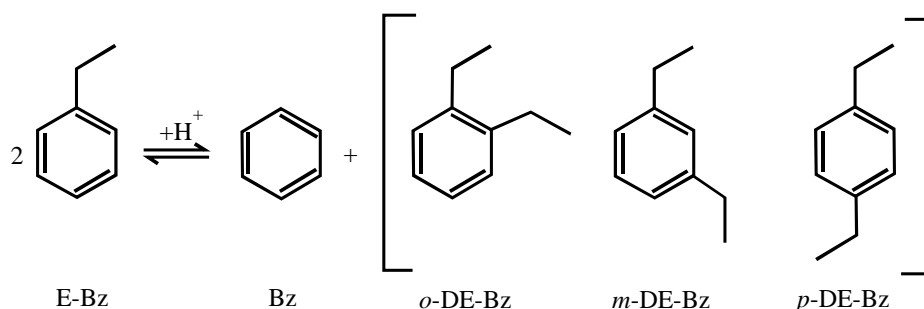


Fig. 14. Product spectrum expected from pure ethylbenzene disproportionation.

#### 2.4.1.2. Mechanism of alkylbenzene disproportionation

The early studies on the mechanism of alkylbenzene disproportionation were carried out in the liquid phase. In 1953, McCaulay and Lien have proposed a displacement mechanism for alkylbenzene disproportionation [98]. They studied the disproportionation of six different alkylbenzenes in the presence of hydrogen fluoride and boron trifluoride (HF-BF<sub>3</sub>) at room temperature. Their mechanism involves the formation of a stable “ $\sigma$ -complex” by the addition of a proton from the strong protonic acid HBF<sub>4</sub> to the ring carbon atom positioning of the alkyl group (Fig. 15a). Then, this  $\sigma$ -complex undergoes a nucleophilic attack by an other aromatic compound opposite to the alkyl group and forms an intermediate carbocation (Fig. 15b). This is supposed to be the rate determining step. Afterwards, the bond of the migrating alkyl group from the first ring is broken and forms a partial bond to the second aromatic ring before the intermediate disproportionates into benzene and a dialkylbenzene.

In 1956, Brown and Smoot investigated the nature of the transition state in the disproportionation of various alkylbenzenes under the influence of hydrogen bromide and aluminium bromide (HBr-Al<sub>3</sub>Br<sub>6</sub>) [99]. The results showed that the monoalkylbenzenes disproportionated rapidly to diethylbenzenes which are in turn relatively slowly converted to

trialkylbenzenes. The difference in the disproportionation rate of mono-, di- and triethylbenzenes could be accounted for in terms of the relative stabilities of their formed  $\sigma$ -complexes. In order to explain the large difference in the reaction rates with varying the alkyl groups, they suggested the following modification in the mechanism of McCaulay and Lien: It was proposed that the  $\sigma$ -complex of the aromatic is first equilibrated with a localized “ $\pi$ -complex” of higher energy and then acts as an intermediate in the displacement reaction instead (Fig. 16). In essence, McCaulay, Lien, Brown and Smoot have a common suggestion, viz. the disproportionation takes place by a “displacement mechanism”.

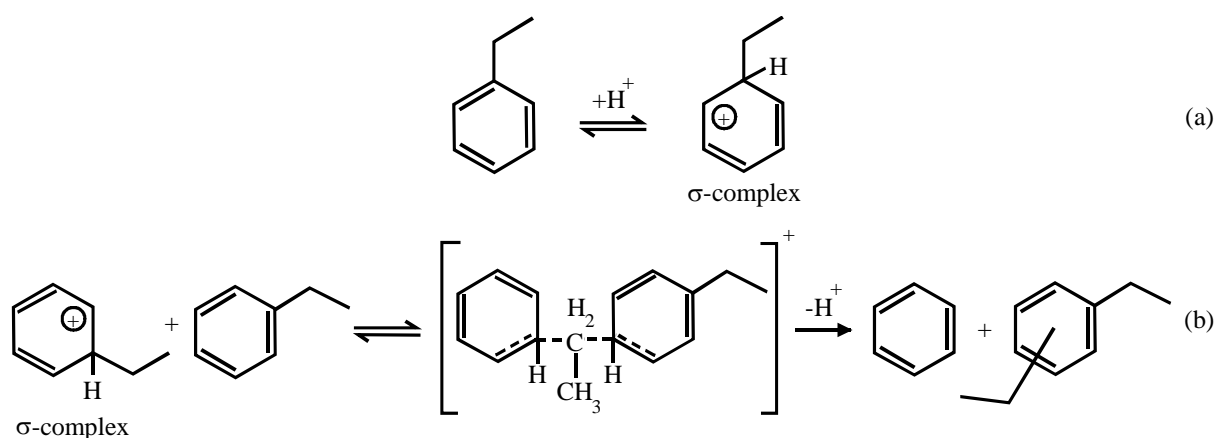


Fig. 15. Mechanism of alkylbenzene transalkylation by McCaulay and Lien (from ref. [98]).

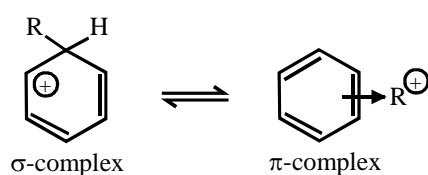


Fig. 16. The proposed intermediate  $\pi$ -complex in the displacement reaction by Brown and Smoot (R: alkyl groups) (from ref. [99]).

In 1960, Streitwieser and Reif investigated the mechanism of transalkylation by applying a radioactive tracer method (labelled ethylbenzene with carbon-14 on the ring and deuterium at the alpha position) [100]. The reaction took place with gallium bromide and hydrogen

bromide ( $\text{GaBr}_3\text{-HBr}$ ) (as catalysts) in benzene at 50 °C. The results suggested that transalkylation is initiated by hydride abstraction to yield carbonium ions because the loss of optical activity and of radioactivity occurred at equal rates. This proposal argued that transalkylation by a displacement mechanism, which was proposed by McCaulay and Lien and Brown and Smoot, is unlikely. Instead, Streitwieser and Reif have proposed that the mechanism involves 1,1-diphenylethane as a short-living intermediate under the conditions of their study. The original  $\alpha$ -phenethyl cation presumably arises from traces of styrene initially present. The mechanistic scheme of transalkylation by Streitwieser and Reif is represented in Fig. 17. Reactions (a), (b) and (c) are postulated to be rapid and (d) is proposed to be the rate-determining step.

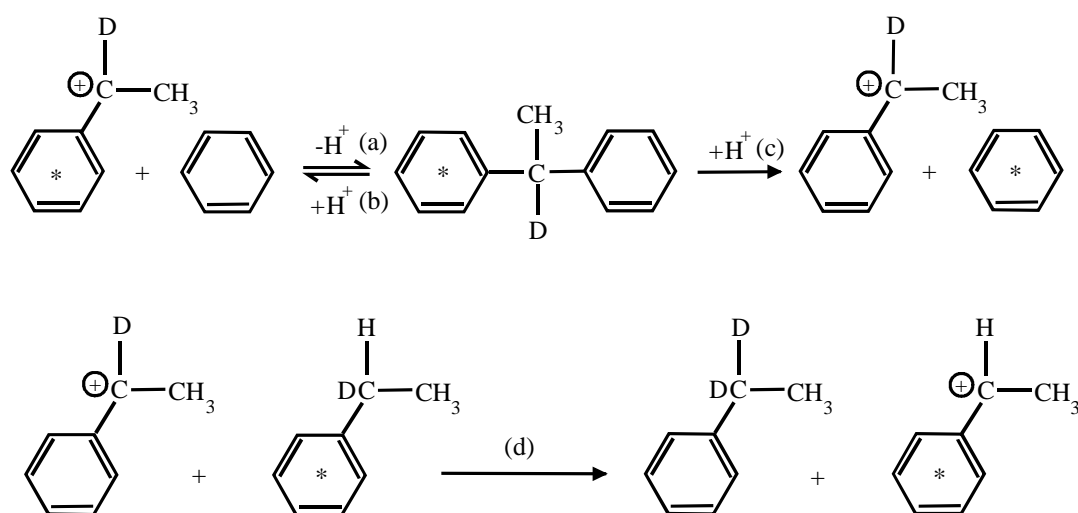


Fig. 17. Transalkylation mechanism via diarylalkanes and hydride transfer as proposed by Streitwieser and Reif (\*: carbon-14-containing ring; from ref. [100]).

Another proposed mechanism proceeds via dealkylation/alkylation. It occurs by cleavage of the alkyl group from one aromatic ring followed by addition of the alkyl group to another aromatic ring and yields unsaturated species, e.g., olefins and diolefins as by-products. In the literature, there are several reports on alkylbenzene transformation via dealkylation. For example, McCaulay and Lien have observed a change in the mechanism at higher reaction

temperatures, in which the alkyl group is eliminated from the aromatic cation [98]. The aromatic cation dissociates into a neutral aromatic molecule and an alkylcarbenium ion. Then, it reacts further via isomerization, alkylation, polymerization and hydride-ion abstraction leading to a complex product spectrum. The transalkylation of aromatics with ethylene groups over acidic zeolites takes place via dealkylation/alkylation. The mechanism is presented in Fig. 18, where (a) the alkylbenzene cation is produced by attack of a proton from the acid catalyst, (b) the alkylbenzene cation is dealkylated into neutral aromatic and alkylcarbenium ion, (c) the deprotonation of the alkylcarbenium ion to produce an alkene, (d) the alkylcarbenium ion alkylates with other alkylbenzene and (e) the deprotonation of alkylated cation molecule to dialkylbenzene.

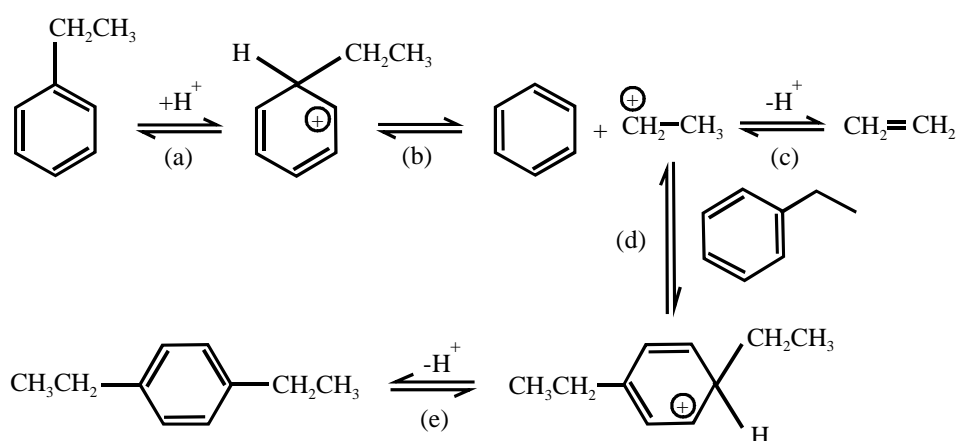


Fig. 18. Mechanism of transalkylation via dealkylation/alkylation (from ref. [101]).

Two mechanisms, viz. the biphenylalkane intermediate (from Streitwieser and Reif) and via dealkylation/alkylation are mainly observed in the disproportionation of ethylbenzene in the presence of zeolite catalysts [101-106]. The relative importance of the two pathways depends on the zeolites and the operating conditions. However, the mechanism via a biphenylalkane intermediate primarily occurs because of its lower activation energy. For example, Amelse has shown the influence of the zeolite structure on the dominating reaction mechanism [101]. Applying radioactive-labelled ethylbenzene, it appeared that the disproportionation occurred

very rapidly via the biphenylethane route for zeolites having large pores, i.e., zeolite Y and mordenite, whereas the dealkylation/alkylation mechanism was predominant for medium pore zeolites, i.e., AMS-1B, since the formation of bulky biphenylethane intermediates is possible only where there is enough space. In medium pore zeolites like ZSM-5, the disproportionation of ethylbenzene occurred mainly through a deethylation/ethylation pathway [102-104, 106].

#### 2.4.1.3. Mechanism of dialkylbenzene isomerization

Two different mechanisms have been proposed for the acid catalyzed isomerization of dialkylbenzenes. In 1964, Olah et al. suggested that the isomerization of diethylbenzenes with water-promoted aluminium chloride at 25 °C proceeds solely through a series of intramolecular 1,2-shifts [107]. Fig. 19 presents the scheme of this proposed isomerization mechanism of diethylbenzenes (in case of *p*-diethylbenzene). On the other hand, in 1968, Bolton et al. found that the isomerization proceeds via a transalkylation mechanism over partially decationized and partially cerium-exchanged Y-type faujasite catalyst at 170 °C, [108]. Fig. 20 shows the isomerization reaction scheme based on the transalkylation mechanism. In 1971, Csicsery experimentally confirmed that the isomerization of polyalkylbenzenes over Ca-NH<sub>4</sub><sup>+</sup> Y-type faujasite catalysts might proceed by the above-mentioned two mechanisms [109]. It was found that the isomerization, which proceeds through 1,2-shifts, has a significantly higher activation energy than the isomerization process involving the transalkylated intermediates. Consequently, the dialkylbenzenes isomerize primarily by 1,2-shifts at higher temperature (i.e., >300 °C), while the intermolecular reaction involving the transalkylated intermediates predominates at lower temperatures (i.e., <200 °C). At intermediate temperatures, both processes contribute to a similar extent.

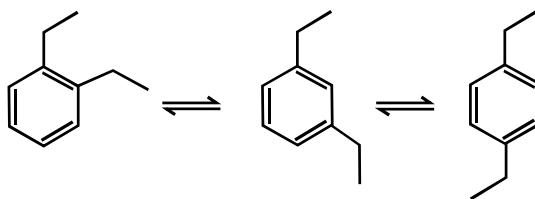


Fig. 19. 1,2-Shift mechanism of the isomerization of diethylbenzenes proposed by Olah et al. (from ref. [107]).

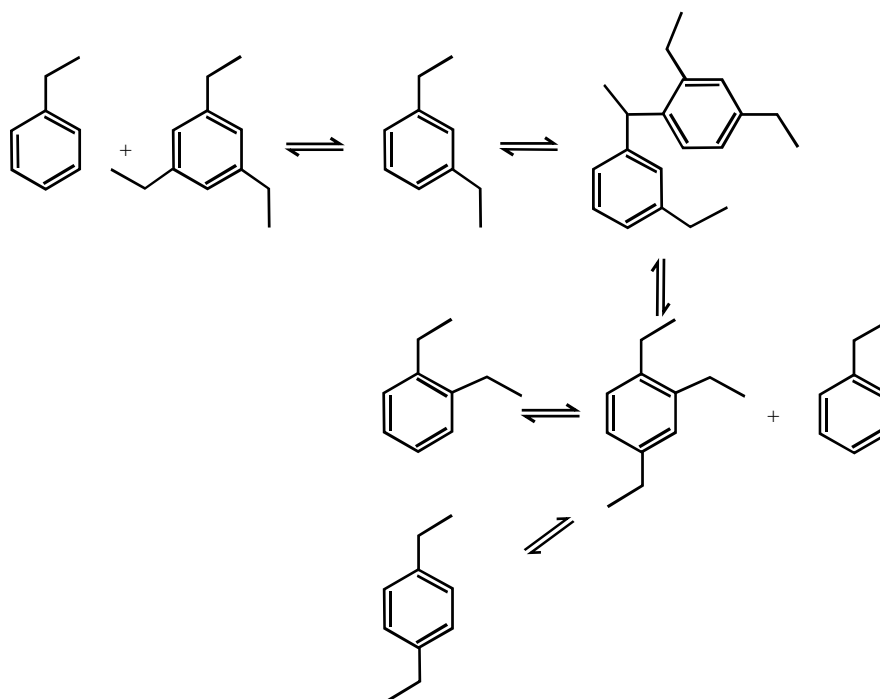


Fig. 20. Transalkylation mechanism of the isomerization of diethylbenzenes proposed by Bolton et al. (from ref. [108]).

#### 2.4.1.4. Thermodynamic equilibrium of the diethylbenzene isomers

In order to investigate the influence of shape-selective effects of the investigated zeolites on the product distribution, the product distribution at the thermodynamic equilibrium should be considered. Assuming pure disproportionation of ethylbenzene (E-Bz), the product consists of benzene (Bz) and three diethylbenzene (DE-Bz) isomers, viz. 1,2-DE-Bz, 1,3-DE-Bz and 1,4-DE-Bz. The calculation is based on the following three equations:



The calculation is based on ref. [110]. The molar fraction of each compound at thermodynamic equilibrium can be obtained from the following equation:

$$x_{i,eq} = \frac{x_i + \frac{v_{i1}}{|v_{k1}|} x_k(U_{k,1})_{eq} + \frac{v_{i2}}{|v_{k2}|} x_k(U_{k,2})_{eq} + \frac{v_{i3}}{|v_{k3}|} x_k(U_{k,3})_{eq}}{1 + \frac{\left(\sum_i v_i\right)_1}{|v_{k1}|} x_k(U_{k,1})_{eq} + \frac{\left(\sum_i v_i\right)_2}{|v_{k2}|} x_k(U_{k,2})_{eq} + \frac{\left(\sum_i v_i\right)_3}{|v_{k3}|} x_k(U_{k,3})_{eq}} \quad \text{equation 4}$$

Where:

- $x_{i,eq}$  = molar fraction of each compound at thermodynamic equilibrium
- $x_i$  = molar fraction of each compound at the beginning of the reaction
- $x_k$  = molar fraction of the reactant at the beginning of the reaction (= 1)
- $U_{k,n}$  = extent of reaction “n” (n = 1,2,3)
- $v$  = stoichiometric coefficient
- $i$  and  $k$  = index for compound  $i$  and reactant, respectively

The index “eq” for “equilibrium” and “k” for “reactant” will be neglected in the later description. Therefore, the numbers of the molar fraction for each compounds in thermodynamic equilibrium are obtained as:

$$x_{E-Bz} = \frac{1 - U_1 - U_2 - U_3}{1} = 1 - (U_1 + U_2 + U_3) \quad \text{equation 5}$$

$$x_{Bz} = \frac{\frac{1}{2}U_1 + \frac{1}{2}U_2 + \frac{1}{2}U_3}{1} = 0.5(U_1 + U_2 + U_3) \quad \text{equation 6}$$

$$x_{1,2-DE-Bz} = \frac{\frac{1}{2}U_1}{1} = 0.5U_1 \quad \text{equation 7}$$

$$x_{1,3-DE-Bz} = \frac{\frac{1}{2}U_2}{1} = 0.5U_2 \quad \text{equation 8}$$

$$x_{1,4-DE-Bz} = \frac{\frac{1}{2}U_3}{1} = 0.5U_3 \quad \text{equation 9}$$

In each equation, assuming that one mole of E-Bz is initially present, there will be x moles of Bz and also x moles of DE-Bz isomer at the thermodynamic equilibrium. Therefore, the equilibrium constants of the three reactions can be written as:

$$K_1 = \frac{x_{Bz} \cdot x_{1,2-DE-Bz}}{(x_{EBz})^2} = \frac{0.5(U_1 + U_2 + U_3)(0.5U_1)}{(1 - (U_1 + U_2 + U_3))^2} \quad \text{equation 10}$$

$$K_2 = \frac{x_{Bz} \cdot x_{1,3-DE-Bz}}{(x_{EBz})^2} = \frac{0.5(U_1 + U_2 + U_3)(0.5U_2)}{(1 - (U_1 + U_2 + U_3))^2} \quad \text{equation 11}$$

$$K_3 = \frac{x_{Bz} \cdot x_{1,4-DE-Bz}}{(x_{EBz})^2} = \frac{0.5(U_1 + U_2 + U_3)(0.5U_3)}{(1 - (U_1 + U_2 + U_3))^2} \quad \text{equation 12}$$

Equations 10-12 can be simplified as:

$$\frac{K_1}{K_2} = \frac{U_1}{U_2}, \quad \frac{K_1}{K_3} = \frac{U_1}{U_3} \quad \text{and} \quad \frac{K_2}{K_3} = \frac{U_2}{U_3}$$

The equilibrium constants of the three reactions can be determined from the change of standard Gibbs free enthalpy of formation,  $\Delta G_{f,T}^o$  and the thermodynamic data are obtained from ref. [111].

$$(\ln K_i)_T = \frac{-1}{R \cdot T} \sum_i \nu_i (\Delta G_{f,T}^o)_i \quad \text{equation 13}$$

Where:

$(K_i)_T$  = equilibrium constant of reaction no.  $i$  ( $i = 1,2,3$ ) at temperature  $T$

$R$  = ideal gas constant ( $\text{J}\cdot\text{mol}^{-1}\cdot\text{K}^{-1}$ )

$T$  = reaction temperature (K)

$\nu_i$  = stoichiometric coefficient of compound  $i$  in the reaction

$(\Delta G_{f,T}^0)_i$  = change of standard Gibbs free enthalpy of formation of compound  $i$  at temperature  $T$  ( $\text{J}\cdot\text{mol}^{-1}$ )

The values of “ $K$ ” and “ $x$ ” for each temperature are solved from equation 5 to 13. Then the obtained molar fractions of diethylbenzene isomers are normalized and are shown in Fig. 21.

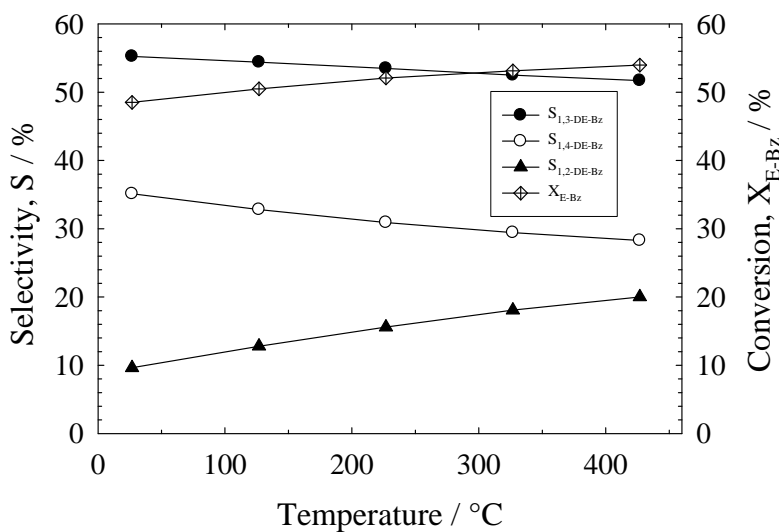


Fig. 21. The distribution of diethylbenzene isomers and conversion of ethylbenzene at thermodynamic equilibrium depending on the reaction temperature.

## 2.4.2. *n*-Decane hydroconversion as test reaction

### 2.4.2.1. Application for characterizing the pore size and architecture of zeolites

*n*-Decane hydroconversion was proven to be a useful test reaction for determining the architecture of intracrystalline void volumes of zeolites with unknown structure [11, 12]. The

bifunctional catalyst, combining acid and hydrogenation properties, is prepared by introducing a well-dispersed metal into the pores of an acid zeolite. The advantage of the bifunctional reaction is that the catalyst deactivation due to coke formation is absent or very slow. This test reaction allows to classify zeolite structures in terms of 12-MR pores, 12-MR pores with cages/lobes, 8-MR pores with cages of different sizes, and 10-MR pores. Its principle is to measure the distribution of isomers and of hydrocracked products of the reaction over a number of zeolites with already known pore structures and to compare to this the respective selectivities measured with zeolites of unknown structure. From this comparison, characteristic structural features of the new zeolite can be derived.

Eight criteria, obtained from the product distribution from *n*-decane conversion, are handled to characterize the pore width and pore architecture of the zeolite as proposed by Martens et al. [11, 12].

1. The relative distribution of mono- to dibranched isomers at maximum yield of isomerization.
2. The relative formation of ethyloctane to methylnonane isomers at ca. 5 % yield of isomerization.
3. The relative distribution of 3- to 4-ethyloctane at different reaction temperatures.
4. The relative distribution of 2- to 5-methylnonane at ca. 5 % yield of isomerization.
5. The yield of isopentane in the hydrocracked products at ca. 35 % hydrocracking yield.
6. The yield of propylheptane in monobranched isomers at ca. 75 % conversion.
7. The relative distribution of 2,7-dimethyloctane in the fraction of dibranched isomers at ca. 5 % yield of dibranched isomers.
8. The symmetry of the molar distribution of hydrocracked products with respect to their carbon numbers or the molar difference between C<sub>3</sub>-C<sub>7</sub> and C<sub>4</sub>-C<sub>6</sub> in the hydrocracked products at ca. 35 % hydrocracking yield.

Quantitatively, the modified constraint index or  $CI^*$  has been defined as the ratio of 2- to 5-methylnonane at ca. 5 % yield of isomerisation (from criterion 4). This index is used to characterize the effective pore width of zeolites. In the absence of geometric constraints in the zeolite pore system, the value of  $CI^*$  is expected to be one. When the effective pore width of the zeolite decreases, this index value increases due to spatial constraints. Table 3 shows the values of  $CI^*$  for some zeolites with known pore structures.

Table 3. Modified constraint indices ( $CI^*$ ) and pore sizes of selected zeolites (ref. [112]).

Zeolite	$CI^*$	Void characteristics	Dimensions (nm)
L	1.0	1D, 12-MR	0.71 (lobe 0.75)
HY	1.3	3D, 12-MR	0.74 (cage 1.2)
mordenite	1.8	2D, 12-MR 8-MR	0.70 x 0.67 0.57 x 0.29
offretite	1.8	2D, 12-MR 8-MR	0.64 0.52 x 0.36
ZSM-12	2.2	1D, 12-MR	0.61 x 0.57
chabasite	2.3	3D, 8-MR	0.37 x 0.36 (cage 1.1 x 0.65)
erionite	2.5	3D, 8-MR	0.52 x 0.36 (cage 1.50 x 0.63)
ZSM-11	2.7	2D, 10-MR	0.55 x 0.51
clinoptilolite	3.6	2D, 10-MR 8-MR 8-MR	0.72 x 0.44 0.55 x 0.44 0.47 x 0.41
ZSM-48	5.2	1D, 10-MR	0.56 x 0.53
ZSM-5	6.8	2D, 10-MR	0.54 x 0.52
ferrierite	10.3	2D, 10-MR 8-MR	0.55 x 0.43 0.48 x 0.34
ZSM-22	14.4	1D, 10-MR	0.55 x 0.45

### 2.4.2.2. Mechanistic concepts for the isomerization and hydrocracking of long chain *n*-alkanes

If an *n*-alkane is converted on a bifunctional catalyst in the presence of hydrogen, two principal reactions take place, namely skeletal isomerization and hydrocracking. The overall reaction network according to the bifunctional mechanism is represented in Fig. 22. This principle follows the widely accepted reaction scheme of hydrocracking presented for the first time by Coonradt and Garwood [113]. It exhibits that isomerization and hydrocracking are consecutive reactions.

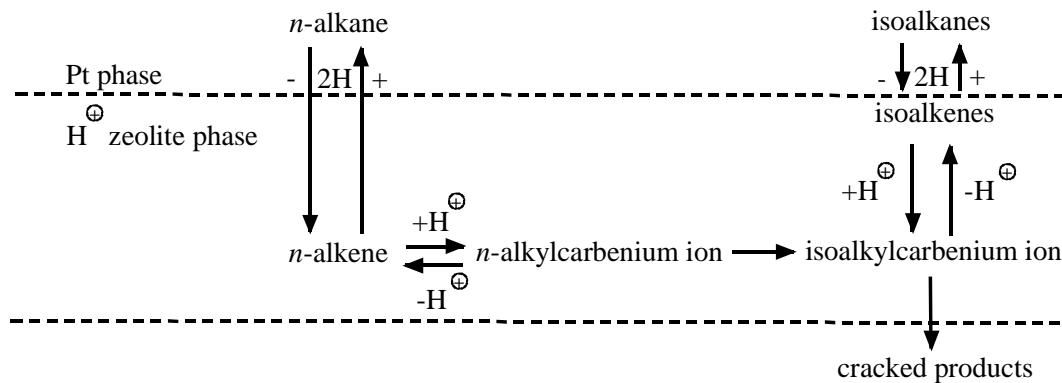


Fig. 22. Classical bifunctional mechanism for *n*-alkane conversion (from ref. [113]).

Details of this reaction network were presented by Weitkamp and Ernst [114] as depicted in Fig 23. It shows that both skeletal isomerization and the carbon-carbon bond cleavage occur in different branching levels of alkylcarbenium ions. The main pathway from long chain *n*-alkanes to the hydrocracked products is shown by the bold arrows.

The feed *n*-alkane is first dehydrogenated on the metal phase producing *n*-alkenes with the same carbon number. These alkenes move to acid sites where they are protonated to alkylcarbenium ions. These alkylcarbenium ions, while chemisorbed at the acid sites, can undergo two principal reactions, either skeletal rearrangement to the branched isomers or  $\beta$ -scission into smaller alkylcarbenium ions and alkenes. The first route is more likely.

At low conversion, the monobranched  $i\text{-C}_m\text{H}_{2m+1}$  cations are desorbed from the acid sites as  $i$ -alkenes and then hydrogenated at the metal sites to monobranched  $i$ -alkanes. These appear as a sole product. The monobranched alkylcarbenium ions could undergo type C  $\beta$ -scissions, but these are too slow, so that upon raising conversion the monobranched alkylcarbenium ions prefer to undergo skeletal rearrangement to dibranched cations. The resulting dibranched alkylcarbenium ions can desorb and appear as dibranched  $i$ -alkanes in the product or undergo type B  $\beta$ -scissions. Upon further increasing conversion, the dibranched cations rearrange once more into tribranched ones. These can undergo the very rapid type A  $\beta$ -scission.

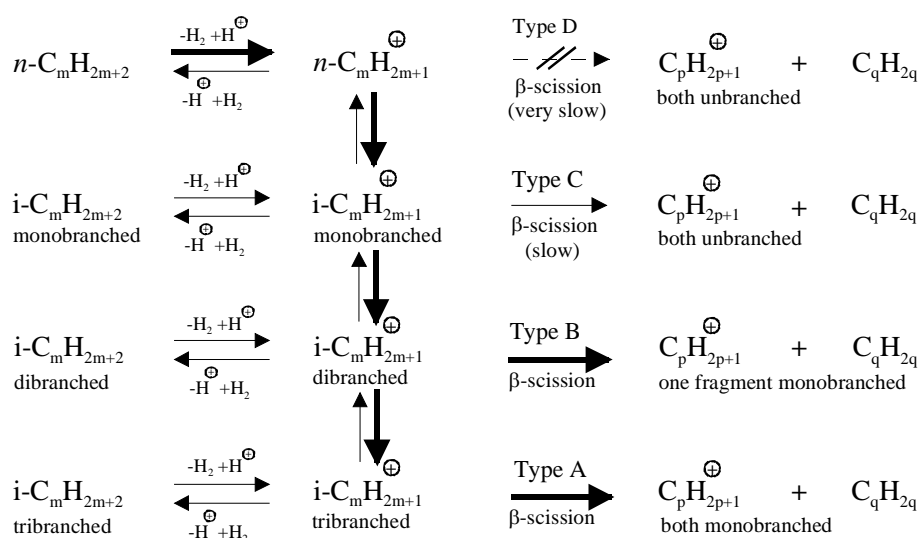


Fig. 23. Detailed reaction network for isomerization and hydrocracking of  $n$ -alkanes on bifunctional catalysts ( $m$ : carbon number of the feed; from ref. [114]).

The skeletal rearrangements of alkylcarbenium ions have been classified as shown in Fig. 24 according to Brouwer and Hogeveen [115] and Weitkamp and Farag [116]. In type A rearrangement, the number of branching remains constant, whereas in type B rearrangement the number of branching increases or decreases. Type A rearrangement proceeds via a more conventional hydride and alkyl shifts, while type B proceeds via protonated cyclopropanes (PCPs). The reaction rate of type A rearrangement is considerably higher than that of type B.

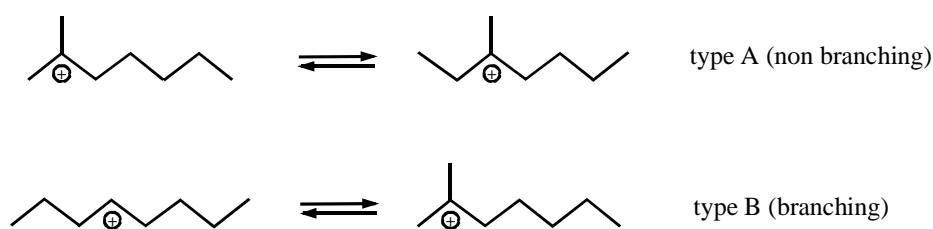


Fig. 24. Classification of skeletal rearrangement reactions of alkylcarbenium ions.

In case of *n*-decane conversion, the product mixture obtained at low conversions consists of all possible isodecanes with one branching, viz. 2-, 3-, 4- and 5-methylnonanes, 3- and 4-ethyloctanes and 4-propylheptane. The formation rate decreases in this order methyl  $\gg$  ethyl  $>$  propyl isomers.

At low conversions or under kinetically controlled conditions, the formation of methylnonane isomers proceeds via the PCPs. This has been concluded from sophisticated experiments which showed that the classical mechanism via alkyl and hydride shifts fails to explain the low formation rate of 2-methylnonane [117]. The distribution of methylnonane isomers formed by isomerization of *n*-decane is presented in Fig. 25.

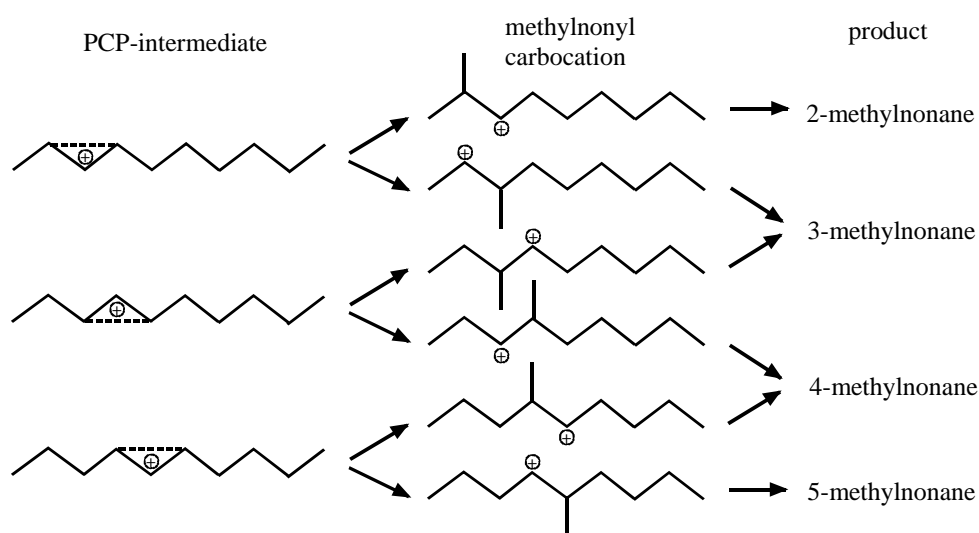


Fig. 25. Distribution of methylnonanes from protonated cyclopropane (PCP) structures.

Table 4. Distribution of methylnonane isomers in the isomerization of *n*-decane as predicted by a PCP mechanism [11] and at thermodynamic equilibrium [117].

	PCP mechanism (%)	Thermodynamic equilibrium (%)
2-methylnonane	16.7	29.4
3-methylnonane	33.3	28.3
4-methylnonane	33.3	28.3
5-methylnonane	16.7	14

Based on the PCP mechanism, the amounts of 2- and 5-methylnonane are formed at equal rates and with only half the formation rates of 3- and 4-methylnonane. The distribution is different from the one obtained at thermodynamic equilibrium. However, at higher conversion, the initially formed isomers can be equilibrated via more conventional methyl shifts and their distribution can reach the thermodynamic equilibrium [118].

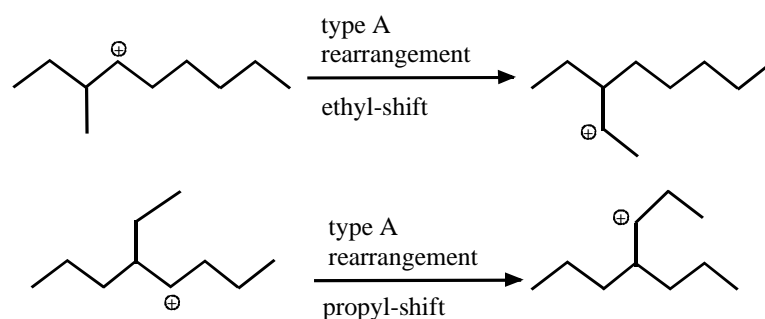


Fig. 26. Principal routes to the formation of ethyl and propyl isomers.

3-Ethyloctane formation can be accounted for via the classical ethyl shift from 3-methylnonane, since the branching mechanism via PCPs fails to explain the relatively low rates of the formation of the 3-ethyl isomer observed experimentally [117]. Another possible route for the propyl-shift from this isomer is unlikely. 4-Ethyloctane is obtained from the 3-ethyl isomer via an ethyl-shift. The formation of propylheptane is possible via a propyl-shift

from 4-ethyloctane. Therefore, the formation of all decane isomers can be explained by the combination of chain branching via PCP ions and fast equilibration via alkyl-shifts. Fig. 26 shows the principal routes of the formation of ethyl and propyl isomers.

The multiply branched isomers are formed in consecutive reactions from monobranched species. Considerable amounts of dimethyl isomers can be produced at elevated conversions. Trimethyl isomers occur in traces only either because  $\beta$ -scission of dibranched carbenium ions is faster than their rearrangement to tribranched species or because  $\beta$ -scission of tribranched carbenium ions is faster than their desorption [117].

According to Fig. 23, normal, mono, dibranched, and tribranched cations can undergo hydrocracking into smaller fragments in different pathways depending on the branching types. Weitkamp et al. have proposed the mechanism of hydrocracking classified by ionic  $\beta$ -scission as shown in Fig. 27 [119].

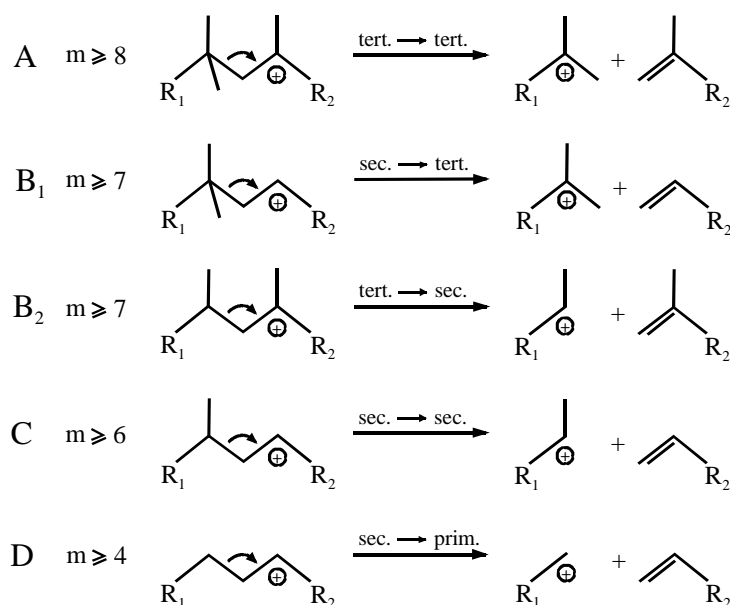


Fig. 27. Classification of  $\beta$ -scissions of alkylcarbenium ions ( $m$ : carbon number of the feed) (from ref. [119]).

- type A:  $\beta$ -scission starts from a tertiary and leads to a tertiary carbenium ion.

- type B:  $\beta$ -scission starts from a secondary and leads to a tertiary carbenium ion or vice versa.
- type C:  $\beta$ -scission starts from a secondary and leads to a secondary carbenium ion.
- type D:  $\beta$ -scission starts from a secondary and leads to a primary carbenium ion.

The relative rates decrease drastically from type A to type D  $\beta$ -scissions. Therefore, type A  $\beta$ -scission is the most likely to occur. This is a result from enthalpy differences in their parent alkylcarbenium ions. From type D to type A  $\beta$ -scissions, the minimum carbon number required in the parent alkylcarbenium ions increases from four to eight. With the ideal bifunctional catalyst and in sufficiently spacious pore systems, hydrocracking occurs mainly via tribranched carbenium ions with type A  $\beta$ -scission. There is also some contribution of type B  $\beta$ -scission starting from dibranched carbenium ions. Type D  $\beta$ -scission is unlikely to occur. It is observed that type A  $\beta$ -scission results only in branched fragments and  $C_3$  and  $C_{m-3}$  fragments are absent.

Under steric constraint, e.g., in a 10-MR pore zeolite, the reaction mechanism as shown in Fig. 23 is forced into alternative routes involving less bulky intermediates. The narrower the pores, the higher will be the contribution of type B and eventually type C or even type D  $\beta$ -scissions because the formation of the bulky alkylcarbenium ions is hindered. This effect is reflected by the skeleton rearrangement route as well. The influence of shape selectivity from the zeolite to the isomerization and hydrocracked products from *n*-alkanes was primarily investigated by Jacobs et al. [120, 121] and Weitkamp et al. [119]. There are some common observations over medium pore Pt/HZSM-5-type catalysts: The predominant feed isomers are those with one single methyl branching and the formation of dimethyl isomers is hindered. Moreover, tribranched, ethyl- or even bulkier side chain isomers are absent. This is in

contrast to the isomerized product distribution on large pore zeolite (in the absence of shape selectivity), e.g., Pt/CaY [117], Pt/USY [120] and Pt/HY [121], for which the formation of all possible decane isomers is observed. This indicates the influence of space restrictions induced by the zeolite pores on the formation and/or desorption of the bulky isomers.

The distribution of individual methylbranched isomers on Pt/HZSM-5 deviates drastically from those observed on a catalyst without spatial constraints. In case of *n*-decane as feed, at low conversion a catalyst without space constraints shows the formation of 2-methylnonane as only one half of the 3- and 4-methylnonanes. By contrast, over Pt/HZSM-5, 2-methylnonane is the preferentially formed isomer.

In the hydrocracked products on Pt/HZSM-5, only *n*-alkanes and *i*-alkanes with one methyl branching are formed. A small amount of dimethyl isomers occurs at high conversions. No *i*-alkanes with an ethyl or bulkier side chains are detected. The cracking products categorized by the carbon number typically exhibit an asymmetrical distribution. This suggests that the cracking mechanism in Pt/HZSM-5 is different from that obtained in large pore zeolites. The asymmetry in the distribution of hydrocracked products indicates that (i) some secondary cracking of the largest fragments formed from the primary cracking step or (ii) some steric hindrance of the largest fragments for diffusing out of the relative narrow pores. Moreover, Pt/HZSM-5 produces relative large amounts of C<sub>3</sub> and C<sub>m-3</sub> products as compared to those of zeolite Y. This can be explained through a preferred cracking route via type C β-scission. A contribution of type A β-scission is unlikely since trimethyl isomers can not enter the intracrystalline pores of the Pt/HZSM-5 as proven in ref. [121].

Jacobs et al. [121] have investigated in detail which cracking route contributes to the hydrocracked products over Pt/HZSM-5. The proposed reaction schemes used to predict the hydrocracked product distribution are given in Fig. 28. In scheme 1, monomethyl isomers

could rearrange via PCPs and form dimethylbranched ions as intermediates. The latter can probably be formed at the channel intersections but are most probably not able to diffuse out of the pores. After their formation, the intermediates are cracked via type B<sub>2</sub> β-scission. Scheme 2 presents hydrocracking starting directly from monobranched carbenium ions via type C β-scission. The combination of both proposed mechanisms is able to fit the experimental results in an acceptable manner. Thus, the combination of both routes is favoured over Pt/HZSM-5-type catalysts and contributes to a large extent to the hydrocracked products.

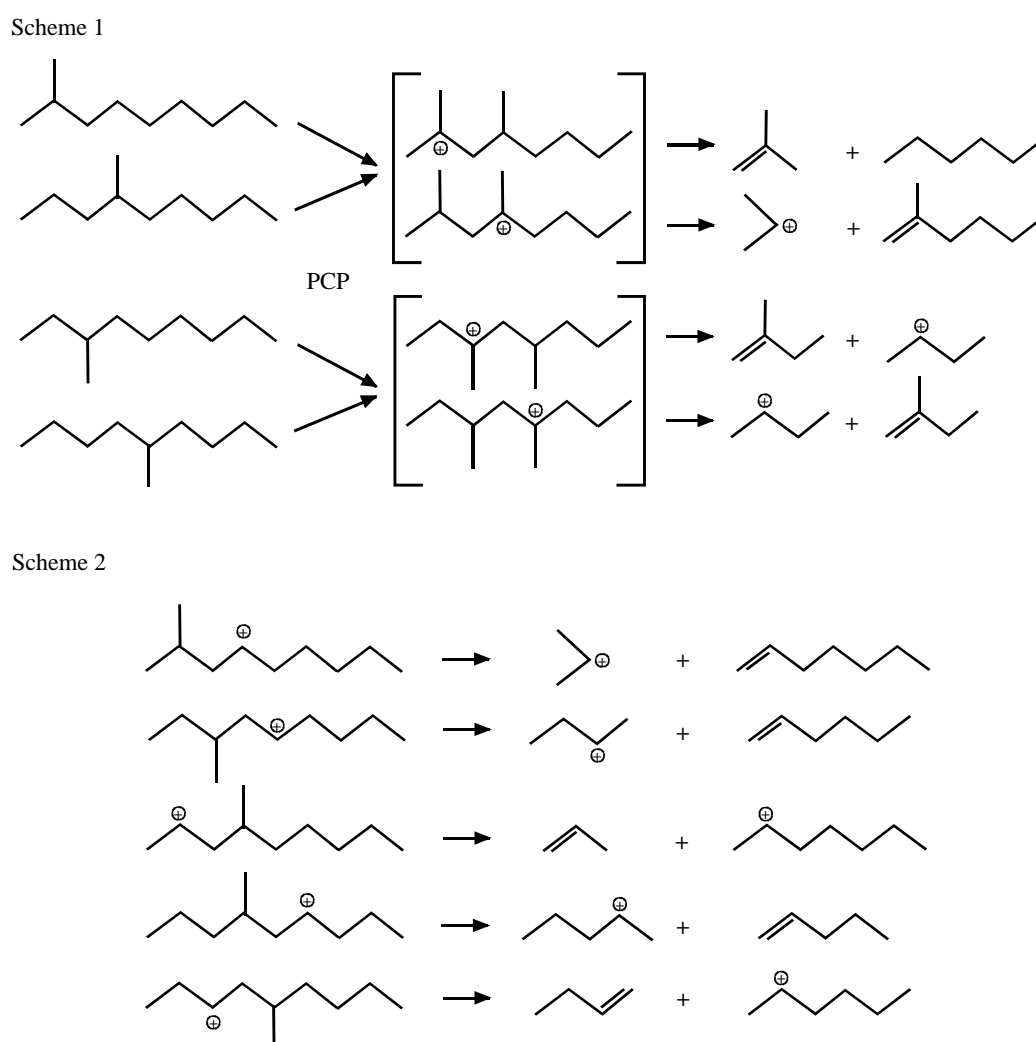


Fig. 28. Hydrocracking of isomeric carbenium ions on Pt/HZSM-5 via type B<sub>2</sub> β-scission (scheme 1) and via type C β-scission (scheme 2) (from ref. [121]).

## 2.5. Competitive hydrogenation of olefins for probing the location of noble metals in zeolites

In order to obtain useful information of the pore size and pore architecture of zeolites by the bifunctional conversion of *n*-decane, it is a prerequisite that most of the noble metal in the bifunctional catalyst is located inside the intracrystalline pores. The location of the noble metal depends mainly on the catalyst preparation and pretreatment methods. Introducing the noble metal via ion-exchange from metal complexes in aqueous phase into the zeolite is probably the most widely used method for the preparation of bifunctional catalysts (zeolites). However, a problem could arise if the pores of the zeolites are smaller than the metal complex. This is the case with certain 10-MR zeolites and, of course, with most 8-MR zeolites so that it is not possible for the noble metal complexes to diffuse into the pores.

An analytical tool to investigate the location of the metal clusters was first presented by Dessau in 1982 [122, 123]. He applied the competitive hydrogenation of an equimolar mixture of 1-hexene and 4,4-dimethyl-1-hexene in order to determine the location of platinum metal in/on the medium pore zeolite ZSM-5. The idea is that if the noble metal is located mainly at the outer surface of the zeolite crystallites, both alkenes can be hydrogenated and should give roughly similar yields of their saturated compounds. However, when most of the noble metal is located inside the pores, only the slim 1-hexene can enter the intracrystalline channels and is hydrogenated to *n*-hexane. Therefore, the resulting saturated product contains only *n*-hexane, while the branched olefin remains unchanged. Hence, the observed effects can be interpreted as reactant shape selectivity.

Later, Weitkamp et al. recommended a test with the same basic idea but applying another bulkier reactant, viz. 2,4,4-trimethyl-1-pentene together with the same slim olefin 1-hexene [124]. These two alkenes exhibit similar rates of hydrogenation over Pt/active charcoal (viz.

in the absence of shape selective). Fig. 29 illustrates the principle of the competitive hydrogenation of the slim 1-hexene and the bulky 2,4,4-trimethyl-1-pentene for two situations: (a) when most of the hydrogenation-active metal is located inside the pores of a zeolite with narrow pores, only the slim 1-hexene is hydrogenated to *n*-hexane; (b) when the metal is located both, inside and outside (i.e., at the external surface of the zeolite crystallites) the pores of the zeolite, both alkenes are hydrogenated to *n*-hexane and 2,2,4-trimethylpentane.

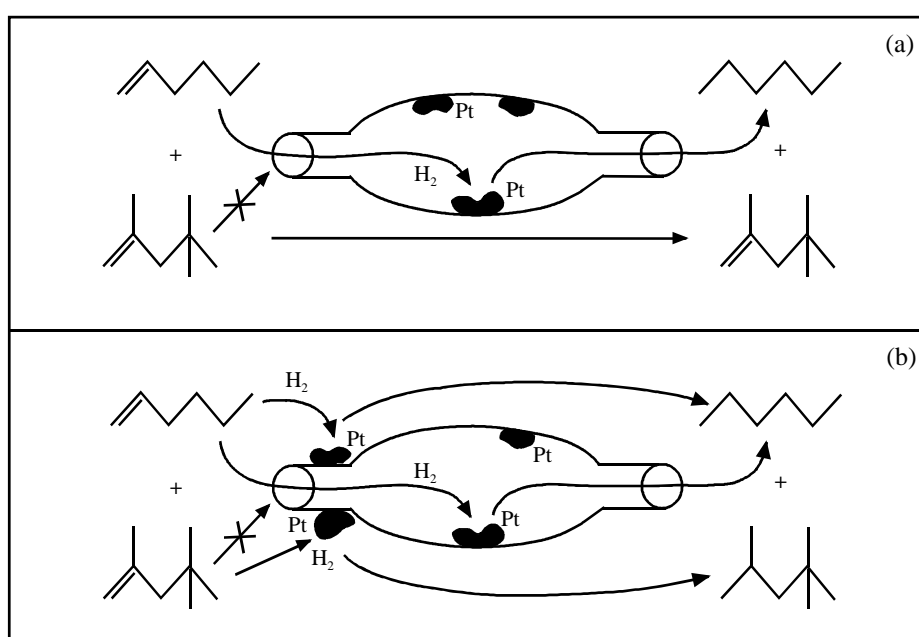


Fig. 29. Schematic representation of the competitive hydrogenation of a mixture of 1-hexene and 2,4,4-trimethyl-1-pentene over a Pt-containing zeolite (from ref. [124]).

Based on the method suggested by Weitkamp et al., various noble metal-loaded zeolite catalysts have been characterized, viz. the 10-MR zeolites Pt/ZSM-5 [124] and Ru/ZSM-5 [125] and the 8-MR zeolites Pt/ZSM-58 [124-126], Pd/ZSM-58, Pd/Rho, Pd/ZK-5 and Pd/SAPO-42 [126].

### 3. Experimental section

#### 3.1. Synthesis and preparation of more recent zeolites with unusual pore architectures

##### 3.1.1. Zeolites based on 14-membered ring pore openings

###### 3.1.1.1. Zeolite UTD-1

###### Template preparation

The starting compounds for the template to synthesize zeolite UTD-1 were obtained from the group of Professor Dr. H. Sitzmann, Inorganic Chemistry, TU Kaiserslautern. They provided bis(pentamethylcyclopentadienyl) cobalt(III) hexafluorophosphate ( $\text{Cp}^*_2\text{CoPF}_6$ ) and bis(pentamethylcyclopentadienyl) cobalt(III) chloride ( $\text{Cp}^*_2\text{CoCl}$ ). The preparation of the final template was modified from ref. [127]. The method started by dissolving 10 g of  $\text{Cp}^*_2\text{CoPF}_6$  in 50 ml of a solution of 10 wt.-%  $\text{H}_2\text{O}$  in acetone. Then, the hexafluorophosphate form was converted to the chloride form over a Dowex-50WX8-100 cation-exchange resin (1.7 meq/ml, Aldrich) by first adsorbing the  $\text{Cp}^*_2\text{Co}^+$  ions onto the resin which was filled into an ion exchanger column. The  $\text{Cp}^*_2\text{Co}^+$  ions were eluted from the resin with 5 l of 2 M HCl (p.a., J.T. Baker). A yellow solid consisting of  $\text{Cp}^*_2\text{CoCl}$  was obtained through completely evaporating the acid solution with a rotary evaporator. The solid  $\text{Cp}^*_2\text{CoCl}$  was dissolved in water and the solution was passed through an anion-exchange resin column containing Dowex-550A (1.1 meq/ml, Aldrich) to convert it to the hydroxide form. Additional 200 ml water was used to flush the column. The collected solution was concentrated using a rotary evaporator. Its concentration was determined by titration with 0.051 M HCl with methyl red as an indicator (obtained concentration: 0.35 mol/kg). Fig. 30 shows the scheme of preparation of bis(pentamethylcyclopentadienyl) cobalt(III) hydroxide ( $\text{Cp}^*_2\text{CoOH}$ ).

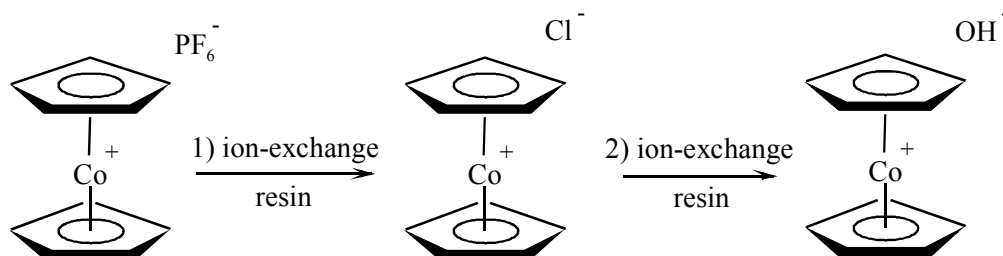


Fig. 30. Scheme of preparation of bis(pentamethylcyclopentadienyl) cobalt(III) hydroxide.

### Synthesis

Zeolite UTD-1 was prepared in two forms, viz. as boron-containing UTD-1 (B-UTD-1) and as high-silica UTD-1 (Si-UTD-1). The recipes were adjusted and modified from refs. [31, 127]. The acidic form of UTD-1 was prepared by adding a boron source to the synthesis mixture. Thus, B-UTD-1 was prepared from the molar gel ratio: 1 SiO<sub>2</sub>: 0.017 B<sub>2</sub>O<sub>3</sub>: 0.13 Cp\*<sub>2</sub>CoOH: 0.05 Na<sub>2</sub>O: 60 H<sub>2</sub>O: 0.23 OH<sup>-</sup> ( $n_{\text{Si}}/n_{\text{B}}$  in the gel = 30). The gel was prepared by mixing 0.06 g NaOH (p.a., Merck), 5.58 g Cp\*<sub>2</sub>CoOH solution (0.35 mol/kg) and 11.3 g distilled water. The mixture was stirred for 15 min. After adding 1 g of calcined boron-containing Beta zeolite (B-Beta) (90.5 wt.-% SiO<sub>2</sub>, 1.75 wt.-% B<sub>2</sub>O<sub>3</sub>, 7.75 wt.-% H<sub>2</sub>O, self-prepared from the modified recipe in the patent [128]), the gel was stirred for another 1 h.

For Si-UTD-1, the gel molar ratio: 1 SiO<sub>2</sub>: 0.13 Cp\*<sub>2</sub>CoOH: 0.05 Na<sub>2</sub>O: 60 H<sub>2</sub>O: 0.23 OH<sup>-</sup> was prepared by mixing 0.063 g NaOH (p.a., Merck), 5.86 g Cp\*<sub>2</sub>CoOH solution (0.35 mol/kg) and 11.9 g distilled water. The mixture was stirred for 15 min. After adding 1 g of silica gel 40 (95 wt.-% SiO<sub>2</sub>, 5 wt.-% H<sub>2</sub>O, Fluka), the gel was stirred for another 1 h.

In both cases, each gel mixtures were transferred to Teflon-lined stainless steel autoclaves (volume: 25 ml). The reaction took place at 165 °C under rotating at 40 rpm for 4 d.

### Modification and preparation of the acidic form

The as-synthesized samples were calcined by heating in a muffle furnace in N<sub>2</sub> at 1.5 °C/min to 120 °C and holding for 2 h. Then, the temperature was ramped at 1.5 °C/min to 540 °C and held for 2 h in N<sub>2</sub> and for another 34 h in air. The removal of cobalt oxide formed in the zeolite channels and on the outer surface of the zeolite crystallites was accomplished by stirring the calcined form in a solution of 2 M HCl (1 g zeolite/100 ml solution) at 90 °C for 24 h. The resulting white solid was filtered, washed with water until chloride-free and dried overnight. To prepare an acidic version with a higher acid strength, viz. aluminium-containing UTD-1, the cobalt-free B-UTD-1 was stirred in a 1 M aluminium nitrate solution (1 g zeolite/25 ml solution) at 95 °C for 6 h. The mixture was then filtered and the recovered zeolite was rinsed with water. The solid was dried at 100 °C for 12 h and thereafter calcined at 540 °C for 24 h in N<sub>2</sub> to give the protonated form of Al-UTD-1 (H-UTD-1).

#### *3.1.1.2. Zeolite CIT-5*

### Template preparation

This preparation was modified from the patent [129]. 20 ml (86 mmol) of (-)-spartein (99 wt.-%, Aldrich) was dissolved in a solution of 18.5 g (129 mmol) iodomethane (≥99 wt.-%, Riedel-de Haën) in 175 ml of acetone (p.a., J.T. Baker). The mixture was stirred at 25 °C in the dark for 24 h. Then 150 ml of diethylether (p.a., Riedel-de Haën) was added to stop the reaction. The cream-coloured solid product was filtrated, washed with diethylether and dried in vacuum (29.2 g, 90 % yield). The product was purified by recrystallization with a mixture of isopropanol (p.a., Merck) and ethyl acetate (p.a., J.T. Baker). The crystals were recovered after cooling down with an ice bath, filtered and washed with ethyl acetate to remove traces of impurities. The purified product was dried under vacuum (23.5 g, 73 % yield). The elemental analysis showed C: 51.09, H: 7.75, N: 7.44 wt.-% (theory C: 51.07, H: 7.77, N:

7.44 wt.-%). Thereafter, the product (-)-N(16)-methylsparteinium iodide mixed with 150 ml distilled water was converted to the hydroxide form by ion-exchanging with Dowex 550A (1.1 meq/ml, Aldrich) in an ion-exchange column. Then, 300 ml of distilled water were used to flush the column. The template solution was collected and concentrated in a rotary evaporator. Finally, its concentration was determined by titration with 0.056 M HCl using methyl red as an indicator (obtained concentration: 1.68 mol/kg). Fig. 31 shows the reaction scheme for the preparation of (-)-N(16)-methylsparteinium hydroxide (MSPTOH).

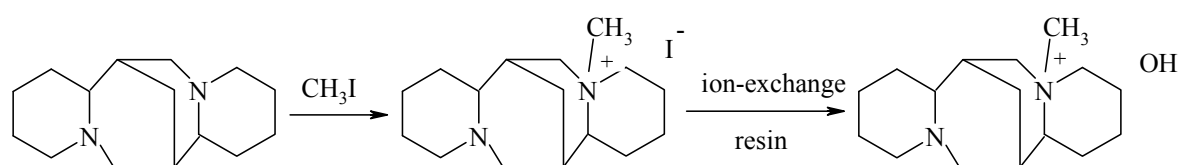


Fig. 31. Scheme of preparation of (-)-N(16)-methylsparteinium hydroxide used as template for CIT-5.

### Synthesis

The synthesis of Li-CIT-5 ( $n_{\text{Si}}/n_{\text{Al}}$  in gel = 150) was modified and optimized from ref. [41]. The gel was prepared with the following molar composition: 1  $\text{SiO}_2$ : 0.25  $\text{LiOH}$ : 0.0033  $\text{Al}_2\text{O}_3$ : 0.3  $\text{C}_{16}\text{H}_{29}\text{N}_2\text{OH}$ : 40  $\text{H}_2\text{O}$ : 0.55  $\text{OH}^-$ . 0.264 g of lithium hydroxide monohydrate (99 wt.-%, Fluka) and 0.063 g aluminium nitrate nonahydrate ( $\geq 99$  wt.-%, Fluka) were dissolved in a mixture of 4.46 g of template solution ((-)-N(16)-methylsparteinium hydroxide, 1.68 mol/kg) in 15.34 g distilled water. The mixture was stirred for 0.5 h. Then 1.5 g Aerosil<sup>®</sup> 200 (99.75 wt.-% of  $\text{SiO}_2$ , Degussa) was gradually added to the solution and the gel was stirred for another 1 h. The gel was then transferred in a Teflon-lined stainless steel autoclave (volume: 25 ml). The crystallization took place at 165 °C under rotation of the autoclave with 40 rpm for 10 d.

### Modification and preparation of the acidic form

The template in the as-synthesized sample was removed by heating in a muffle furnace in N<sub>2</sub> at 1.5 °C/min from RT to 600 °C and holding for 5 h in air. Thereafter, the calcined form was ion-exchanged by stirring in 1 M ammonium nitrate (1 g zeolite/100 g solution) at 80 °C for 3 h. This was repeated for 3 times. Then, the solid was filtered, rinsed with water and dried at 100 °C overnight. The protonated form of Al-CIT-5 (H-CIT-5) was obtained after heating the ammonium form in a furnace from RT to 450 °C with 1.5 °C/min and keeping this for 12 h.

#### *3.1.1.3. Zeolite SSZ-53*

### Template preparation

The preparation of N,N,N-trimethyl-[1-(4-fluorophenyl)cyclopentyl]methyl ammonium hydroxide was modified from the patent [45]. It was performed by the following three steps.

#### Step 1: Preparation of [1-(4-fluorophenyl)cyclopentyl]methyl amine

All glassware was dried in an oven at 150 °C for at least 12 h. A 500ml 3-necked round-bottomed flask equipped with a magnetic stirrer, a reflux condenser and an outlet gas bubbler was setup. The system was connected with argon as purging gas. 170 ml Tetrahydrofuran (p.a., J.T. Baker) were charged into the flask and 6.3 g (157 mmol) of lithium aluminium hydride (95 wt.-%, Acros) were slowly added under thorough stirring and purging with argon gas. The grey suspension was cooled down to 0 °C by means of an ice bath. To the suspension, 10 g (52.3 mmol) 1-(4-fluorophenyl)cyclopentylcarbonitrile (99 wt.-%, Acros) in 20 ml tetrahydrofuran were added dropwise via a pressure equalized additional funnel over a duration of 1 h. Once the addition was completed, the ice bath was replaced with a heating bath and the reaction mixture was refluxed overnight. Thereafter, the reaction mixture was cooled down to 0 °C by an ice bath and diluted with 200 ml diethylether (p.a., Riedel-de

Haën). The reaction was quenched with ca. 25 ml NaOH solution (15 wt.-% in H<sub>2</sub>O) and then water by keeping the temperature below 10 °C. The colourless liquid phase was filtered. The remaining product from the solid part was washed with diethylether. The combined solution was dried over magnesium sulphate (≥99.5 wt.-%, Sigma-Aldrich), filtered and concentrated to give 8.9 g (49.6 mmol, 95 % yield) of [1-(4-fluorophenyl)cyclopentyl]methyl amine.

Step 2: Preparation of N,N,N-trimethyl-[1-(4-fluorophenyl)cyclopentyl]methyl ammonium iodide

To a 250ml 3-necked round-bottomed flask equipped with a magnetic stirrer and a reflux condenser, the 8.9 g (49.6 mmol) amine product from step 1 was charged followed by 110 ml methanol (99.8 wt.-%, Acros). After thorough stirring, 15 g (149 mmol) of potassium hydrogen carbonate (≥99.5 wt.-%, Merck) and 32 g (223 mmol) of iodomethane (≥99 wt.-%, Riedel-de Haën) were added. The resulting mixture was stirred at room temperature for 2 d and was then heated to reflux for 6 h. Then the reaction was cooled down and the resulting solution was concentrated by a rotary evaporator giving a white solid material. The solid was rinsed with chloroform (p.a., Merck) and filtered after each rinse. All the chloroform was combined and concentrated to give a white powder of the quaternary ammonium iodide salt. 14.2 g (39.1 mmol, 79 % yield) of product were obtained. Recrystallization of the powder from isopropyl alcohol gave 11.5 g (31.7 mmol, 61 % yield) of pure N,N,N-trimethyl-[1-(4-fluorophenyl) cyclopentyl]methyl ammonium iodide salt as shiny white flakes. The elemental analysis showed C: 49.4, H: 6.14, N: 3.75 wt.-% (Theory C: 49.6, H: 6.38, N: 3.86 wt.-%).

Step 3: Preparation of N,N,N-trimethyl-[1-(4-fluorophenyl)cyclopentyl]methyl ammonium hydroxide

The obtained product in the form of the iodide salt was converted to the hydroxide form by dissolving the solid in 50 ml of a solution of 50 wt.-% H<sub>2</sub>O in acetone and contacting it with

Dowex 550A (1.1 meq/ml, Aldrich) in an ion-exchange column. 300 ml of distilled water were needed to flush the column. The collected template solution was concentrated in a rotary evaporator. The concentration was determined by titration with 0.056 M HCl using methyl red as an indicator (result: 0.97 mol/kg). The scheme of preparation of this template, viz. N,N,N-trimethyl-[1-(4-fluorophenyl)cyclopentyl]methyl ammonium hydroxide is depicted in Fig. 32.

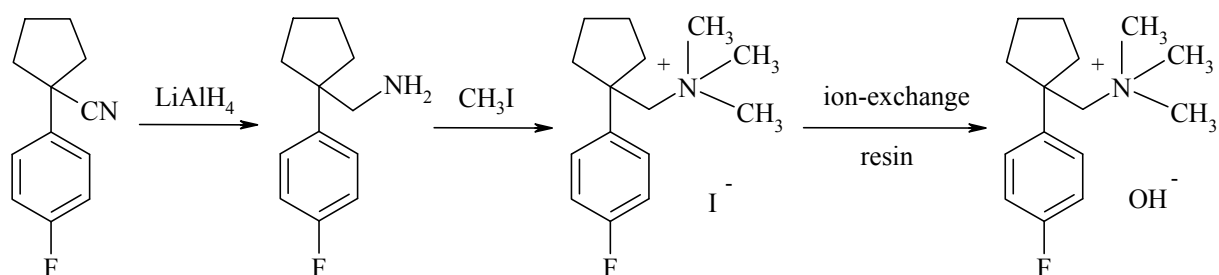


Fig. 32. Scheme of preparation for the template N,N,N-trimethyl-[1-(4-fluorophenyl)cyclopentyl]methyl ammonium hydroxide.

### Synthesis

The synthesis conditions were modified and optimized based on the patent [45]. The synthesis gel was prepared with the molar composition: 1  $\text{SiO}_2$ : 0.035  $\text{Na}_2\text{O}$ : 0.0217  $\text{B}_2\text{O}_3$ : 0.17  $\text{C}_{15}\text{H}_{23}\text{FNOH}$ : 42  $\text{H}_2\text{O}$  ( $n_{\text{Si}}/n_{\text{B}}$  in gel = 23). 4.27 g (0.97 mol/kg) of template solution of N,N,N-trimethyl-[1-(4-fluorophenyl)cyclopentyl]methyl ammonium hydroxide and 15 g distilled water were added to a mixture of 0.047 g NaOH (p.a., Merck) and 0.1 g sodium tetraborate decahydrate ( $\geq 99.5$  wt.-%, Fluka). This mixture was stirred until the solid was dissolved. Then, 1.5 g Cabosil<sup>®</sup> M5 (97 wt.-%  $\text{SiO}_2$ , 3 wt.-%  $\text{H}_2\text{O}$ , Riedel-de Haën) were slowly added and the gel was stirred for another 0.5 h. The gel was transferred to a Teflon-lined stainless steel autoclave (volume: 25 ml). The reaction took place at 160 °C under rotation at 40 rpm for 7 d.

### Modification and preparation of the acidic form

The obtained B-SSZ-53 was calcined through heating in N<sub>2</sub> with 1.5 °C/min from RT to 540 °C with holding for 5 h in air. Then, the temperature was ramped with 1.5 °C/min to 594 °C with holding for 5 h in air. B-SSZ-53 was converted to the more acidic Al-SSZ-53 form by stirring the calcined form in 1 M aluminium nitrate solution (1 g zeolite/25 ml solution) at 95 °C for 12 h. The mixture was then filtered and the recovered solid was thoroughly rinsed with water. The zeolite was dried at 100 °C for 12 h and thereafter calcined at 540 °C for 12 h in N<sub>2</sub> to give the protonated form of Al-SSZ-53 (H-SSZ-53).

#### *3.1.1.4. Zeolite IM-12*

### Template preparation

The preparation was modified from ref. [50]. A 500ml round-bottomed flask equipped with a magnetic stirrer and a reflux condenser was setup. The flask was charged with a solution of 5.68 g NaOH (p.a., Merck) in 140 ml distilled water and then with 31 g (142 mmol) 1,4-dibromobutane (99 wt.-%, Aldrich). The mixture was stirred and heated to 90 °C. Then, 16.4 g (142 mmol) of (2R, 6S)-2,6-dimethylpiperidine (98 wt.-%, Aldrich) were introduced via a dropping funnel over a duration of 0.5 h. After that, the whole mixture was stirred and refluxed at 120 °C for 2.5 h. After the reaction was complete, it was cooled down with an ice bath and 70 ml ice-cooled NaOH solution (40 wt.-% in H<sub>2</sub>O) was added until two phases formed. The mixture was concentrated in a rotary evaporator until a yellow solid formed out of the solution. The yellow solid was filtered and purified by extracting with chloroform (p.a., Merck). Then the chloroform was removed with a rotary evaporator and a white solid of the ammonium salt was obtained. The product was further washed with diethylether (p.a., Riedel-de Haën), filtered and dried in vacuum using a vacuum pump. As product, 25.5 g (103 mmol, 73 % yield) of (6R, 10S)-6, 10-dimethyl-5-azoniaspiro [4, 5] decane bromide was obtained.

The elemental analysis showed C: 53.31, H: 8.90, N: 5.64 wt.-% (Theory C: 53.23, H: 8.93, N: 5.64 wt.-%). Thereafter, the bromide form was converted to the hydroxide form by ion-exchanging with Dowex 550A (1.1 meq/ml, Aldrich) in a column. Then, 1 l of distilled water was used to flush the column. All template solutions were collected and concentrated in a rotary evaporator. Finally, the concentration was determined by titration with 0.056 M HCl using methyl red as an indicator (obtained: 2 mol/kg).

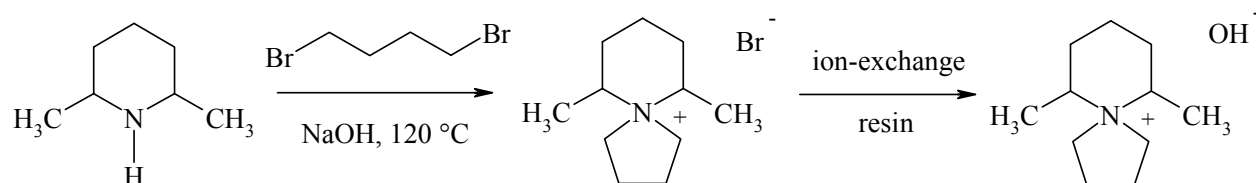


Fig. 33. Scheme of preparation of the template (6R, 10S)-6, 10-dimethyl-5-azoniaspiro [4, 5] decane hydroxide.

### Synthesis

The gel was prepared with the following molar composition: 0.67 SiO<sub>2</sub>: 0.33 GeO<sub>2</sub>: 0.25 C<sub>11</sub>H<sub>22</sub>NOH: 25 H<sub>2</sub>O. 1.3 g of amorphous germanium dioxide (≥99.99 wt.-%, Aldrich) was dissolved in a mixture of 4.67 g (2 mol/kg) template solution of (6R, 10S)-6, 10-dimethyl-5-azoniaspiro [4, 5] decane hydroxide and 13.9 g distilled water. The mixture was stirred until the solid was completely dissolved. Then, 1.5 g Aerosil® 200 (99.75 wt.-% SiO<sub>2</sub>, Degussa) were slowly added during stirring. The mixture was stirred for another 0.5 h. The gel was transferred into a Teflon-lined stainless steel autoclave (volume: 25 ml). The reaction took place at 160 °C under rotation at 40 rpm for 8 d.

### Modification

The template was removed by heating the as-synthesized form in a muffle furnace in N<sub>2</sub> with 1.5 °C/min from RT to 600 °C and holding at this temperature for 8 h in air.

### 3.1.2. Zeolites based on 12-membered ring pore openings

#### 3.1.2.1. Zeolite ITQ-21

##### Template preparation

The required template, viz. (-)-N(16)-methylsperminium hydroxide (MSPTOH) was prepared as previously described in chap. 3.1.1.2 with the obtained concentration of 0.2 mol/kg.

##### Synthesis

The synthesis recipes for the low germanium-containing version with aluminium (ITQ-21) and for the high germanium-containing version (Ge-ITQ-21) were modified and optimized based on refs. [53, 130]. The following is an example of the synthesis of ITQ-21 with  $n_{\text{Si}}/n_{\text{Al}} = 46$  in the gel using the following molar composition: 0.91 SiO<sub>2</sub>: 0.09 GeO<sub>2</sub>: 0.02 Al<sub>2</sub>O<sub>3</sub>: 0.55 C<sub>16</sub>H<sub>29</sub>N<sub>2</sub>OH: 0.55 HF: 3 H<sub>2</sub>O. The gel was prepared by mixing 0.243 g crystalline germanium dioxide (99.998 wt.-%, Aldrich) and 72 g of MSPTOH template solution (0.2 mol/kg). The mixture was stirred until the germanium oxide was completely dissolved. Additional 8 g of distilled water were added in order to increase the hydrolysis rate. 5 g Tetraethylorthosilicate (TEOS) (98 wt.-%, Aldrich) were added dropwise while vigorously stirring and the mixture was further stirred for 3 h to ensure completion of the hydrolysis. Then, 0.108 g aluminium triisopropoxide ( $\geq 98$  wt.-%, Aldrich) were added and the gel was stirred for another 3 h. Thereafter, the required amount of ethanol and water was removed, by taking into account that part of these components was evaporated during the stirring steps, with a rotary evaporator. Once the solution reached to the right water content, 0.71 g HF (40 wt.-% in H<sub>2</sub>O, Riedel-de Haën) were added and the mixture was stirred mechanically until it turned homogeneous. The dry gel was put in a Teflon-lined stainless steel autoclave (volume: 25 ml). The reaction took place at 175 °C under rotation at 40 rpm for 4 d. Ge-ITQ-21 was

prepared using the following molar composition: 0.67 SiO<sub>2</sub>: 0.33 GeO<sub>2</sub>: 0.55 C<sub>16</sub>H<sub>29</sub>N<sub>2</sub>OH: 0.55 HF: 20 H<sub>2</sub>O. Different types of ITQ-21 were prepared in a similar manner with different gel compositions and reaction times according to Table 5.

Table 5. Amount of reactants used for the synthesis of different types of ITQ-21. The concentration of template MSPTOH was 0.2 mol/kg. All weights are in gram units.

Chemical	Ge-ITQ-21	ITQ-21, $n_{Si}/n_{Al}$ in gel			
		$\infty$	46	23	13.7
TEOS	5	5	5	5	5
GeO <sub>2</sub>	1.21	0.243	0.243	0.243	0.243
MSPTOH	97.5	72	72	72	72
aluminium triisopropoxide	0	0	0.108	0.215	0.36
HF	0.97	0.71	0.71	0.71	0.71
removed H <sub>2</sub> O and ethanol	-84.3	-70.9	-70.9	-70.9	-70.9
Reaction time (d)	2	1	4	4	4

#### Modification and preparation of the acidic form

The calcined forms of ITQ-21 ( $n_{Si}/n_{Al}$  in gel = 23, 46 and  $\infty$ ) were obtained by heating the as-synthesized samples from RT to 540 °C with 1.5 °C/min in N<sub>2</sub> and holding at this temperature for 3 h in air. For ITQ-21 with  $n_{Si}/n_{Al}$  = 13.7 in the gel, it was obtained by heating to 470 °C in N<sub>2</sub> and holding for 3 h in air. It is not possible to remove the template of Ge-ITQ-21 by calcination at temperature as low as 300 °C for 3 h in air without its structural destruction. The calcined forms of ITQ-21 are already in the acidic (H<sup>+</sup>-) form without further modification.

### 3.1.2.2. Zeolite MCM-68

#### Template preparation

The template preparation was modified based on the corresponding patent [62].

Step 1 : Preparation of N,N'-diethyl-exo,exo-bicyclo[2.2.2]oct-7-ene-2,3:5,6-tetracarboxylic diimide

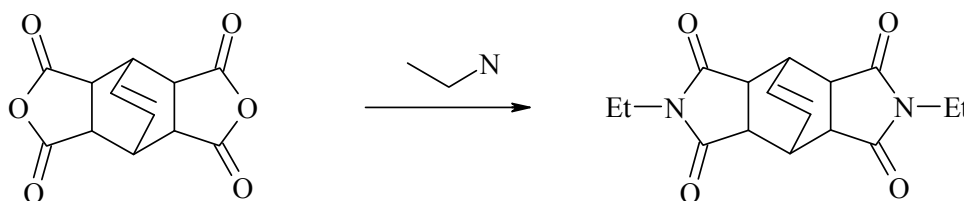


Fig. 34. Scheme of the preparation of N,N'-diethyl-exo,exo-bicyclo[2.2.2]oct-7-ene-2,3:5,6-tetracarboxylic diimide (Et: ethyl group).

To a 1000ml 3-necked round-bottomed flask equipped with a magnetic stirrer and a reflux condenser, 258 g (4 mol) ethylamine (70 wt.-% in H<sub>2</sub>O, Fluka) were introduced followed by 49.6 g (0.2 mol) exo,exo-bicyclo[2.2.2]oct-7-ene-2,3:5,6-tetracarboxylic dianhydride (Aldrich) in small portions during vigorous stirring. After 2 h of stirring at RT, 150 ml distilled water were added. The mixture was stirred at 70 °C for 48 h and then at 100 °C for 18 h in order to drive off the excess amine. Then, the reaction mixture was cooled to RT and the remaining amine was quenched dropwise with HCl (37 wt.-% in H<sub>2</sub>O, J.T. Baker). The obtained solid was filtered, washed with water and dried in vacuum. 58 g (192 mmol, 96 % yield) of white crystal product N,N'-diethyl-exo,exo-bicyclo[2.2.2]oct-7-ene-2,3:5,6-tetracarboxylic diimide were obtained. The elemental analysis showed C: 63.55, H: 6.01, N: 9.27 wt.-% (Theory C: 63.56, H: 6, N: 9.27 wt.-%).

Step 2 : Preparation of N,N'-diethyl-exo,exo-bicyclo[2.2.2]oct-7-ene-2,3:5,6-dipyrrolidine



Fig. 35. Scheme of the preparation of N,N'-diethyl-exo,exo-bicyclo[2.2.2]oct-7-ene-2,3:5,6-dipyrrolidine (Et: ethyl group).

All glassware was dried in an oven at 150 °C for at least 12 h. A 1000ml 3-necked round-bottomed flask equipped with a magnetic stirrer, a Soxhlet extractor, a reflux condenser and an outlet gas bubbler were setup. The system was connected with argon purging gas. The Soxhlet extractor with thimble contained 16 g (52.9 mmol) of the diimide product from step 1. Then 750 ml of tetrahydrofuran (p.a., J.T. Baker) was charged into the flask with slowly adding of 7.4 g (185.2 mmol) lithium aluminium hydride (95 wt.-%, Acros) under thorough stirring and purging with argon gas. After 24 h of reflux at 85 °C to fully extract the diimide, the reaction was first cooled down slowly to RT and then with an ice bath. Then, the reaction was quenched with water and NaOH solution (15 wt.-% in H<sub>2</sub>O) keeping the temperature below 10 °C. Thereafter, the solution was filtered. The remaining solid product was washed with ca. 150 ml dichloromethane (≥99.8 wt.-%, Merck). Both solutions were combined.

Tetrahydrofuran was removed from the organic solution using a rotary evaporator. 300 ml distilled water were added to the recovered product. During stirring, HCl (37 wt.-% in H<sub>2</sub>O, J.T. Baker) was added dropwise until pH ≈ 1-2 in order to acidify the solution. The organic product in the aqueous phase was separated, an additional 300 ml water were added and the pH was adjusted again to 1-2. The aqueous layer was separated and combined with the previous one. The combined organic solution was brought to basicify with NaOH (50 wt.-% in H<sub>2</sub>O) until pH ≈ 11-12. Dichloromethane was used to extract the organic product. The

combined organic fraction was dried over sodium sulphate ( $\geq 99$  wt.-%, Merck). After the solution was filtered, dichloromethane was removed via a rotary evaporator. The product was further purified by extracting with diethylether (p.a., Riedel-de Haën) and dried with sodium sulphate. Finally the diethylether was removed using a rotary evaporator. 7 g (28.4 mmol, 54 % yield) of a gold-coloured oil as product N,N'-diethyl-exo,exo-bicyclo[2.2.2]oct-7-ene-2,3:5,6-dipyrrolidine were obtained. The elemental analysis showed C: 77.66, H: 10.67, N: 11.37 wt.-% (Theory C: 77.99, H: 10.64, N: 11.37 wt.-%).

Step 3 : Preparation of N,N,N',N'-tetraethyl-exo,exo-bicyclo[2.2.2]oct-7-ene-2,3:5,6-dipyrrolidinium diiodide

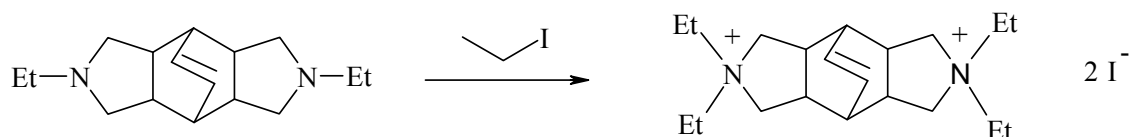


Fig. 36. Scheme of the preparation of N,N,N',N'-tetraethyl-exo,exo-bicyclo[2.2.2]oct-7-ene-2,3:5,6-dipyrrolidinium diiodide (Et: ethyl group).

To a 250ml 3-necked round-bottomed flask equipped with a magnetic stirrer, a reflux condenser and a pressure equalized additional funnel containing a solution of 26.9 g (171 mmol) iodoethane ( $\geq 99$  wt.-%, Fluka) in 86 ml ethanol ( $\geq 99.8$  wt.-%, Roth) were attached. The flask was then charged with 14 g (56.8 mmol) of the solid product from step 2 and 57 ml ethanol ( $\geq 99.8$  wt.-%, Roth). After stirring until all the solid was dissolved, the iodoethane solution was added slowly and the mixture was refluxed at room temperature overnight. After subsequent cooling with an ice bath, the crystalline solid product was filtered and washed with acetone. The solid was then refluxed in acetone for 15 min, filtered and dried in vacuum. 20.94 g (37.5 mmol, 66 % yield) of the product N,N,N',N'-tetraethyl-exo,exo-bicyclo[2.2.2]oct-7-ene-2,3:5,6-dipyrrolidinium diiodide (Bicyclodiquat-Et<sub>4</sub> 2I) were

obtained. The elemental analysis showed C: 42.51, H: 6.17, N: 4.84 wt.-% (Theory C: 43.02, H: 6.05, N: 5.02 wt.-%).

### Synthesis

The synthesis gel was modified and optimized based on the patent [62] with the following molar composition: 1 SiO<sub>2</sub>: 0.056 Al<sub>2</sub>O<sub>3</sub>: 0.375 KOH: 0.1 C<sub>20</sub>H<sub>36</sub>N<sub>2</sub>I<sub>2</sub>: 30 H<sub>2</sub>O ( $n_{\text{Si}}/n_{\text{Al}}$  in gel = 9). 15 g Ludox SM-30 (30 wt.-% in H<sub>2</sub>O, Aldrich) was mixed with 23.5 g distilled water. 7.88 g of KOH solution (20 wt.-% in H<sub>2</sub>O, Fluka) was added and the mixture was stirred until well-mixed. Then, 0.045 g of calcined MCM-22 as seed and 0.79 g aluminium hydroxide (53.8 wt.-% Al<sub>2</sub>O<sub>3</sub>, Aldrich) were gradually added during vigorous stirring. The gel was stirred for 0.5 h. Thereafter, 4.18 g of template N,N,N',N'-tetraethyl-exo,exo-bicyclo[2.2.2]oct-7-ene-2,3:5,6-dipyrrolidinium diiodide (Bicyclodiquat-Et<sub>4</sub> 2I) were added and the mixture was stirred for another 0.5 h. The gel was filled in a Teflon-lined stainless steel autoclave (volume: 60 ml). The reaction took place at 160 °C under static conditions for 14.5 d.

### Modification and preparation of the acidic form

The calcined form was obtained by heating the as-synthesized sample from RT to 540 °C at 1.5 °C/min in N<sub>2</sub> and holding at this temperature for 18 h in air. Then, it was ion-exchanged with 1 M ammonium nitrate (1 g zeolite/100 g solution) at 80 °C for 3 h. This was repeated for 3 times. The mixture was filtered and the recovered solid was rinsed with water and dried at 100 °C overnight. Thereafter, the ammonium form was heated from RT to 540 °C in N<sub>2</sub> for 12 h and finally the protonated H-MCM-68 was obtained.

### 3.1.3. Zeolites based on 10-membered ring pore openings

#### 3.1.3.1. Zeolite SSZ-35

##### Template preparation

Analogous to the one that was previously described in chap. 3.1.1.4.

##### Synthesis

The synthesis of zeolite SSZ-35 was modified and optimized based on refs. [72, 74, 77] using a starting chemical gel composition with the molar ratio: 1 SiO<sub>2</sub>:  $x$  Al<sub>2</sub>O<sub>3</sub>: 0.35 C<sub>11</sub>H<sub>22</sub>NOH: 25 H<sub>2</sub>O ( $x = 0 - 0.028$ ). A gel with  $n_{\text{Si}}/n_{\text{Al}} = 18$  was prepared by dissolving 0.175 g aluminium hydroxide (53.8 wt.-% Al<sub>2</sub>O<sub>3</sub>, Aldrich) in a mixture of 5.81 g template solution of (6R, 10S)-6, 10-dimethyl-5-azoniaspiro [4, 5] decane hydroxide (2 mol/kg) and 11.3 g distilled water. The gel was stirred until the solid was completely dissolved. Then 2 g of Aerosil<sup>®</sup> 200 (99.75 wt.-%, Degussa) were gradually added to the gel. The gel was stirred for another 0.5 h before transferring it into a Teflon-lined stainless steel autoclave (volume: 25 ml). The reaction took place at 160 °C under rotation at 40 rpm for 8 d.

Table 6. Amount of reactants used for the synthesis of SSZ-35 with different  $n_{\text{Si}}/n_{\text{Al}}$  ratios.

The concentration of the template is 2 mol/kg. All weights are in gram units.

Chemical	$n_{\text{Si}}/n_{\text{Al}}$ in gel				
	$\infty$	73	55	36	18
Aerosil <sup>®</sup> 200	2	2	2	2	2
C <sub>11</sub> H <sub>22</sub> NOH	5.81	5.81	5.81	5.81	5.81
Aluminium hydroxide	0	0.043	0.057	0.087	0.175
H <sub>2</sub> O	11.3	11.3	11.3	11.3	11.3
Reaction time (d)	4	4	6	8	8

### Modification and preparation of the acidic form

The calcined form of SSZ-35 was obtained from heating the as-synthesized sample from RT to 600 °C at 1.5 °C/min in N<sub>2</sub> and holding it for 5 h in air. Then, the calcined sample was ion-exchanged by stirring in 1 M ammonium nitrate (1 g zeolite/100 g solution) at 80 °C for 3 h. This was repeated for 3 times. The zeolite was filtered, rinsed with water and dried at 100 °C overnight. The ammonium form was heated from RT to 450 °C in N<sub>2</sub> for 12 h and finally the protonated form of H-SSZ-35 was obtained.

#### *3.1.3.2. Zeolite MCM-71*

The synthesis gel was modified and optimized from the original patent [79]. It was prepared with the molar composition: 1 SiO<sub>2</sub>: 0.05 Al<sub>2</sub>O<sub>3</sub>: 0.375 KOH: 0.2 C<sub>6</sub>H<sub>15</sub>NO<sub>3</sub>: 30 H<sub>2</sub>O. 15 g Ludox AS-30 (30 wt.-% in H<sub>2</sub>O, Aldrich) were mixed with 23.5 g distilled water. 7.88 g of KOH solution (20 wt.-% in H<sub>2</sub>O, Fluka) were added and the resulting mixture was stirred for 5 min. Then, 0.71 g aluminium hydroxide (53.8 wt.-% Al<sub>2</sub>O<sub>3</sub>, Aldrich) were gradually added during vigorous stirring. The resulting gel was further stirred for 0.5 h. Then 2.26 g of triethanolamine (C<sub>6</sub>H<sub>15</sub>NO<sub>3</sub>) (99 wt.-%, Riedel-de Haën) were added and the gel was stirred for another 0.5 h. Thereafter, the gel was transferred into a Teflon-lined stainless steel autoclave (volume: 60 ml). The reaction took place at 160 °C under static condition for 16.5 d or alternatively at 160 °C for 10 d and 165 °C for another 3.75 d.

### Modification and preparation of the acidic form

The calcined form was obtained by heating the as-synthesized sample from RT to 540 °C at 1.5 °C/min in N<sub>2</sub> and holding it for 8 h in air. Then the calcined form was ion-exchanged with 1 M ammonium nitrate (1 g zeolite/100 g solution) at 80 °C for 3 h. This was repeated for 4 times. The mixture was filtered and the recovered solid was rinsed with water and dried at

100 °C overnight. The protonated form of H-MCM-71 was obtained after heating the ammonium form in a furnace from RT to 540 °C for 12 h in N<sub>2</sub>.

### 3.2. Preparation of bifunctional catalysts

The bifunctional forms of the catalysts were prepared to be able to perform *n*-decane hydroconversion and the competitive hydrogenation of olefins as catalytic tests. The bifunctional catalyst containing 0.27 wt.-% palladium was prepared by ion-exchanging the ammonium form of the zeolite with a complex salt of the noble metal, viz. [Pd(NH<sub>3</sub>)<sub>4</sub>]Cl<sub>2</sub> in aqueous solution. The required amount of the complex to obtain a final loading of 0.27 wt.-% palladium was calculated according to equation 14. It was diluted in distilled water (amount 10x of dry zeolite). The zeolite was stirred with distilled water (amount 10x of dry zeolite) in a round-bottomed glass. The round-bottomed glass was equipped with a dropping funnel and a reflux condenser. The complex solution was stored in the dropping funnel and introduced dropwise to the suspended zeolite within ca. 1 h. The ion-exchange took place at 30 °C for 24 h. Afterwards, the water was removed from the catalyst by using a rotary evaporator. The obtained complex-containing zeolites were dried at 120 °C for 12 h.

$$E_{m-c} = \frac{M_{m-c}}{M_m} \cdot P \cdot \frac{(1-L_w)}{(1-P)} \cdot E_w \quad \text{equation 14 (from ref. [131])}$$

Where:

$E_{m-c}$  = weight of noble metal complex (g)

$M_{m-c}$  = molecular weight of noble metal complex (g·mol<sup>-1</sup>)

$M_m$  = molecular weight of noble metal (g·mol<sup>-1</sup>)

$P$  = desired amount of noble metal in the dried zeolite catalyst (g·g<sup>-1</sup>)

$L_w$  = water content in the zeolite (g·g<sup>-1</sup>)

$E_w$  = weight of humid zeolite (g)

### **3.3. Physicochemical characterization**

#### **3.3.1. Powder X-ray diffractometry (XRD)**

Powder X-ray diffraction patterns were recorded on a Siemens/Bruker D5005 diffractometer using  $\text{CuK}\alpha$  radiation ( $\lambda = 0.15405 \text{ nm}$ ). The X-ray tube was operated at 40 kV and 30 mA. The measurement run between the angle from 3 to 50 ° of  $2\theta$  with a step size of 0.03 ° of  $2\theta$  and a step time of 1.5 s.

#### **3.3.2. Thermogravimetric analysis coupled to mass spectrometry (TGA/DTA/MS)**

Thermogravimetric analysis was performed using a SETARAM setsys16/MS-system. This was coupled to a mass spectrometer. The water content was determined under  $\text{N}_2$  flow ( $V_{\text{N}_2} = 50 \text{ ml/min}$ ) by heating with 10 °C/min from 20 to 500 °C. The template weight loss was analyzed using different media, viz. either  $\text{N}_2$  or air ( $\text{O}_2+\text{N}_2$ ) by heating from 20 to 1000 °C with a heating rate of 10 °C/min.

#### **3.3.3. $\text{N}_2$ adsorption**

Adsorption and desorption of  $\text{N}_2$  at -190 °C on the zeolites were measured with an Autosorp 1 instrument from Quantachrome. Prior to the adsorption, the sample (ca. 30-50 mg in dry weight) was degassed at 250 °C in a vacuum of  $<10^{-4} \text{ Pa}$  for 12 h. The specific surface area was determined by the multipoint BET-method (Brunauer-Emmett-Teller) in the partial pressure range of ca. 0.035-0.1. The specific pore volume was determined from the adsorbed volume of  $\text{N}_2$  in the liquid state at a partial pressure ca. 0.2.

#### **3.3.4. Infrared (IR) spectroscopy**

Infrared spectroscopy was applied to identify the presence of organic molecules in the zeolite structure such as template molecules and/or to investigate the surface properties and the

nature of the acid sites of the zeolite. The measurements were carried out using a Nexus FT-IR spectrometer from Nicolet in the diffuse reflection mode (DRIFT). The spectra were collected by a DTGS KBr detector with a scan number of 200 at a resolution of  $8\text{ cm}^{-1}$  in the  $4000\text{-}720\text{ cm}^{-1}$  scan range. A cell with ZnSe crystal windows from Spectra-Tech was used for the IR measure at high temperature and pressure. The reference KBr was measured after desorbing water by heating at  $250\text{ }^{\circ}\text{C}$  for 0.5 h. The characterization of different forms of the zeolite was carried out at different heating temperatures: The as-synthesized forms were studied at  $100\text{ }^{\circ}\text{C}$ , while the calcined and protonated forms were characterized at  $300\text{ }^{\circ}\text{C}$ .

The observation of nature of acid sites in the zeolites will be described in chap. 3.3.8.2.

### **3.3.5. Ultraviolet-visible (UV-Vis) spectroscopy**

This method was applied to detect the presence of cobalt complexes in zeolite UTD-1. The measurement was performed using a Lambda 18 UV/Vis spectrometer from Perkin-Elmer in the  $185\text{-}900\text{ nm}$  range. Barium sulphate was used as the reference.

### **3.3.6. Scanning electron microscopy (SEM)**

The crystal size and morphology of the zeolites were recorded using a scanning electron microscope JSM-6490LA from JEOL with an accelerating voltage of  $20\text{ kV}$ . Prior to the measure, the sample was coated with a thin layer of gold using the sputter coater JFC-1200 from JEOL in order to avoid charging effects which cause poor quality images. Approximately  $8\text{ nm}$  of the gold layer was coated onto the sample using an operating current of  $30\text{ mA}$ , a pressure in the vacuum chamber of  $8\text{ Pa}$  and an operating time of  $30\text{ s}$ .

### **3.3.7. Atomic absorption spectroscopy (AAS)**

Elemental analyses for silicon, aluminium, sodium, boron and cobalt were performed by atomic absorption spectroscopy using an AAnalyst 300 spectrometer from Perkin-Elmer. The

analyzed samples were prepared by dissolving the zeolite with HF and water in 30ml polypropylene bottles. The amount of zeolite depends on the required concentration of each element. The calibration was done with at least four points prior to the measurement.

### **3.3.8. Temperature-programmed desorption of pyridine (pyridine TPD)**

#### *3.3.8.1. Pyridine TPD in a flow-type apparatus*

Temperature-programmed desorption (TPD) of pyridine was carried out in a flow-type apparatus with a fixed-bed adsorber. Prior to the TPD experiment, 25 mg of the acidic/protonated form of the sample were activated in-situ at 400 °C for 12 h in a N<sub>2</sub> flow ( $V_{N_2} = 80$  ml/min). The sample was then loaded with pyridine ( $p_{\text{pyridine}} = 1.3$  kPa,  $T_s = 15.1$  °C) in a N<sub>2</sub> flow at 180 °C for 0.5 h. Subsequently, the sample was flushed for 3 h with N<sub>2</sub> at the same temperature to remove physisorbed pyridine. The TPD was carried out with a heating rate of 5 °C/min from 180 to 800 °C in a N<sub>2</sub> flow ( $V_{N_2} = 80$  ml/min) and the desorbed pyridine was quantitatively determined by a gas chromatograph (GC) equipped with a flame ionization detector (FID).

#### *3.3.8.2. Pyridine TPD coupled with IR spectroscopy*

The nature of the acid sites in the prepared zeolites was investigated by pyridine adsorption and the strength of acid sites was determined via temperature-programmed desorption. The samples were dried in the measuring cell by heating under a flow of N<sub>2</sub> to 300 °C for 1 h and then they were cooled to 180 °C. After the temperature was stabilized, the sample was loaded with pyridine ( $p_{\text{pyridine}} = 1.3$  kPa,  $T_s = 15.1$  °C) for 0.5 h. Then, the loaded sample was flushed for 3 h before desorbing by stepwise heating from 180 to 500 °C under N<sub>2</sub> flow ( $V_{N_2} = 80$  ml/min).

### **3.3.9. $^{27}\text{Al}$ and $^{29}\text{Si}$ magic angle spinning nuclear magnetic resonance (MAS NMR) spectroscopy**

The measurement was carried out in cooperation with the department of physics and geosciences at the university of Leipzig (Dr. A. Pöpl) and the institute of physics at the university of Augsburg (Prof. Dr. M. Hartmann).  $^{27}\text{Al}$  and  $^{29}\text{Si}$  MAS NMR spectra of zeolite MCM-71 and MCM-68 were obtained using MSL 500 and MSL 300 spectrometers from Bruker at the resonance frequencies of 130.32 and 59.63 MHz with standard 4 and 7 mm  $\text{ZrO}_2$  probe heads, respectively. The rotors were operated at a spinning rate of 12 and 4.5 kHz, respectively.

For zeolite SSZ-35,  $^{27}\text{Al}$  and  $^{29}\text{Si}$  MAS NMR spectra were obtained using a MSL 500 spectrometer from Bruker at resonance frequencies of 130.32 and 99.36 MHz with standard 4 and 7 mm  $\text{ZrO}_2$  rotors. The rotors were operated at a spinning rate of 12 and 4.5 kHz with excitation pulses of 2.1 and 3  $\mu\text{s}$  and recycle times of 200 and 20 ms at 2048 and 1024 scans per spectrum. The chemical shifts of Al and Si were measured with respect to  $\text{AlCl}_3 \times 6\text{H}_2\text{O}$  and TMS as references, respectively.

### **3.3.10. Temperature-programmed reduction (TPR)**

This method was applied to investigate the reducibility of cobalt species in calcined UTD-1 using an Altamira instrument. A reducing gas consisting of 5 vol.-%  $\text{H}_2$  in argon was used and the consumption of  $\text{H}_2$  was measured using a thermal conductivity detector (TCD). Molecular sieve A was used to trap the water formed during the reduction reaction. The reaction took place in a quartz-tube reactor with a thermocouple inserted into the position where the sample was located. 100 mg of dry zeolite were mixed with 3 g quartz (p.a., bead size 0.26-0.6 mm, Fluka) and the admixed sample was placed in the reactor with a quartz wool plug. The sample was activated in a flow of argon ( $V_{\text{Ar}} = 30 \text{ ml/min}$ ) with a heating rate

of 20 °C/min from RT to 300 °C and a holding time of 1 h. The TPR step was performed under a reducing gas flow ( $V_{\text{reduce}} = 30$  ml/min) with a heating rate of 5 °C/min from 40 to 870 °C and a holding time of 15 min. A TCD measured the uptake of H<sub>2</sub> by the difference in the thermal conductivity of the gas before and after the reduction. A reference gas was used with low concentrations of H<sub>2</sub> in N<sub>2</sub> ( $V_{\text{ref}} = 30$  ml/min). After the TPR step, 10 further pulses used for calibration were performed.

### 3.3.11. Characterization of the pore size by adsorption experiments

Adsorption is widely used to characterize the pore size of zeolites with unknown structure. The adsorption measurements in the present study were carried out with two catalysts, viz. H-MCM-68 and H-MCM-71 in a home-made volumetric apparatus made from stainless steel. A series of hydrocarbon adsorptives with varying molecular sizes were applied, i.e., *n*-pentane, *n*-hexane, *n*-heptane, 2-methylhexane, cyclohexane, benzene and toluene. All adsorptives (as liquids) were pure grade. The adsorption took place at 30 °C. The vapour of adsorptive was delivered from the liquid phase. The relative pressure was monitored by pressure gauges and was adjusted by the inlet needle valve before entering the adsorption section. Prior to the adsorption experiments, the sample was degassed at 300 °C in a vacuum of ca. 10<sup>-4</sup> Pa for 5 h. The adsorption capacity in mmol of adsorptive per gram of dry zeolite was determined using the ideal gas law.

## 3.4. Catalytic experiments

### 3.4.1. Ethylbenzene disproportionation

#### 3.4.1.1. Experimental setup

Ethylbenzene disproportionation as test reaction was performed at atmospheric pressure in a flow-type apparatus equipped with a fixed-bed reactor, a saturator and an on-line sampling

GC as shown in Fig. 37. The acidic form of the catalysts was pressed binder-free, crushed and sieved to obtain the particle size fraction between 0.26 and 0.35 mm. The required amount of catalyst admixed with 3 ml quartz (p.a., bead size 0.26-0.6 mm, Fluka) was loaded into the reactor and activated in-situ in a N<sub>2</sub> flow ( $V_{N_2} = 60$  ml/min) by heating to 400 °C for 12 h. The feed consists of a stream of N<sub>2</sub> containing ethylbenzene ( $p_{E-Bz} = 1$  kPa,  $T_s = 21.1$  °C). Ethylbenzene ( $\geq 99$  wt.-%, Fluka) was purified according to ref. [97] and thereafter distilled to achieve a purity  $\geq 99.8$  wt.-%. The catalyst weight and the carrier gas flow were adjusted such as to achieve the desired modified residence time. The analysis of the reaction products with time-on-stream was achieved by an on-line capillary GC. The conditions of the GC analysis are presented in Table 7.

Table 7. Conditions for the gas chromatographic analysis of the products from ethylbenzene disproportionation.

sample volume	1000 $\mu$ l
sample injection time	0.5 min
injection temperature	200 °C
oven temperature program	100 °C $\xrightarrow{5^\circ C/min}$ 180 °C $\xrightarrow{10 \text{ min}}$ 180 °C
carrier gas	N <sub>2</sub>
column flow	1 ml/min (constant flow mode)
column pressure	221 kPa (at 100 °C)
split ratio	30:1
column type	CP-Sil PONA from Varian (length: 100 m, inner diameter: 0.25 mm, film thickness: 0.5 $\mu$ m)
detector	flame ionization detector (FID)
detector temperature	250 °C
valve box temperature	160 °C

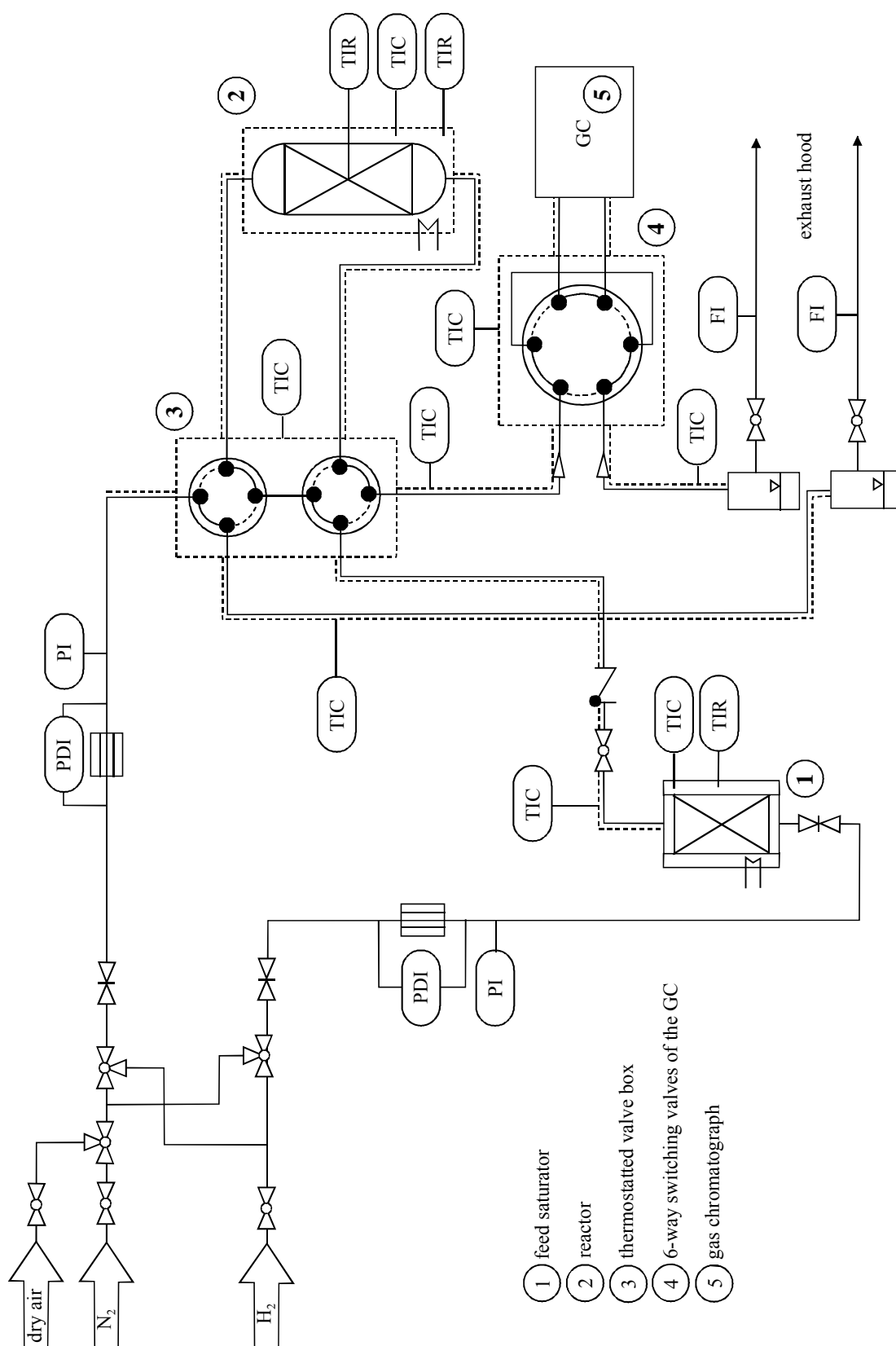


Fig. 37. Schematic diagram of the fixed-bed flow-type apparatus for ethylbenzene disproportionation or for *n*-decane hydroconversion.

An important parameter is the modified residence time. It is defined as:

$$\tau_{\text{mod}} = \frac{W_{\text{cat}}}{F_{\text{E-Bz}}} \quad \text{equation 15}$$

Where:

$\tau_{\text{mod}}$  = modified residence time ( $\text{g}\cdot\text{h}\cdot\text{mol}^{-1}$ )

$W_{\text{cat}}$  = catalyst weight (g)

$F_{\text{E-Bz}}$  = molar flow of ethylbenzene at the reactor inlet ( $\text{mol}\cdot\text{h}^{-1}$ )

Retention times of each reactant/product component were determined using GC coupled to mass spectrometry as shown in Table 8.

Table 8. Retention times of components involved in ethylbenzene disproportionation.

Component	Retention time (min)
benzene	8.2
ethylbenzene	10.6
1,3-diethylbenzene	14.4
1,4-diethylbenzene	14.6
1,2-diethylbenzene	14.8
1,3,5-triethylbenzene	18.9
1,2,4-triethylbenzene	19.6

## 3.4.1.2. Catalytic evaluation

The conversion, yield and selectivity in a continuous flow-type reactor are generally defined as:

$$X_i = \frac{\dot{n}_{i,0} - \dot{n}_i}{\dot{n}_{i,0}} \quad \text{equation 16}$$

$$Y_{j,i} = \frac{\dot{n}_j - \dot{n}_{j,0}}{\dot{n}_{i,0}} \cdot \left| \frac{v_i}{v_j} \right| \quad \text{equation 17}$$

$$S_{j,i} = \frac{\dot{n}_j - \dot{n}_{j,0}}{\dot{n}_{i,0} - \dot{n}_i} \cdot \left| \frac{v_i}{v_j} \right| \quad \text{equation 18}$$

Where:

- $X_i$  = conversion of reactant i (-)
- $Y_{j,i}$  = yield of product j referring to reactant i (-)
- $S_{j,i}$  = selectivity of product j referring to reactant i (-)
- $\dot{n}_{i,0}$  = molar flow of reactant i at the reactor inlet ( $\text{mol} \cdot \text{h}^{-1}$ )
- $\dot{n}_i$  = molar flow of reactant i at the reactor outlet ( $\text{mol} \cdot \text{h}^{-1}$ )
- $\dot{n}_{j,0}$  = molar flow of product j at the reactor inlet ( $\text{mol} \cdot \text{h}^{-1}$ )
- $\dot{n}_j$  = molar flow of product j at the reactor outlet ( $\text{mol} \cdot \text{h}^{-1}$ )
- $v_i$  = stoichiometric coefficient of reactant i (-)
- $v_j$  = stoichiometric coefficient of product j (-)

In this thesis, the conversion of ethylbenzene,  $X_{E-Bz}$ , will be calculated in a similar way as described in ref. [97], viz. by the sum of yields of benzene, diethylbenzenes and triethylbenzenes based on the stoichiometry given in equation 19 and 20. Hence, conversion

and yields can be calculated from the (corrected) peak areas as determined by GC using equations 21-24.



$$X_{E-BZ} = \frac{(a_{Bz} + a_{DE-Bz} + a_{E-Bz} + a_{TE-Bz}) - a_{E-Bz}}{a_{Bz} + a_{DE-Bz} + a_{E-Bz} + a_{TE-Bz}} \quad \text{equation 21}$$

$$Y_{Bz} = 2 \cdot \frac{a_{Bz}}{a_{Bz} + a_{DE-Bz} + a_{E-Bz} + a_{TE-Bz}} \quad \text{equation 22}$$

$$Y_{DE-Bz} = 2 \cdot \frac{a_{DE-Bz}}{a_{Bz} + a_{DE-Bz} + a_{E-Bz} + a_{TE-Bz}} \quad \text{equation 23}$$

$$Y_{TE-Bz} = \frac{a_{TE-Bz}}{a_{Bz} + a_{DE-Bz} + a_{E-Bz} + a_{TE-Bz}} \quad \text{equation 24}$$

The area under the peak from the GC,  $A_i$ , is related to the mass of the identified component.

The corrected peak area,  $a_i$ , is defined by the peak area divided by the molecular weight of the respective component and multiplied by a specific sensitivity factor (FID factor):

$$a_i = \frac{A_i \cdot f_i}{M_i} \quad \text{equation 25}$$

Where:

$a_i$  = corrected values of area under the peak of component i corresponding to the molar amount from the gas chromatogram

$A_i$  = area under the peak of component i from the gas chromatogram

$f_i$  = FID factor of component i (-)

$M_i$  = molecular weight of component i ( $\text{g} \cdot \text{mol}^{-1}$ )

The FID factors for hydrocarbons can be obtained from the following:

$$f_i = f_j \cdot \frac{Z_j \cdot M_i}{Z_i \cdot M_j} \quad \text{equation 26}$$

Where:

- f = FID factor of each component (-)
- Z = carbon number of each component (-)
- M = molecular weight ( $\text{g} \cdot \text{mol}^{-1}$ )
- i = index for component i
- j = index for benzene taken as reference

Benzene is selected as reference and its FID factor is 1.000.

Table 9. FID factors of components involved in ethylbenzene disproportionation.

Component	Formula	M ( $\text{g} \cdot \text{mol}^{-1}$ )	$f_i$
benzene	$\text{C}_6\text{H}_6$	78.1	1.000
ethylbenzene	$\text{C}_8\text{H}_{10}$	106.2	1.019
1,3-diethylbenzene	$\text{C}_{10}\text{H}_{14}$	134.2	1.031
1,4-diethylbenzene	$\text{C}_{10}\text{H}_{14}$	134.2	1.031
1,2-diethylbenzene	$\text{C}_{10}\text{H}_{14}$	134.2	1.031
1,2,4-triethylbenzene	$\text{C}_{12}\text{H}_{18}$	162.3	1.039
1,3,5-triethylbenzene	$\text{C}_{12}\text{H}_{18}$	162.3	1.039

### 3.4.2. *n*-Decane hydroconversion

#### 3.4.2.1. Experimental setup

*n*-Decane hydroconversion was carried out at atmospheric pressure in a flow-type apparatus with a fixed-bed reactor, a saturator and on-line sampling GC as shown in Fig. 37 (the same as used for ethylbenzene disproportionation). The catalysts were pressed binder-free, crushed and sieved to obtain the particle size fraction between 0.26 and 0.35 mm. The bifunctional form of the catalyst (ca. 0.4 g) admixed with 3 ml quartz sand (p.a., bead size 0.26-0.6 mm, Fluka) was loaded into the reactor. The activation was carried out in-situ according to the program shown in Table 10. The reaction took place under H<sub>2</sub> atmosphere with partial pressures of *n*-decane and H<sub>2</sub> amounting to 1 kPa and ca. 101.3 kPa ( $\dot{n}_{\text{H}_2} / \dot{n}_{n\text{-De}} \approx 100$ ), respectively. The saturator temperature of *n*-decane ( $\geq 99$  wt.%, Alfa Aesar) was adjusted at 52.6 °C. The modified residence time was kept constant at  $W_{\text{cat}}/F_{n\text{-De}} = 400$  g·h/mol, while the reaction temperature was varied in order to vary the conversion.

Table 10. Conditions for catalyst activation prior to *n*-decane hydroconversion.

Step	Media	Program
dehydration	N <sub>2</sub>	RT $\xrightarrow{2^\circ\text{C}/\text{min}}$ 400 °C $\xrightarrow{12\text{ h}}$ 400 °C $\longrightarrow$ 300 °C
calcination	air	300 °C $\xrightarrow{7\text{ h}}$ 300 °C $\longrightarrow$ 310 °C
flushing	N <sub>2</sub>	310 °C $\xrightarrow{1\text{ h}}$ 310 °C $\longrightarrow$ 300 °C
reduction	H <sub>2</sub>	300 °C $\xrightarrow{10\text{ h}}$ 300 °C $\longrightarrow$ T <sub>R</sub>

The protocol for GC analysis and the retention times for all components are shown in Tables 11 and 12, respectively.

Table 11. Conditions for the gas chromatographic analysis of the products from *n*-decane hydroconversion.

sample volume	1000 $\mu$ l
sample injection time	0.5 min
injection temperature	200 $^{\circ}$ C
oven temperature program	10 $^{\circ}$ C $\xrightarrow{5^{\circ}\text{C}/\text{min}}$ 160 $^{\circ}$ C $\xrightarrow{5\text{ min}}$ 160 $^{\circ}$ C
carrier gas	H <sub>2</sub>
column flow	1.2 ml/min (constant flow mode)
split ratio	30:1
column type	CP-Sil PONA from Varian (length: 100 m, inner diameter: 0.25 mm, film thickness: 0.5 $\mu$ m)
detector	flame ionization detector (FID)
detector temperature	250 $^{\circ}$ C
valve box temperature	160 $^{\circ}$ C

Table 12. Retention times of components involved in *n*-decane hydroconversion.

Component	Retention time (min)
propane	7.2
i-butane	7.7
<i>n</i> -butane	8.1
2-methylbutane	9.4
<i>n</i> -pentane	10
2,2-dimethylbutane	11
2,3-dimethylbutane	11.9
2-methylpentane	12.1
3-methylpentane	12.5
<i>n</i> -hexane	13.1
2,2-dimethylpentane	14
2,4-dimethylpentane	14.2
2-methylhexane	15.7

Table 12. Retention times of components involved in *n*-decane hydroconversion (continued).

Component	Retention time (min)
2,3-dimethylpentane	15.8
3-methylhexane	16
3-ethylpentane	16.4
<i>n</i> -heptane	16.9
2,3-dimethylhexane	19.4
2-methylheptane	19.6
4-methylheptane	19.7
3-methylheptane	19.9
<i>n</i> -octane	20.9
2,4,6-trimethylheptane	23.8
2,2,6-trimethylheptane	23.9
2,2,5-trimethylheptane	24.2
<i>n</i> -nonane	24.6
2,4,5-trimethylheptane	24.7
2,2-dimethyloctane	25.2
2,4-dimethyloctane	25.3
4,4-dimethyloctane	25.5
2,5-dimethyloctane	25.6
3,5-dimethyloctane	25.6
2,7-dimethyloctane	25.7
3,6-dimethyloctane	25.8
2,6-dimethyloctane	25.9
3,3-dimethyloctane	26
3,4-dimethyloctane	26.1
3-ethyl-4-methylheptane	26.2
4-propylheptane	26.3
4,5-dimethyloctane	26.4
3-ethyl-3-methylheptane	26.4
2,3-dimethyloctane	26.6
4-ethyloctane	26.7
5-methylnonane	26.8
4-methylnonane	26.9
2-methylnonane	27
3-ethyloctane	27.1
3-methylnonane	27.2
<i>n</i> -decane	28.2

## 3.4.2.2. Catalytic evaluation

The conversion, yield and selectivity in this reaction are determined referring to mass fractions via the following equations:

$$X_i = \frac{\dot{m}_{i,0} - \dot{m}_i}{\dot{m}_{i,0}} \quad \text{equation 27}$$

$$Y_{j,i} = \frac{\dot{m}_j - \dot{m}_{j,0}}{\dot{m}_{i,0}} \quad \text{equation 28}$$

$$S_{j,i} = \frac{\dot{m}_j - \dot{m}_{j,0}}{\dot{m}_{i,0} - \dot{m}_i} \quad \text{equation 29}$$

$$\dot{m}_i = A_i \cdot f_i \cdot C \quad \text{equation 30}$$

Where:

- $X_i$  = conversion of reactant i (-)
- $Y_{j,i}$  = yield of product j referring to reactant i (-)
- $S_{j,i}$  = selectivity of product j referring to reactant i (-)
- $\dot{m}_{i,0}$  = mass flow of reactant i at the reactor inlet ( $\text{g} \cdot \text{h}^{-1}$ )
- $\dot{m}_i$  = mass flow of reactant i at the reactor outlet ( $\text{g} \cdot \text{h}^{-1}$ )
- $\dot{m}_{j,0}$  = mass flow of product j at the reactor inlet ( $\text{g} \cdot \text{h}^{-1}$ )
- $\dot{m}_j$  = mass flow of product j at the reactor outlet ( $\text{g} \cdot \text{h}^{-1}$ )
- $A_i$  = area under the peak of component i from the gas chromatogram
- $f_i$  = FID factor of component i (-)
- $C$  = gas chromatographic constant (-)

The FID factors of the components occurring in *n*-decane hydroconversion are presented in Table 13.

Table 13. FID factors of the components involved in *n*-decane hydroconversion.

Component	Formula	M (g·mol <sup>-1</sup> )	f <sub>i</sub>
propane	C <sub>3</sub> H <sub>8</sub>	44.1	1.129
i-butane	C <sub>4</sub> H <sub>10</sub>	58.1	1.116
<i>n</i> -butane	C <sub>4</sub> H <sub>10</sub>	58.1	1.116
2-methylbutane	C <sub>5</sub> H <sub>12</sub>	72.2	1.108
<i>n</i> -pentane	C <sub>5</sub> H <sub>12</sub>	72.2	1.108
2,2-dimethylbutane	C <sub>6</sub> H <sub>14</sub>	86.2	1.103
2,3-dimethylbutane	C <sub>6</sub> H <sub>14</sub>	86.2	1.103
2-methylpentane	C <sub>6</sub> H <sub>14</sub>	86.2	1.103
3-methylpentane	C <sub>6</sub> H <sub>14</sub>	86.2	1.103
<i>n</i> -hexane	C <sub>6</sub> H <sub>14</sub>	86.2	1.103
2,2-dimethylpentane	C <sub>7</sub> H <sub>16</sub>	100.2	1.100
2,4-dimethylpentane	C <sub>7</sub> H <sub>16</sub>	100.2	1.100
2-methylhexane	C <sub>7</sub> H <sub>16</sub>	100.2	1.100
2,3-dimethylpentane	C <sub>7</sub> H <sub>16</sub>	100.2	1.100
3-methylhexane	C <sub>7</sub> H <sub>16</sub>	100.2	1.100
3-ethylpentane	C <sub>7</sub> H <sub>16</sub>	100.2	1.100
<i>n</i> -heptane	C <sub>7</sub> H <sub>16</sub>	100.2	1.100
2,3-dimethylhexane	C <sub>8</sub> H <sub>18</sub>	114.2	1.097
2-methylheptane	C <sub>8</sub> H <sub>18</sub>	114.2	1.097
4-methylheptane	C <sub>8</sub> H <sub>18</sub>	114.2	1.097
3-methylheptane	C <sub>8</sub> H <sub>18</sub>	114.2	1.097
<i>n</i> -octane	C <sub>8</sub> H <sub>18</sub>	114.2	1.097
2,4,6-trimethylheptane	C <sub>10</sub> H <sub>22</sub>	142.3	1.093
2,2,6-trimethylheptane	C <sub>10</sub> H <sub>22</sub>	142.3	1.093
2,2,5-trimethylheptane	C <sub>10</sub> H <sub>22</sub>	142.3	1.093
<i>n</i> -nonane	C <sub>9</sub> H <sub>20</sub>	128.3	1.095
2,4,5-trimethylheptane	C <sub>10</sub> H <sub>22</sub>	142.3	1.093
2,2-dimethyloctane	C <sub>10</sub> H <sub>22</sub>	142.3	1.093
2,4-dimethyloctane	C <sub>10</sub> H <sub>22</sub>	142.3	1.093
4,4-dimethyloctane	C <sub>10</sub> H <sub>22</sub>	142.3	1.093
2,5-dimethyloctane	C <sub>10</sub> H <sub>22</sub>	142.3	1.093
3,5-dimethyloctane	C <sub>10</sub> H <sub>22</sub>	142.3	1.093
2,7-dimethyloctane	C <sub>10</sub> H <sub>22</sub>	142.3	1.093
3,6-dimethyloctane	C <sub>10</sub> H <sub>22</sub>	142.3	1.093
2,6-dimethyloctane	C <sub>10</sub> H <sub>22</sub>	142.3	1.093
3,3-dimethyloctane	C <sub>10</sub> H <sub>22</sub>	142.3	1.093

Table 13. FID factors of components involved in *n*-decane hydroconversion (continued).

Component	Formula	M (g·mol <sup>-1</sup> )	f <sub>i</sub>
3,4-dimethyloctane	C <sub>10</sub> H <sub>22</sub>	142.3	1.093
3-ethyl-4-methylheptane	C <sub>10</sub> H <sub>22</sub>	142.3	1.093
4-propylheptane	C <sub>10</sub> H <sub>22</sub>	142.3	1.093
4,5-dimethyloctane	C <sub>10</sub> H <sub>22</sub>	142.3	1.093
3-ethyl-3-methylheptane	C <sub>10</sub> H <sub>22</sub>	142.3	1.093
2,3-dimethyloctane	C <sub>10</sub> H <sub>22</sub>	142.3	1.093
4-ethyloctane	C <sub>10</sub> H <sub>22</sub>	142.3	1.093
5-methylnonane	C <sub>10</sub> H <sub>22</sub>	142.3	1.093
4-methylnonane	C <sub>10</sub> H <sub>22</sub>	142.3	1.093
2-methylnonane	C <sub>10</sub> H <sub>22</sub>	142.3	1.093
3-ethyloctane	C <sub>10</sub> H <sub>22</sub>	142.3	1.093
3-methylnonane	C <sub>10</sub> H <sub>22</sub>	142.3	1.093
<i>n</i> -decane	C <sub>10</sub> H <sub>22</sub>	142.3	1.093

### 3.4.3. Competitive hydrogenation of olefins

#### 3.4.3.1. Experimental setup

The competitive hydrogenation of a slim and a more bulky olefin was performed at atmospheric pressure in a flow-type apparatus with fixed-bed reactor, two saturators containing 1-hexene (97 %, Aldrich) and 2,4,4-trimethyl-1-pentene ( $\geq 98$  %, Fluka), respectively, and on-line analysis via GC as depicted in Fig. 38. H<sub>2</sub> as a carrier gas was loaded with equimolar amounts of 1-hexene and 2,4,4-trimethyl-1-pentene with partial pressures amounting to 7.15 kPa each ( $T_{s,1\text{-hexene}} = -1.4$  °C and  $T_{s,2,4,4\text{-trimethyl-1-pentene}} = 27.6$  °C). The modified residence time,  $W_{\text{cat}}/F_{\text{alkenes}}$ , was adjusted to 10 g·h/mol. The palladium-containing catalysts were pressed binder-free, crushed and sieved to obtain the particle size fraction between 0.26 and 0.35 mm. The catalyst (ca. 0.2 g) was diluted with 3 ml of quartz sand (p.a., bead size 0.26-0.6 mm, Fluka). The catalytic tests were carried out at reaction temperatures of 75 and 100 °C for a period of ca. 4 h. Before each test, the catalysts were

treated in a similar way as already described for *n*-decane hydroconversion (cf. Table 10). Additionally, after the reduction step, the catalyst was flushed with NH<sub>3</sub> at 100 °C for 1 h ( $V_{\text{NH}_3} = 40 \text{ ml/min}$ ) to poison the strong acid sites in the catalyst. Afterwards, the catalyst was flushed with N<sub>2</sub> for another 0.5 h before the reaction was started under a flow of H<sub>2</sub>. The complete treatment program is shown in Table 14.

Table 14. Conditions for catalyst activation prior to competitive hydrogenation of an olefin mixture.

Step	Media	Program
dehydration	N <sub>2</sub>	RT $\xrightarrow{2^\circ\text{C/min}}$ 400 °C $\xrightarrow{12 \text{ h}}$ 400 °C $\longrightarrow$ 300 °C
calcination	air	300 °C $\xrightarrow{7 \text{ h}}$ 300 °C $\longrightarrow$ 310 °C
flushing	N <sub>2</sub>	310 °C $\xrightarrow{1 \text{ h}}$ 310 °C $\longrightarrow$ 300 °C
reduction	H <sub>2</sub>	300 °C $\xrightarrow{10 \text{ h}}$ 300 °C $\longrightarrow$ 100 °C
flushing	N <sub>2</sub>	100 °C $\xrightarrow{0.5 \text{ h}}$ 100 °C
neutralization of strong acid sites	NH <sub>3</sub>	100 °C $\xrightarrow{1 \text{ h}}$ 100 °C
flushing	N <sub>2</sub>	100 °C $\xrightarrow{0.5 \text{ h}}$ 100 °C
reaction	H <sub>2</sub>	75 °C and 100 °C

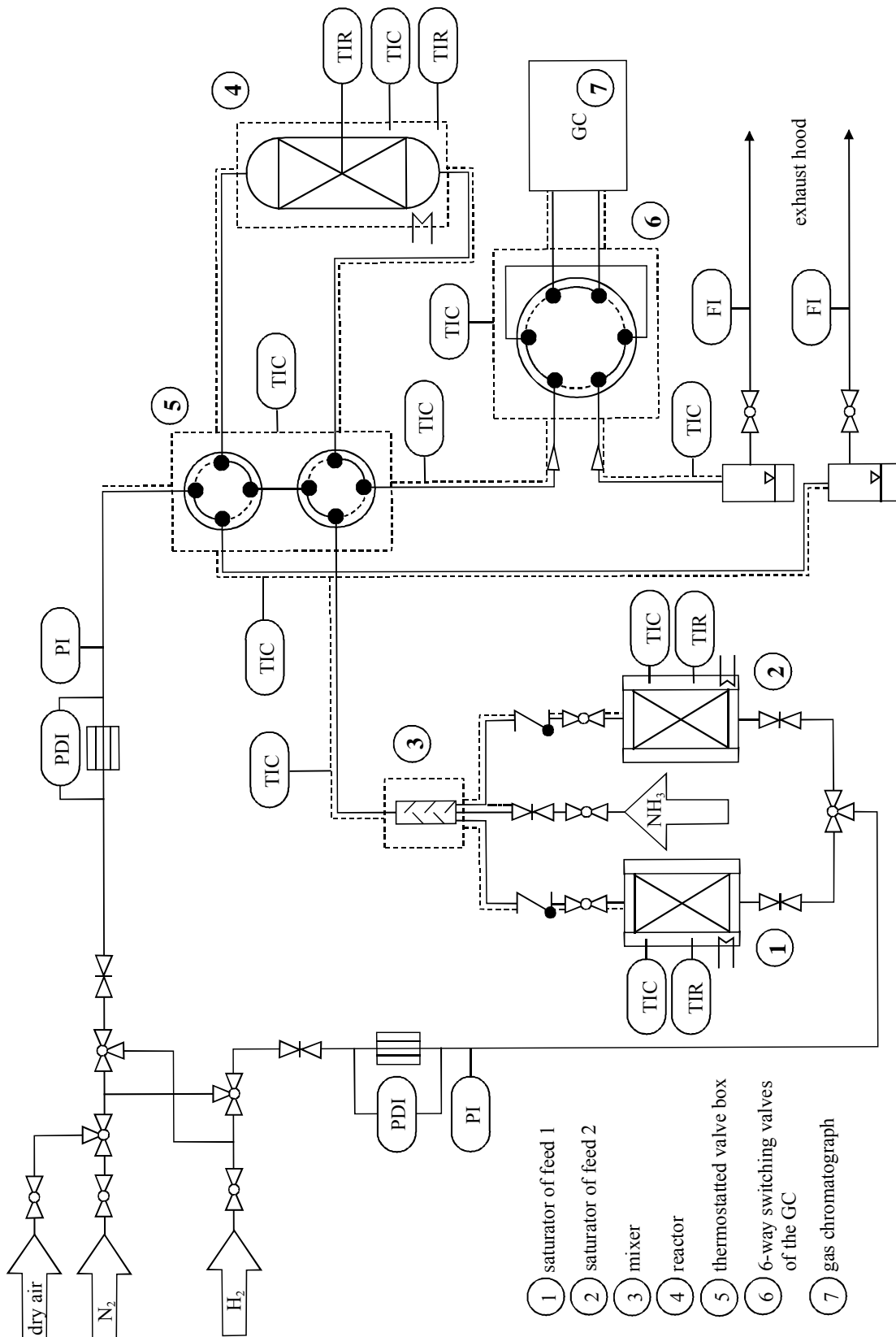


Fig. 38. Schematic diagram of the fixed-bed flow-type apparatus for the competitive hydrogenation of an olefin mixture.

The conditions of GC analysis and the retention times of the components involved in olefin hydrogenation are shown in Table 15 and 16, respectively.

Table 15. Conditions for the gas chromatographic analysis of the products from the competitive hydrogenation of olefins.

sample volume	1000 $\mu$ l
sample injection time	0.5 min
injection temperature	200 $^{\circ}$ C
oven temperature program	60 $^{\circ}$ C $\xrightarrow{5^{\circ}\text{C}/\text{min}}$ 120 $^{\circ}$ C
carrier gas	H <sub>2</sub>
column flow	1.2 ml/min (constant flow mode)
split ratio	30:1
column type	CP-Sil PONA from Varian (length: 100 m, inner diameter: 0.25 mm, film thickness: 0.5 $\mu$ m)
detector	flame ionization detector (FID)
detector temperature	250 $^{\circ}$ C
valve box temperature	160 $^{\circ}$ C

Table 16. Retention times of components involved in the competitive hydrogenation of olefins.

Component	Retention time (min)
1-hexene	8.2
<i>n</i> -hexane	8.4
2,2,4-trimethylpentane	10
2,4,4-trimethyl-1-pentene	10.4

## 3.4.3.2. Catalytic evaluation

The evaluation of the catalytic data was carried out analogous to equation 17 as:

$$Y_{n\text{-hexane}} = \frac{\dot{n}_{n\text{-hexane}} - \dot{n}_{n\text{-hexane},0}}{\dot{n}_{1\text{-hexene},0}} \quad \text{equation 31}$$

$$Y_{2,2,4\text{-trimethylpentane}} = \frac{\dot{n}_{2,2,4\text{-trimethylpentane}} - \dot{n}_{2,2,4\text{-trimethylpentane},0}}{\dot{n}_{2,4,4\text{-trimethyl-1-pentene},0}} \quad \text{equation 32}$$

Where:

$Y_{n\text{-hexane}}$  = yield of the product *n*-hexane referring to the reactant 1-hexene (-)

$Y_{2,2,4\text{-trimethylpentane}}$  = yield of the product 2,2,4-trimethylpentane referring to the reactant 2,4,4-trimethyl-1-pentene (-)

$\dot{n}_{n\text{-hexane}}$  = molar flow of the product *n*-hexane at the reactor outlet (mol·h<sup>-1</sup>)

$\dot{n}_{n\text{-hexane},0}$  = molar flow of the product *n*-hexane at the reactor inlet (mol·h<sup>-1</sup>)

$\dot{n}_{1\text{-hexene},0}$  = molar flow of the reactant 1-hexene at the reactor inlet (mol·h<sup>-1</sup>)

$\dot{n}_{2,2,4\text{-trimethylpentane}}$  = molar flow of the product 2,2,4-trimethylpentane at the reactor outlet (mol·h<sup>-1</sup>)

$\dot{n}_{2,2,4\text{-trimethylpentane},0}$  = molar flow of the product 2,2,4-trimethylpentane at the reactor inlet (mol·h<sup>-1</sup>)

$\dot{n}_{2,4,4\text{-trimethyl-1-pentene},0}$  = molar flow of the reactant 2,4,4-trimethyl-1-pentene at the reactor inlet (mol·h<sup>-1</sup>)

Table 17. FID factors of components involved in the competitive hydrogenation of olefins.

Component	Formula	M (g·mol <sup>-1</sup> )	f <sub>i</sub>
1-hexene	C <sub>6</sub> H <sub>12</sub>	84.2	1.077
<i>n</i> -hexane	C <sub>6</sub> H <sub>14</sub>	86.2	1.103
2,2,4-trimethylpentane	C <sub>8</sub> H <sub>18</sub>	114.2	1.097
2,4,4-trimethyl-1-pentene	C <sub>8</sub> H <sub>16</sub>	112.2	1.078

## 4. Results and discussions

### 4.1. Synthesis and characterization of zeolites based on 14-membered ring pore openings

#### 4.1.1. Zeolite UTD-1

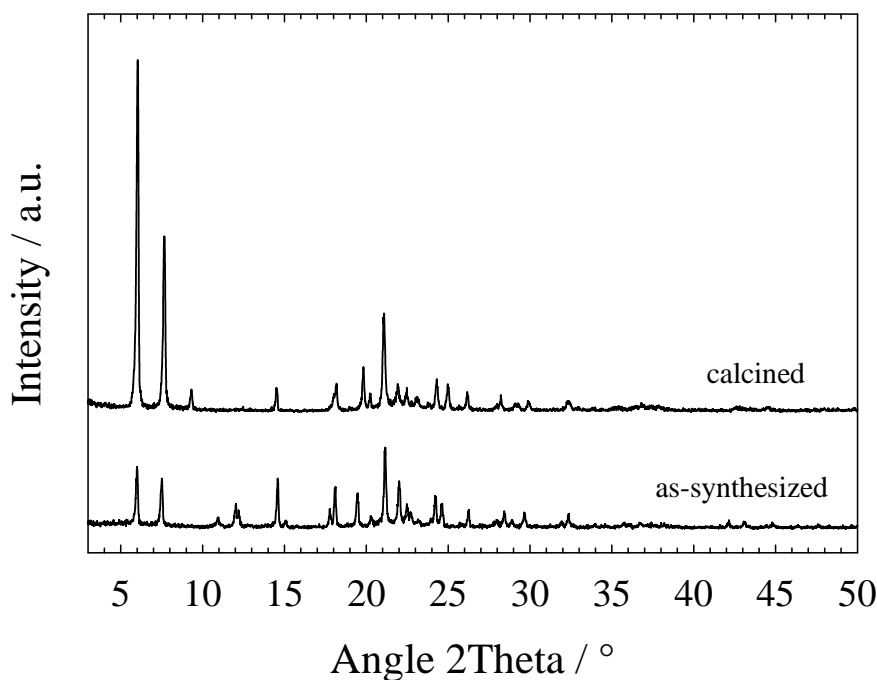


Fig. 39. XRD patterns of as-synthesized and calcined Si-UTD-1.

Fig. 39 and 40 show the XRD patterns of the as-synthesized and the calcined forms of all-silica UTD-1 (Si-UTD-1) and boron-containing UTD-1 (B-UTD-1), respectively. The XRD patterns show pure phases of UTD-1 with the main peaks at  $2\theta \approx 6$  and  $7.5^\circ$  [20, 33]. The intensities of the main peaks increase after calcination. The changes in the relative intensities result from the removal of the template from the structure. After the modification of B-UTD-1 to protonated Al-UTD-1 by removing of cobalt species in the pores followed by insertion of aluminium, the structure still maintained, as can be seen from Fig. 41. A slight increase of the intensities of the main peaks in the cobalt-free and the protonated samples is observed.

Zeolite UTD-1 possesses a high thermal stability of up to 800 °C. The chemical analysis of the protonated Al-UTD-1 reveals a molar ratio of  $n_{\text{Si}}/n_{\text{Al}} = 28$ .

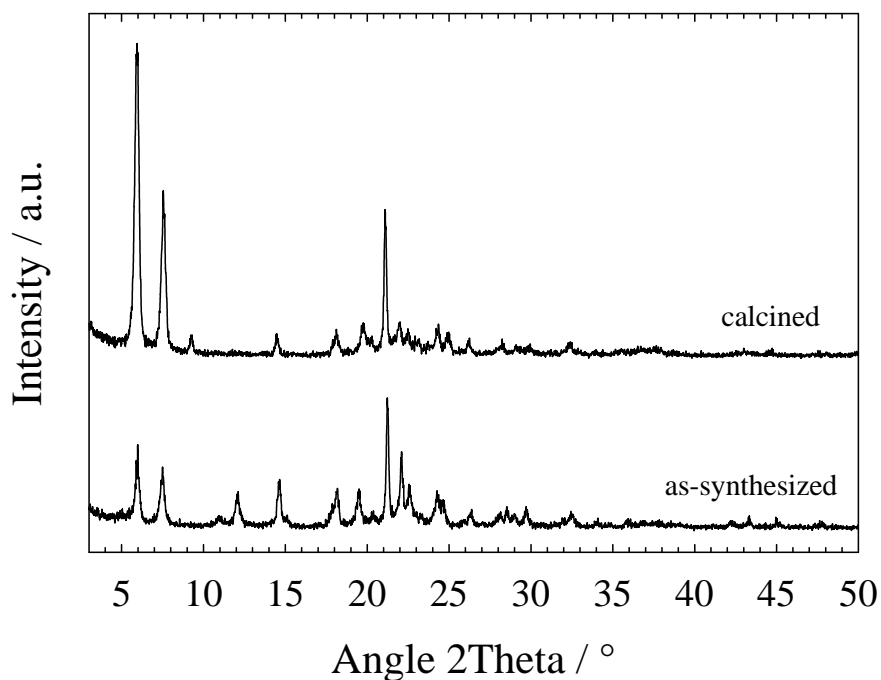


Fig. 40. XRD patterns of as-synthesized and calcined B-UTD-1.

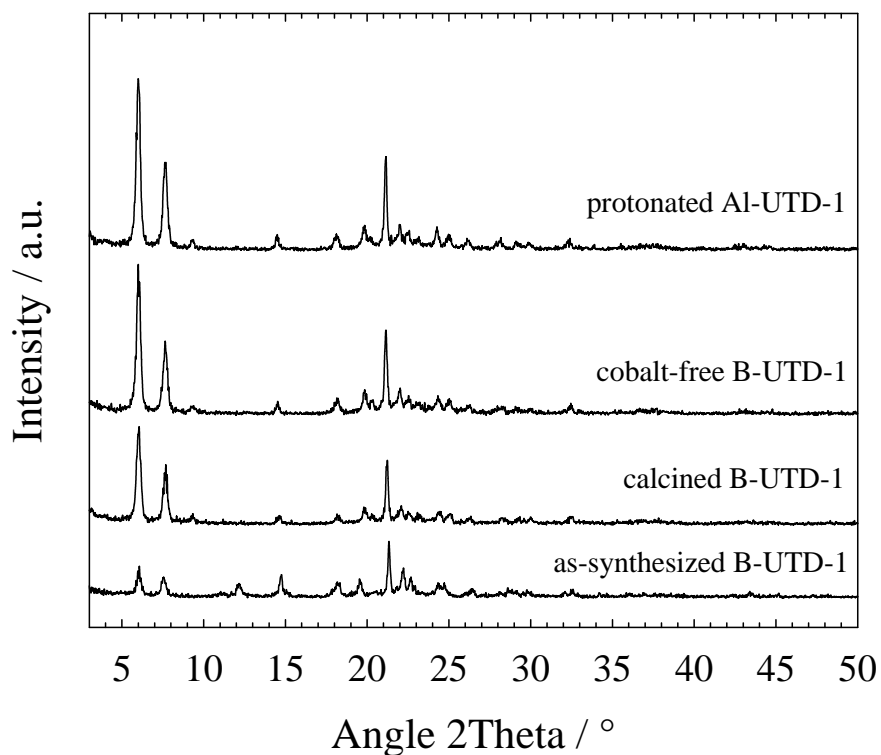


Fig. 41. XRD patterns of as-synthesized B-UTD-1 and after modification steps.

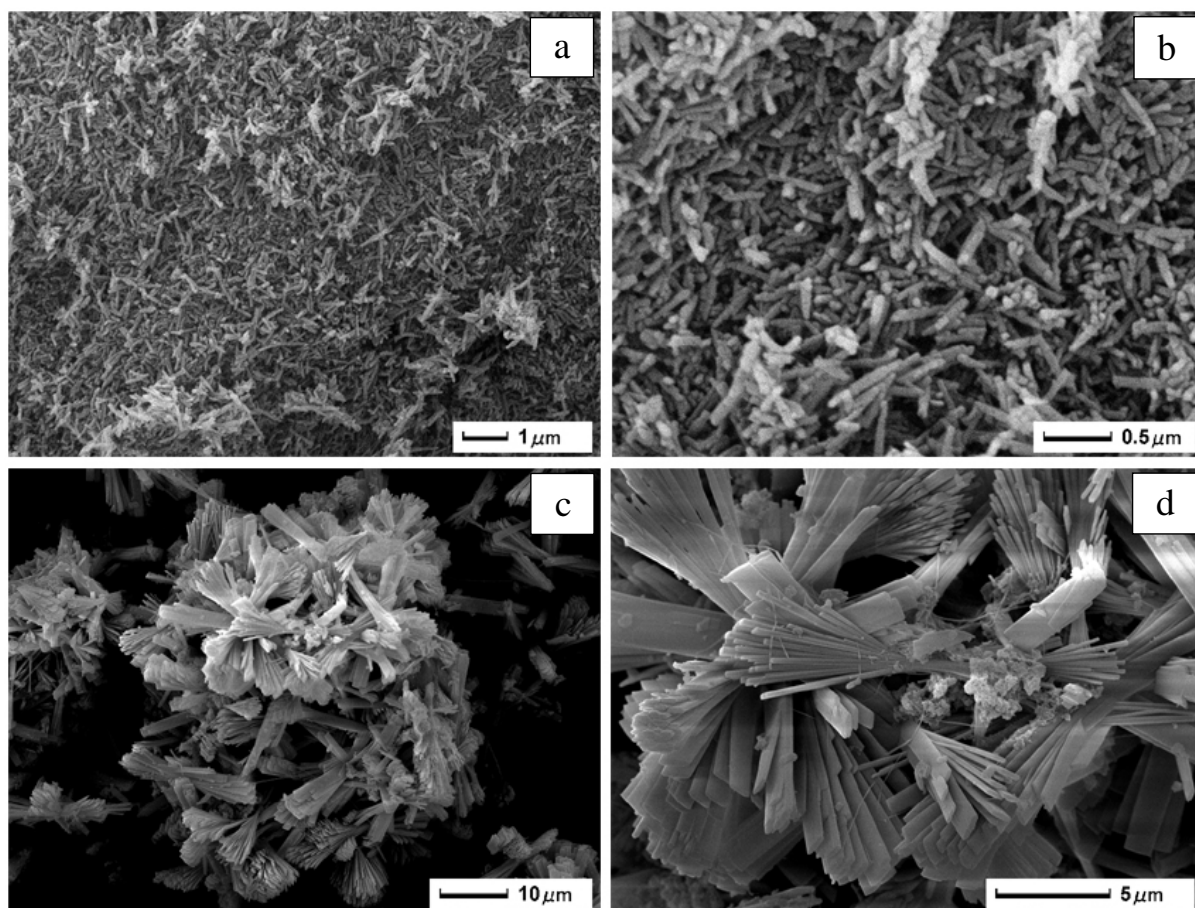


Fig. 42. SEM pictures of (a), (b) calcined B-UTD-1 and (c), (d) calcined Si-UTD-1.

The crystal morphology of B-UTD-1 exhibits a rod-like shape ca. 0.4-1 μm long, while the crystal shape of Si-UTD-1 shows thin laths with dimension ca. 10 μm long and ca. 1-2 μm wide. The differences in the crystal shape and size could result from the differences in the gel composition by using B-Beta zeolite as boron and silica sources in B-UTD-1 synthesis instead of silica gel as the only silica source in Si-UTD-1.

After calcination, the yellow colour of the as-synthesized form has changed to an olive green-grey. The yellow colour and the UV-Vis spectroscopic characterization of the as-synthesized sample indicate that the  $\text{Cp}^*_2\text{Co}^+$  template used for the synthesis is still intact in the final zeolite. Fig. 43 presents the UV-Vis spectra of as-synthesized and calcined B-UTD-1 as well as a spectrum of the template solution as reference. The as-synthesized form of B-UTD-1 exhibits an absorption band at wavelength of ca. 300 nm with a shoulder at ca. 350 and a

weak band at ca. 400 nm, whereas no absorption band is observed for the calcined form. The transition responsible for the yellow colour of  $\text{Cp}^*_2\text{Co}^+$  at ca. 350 and 400 nm can be assigned to the spin-allowed d-d transition, whereas the high-energy band at ca. 300 nm arises from ligand-to-metal (L $\rightarrow$ M) charge transfer transition ( $\pi\rightarrow\pi^*$ ) [132]. There is a slightly red shift relative to that of the template solution.

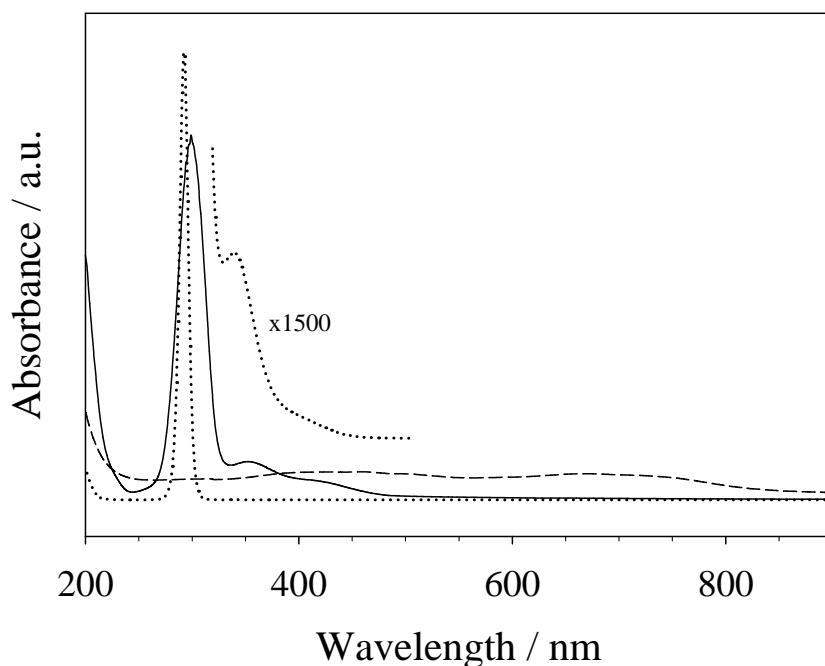


Fig. 43. UV-Vis spectroscopy of as-synthesized B-UTD-1 (solid line), calcined B-UTD-1 (dashed line) and the solution of  $\text{Cp}^*_2\text{CoOH}$  (template) with intensification (dotted lines).

The IR spectra of the template complex ( $\text{Cp}^*_2\text{CoCl}$ ), the as-synthesized and calcined forms and of protonated Al-UTD-1 are depicted in Fig. 44. This method is applied to examine the surface properties of the catalyst, e.g., the presence of template and acid sites. The presence of template in the as-synthesized form is indicated by the vibration bands at wave numbers of 1390, 1430, 1460, 1480, 2920 and 2970  $\text{cm}^{-1}$  (Fig. 44b). This is consistent with the bands from the solid template (Fig. 44a) and with the result from the UV-Vis spectrum (Fig. 43) suggesting that the template is intact in the zeolite. The assignment of the vibration bands of the as-synthesized form and of the template are presented in Table 18.

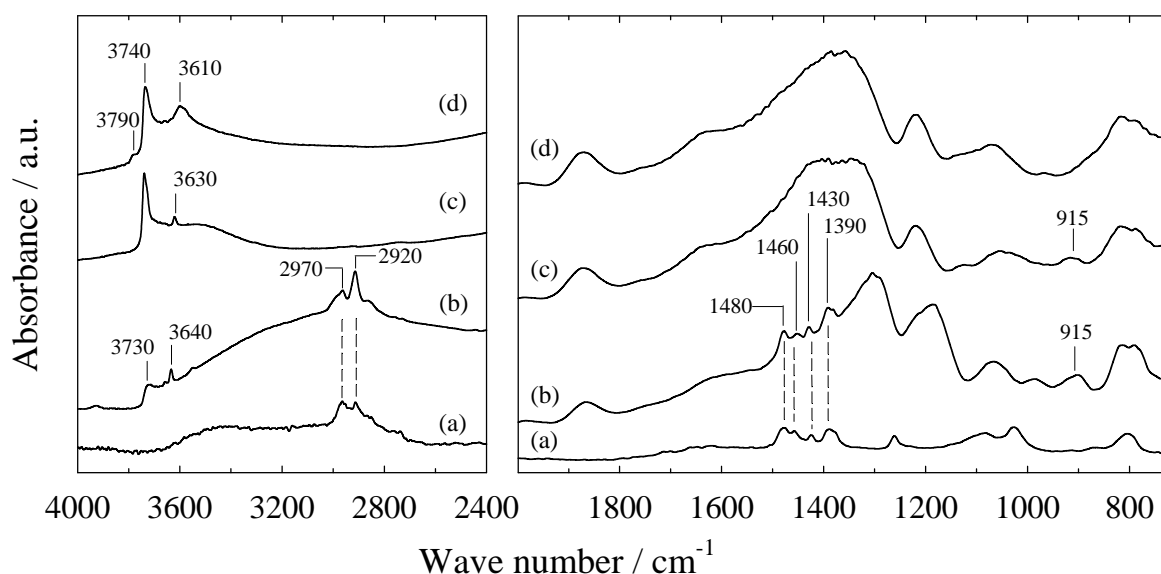


Fig. 44. IR spectra of (a) template  $\text{Cp}^*_2\text{CoCl}$  (b) as-synthesized B-UTD-1 (c) calcined B-UTD-1 and (d) protonated Al-UTD-1.

The vibration bands of the template are no more detected for the calcined sample (Fig. 44c). This suggests that the template is properly removed by the calcination treatment. The presence of the band at wave numbers of ca.  $915\text{ cm}^{-1}$  in the as-synthesized and calcined forms (Fig. 44b and c) is indicative of the presence of boron in tetrahedral coordination in the zeolite framework as observed in various boron-containing zeolites [133-135]. This band is not present in the Si-UTD-1 sample (not shown here). In the hydroxyl region, the bands of the silanol groups are observed at wave numbers of ca.  $3740\text{ cm}^{-1}$  for all samples (Fig. 44b, c and d) with more intense bands for the calcined and the protonated forms. The bands in the Brønsted-acid site region are observed at wave numbers of ca.  $3640$ ,  $3630$  and  $3610\text{ cm}^{-1}$  for the as-synthesized, calcined and protonated forms, respectively. However, the most intense band is observed for the protonated form of Al-UTD-1. This indicates the higher number/density of Brønsted-acid sites in the Al-UTD-1 sample. The band at ca.  $3790\text{ cm}^{-1}$  is detected only in the Al-UTD-1 sample (cf. Fig. 44d). This band might be assigned to the

presence of extra-framework aluminium as such a vibration band was observed in the same wave number range on zeolite Beta [136, 137].

Table 18. Assigned groups in the vibration bands of the  $\text{Cp}^*_2\text{CoCl}$  complex and of as-synthesized B-UTD-1.

Wave number ( $\text{cm}^{-1}$ )		Assigned group
$\text{Cp}^*_2\text{CoCl}$	B-UTD-1	
2970	2970	C-H asymmetric stretching
2920	2920	C-H symmetric stretching
1480	1480	C=C or C-C stretching
1470	1460	C=C or C-C stretching
1430	1430	C=C or C-C stretching
1390	1390	C=C or C-C stretching
1080	-	C-H bending
810	-	C-H out of plane bending

The thermogravimetric analysis of B-UTD-1 in air exhibits three stages of weight loss as shown in Fig. 45. The first stage from 20-200 °C (0.4 wt.-%) is assigned to the desorption of water. The second and third stages from 200-400 °C (7.5 wt.-%) and from 400-600 °C (6.5 wt.-%), respectively, are assigned to the combustion of the template with a total weight loss of 14 wt.-%. This was verified by mass spectrometry and the observed exothermal behaviour also confirms the combustion of the organic template. Further weight loss is not observed after 600 °C and also until the final temperature of ca. 1000 °C.

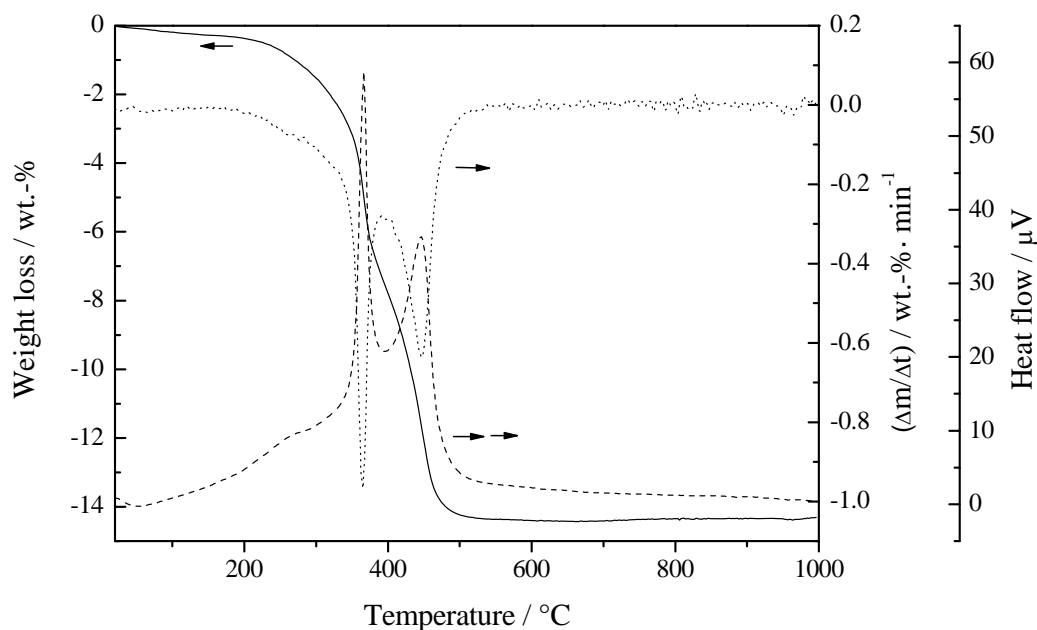


Fig. 45. Thermogravimetric analysis of as-synthesized B-UTD-1 in an air flow: weight loss (solid line), differential weight loss (dotted line) and heat flow (dashed line).

The adsorption properties of different forms of Si-UTD-1 and B-UTD-1 for  $N_2$  are presented in Table 19. As expected, an increase of the specific surface area and the specific pore volume of the cobalt-free B-UTD-1 as compared to the cobalt-containing sample is observed. This suggests that small cobalt-containing species which are occluded in the pores can partially block the channels of the zeolite, hence, they are most probably located inside the pores. A decrease of the specific surface area and the specific pore volume for protonated Al-UTD-1 indicates a partial deterioration of the structure due to the post-synthesis treatments.

Table 19. Adsorption properties of Si-UTD-1 and B-UTD-1 in different forms.

Material	$S_{BET}$ ( $m^2 \cdot g^{-1}$ )	$V_{pore}$ ( $cm^3 \cdot g^{-1}$ )
calcined Si-UTD-1	285	0.13
calcined B-UTD-1 (cobalt-containing)	374	0.18
calcined B-UTD-1 (cobalt-free)	441	0.21
Al-UTD-1	307	0.13

The acidic properties of protonated Al-UTD-1 were investigated by temperature-programmed desorption of pyridine. The obtained desorption profile is shown in Fig. 46. There are virtually four maxima at 290, 340, 427 and 565 °C. The presence of the relatively large desorption peak at the high temperature of ca. 565 °C exhibits that Al-UTD-1 possesses a large amount of strong acid sites quite comparable to the weak and medium ones.

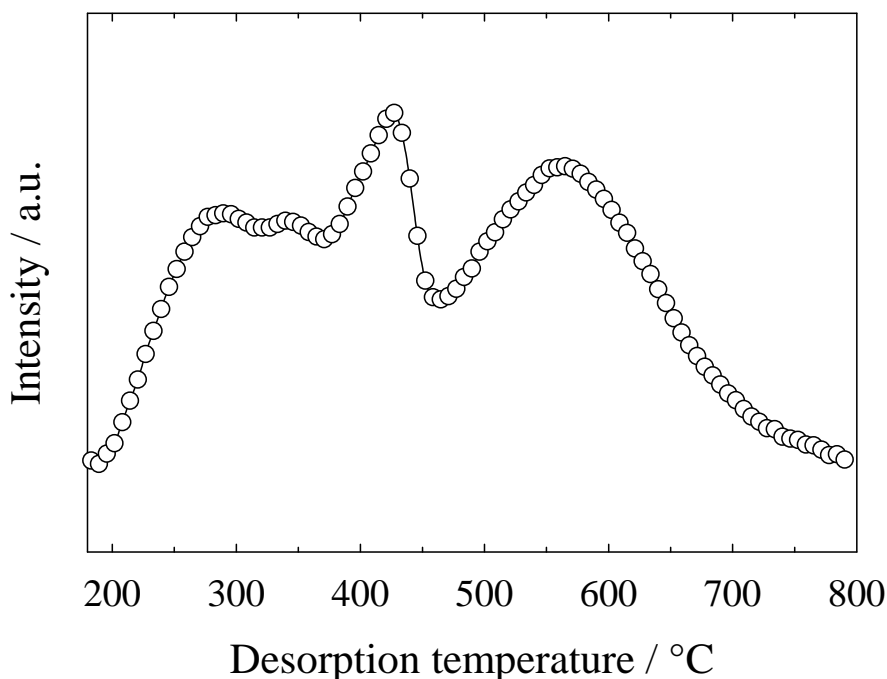


Fig. 46. Temperature-programmed desorption of pyridine from protonated Al-UTD-1.

The nature and properties of cobalt species in the zeolite structure were also investigated. After the calcination, the hydrocarbon fractions of the template molecules are removed while the cobalt species are still occluded in the channels and/or cavities. The colour changes to olive green-grey after the calcination indicates the presence of cobalt oxide species (CoO: olive green-brown and  $\text{Co}_3\text{O}_4$ : black) as common compounds formed when contacting with oxygen. The formation of the cobalt oxides after the calcination of Si-UTD-1 was confirmed using X-Ray absorption spectroscopic methods by Behrens et al. [138].

The reducibility of the cobalt species located in the structure of UTD-1 was investigated using temperature-programmed reduction. Fig. 47 presents the reduction profile from the calcined Si-UTD-1 sample. The reduction starts at ca. 200 °C and ends at ca. 870 °C with three small maxima at 230, 320, 410 °C and a large one at 690 °C (83 % of the total H<sub>2</sub> consumption). The major part of cobalt species in Si-UTD-1 (as seen by the peak maximum at 690 °C) is difficult to reduce as compared to the bulk CoO and Co<sub>3</sub>O<sub>4</sub> phases (also tested in the same apparatus) showing maxima at 320 and 280 °C, respectively.

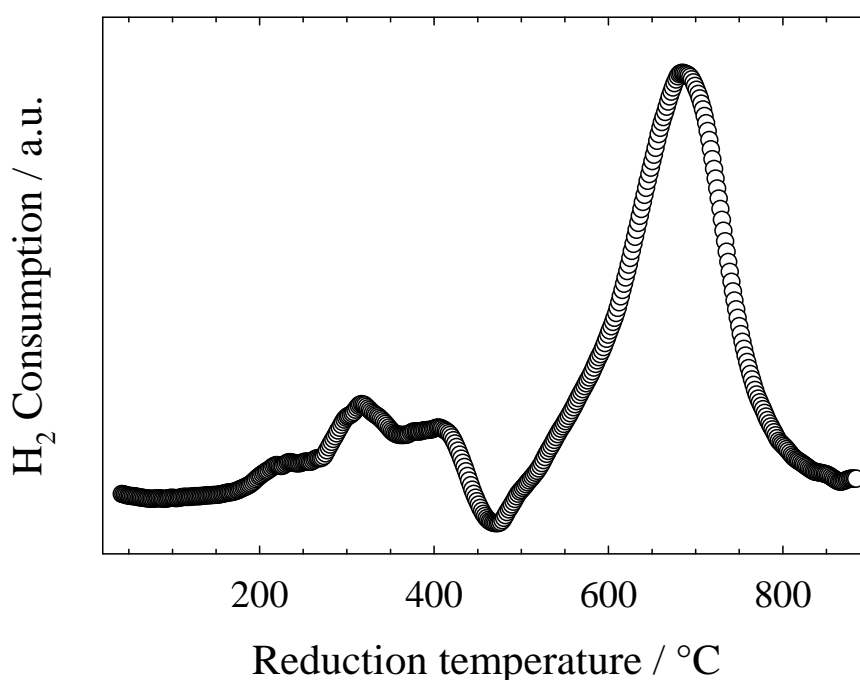


Fig. 47. Temperature-programmed reduction profile of calcined Si-UTD-1.

The oxidation state of the cobalt species was evaluated using TPR and AAS (chemical analysis) methods. According to reduction reaction in equation 33, the H<sub>2</sub> consumption and the amount of the cobalt species present in the sample are used to determine the oxidation state of the cobalt species. The H<sub>2</sub> consumption is determined by integration of the reduction peaks with a pulse calibration and the amount of cobalt is obtained by AAS. The results are summarized in Table 20.



where:

- X = oxidation state of cobalt species (-)  
 $n_{H_2}$  = amount of H<sub>2</sub> consumed by the cobalt species (μmol)  
 $n_{Co}$  = amount of cobalt in the zeolite sample (μmol)

Table 20. Results of the characterization of calcined Si-UTD-1 by TPR and chemical analysis (AAS).

Sample	Co-content (wt.-%)	Integrated area of the TPR profile	Average integrated area of the pulse calibration
calcined Si-UTD-1	3.67	783328	2032.3

The amount of H<sub>2</sub> from the pulse calibration is determined from the ideal gas laws.

$$n_{H_2, cali} = \frac{P \cdot V \cdot \gamma}{R \cdot T} = \frac{1 \cdot 89.32 \cdot 0.05}{0.08206 \cdot (25 + 273.15)} = 0.1825 \mu mol \quad \text{equation 34}$$

Where:

- $n_{H_2, cali}$  = amount of H<sub>2</sub> in the calibration valve (μmol)  
P = pressure at the operation (atm)  
V = volume of the calibration valve (μl)  
γ = volume fraction of H<sub>2</sub> in argon (-)  
R = ideal gas constant (l·atm·mol<sup>-1</sup>·K<sup>-1</sup>)  
T = temperature at the operation (K)

The amount of H<sub>2</sub> consumed by the cobalt species is calculated as follow.

$$n_{H_2} = \frac{n_{H_2, cali} \cdot A}{a} = \frac{0.1825 \cdot 783328}{2032.3} = 70.3 \mu mol \quad \text{equation 35}$$

Where:

$n_{H_2}$  = amount of  $H_2$  consumed by the cobalt species ( $\mu\text{mol}$ )

A = integrated area of the TPR profile (-)

a = average integrated area of the pulse calibration (-)

The amount of cobalt is determined as follows:

$$n_{Co} = \frac{w \cdot c}{M} = \frac{0.1 \cdot 0.0367}{58.933} = 62.3 \mu\text{mol} \quad \text{equation 36}$$

Where:

$n_{Co}$  = amount of cobalt in the sample ( $\mu\text{mol}$ )

w = sample mass (g)

c = cobalt fraction in the zeolite (-)

M = molecular weight of cobalt ( $\text{g} \cdot \text{mol}^{-1}$ )

Therefore,

$$\frac{n_{H_2}}{n_{Co}} = \frac{70.3}{62.3} = 1.13 \quad \text{equation 37}$$

From equation 33, The cobalt species residing in the calcined Si-UTD-1 exhibit oxidation states between +2 and +3. This result is consistent with the presence of cobalt oxides as  $\text{CoO(II)}$  and  $\text{Co}_3\text{O}_4(\text{II, III})$  as reported by Behrens et al. [138].

#### 4.1.2. Zeolite CIT-5

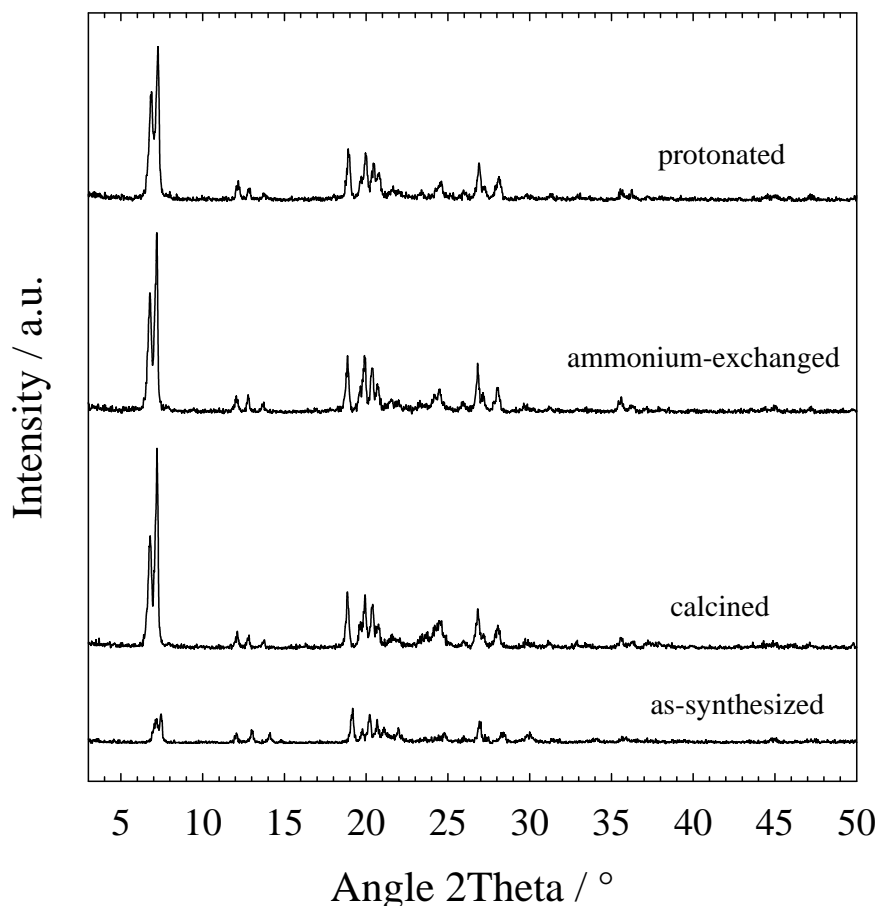


Fig. 48. XRD patterns of as-synthesized CIT-5 and after modification steps.

Zeolite CIT-5 was successfully synthesized as a pure phase as revealed by the measured powder pattern comparing to published data [20, 42]. The XRD patterns of CIT-5 in different forms are shown in Fig. 48 with the main peaks at  $2\theta \approx 7.1$  and  $7.4^\circ$ . The intensities of the main peaks increase significantly upon calcination. After the calcination and ion-exchange steps, it was observed that the structure of CIT-5 is well maintained. The chemical analysis of the protonated sample yielded a molar ratio of  $n_{\text{Si}}/n_{\text{Al}} = 116$ . The crystal morphology of calcined CIT-5 shows thin laths ca. 8-10  $\mu\text{m}$  long and ca. 0.5  $\mu\text{m}$  wide, as can be seen from Fig. 49.

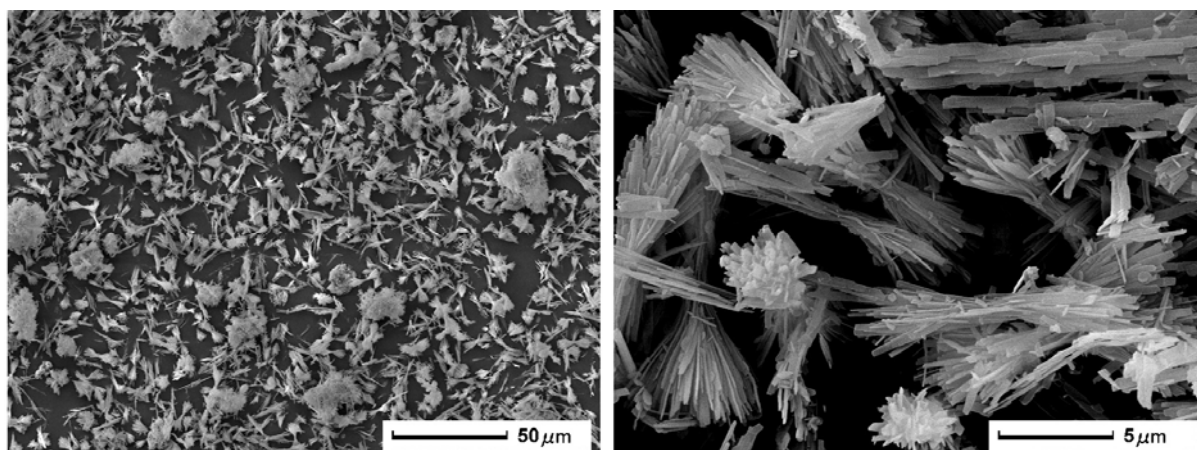


Fig. 49. SEM pictures of calcined CIT-5.

The thermogravimetric analysis of as-synthesized CIT-5 in an air flow shows three stages of weight loss. The first stage from 20-150 °C (1.5 wt.-%) is assigned to water desorbing from the zeolite structure. The second and third stages from 150-250 °C (2.9 wt.-%) and from 250-700 °C (8.7 wt.-%), respectively, are assigned to the combustion of the organic template in two steps with a total weight loss due to the template of 11.6 wt.-%. Nitrogen adsorption at 77 K on calcined CIT-5 yielded a specific surface area of 430 m<sup>2</sup>/g and a specific pore volume of 0.12 cm<sup>3</sup>/g, respectively.

The IR spectra of the solid template (-)-N(16)-methylsparteinium iodide (C<sub>16</sub>H<sub>29</sub>N<sub>2</sub>I) as well as the as-synthesized, calcined and protonated forms of CIT-5 are shown in Fig. 50. In the as-synthesized form, the vibration bands of the template are detected in the range of 2780-2950 cm<sup>-1</sup> for C-H stretching and at 1450 cm<sup>-1</sup> for C-C stretching (Fig. 50b). This is consistent with the wave number range of the vibration bands of the template (Fig. 50a). The absence of these vibrations in the calcined form indicates the complete removal of the template from the zeolite structure (Fig. 50c). Hence, the calcinations procedure was successful. Only silanol groups (vibration bands at wave numbers ca. 3734 cm<sup>-1</sup>) are found in the calcined form, whereas the bands in the Brønsted-acid site region at ca. 3680 cm<sup>-1</sup> and of the silanol groups at ca. 3734 cm<sup>-1</sup> are present in the protonated form (Fig. 50d). This indicates that Brønsted-

acid sites are largely generated after ion-exchanging of lithium ions present from the synthesis with ammonium ions followed by removing of the  $\text{NH}_3$ .

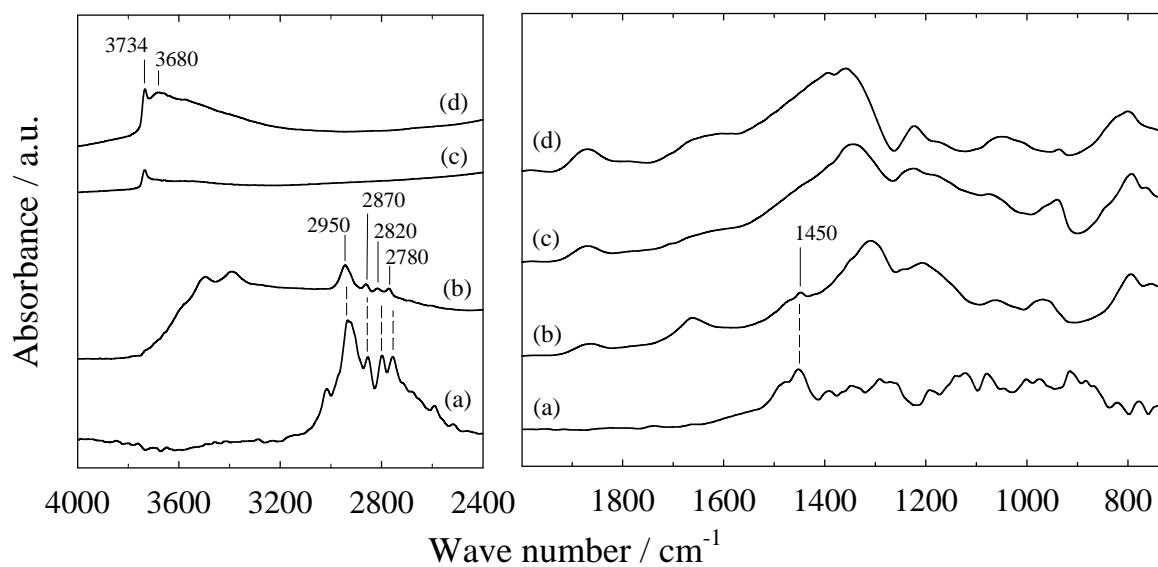


Fig. 50. IR spectra of (a) the template  $\text{C}_{16}\text{H}_{29}\text{N}_2\text{I}$  (b) as-synthesized (c) calcined and (d) protonated CIT-5.

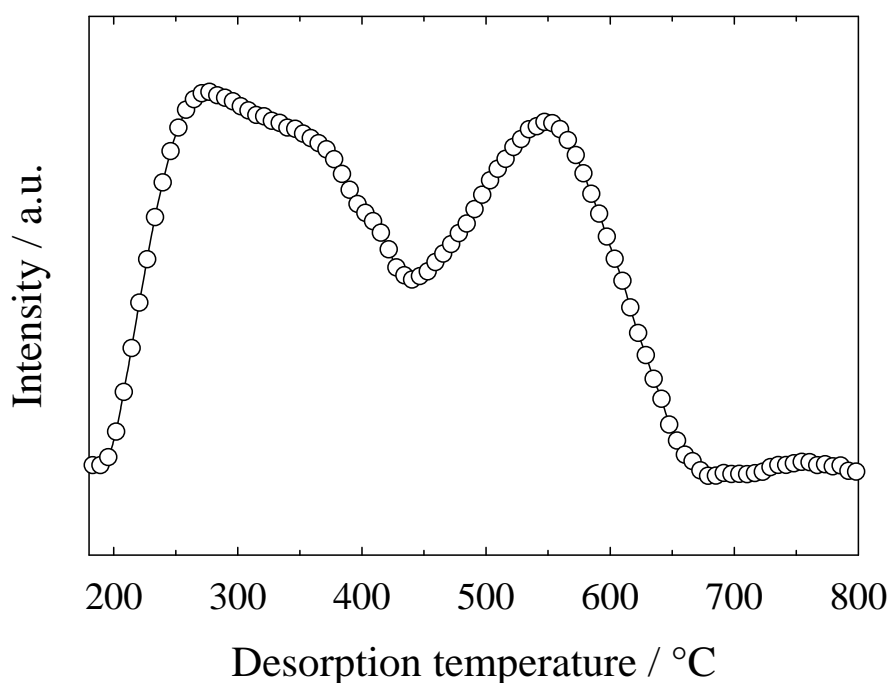


Fig. 51. Temperature-programmed desorption of pyridine from protonated CIT-5.

The profile of pyridine TPD from protonated CIT-5 is shown in Fig. 51. The profile is characterized by two desorption peaks with maxima at ca. 270 and 550 °C. The lower-temperature and the higher-temperature maxima are assigned to the interactions of pyridine molecules with weak and strong acid sites, respectively.

#### 4.1.3. Zeolite SSZ-53

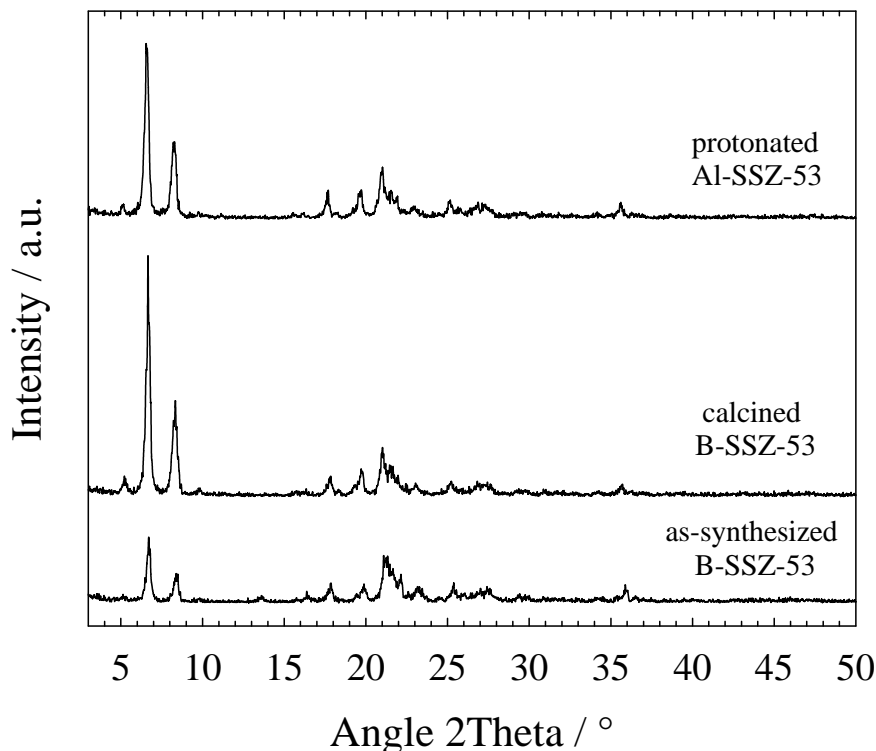


Fig. 52. XRD patterns of as-synthesized SSZ-53 and after modification steps.

The XRD patterns of SSZ-53 in its as-synthesized, calcined and protonated (Al-SSZ-53) form are depicted in Fig. 52. The peak positions and peak intensities are closely similar to those reported in the patent literature [45] with the location of the two main peaks at  $2\theta \approx 6.7$  and  $8.5^\circ$ . The synthesis of B-SSZ-53 started using sodium borate as the source of boron. After the synthesis of B-SSZ-53, this sample was modified to the acidic version of Al-SSZ-53 by post-synthetic Al-insertion. The structure is well preserved after the modification and it is, moreover, found that the structure of SSZ-53 is thermally stable up to at least 1000 °C. The chemical analysis of the protonated Al-SSZ-53 yields a molar ratio of  $n_{\text{Si}}/n_{\text{Al}} = 55$ . The

crystal morphology shows basically a needle-like shape with crystallites which are ca. 1-2  $\mu\text{m}$  long, as shown in Fig. 53.

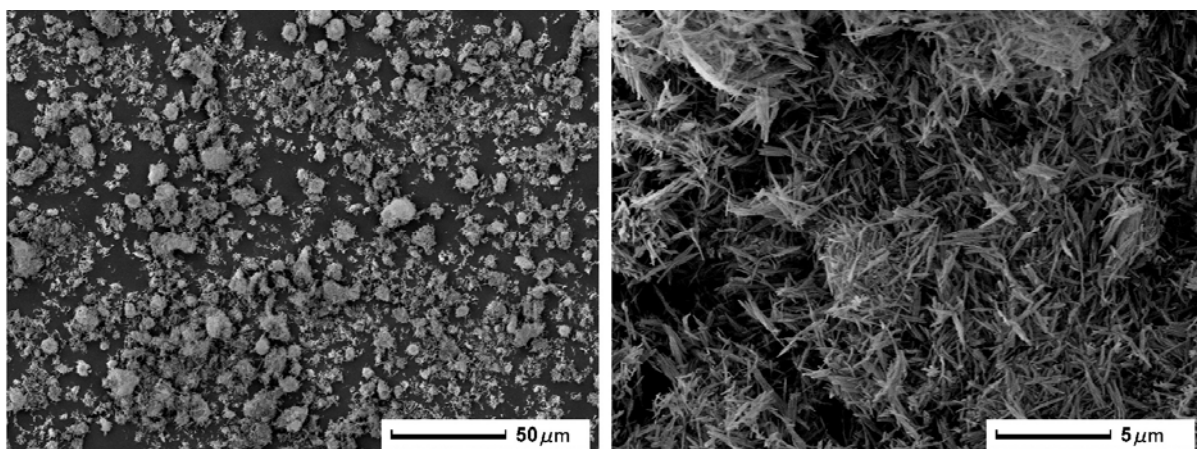


Fig. 53. SEM pictures of calcined SSZ-53.

The thermogravimetric analysis of as-synthesized SSZ-53 in an air flow shows four stages of weight loss. The first stage between 25-250  $^{\circ}\text{C}$  (1.1 wt.-%, endothermic) is assigned to water desorption and the second to fourth stages between 250-355, 355-470 and 470-750  $^{\circ}\text{C}$ , respectively (total weight loss of 15.4 wt.-%, exothermic), are assigned to the combustion of the template. Calcined B-SSZ-53 possesses a high specific surface area of 440  $\text{m}^2/\text{g}$  and a specific pore volume of 0.19  $\text{cm}^3/\text{g}$ . Among the unidimensional 14-MR pore zeolites, SSZ-53 exhibits a specific pore volume which is similar to that of B-UTD-1 (0.18  $\text{cm}^3/\text{g}$ ) but higher than that of CIT-5 (0.12  $\text{cm}^3/\text{g}$ ) reported in this work.

Fig. 54a shows the IR spectrum of as-synthesized B-SSZ-53. The presence of the vibration bands at ca. 2890, 2970  $\text{cm}^{-1}$  (C-H stretching) and 1477-1512  $\text{cm}^{-1}$  (C-C stretching) indicates that the template molecules are intact and did not decompose under the synthesis conditions. Note that the pure template can be decomposed at quite low temperature, viz. ca. 260  $^{\circ}\text{C}$ . These template vibration bands disappear during calcination (Fig. 54b) indicating complete removal of the organic. The vibration band at ca. 900  $\text{cm}^{-1}$  is found both in the as-synthesized and in the calcined form of B-SSZ-53 (Fig. 54a and b) which indicate the presence of boron

in tetrahedral coordination as reported for various boron-containing zeolites [133-135] and also for B-UTD-1 (cf. Fig. 44). This vibration band disappears in the protonated Al-SSZ-53 (Fig. 54c) which is in agreement with the substitution of boron by aluminium in the post-treatment steps. Two vibration bands which can be attributed to Brønsted-acid sites (at ca. 3630 and ca. 3690  $\text{cm}^{-1}$ ) are observed in the protonated Al-SSZ-53 (Fig. 54c). Hence, via Al-insertion, relatively strong Brønsted-acid sites could be created in SSZ-53.

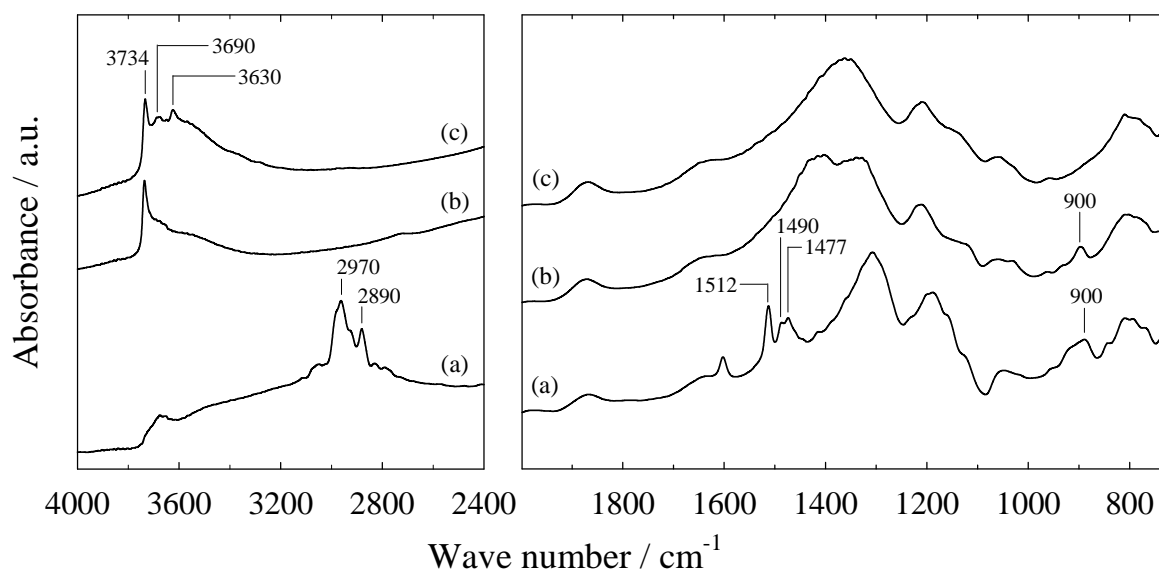


Fig. 54. IR spectra of (a) as-synthesized B-SSZ-53 (b) calcined B-SSZ-53 and (c) protonated Al-SSZ-53.

The profile of pyridine TPD from protonated Al-SSZ-53 is depicted in Fig. 55. It consists of three desorption maxima at ca. 280, 410 and 615  $^{\circ}\text{C}$ , which are ascribed to the desorption of pyridine molecules from weak, medium and strong acid sites, respectively. Hence, a relatively large amount of strong acid sites is present in the protonated form of Al-SSZ-53.

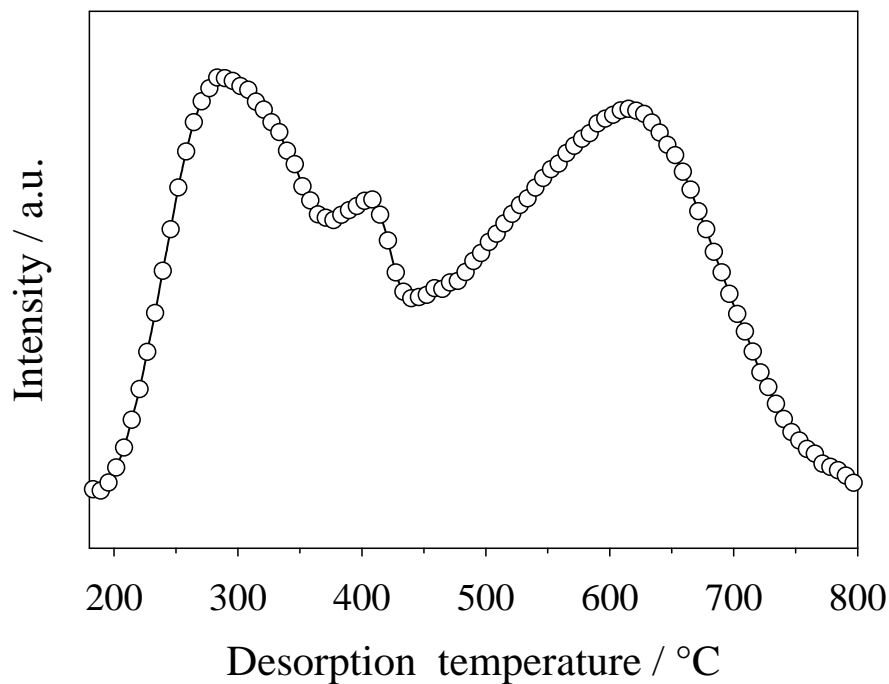


Fig. 55. Temperature-programmed desorption of pyridine from protonated Al-SSZ-53.

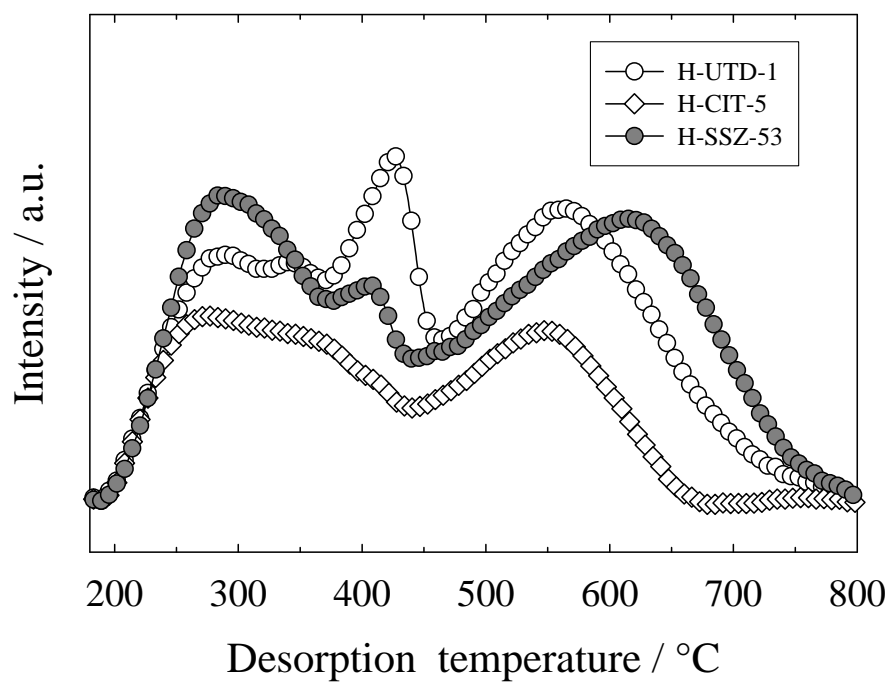


Fig. 56. Temperature-programmed desorption of pyridine from protonated samples of UTD-1, CIT-5 and SSZ-53.

The acidity of the acid forms of the 14-MR zeolites studied in the present thesis, viz. H-UTD-1, H-CIT-5 and H-SSZ-53 was compared using TPD of pyridine. The results are summarized in Fig. 56. It is observed that H-UTD-1 and H-SSZ-53 possess a larger amount of acid sites as compared to H-CIT-5 as can be seen from the larger corresponding peak area. This is consistent with the Al-content or the  $n_{\text{Si}}/n_{\text{Al}}$  ratios determined by AAS: H-UTD-1 ( $n_{\text{Si}}/n_{\text{Al}} = 28$ ), H-SSZ-53 ( $n_{\text{Si}}/n_{\text{Al}} = 55$ ) and H-CIT-5 ( $n_{\text{Si}}/n_{\text{Al}} = 116$ ). Moreover, the number of strong acid sites for peak maxima  $\geq 550$  °C of H-SSZ-53 and H-UTD-1 is larger than the one of H-CIT-5.

#### 4.1.4. Zeolite IM-12

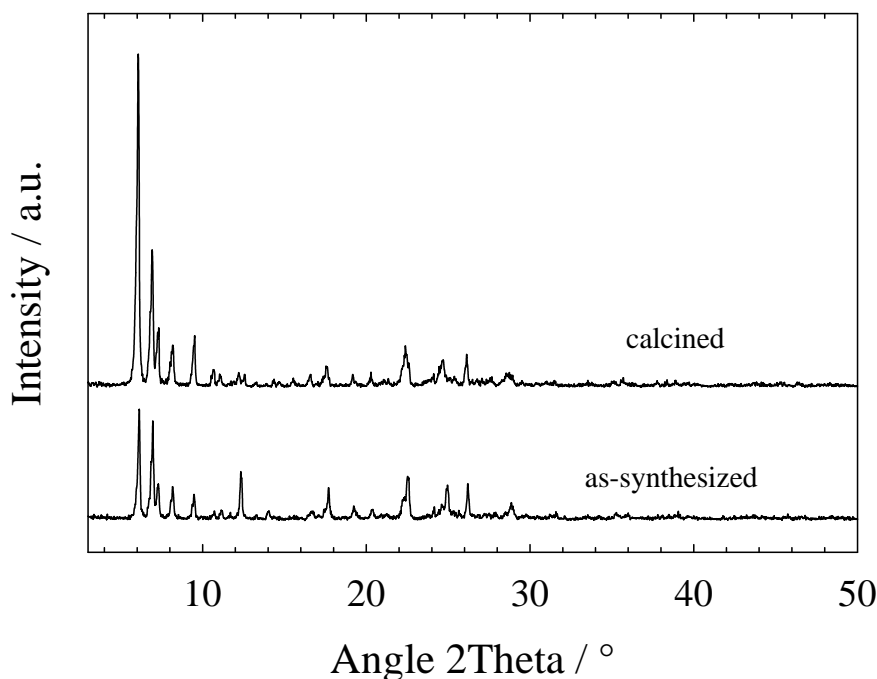


Fig. 57. XRD patterns of as-synthesized and calcined IM-12.

Fig. 57 shows the XRD patterns of IM-12 in the as-synthesized and the calcined form. The peak positions and peak intensities are in agreement with those previously reported in the corresponding patent [51] and no amorphous or crystalline impurities are observed in this sample. The main peaks are located at  $2\theta \approx 6.2, 7, 7.3, 8.2$  and  $9.5$  °. In the synthesis, it was found that germanium is necessary for the formation of IM-12 because it induces the

formation of double four rings (D4Rs) as secondary building units, which are required for the structure of IM-12. Interestingly, the introduction of aluminium into the gel results in the formation of zeolite SSZ-35. Even though the structure of IM-12 is thermally stable up to 600 °C, the structure of the calcined sample collapses after exposure to the atmosphere for a certain period of time. This instability could result from a high germanium content in the structure, which has also been observed in the case of zeolite Ge-ITQ-21 (higher Ge-content version) with  $n_{\text{Si}}/n_{\text{Ge}} = 2$  [57]. The SEM pictures of the as-synthesized IM-12 as shown in Fig. 58 reveal large crystals with a square plate-like shape, with dimensions of ca. 10 x 5  $\mu\text{m}$ . Moreover, the crystallites seem to be composed of staged layers.

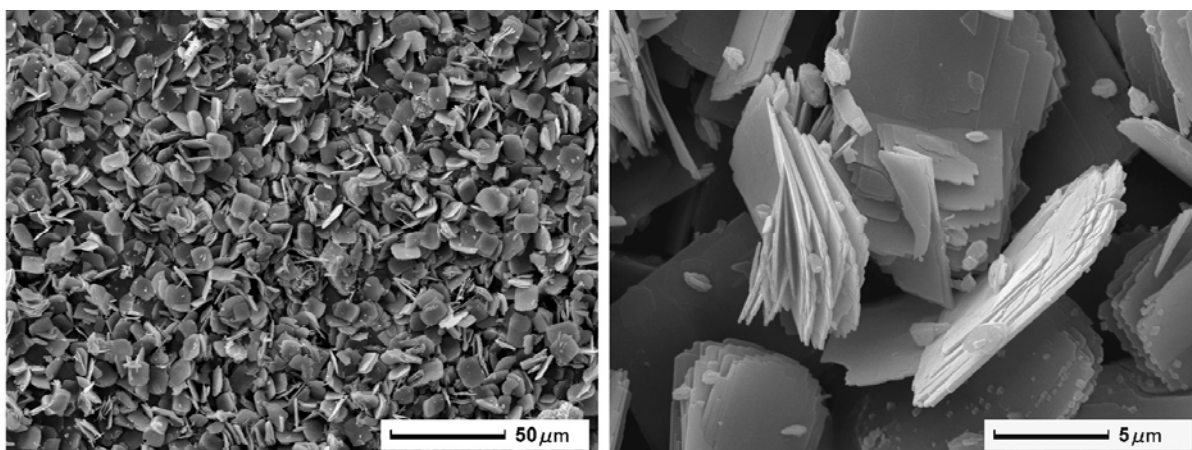


Fig. 58. SEM pictures of as-synthesized IM-12.

The thermogravimetric analysis of an as-synthesized sample shows three stages of weight loss. The first stage occurring from 20-130 °C (0.13 wt.-%) is assigned to the desorption of water. The second and third stage from 130-280 °C (2.3 wt.-%) and 280-700 °C (12.8 wt.-%), respectively, are assigned to the combustion of the template as confirmed by on-line mass spectrometry. The total weight loss resulting from removal of the template is 15.1 wt.-%. For the calcined form, a specific surface area of 490  $\text{m}^2/\text{g}$  and a specific pore volume of 0.21  $\text{cm}^3/\text{g}$  were determined from nitrogen adsorption data at 77 K.

## 4.2. Synthesis and characterization of zeolites based on 12-membered ring pore openings

### 4.2.1. Zeolite ITQ-21

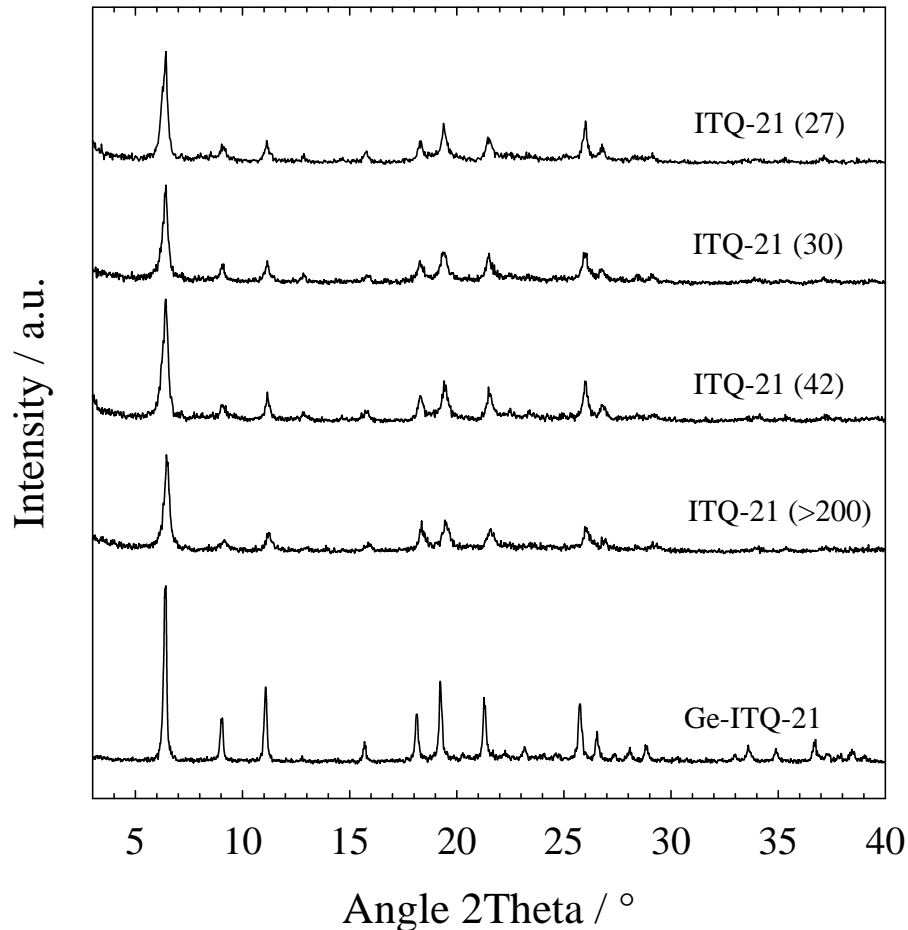


Fig. 59. XRD patterns of as-synthesized Ge-ITQ-21 and ITQ-21 with different  $n_{\text{Si}}/n_{\text{Al}}$  ratios (in parentheses).

The XRD patterns of ITQ-21 with both, higher Ge-content (Ge-ITQ-21) and lower Ge-content (ITQ-21) and with different  $n_{\text{Si}}/n_{\text{Al}}$  ratios are presented in Fig. 59. The patterns show essentially pure phases by comparison with data from the patent literature [52] with the main peaks at  $2\theta \approx 6.4, 9.1$  and  $11.1^\circ$ . No other amorphous or crystalline impurity phases are observed. It can be seen that Ge-ITQ-21 exhibits a very good crystallinity as compared to the

one of ITQ-21. The crystal morphology of calcined ITQ-21 ( $n_{\text{Si}}/n_{\text{Al}} = 27$ ) appears as platelet with the size ca. 0.3-0.6  $\mu\text{m}$  as shown in Fig. 60.

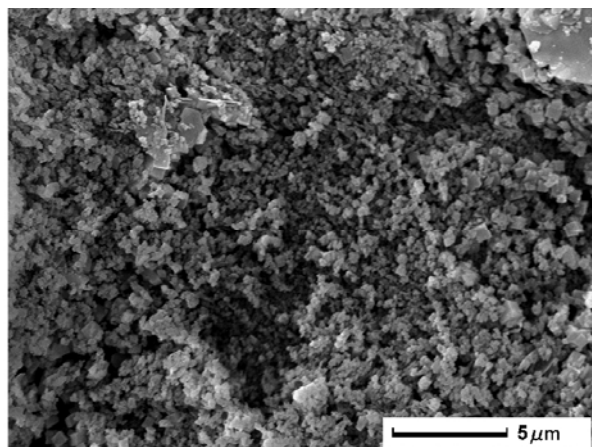


Fig. 60. SEM picture of calcined ITQ-21 ( $n_{\text{Si}}/n_{\text{Al}} = 27$ ).

In the synthesis of Ge-ITQ-21, it was found that the amount of template influences the purity of the resulting crystalline phase. A low quantity of template results in the appearance of quartz-like germanium oxide (assigned peaks at  $2\theta \approx 20.6$  and  $26.2^\circ$ ) which is easily detected by XRD. For the lower Ge-content version, it is revealed that ITQ-21 can be synthesized with  $n_{\text{Si}}/n_{\text{Al}}$  ratios between 27 and  $>200$ . Table 21 shows the chemical composition ( $n_{\text{Si}}/n_{\text{Al}}$ ) in the gel and in the obtained zeolite as determined by AAS. The lowest  $n_{\text{Si}}/n_{\text{Al}}$  ratio (viz. 27) is found in sample no. 2.

Table 21. Elemental analysis of calcined ITQ-21 ( $n_{\text{Si}}/n_{\text{Ge}} = 10.1$ ).

Sample no.	$n_{\text{Si}}/n_{\text{Al}}$ in gel	$n_{\text{Si}}/n_{\text{Al}}$ in zeolite
1	13.7	30
2	23	27
3	46	42
4	$\infty$	$>200$

The calcination of Ge-ITQ-21 fails even at temperature as low as 300 °C for 3 h in an air flow. The structure completely collapses under these conditions to amorphous phase. Moreover, a partial destruction of the structure was also observed after leaving the as-synthesized sample under the atmosphere for a certain period of time. While the calcination of ITQ-21 is possible without structural destruction, the calcination conditions are very restricted for both, temperature and time, in order to prevent the collapse of the structure. The instability of the zeolite structure due to the presence of Ge has been reported in ref. [57] by Blasco et al. These authors suggested that ITQ-21 could possess high thermal and hydrothermal stability when the  $n_{\text{Si}}/n_{\text{Ge}}$  ratio is above 10 and this is in agreement with our own results.

The degree of template removal is determined based on the carbon content of the template in the samples before and after the calcination (shown in Table 22). A removal degree of 99 % suggests that the calcination methods reported in this work are close to an optimum with respect to the degree of template removal and structure integrity.

Table 22. Results of the carbon content for as-synthesized and calcined ITQ-21 with different  $n_{\text{Si}}/n_{\text{Al}}$  ratios and degree of template removal (the results are given in wt.-%).

Sample	ITQ-21 ( $n_{\text{Si}}/n_{\text{Al}} = 27$ )	ITQ-21 ( $n_{\text{Si}}/n_{\text{Al}} = 30$ )	ITQ-21 ( $n_{\text{Si}}/n_{\text{Al}} = 42$ )	ITQ-21 ( $n_{\text{Si}}/n_{\text{Al}} > 200$ )
as-synthesized (wt.-%)	18.6	18	17.4	15.9
calcined (wt.-%)	0.11	0.23	0.19	0.15
Degree of template removal (%)	99	99	99	99

For ITQ-21, it is not possible to prepare the protonated form via the standard ammonium ion-exchange in solution route without structural destruction even at room temperature. However,

a certain amount of acid sites in the calcined sample can be detected by IR spectroscopy and pyridine TPD (in Fig. 61 and 62, respectively).

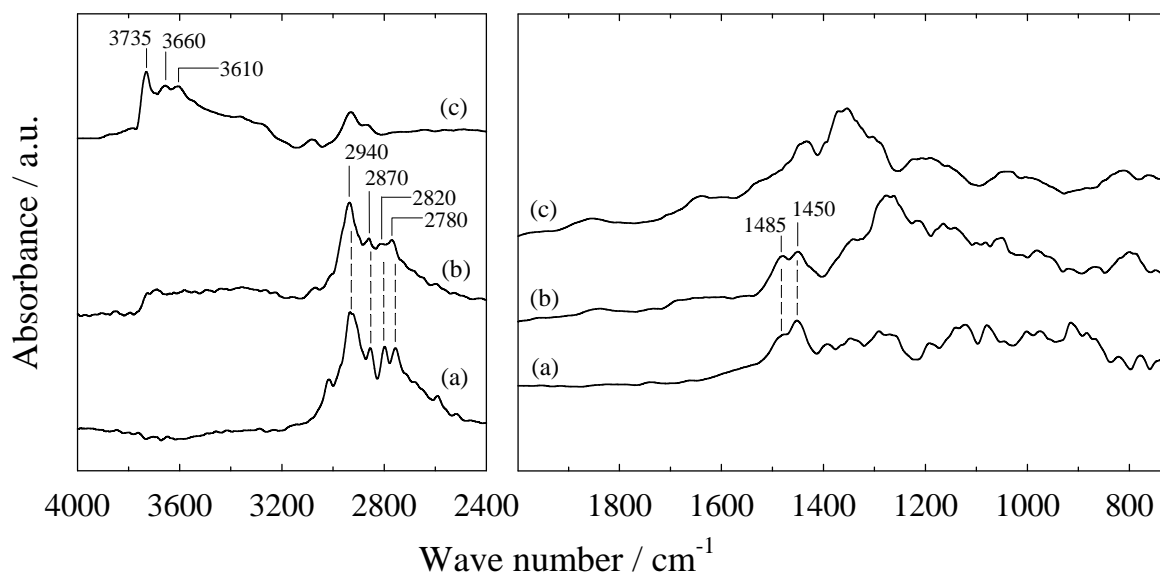


Fig. 61. IR spectra of (a) the template  $C_{16}H_{29}N_2I$  (b) as-synthesized ITQ-21 ( $n_{Si}/n_{Al} = 27$ ) and (c) calcined ITQ-21 ( $n_{Si}/n_{Al} = 27$ ).

Fig. 61 shows the IR spectra of the solid template  $C_{16}H_{29}N_2I$  and the as-synthesized and calcined forms of ITQ-21 with  $n_{Si}/n_{Al} = 27$ . The integrity of the template occluded in the structure is recognized from the vibration bands between  $2780-2940\text{ cm}^{-1}$  (C-H stretching) and the bands at  $1450$  and  $1485\text{ cm}^{-1}$  (C-C stretching) (Fig. 61b) and this is in-line with the spectrum of the neat template (Fig. 61a). The remainder of the template after calcination is still detectable via IR as shown by the vibration bands between  $2870-2940\text{ cm}^{-1}$  (Fig. 61c). Vibration bands from acid OH-groups in the Brønsted-acid site region at ca.  $3610$  and ca.  $3660\text{ cm}^{-1}$  and from silanol groups at ca.  $3735\text{ cm}^{-1}$  are observed for the calcined form (Fig. 61c).

For ITQ-21, the thermogravimetric analysis in an air flow shows three stages of weight loss, viz. at  $20-250$ ,  $220-440$  and  $440-750\text{ °C}$ , respectively. The first stage is assigned to the desorption of water, while the last two stages are assigned to the combustion of the template

as confirmed by mass spectrometry. The weight losses of water and of template together with the specific surface areas and specific pore volumes of all prepared ITQ-21 samples are presented in Table 23.

Table 23. Weight losses due to water and template removal from as-synthesized ITQ-21 in an air flow and specific surface areas and specific pore volumes of the calcined forms.

$n_{\text{Si}}/n_{\text{Al}}$	Weight loss of water (wt.-%)	Weight loss of template (wt.-%)	$S_{\text{BET}}$ ( $\text{m}^2 \cdot \text{g}^{-1}$ )	$V_{\text{pore}}$ ( $\text{cm}^3 \cdot \text{g}^{-1}$ )
27	1.2	24.7	546	0.16
30	1.1	25.5	630	0.14
42	1.7	24.4	657	0.19
>200	0.3	22.3	525	0.13

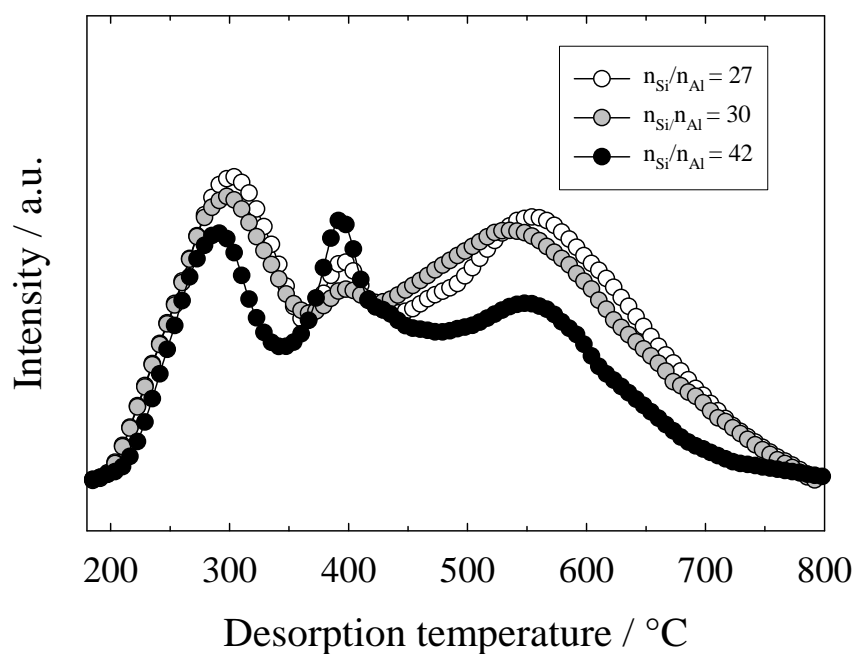


Fig. 62. Temperature-programmed desorption of pyridine from calcined ITQ-21 with different  $n_{\text{Si}}/n_{\text{Al}}$  ratios.

The acid properties of the calcined ITQ-21 samples were investigated by pyridine TPD. The desorption profiles of the samples with  $n_{\text{Si}}/n_{\text{Al}} = 27, 30$  and  $42$  are depicted in Fig. 62. They all exhibit three desorption maxima at ca.  $300, 400$  and  $550$  °C. These maxima can be assigned to the coordination of pyridine to weak, medium and strong acid sites, respectively. The results show that the samples with  $n_{\text{Si}}/n_{\text{Al}} = 27$  and  $30$  possess similar amounts of acid sites, while ITQ-21 with  $n_{\text{Si}}/n_{\text{Al}} = 42$  (lower Al-content) has a smaller number of acid sites.

#### 4.2.2. Zeolite MCM-68

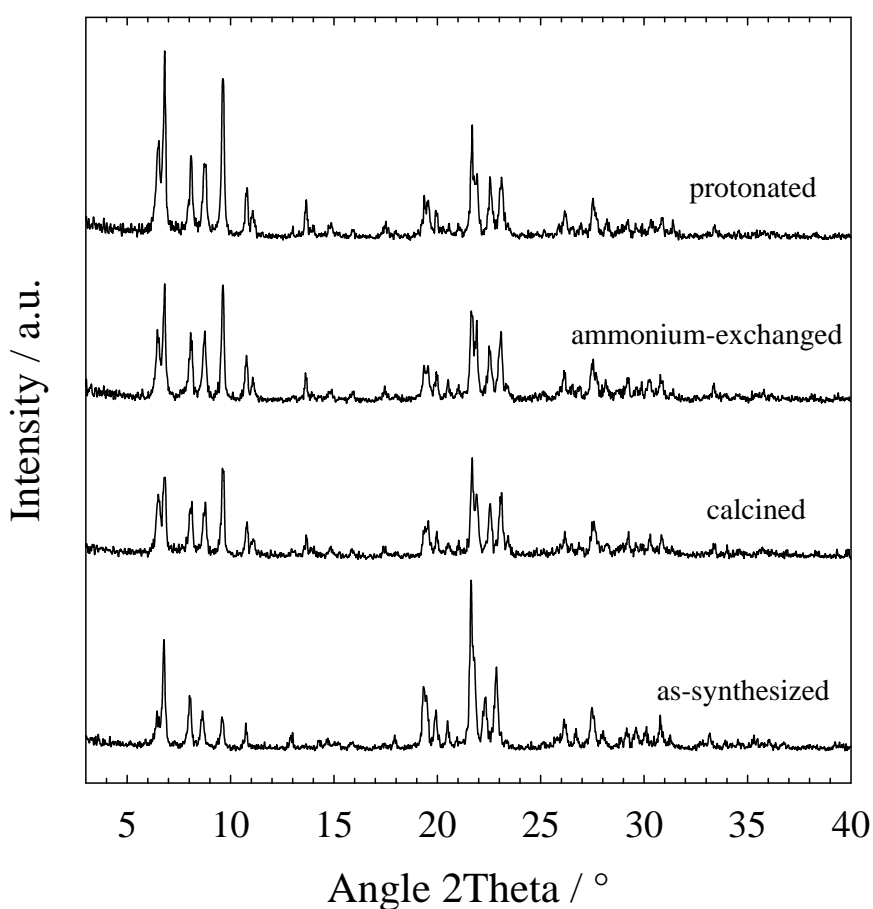


Fig. 63. XRD patterns of as-synthesized MCM-68 and after modification steps.

The XRD patterns of MCM-68 in different forms are depicted in Fig. 63. The peak positions and peak intensities of the as-synthesized and the calcined forms resemble those reported in the patent literature [62]. The chemical analysis of protonated MCM-68 yields a molar ratio of  $n_{\text{Si}}/n_{\text{Al}} = 9$  which is similar to the ratio in the synthesis gel. The SEM pictures show that MCM-68 crystallizes in tiny crystallites (platelet) ca. 0.2  $\mu\text{m}$  in size as shown in Fig. 64.

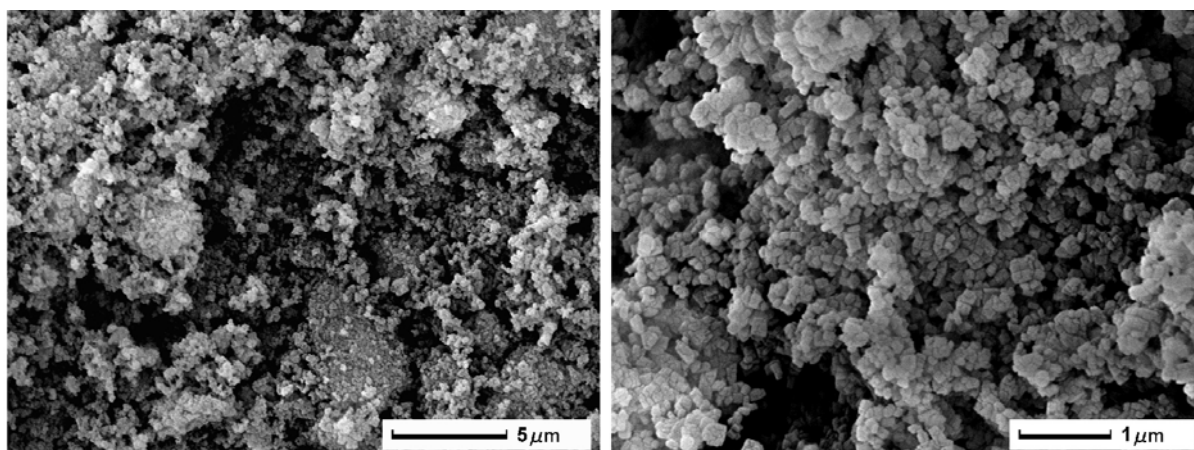


Fig. 64. SEM pictures of calcined MCM-68.

Fig. 65 shows the results of the thermogravimetric analysis of as-synthesized MCM-68 in  $\text{N}_2$  and in air. In an air flow, the weight loss exhibits four stages: The first stage from 20-200  $^{\circ}\text{C}$  (0.5 wt.-%, endothermic) is assigned to water desorption and the second to fourth stages from 200-400, 400-500 and 500-800  $^{\circ}\text{C}$  (total weight loss of 18.8 wt.-%, exothermic) are ascribed to the combustion of the template. The reaction products were checked by mass spectrometry. By contrast, in a  $\text{N}_2$  flow, only three stages of weight loss are observed. The first stage from 20-200  $^{\circ}\text{C}$  (0.5 wt.-%, endothermic) is assigned to water desorption. The second and third stages from 200-400 and 400-600  $^{\circ}\text{C}$  (total weight loss of 16.3 wt.-%, endothermic) are assigned to the decomposition of the template via a Hoffman-type degradation as the typical products ammonia, isopropylamine, propane/propene and butane/butene are found using mass spectrometry.

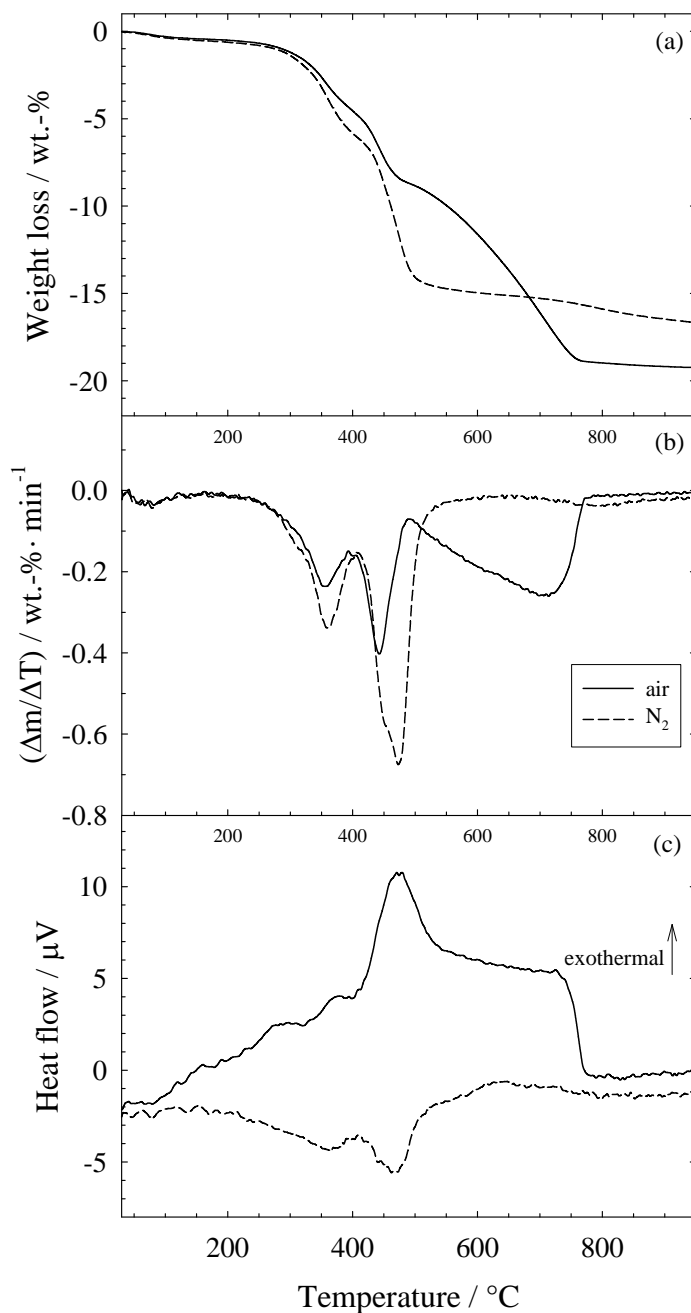


Fig. 65. Thermogravimetric analysis of as-synthesized MCM-68 in an air and in a N<sub>2</sub> flow:

(a) weight loss (b) differential weight loss and (c) heat flow.

The calcined and the protonated forms of MCM-68 possess specific surface areas of 550 and 720 m<sup>2</sup>/g and specific pore volumes of 0.21 and 0.27 cm<sup>3</sup>/g, respectively. The higher specific surface area and pore volume of the protonated form (as compared to the calcined form) can

be tentatively explained by a removal of potassium cations during the ion-exchange step, which otherwise could partially block the pores or reduce the free channel diameter.

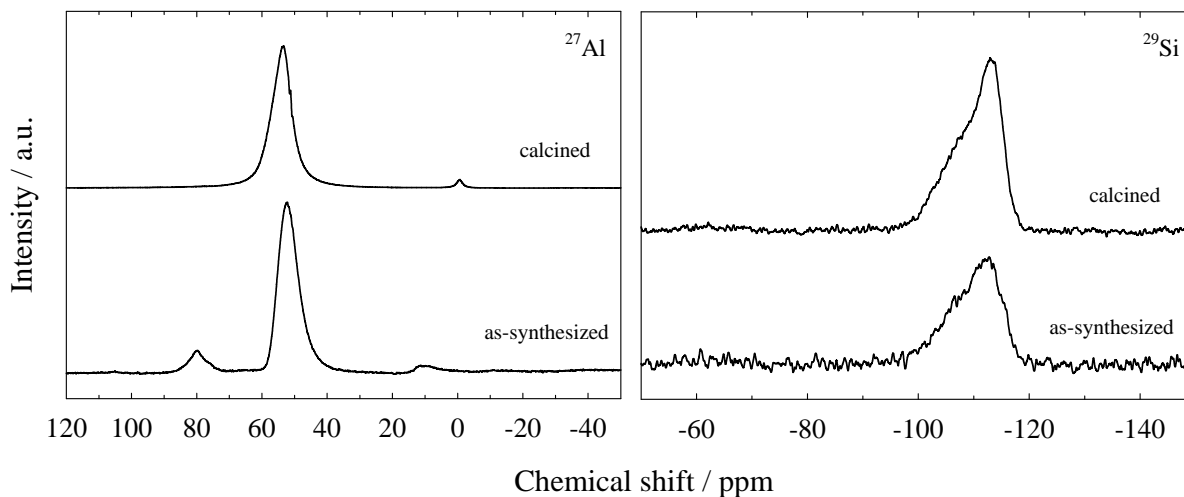


Fig. 66.  $^{27}\text{Al}$  and  $^{29}\text{Si}$  MAS NMR spectra of as-synthesized and calcined MCM-68.

The  $^{27}\text{Al}$  and  $^{29}\text{Si}$  MAS NMR spectra of as-synthesized and calcined MCM-68 are presented in Fig. 66. In the  $^{27}\text{Al}$  NMR spectra of both forms, the major line is centered at a chemical shift of ca. 52 ppm and is assigned to tetrahedrally coordinated aluminium in the zeolite framework. This means that every aluminium in the framework has the environment of  $\text{Al}(\text{4Si})$  [139]. The small resonance at -0.7 ppm as found only for the calcined sample is assigned to octahedrally coordinated aluminium or extra-framework aluminium [139]. Therefore, the major part of the aluminium is incorporated into the framework. The  $^{29}\text{Si}$  NMR spectra of both forms show a distinct broad peak at ca. -112.8 ppm with a low-field shoulder at ca. -106 ppm. The resonance at ca. -113 ppm is tentatively assigned to  $\text{Si}(\text{0Al})$  species, viz. tetrahedrally coordinated silicon atoms with four silicon atoms as next nearest neighbours. The shoulder at ca. -106 ppm (clearly observed on the calcined sample) is attributed to a superposition of the signal due to  $\text{Si}(\text{1Al})$  species, viz. silicon tetrahedrally coordinated with one aluminium and three silicon atoms [139].

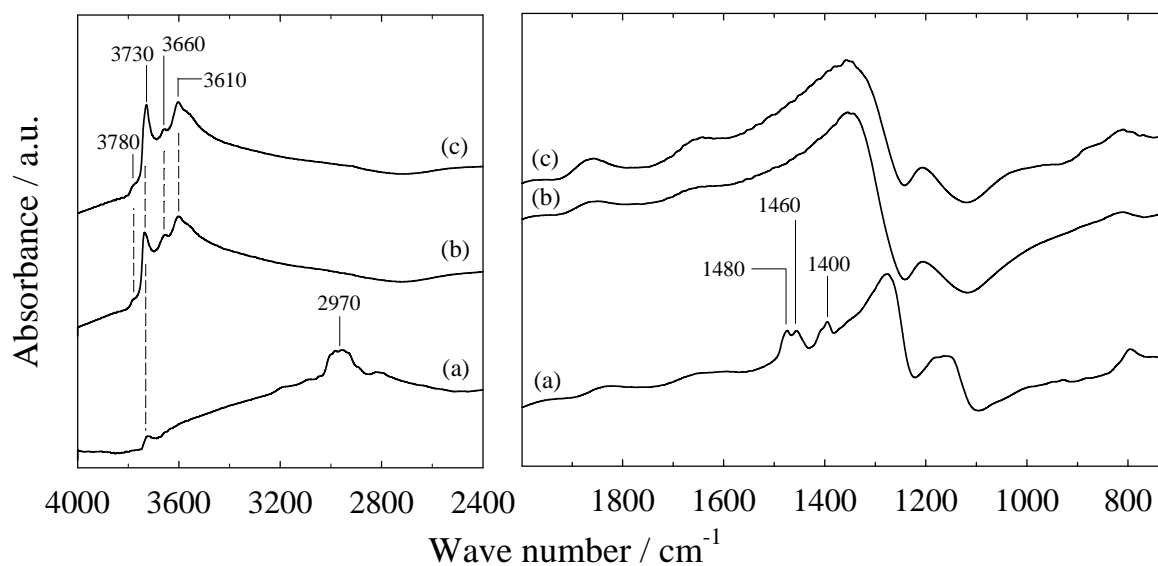


Fig. 67. IR spectra of (a) as-synthesized (b) calcined and (c) protonated MCM-68.

The IR spectra of as-synthesized, calcined and protonated MCM-68 are presented in Fig. 67. The vibration bands at  $2970\text{ cm}^{-1}$  (C-H stretching) and  $1400\text{--}1480\text{ cm}^{-1}$  (C-C stretching) show a presence of the template in the structure of the as-synthesized material (Fig. 67a) and these bands are absent in the calcined form (Fig. 67b). The presence of hydroxyl groups (viz. at bands between  $3610\text{--}3780\text{ cm}^{-1}$ ) is already observed in the calcined form (Fig. 67b) and similarly in the protonated form. The band at  $3730\text{ cm}^{-1}$  is assigned to silanol groups. The bands at  $3610$  and  $3660\text{ cm}^{-1}$  are assigned to bridging hydroxyl groups formed by Brønsted-acid sites. The band at  $3780\text{ cm}^{-1}$  is assigned to hydroxyl groups coordinated to extra-framework aluminium as has also been found in the case of Beta zeolites [136, 137] and in H-UTD-1 (cf. chap. 4.1.1.). The presence of extra-framework aluminium is also indicated by a peak at ca. 0 ppm in the  $^{27}\text{Al}$  NMR spectra of calcined MCM-68 (cf. Fig. 66). It has to be pointed out that calcined MCM-68 already exhibits a relatively large amount of Brønsted-acid sites.

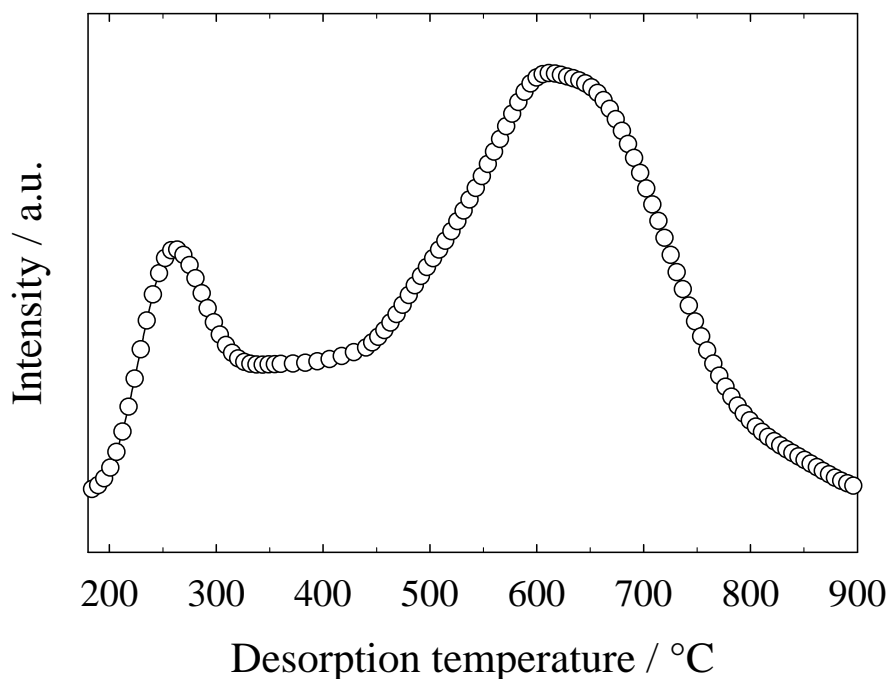


Fig. 68. Temperature-programmed desorption of pyridine from protonated MCM-68.

The pyridine TPD profile for the protonated MCM-68 is depicted in Fig. 68. It consists of maxima at 260 and 630 °C which are ascribed to the desorption of pyridine from weak and strong acid sites, respectively. The acid sites in the protonated MCM-68 exhibit the highest strength as defined by the maximum desorption peak at 630 °C as compared to other materials investigated in the present study (SSZ-53: 615 °C, UTD-1: 565 °C, CIT-5: 550 °C, ITQ-21: 550 °C, SSZ-35: 590 °C (cf. Fig. 74) and MCM-71: 600 °C (cf. Fig. 84)).

### 4.3. Synthesis and characterization of zeolites based on 10-membered ring pore openings

#### 4.3.1. Zeolite SSZ-35

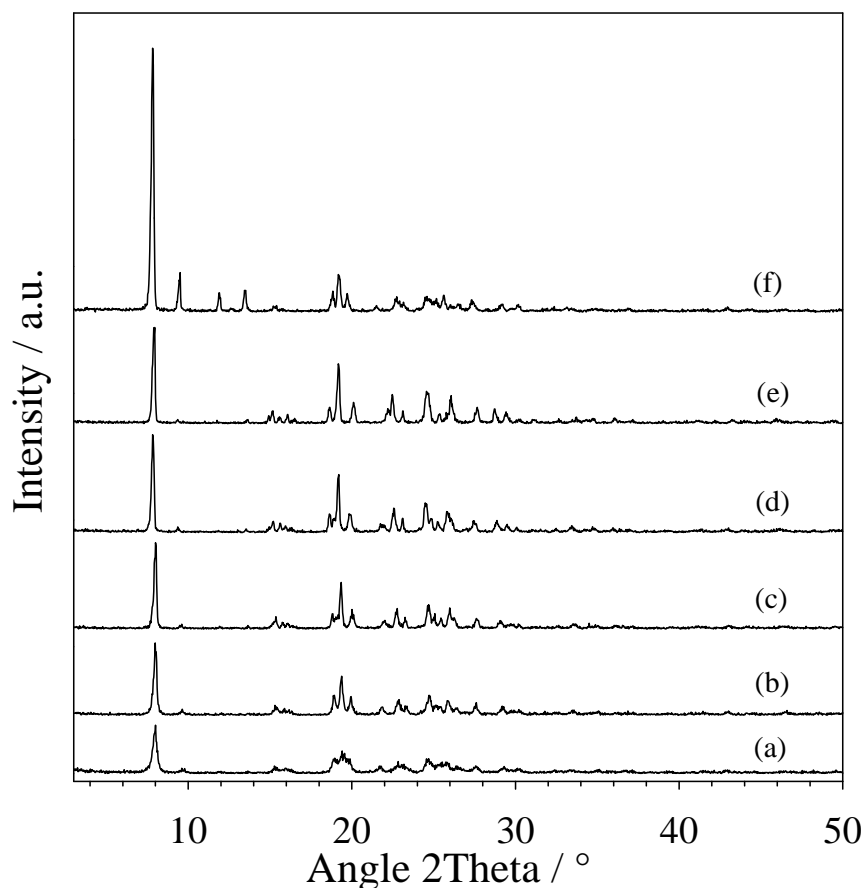


Fig. 69. XRD patterns of as-synthesized SSZ-35 with different  $n_{Si}/n_{Al}$  ratios: (a) 11 (b) 33 (c) 42 (d) 65 (e) >500 and (f) calcined form with  $n_{Si}/n_{Al} > 500$ .

Fig. 69 shows the XRD patterns of SSZ-35 with different  $n_{Si}/n_{Al}$  ratios. The peak positions of the XRD patterns resembles those reported in the patent literature [72] with the main peak at  $2\theta \approx 8^\circ$ . SSZ-35 can be synthesized in pure form in a broad range of  $n_{Si}/n_{Al}$  ratios from 11 to >500, as determined by chemical analysis (AAS). The results from elemental analysis are presented in Table 24. The crystallite morphologies of SSZ-35 samples are depicted in Fig. 70. The crystallites shape of the sample with  $n_{Si}/n_{Al} = 11$  is platelet. By reducing the Al-

content to  $n_{\text{Si}}/n_{\text{Al}} = 33$ , the crystal size increases and changes to a rectangular shape with rounded edges. The crystallite morphologies of the samples with  $n_{\text{Si}}/n_{\text{Al}} = 42, 65$  and  $>500$  are cubic in general. The data collected for the crystallite sizes and morphologies for all samples are summarized in Table 25.

Table 24. Elemental analysis of protonated SSZ-35.

Sample no.	$n_{\text{Si}}/n_{\text{Al}}$ in gel	$n_{\text{Si}}/n_{\text{Al}}$ in zeolite
1	18	11
2	36	33
3	55	42
4	73	65
5	$\infty$	$>500$

Table 25. Crystallite sizes and morphologies of calcined samples of zeolite SSZ-35 with different  $n_{\text{Si}}/n_{\text{Al}}$  ratios.

$n_{\text{Si}}/n_{\text{Al}}$	Crystallite size ( $\mu\text{m}$ )	Morphology
11	ca. 0.2	platelet
33	1x2x0.5 – 2x4x1	rectangular with round edges
42	1-2	cubic
65	1.5-2	cubic
$>500$	ca. 2	cubic

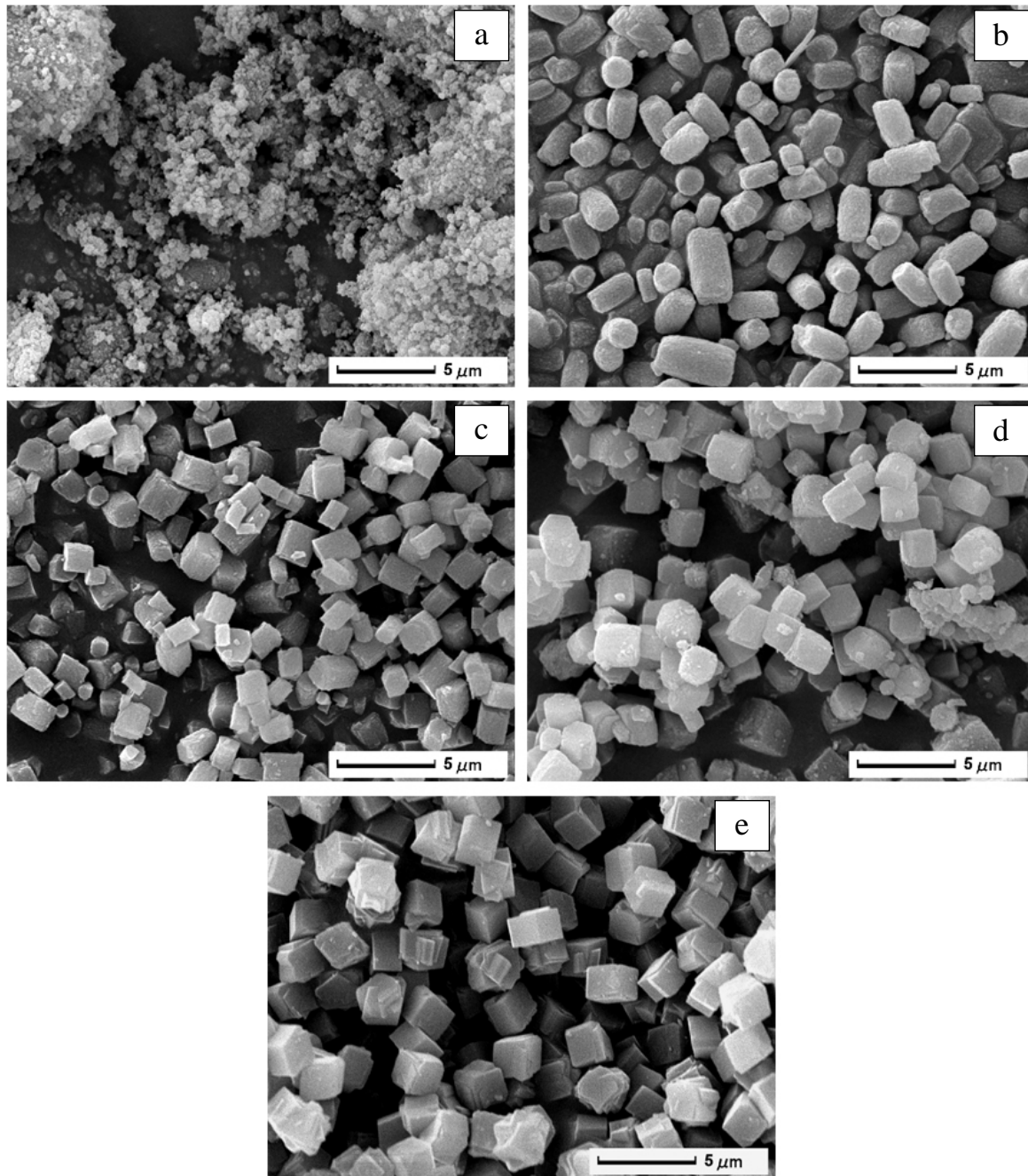


Fig. 70. SEM pictures of calcined SSZ-35 with different  $n_{Si}/n_{Al}$  ratios: (a) 11 (b) 33 (c) 42 (d) 65 and (e) >500.

The thermogravimetric analysis exhibits three stages of weight loss for the as-synthesized sample with  $n_{Si}/n_{Al} > 500$  in an air flow. The first stage from 20-270 °C (0.2 wt.-%) is assigned to water desorbing from the sample. The second stage from 270-500 °C and the third stage from 500-750 °C (total weight loss of 19.2 wt.-%) are assigned to the combustion

of template. It was found that the structure of SSZ-35 is thermally stable up to ca. 1000 °C. The weight losses from template of all samples including the specific surface areas and the specific pore volumes are summarized in Table 26.

Table 26. Weight losses due to template removal from as-synthesized SSZ-35 in an air flow, specific surface areas and specific pore volumes of calcined forms.

$n_{\text{Si}}/n_{\text{Al}}$	Weight loss from template (wt.-%)	$S_{\text{BET}}$ ( $\text{m}^2 \cdot \text{g}^{-1}$ )	$V_{\text{pore}}$ ( $\text{cm}^3 \cdot \text{g}^{-1}$ )
11	16.7	561	0.24
33	16.7	546	0.23
42	18	585	0.24
65	17.7	561	0.22
>500	19.2	525	0.22

$^{27}\text{Al}$  MAS NMR spectra of calcined SSZ-35 are presented in Fig. 71. The spectra of the samples with  $n_{\text{Si}}/n_{\text{Al}} = 11, 33, 42$  and  $65$  (Fig. 71a, b, c and d) show two distinct peaks at ca. 52 and -2 ppm. These two resonances are assigned to aluminium in tetrahedral and octahedral coordination, respectively. Therefore, the spectra reveal that the aluminium atoms are incorporated in the framework (in tetrahedral coordination) and are (to a lesser extent) located in extra-framework positions (in octahedral coordination). For the sample with  $n_{\text{Si}}/n_{\text{Al}} > 500$  (Fig. 71e), no peak appears. This indicates that the sample with  $n_{\text{Si}}/n_{\text{Al}} > 500$  synthesized in the present study is virtually completely siliceous.

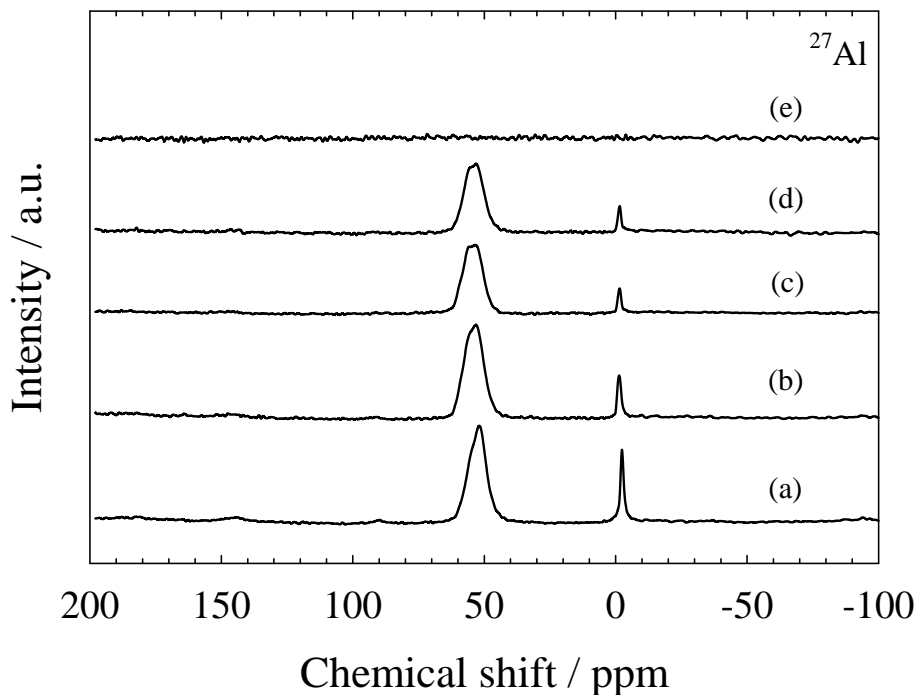


Fig. 71.  $^{27}\text{Al}$  MAS NMR of calcined SSZ-35 with different  $n_{\text{Si}}/n_{\text{Al}}$  ratios: (a) 11 (b) 33 (c) 42 (d) 65 and (e) >500.

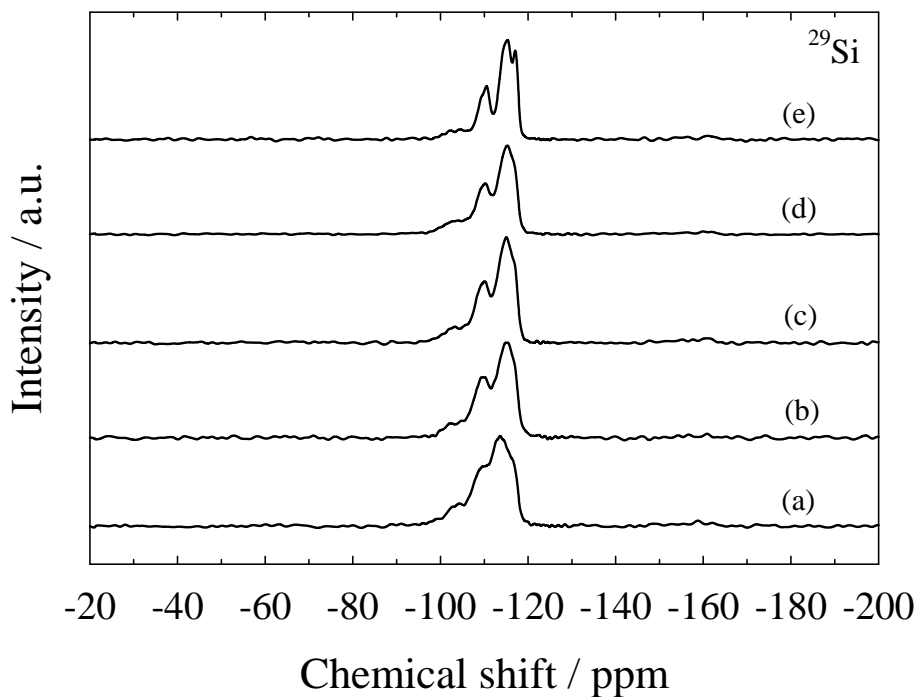


Fig. 72.  $^{29}\text{Si}$  MAS NMR of calcined SSZ-35 with different  $n_{\text{Si}}/n_{\text{Al}}$  ratios: (a) 11 (b) 33 (c) 42 (d) 65 and (e) >500.

The  $^{29}\text{Si}$  MAS NMR spectra of calcined SSZ-35 with different  $n_{\text{Si}}/n_{\text{Al}}$  ratios are shown in Fig. 72 and the peak positions of all samples are summarized in Table 27. In SSZ-35 with  $n_{\text{Si}}/n_{\text{Al}} > 500$  (Fig. 72e), at least three distinct peaks in the spectrum at -111, -115 and -117 ppm are detected. Because there is no aluminium in the sample (cf. result from  $^{27}\text{Al}$  MAS NMR), the observed chemical shifts are due to only Si(4Si) groupings. The observed multiplicity arises from crystallographically inequivalent T sites in the asymmetric unit of the unit cell [140]. Thus, this spectrum indicates that zeolite SSZ-35 is built up by silicon atoms located on at least 3 crystallographically inequivalent sites. However, the published structural data of SSZ-35 reports 8 crystallographically inequivalent sites [74]. The difference in the number of sites could result from the limited resolution in the spectrum from our measurement.

In the aluminium-containing samples, peaks due to Si(1Al) species should be present, which are shifted to lower field strengths by ca. 5-6 ppm [141]. In agreement with this assumption, peaks at -103 ppm are observed in the spectra of the Al-containing samples (Fig. 72a-d). The intensities of these peaks are virtually increasing especially with increasing Al-content. The chemical shift value of this resonance is in the typical range of Si(1Al) in zeolites [139]. Therefore, this resonance is assigned to Si(1Al) species, viz. silicon tetrahedrally connected to one aluminium and three silicon atoms as next nearest neighbours. The interpretation of the  $^{29}\text{Si}$  MAS NMR spectra of the Al-containing samples is quite complicated because there are overlapping peaks for different environments.

Table 27. Chemical shifts of  $^{29}\text{Si}$  MAS NMR spectra of calcined SSZ-35 with different  $n_{\text{Si}}/n_{\text{Al}}$  ratios.

SSZ-35 with $n_{\text{Si}}/n_{\text{Al}}$	$^{29}\text{Si}$ chemical shift (ppm)			
11	-103	-110	-114	
33	-103	-110	-115	
42	-103	-110	-115	
65	-103	-110	-115	
>500		-111	-115	-117

The protonated sample of SSZ-35 with  $n_{\text{Si}}/n_{\text{Al}} = 11$  was selected to investigate its acidic properties by IR spectroscopy with pyridine adsorption and stepwise desorption as described in chap. 3.3.8.2. Fig. 73 presents the IR spectra of H-SSSZ-35 without adsorbed pyridine (Fig. 73i), with adsorbed pyridine (Fig. 73b) and after desorption by flushing with inert gas (Fig. 73c-h) at different desorption temperatures. After pyridine adsorption at 180 °C (Fig. 73b), the vibration bands at 3530, 3620 and 3780  $\text{cm}^{-1}$  in the hydroxyl region completely disappear and the intensity of the band at 3740  $\text{cm}^{-1}$  decreases. At the same time, bands assigned to the pyridine ring vibrations appear at 1450, 1490, 1550, 1600, 1670 with ca. 1640  $\text{cm}^{-1}$  as shoulder. After flushing at 180 °C for 3 h (Fig. 73c), the bands at 1450 and 1600  $\text{cm}^{-1}$  almost disappear and they are completely absent after flushing at 250 °C (Fig. 73d). These bands are assigned to the vibrations of physisorbed pyridine or the vibrations of pyridine molecules weakly bound to the hydroxyl groups.

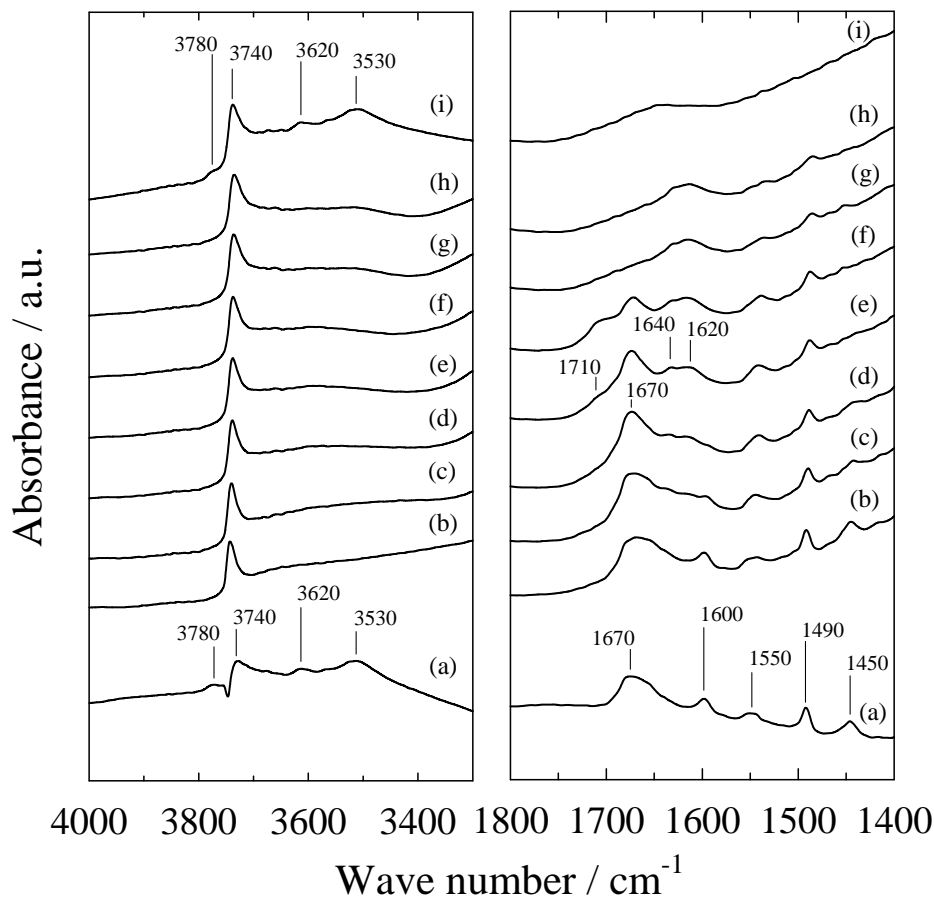


Fig. 73. IR spectra of protonated SSZ-35 ( $n_{\text{Si}}/n_{\text{Al}} = 11$ ) with adsorbed pyridine: (a) spectrum resulting from subtracting the protonated from the pyridine-loaded samples (b) pyridine adsorbed at 180 °C (c) flushed at 180 °C (d) flushed at 250 °C (e) flushed at 300 °C (f) flushed at 350 °C (g) flushed at 450 °C (h) flushed at 500 °C and (i) protonated form.

After desorption at 300 °C (Fig. 73e), the combined peaks between 1620-1710  $\text{cm}^{-1}$  start to resolve as four bands at 1620, 1640, 1670 and 1710  $\text{cm}^{-1}$ . The bands at 1670 and 1710  $\text{cm}^{-1}$  disappear after desorption at a temperature of 450 °C (Fig. 73g). These bands could be assigned to pyridinium ion/pyridine adsorbed on medium-strength acid sites, whether Brønsted- or Lewis-sites is not yet clear. The bands at 1490, 1550, 1620 and 1640  $\text{cm}^{-1}$  still remain visible even after desorption at 500 °C (Fig. 73h). The bands at 1550, 1640  $\text{cm}^{-1}$  are typically assigned to pyridinium ions adsorb on Brønsted-acid sites, while the band at 1620

$\text{cm}^{-1}$  is assigned to pyridine molecules coordinated to Lewis-acid sites. The band at  $1490 \text{ cm}^{-1}$  could be assigned to both types of acid sites (Brønsted and Lewis).

In the hydroxyl region, the bands at  $3530$ ,  $3620$  and  $3780 \text{ cm}^{-1}$  are not completely restored after desorption at a temperature of  $500 \text{ }^\circ\text{C}$  (Fig. 73h). These bands could be correlated to the vibrations of pyridine adsorbed on the strong acid sites. The weak band appearing as shoulder at  $3780 \text{ cm}^{-1}$  (Fig. 73i) could be assigned to Al-OH or strong Lewis-acid sites as also found in a similar region in zeolite H-Beta [136, 137]. This band is also observed in H-UTD-1 (cf. chap. 4.1.1.) and H-MCM-68 (cf. chap. 4.2.2.). The bands at  $3530$  and  $3620 \text{ cm}^{-1}$ , which occur in the typical region for acidic bridging hydroxyl groups, are assigned to strong Brønsted-acid sites. The area of the band at  $3740 \text{ cm}^{-1}$ , which represents the surface silanol groups, increase gradually during increasing of the desorption temperature.

These results suggest that the protonated form of SSZ-35 with  $n_{\text{Si}}/n_{\text{Al}} = 11$  consists of a combination of weak, medium and strong acid sites. The weak and medium acid sites could result from the silanol groups, however strong Brønsted- and Lewis-acid sites (as Al-OH) are also present.

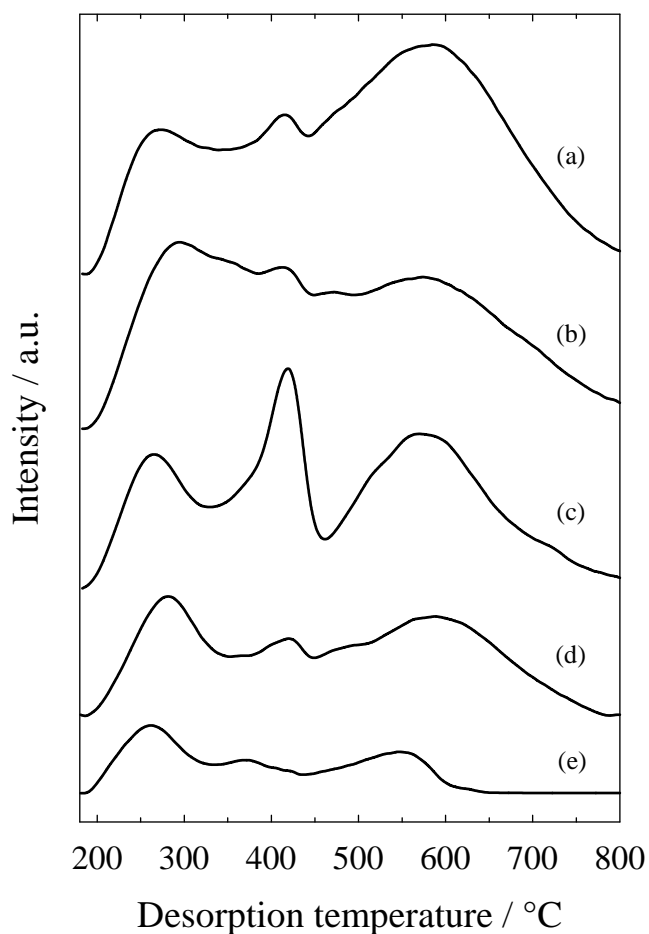


Fig. 74. Temperature programmed desorption of pyridine from protonated SSZ-35 with different  $n_{\text{Si}}/n_{\text{Al}}$  ratios: (a) 11 (b) 33 (c) 42 (d) 65 and (e)  $>500$ .

The profiles of pyridine TPD from the protonated SSZ-35 samples with different  $n_{\text{Si}}/n_{\text{Al}}$  ratios are shown in Fig. 74. The profiles show essentially three maxima, viz. at 260-290, 380-430 and 550-590 °C corresponding to weak, medium and strong acid sites, respectively. With increasing Al-content (decreasing  $n_{\text{Si}}/n_{\text{Al}}$  ratio), the adsorption bands increase in size, hence, the number of acid sites increases.

### 4.3.2. Zeolite MCM-71

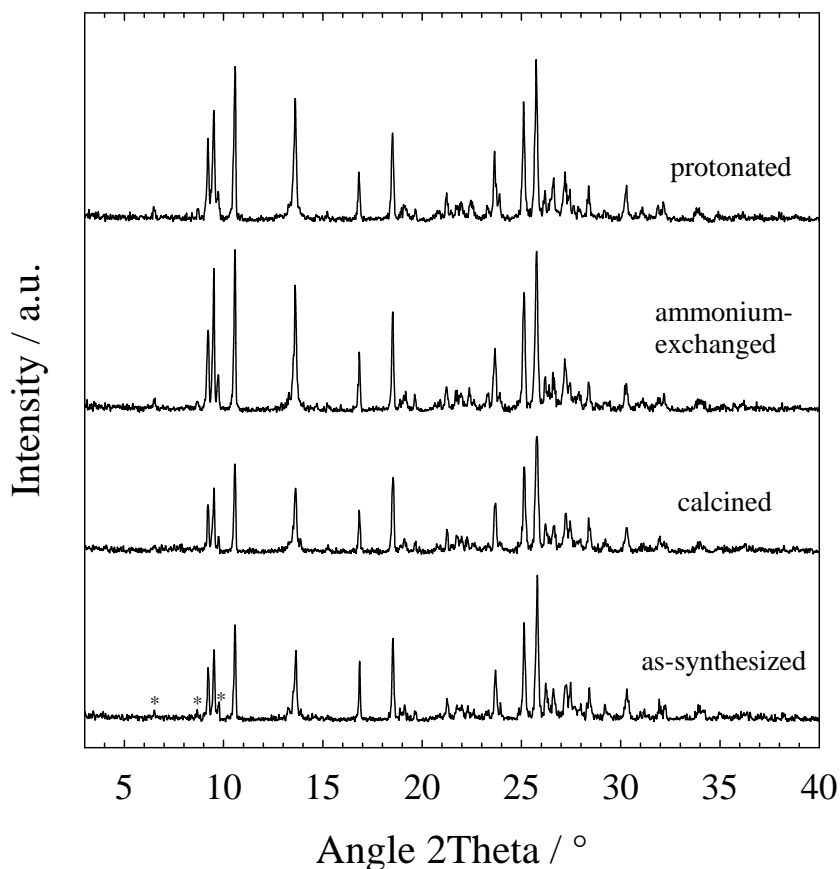


Fig. 75. XRD patterns of as-synthesized MCM-71 and after modification steps.

Fig. 75 shows the XRD patterns of MCM-71 in different forms. The peak positions and the patterns are similar to those reported in the patent literature [79]. Mordenite is often observed as a minor impurity phase (main peaks at  $2\theta \approx 6.5, 8.7$  and  $9.8^\circ$ , marked with asterisks in Fig. 75). This crystalline impurity is also found in the XRD patterns reported in the patent. The structure of MCM-71 after modification is well maintained. The peak intensities after calcination virtually do not change as compared to those of the as-synthesized form. However, an increase in the peak intensities between  $2\theta \approx 9-15^\circ$  is observed for the ammonium and the protonated forms for which the exchange of potassium ions with ammonium ions has already taken place. This, in turn, could influence the relative peak intensities.

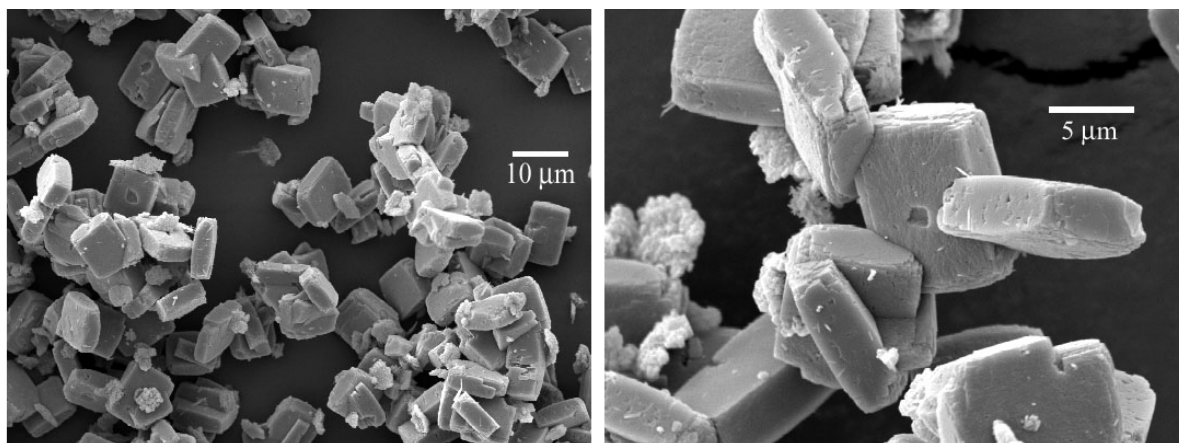


Fig. 76. SEM pictures of calcined MCM-71.

The SEM pictures (Fig. 76) show that MCM-71 crystallizes as rather large crystals with rectangular shape and an average size of  $12 \times 8 \times 4 \mu\text{m}$ .

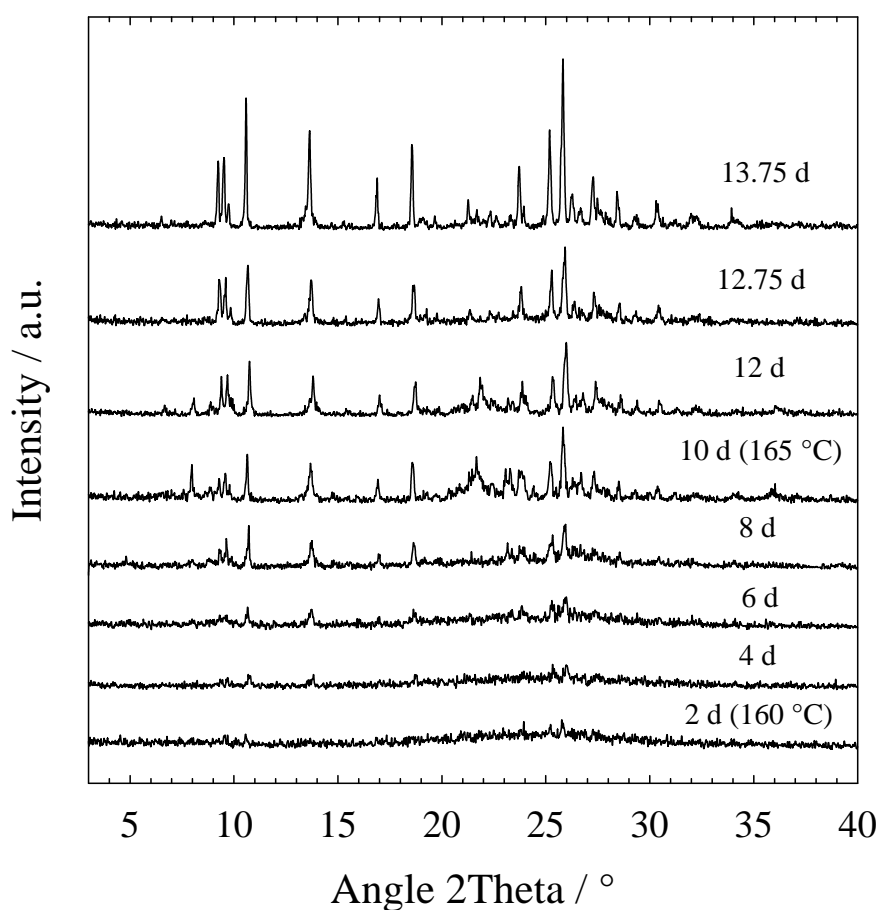


Fig. 77. Crystallization kinetics for MCM-71.

The crystallization kinetics of MCM-71 was investigated by observing the change of XRD patterns during the reaction time as shown in Fig. 77. The reaction took place in two steps with intermediate temperature change at 160 °C (from the beginning to 10 d) and 165 °C (from 10 to 13.75 d). The peaks related to the structure of MCM-71 appear continuously and are mainly recognizable after 8 d of the reaction time. The crystallization continuously progresses until 13.75 d. To quantify the crystallization kinetics, the intensity ratios between the main peaks at  $2\theta \approx 10.6$  and  $25.9^\circ$  to its individual highest peak of MCM-71 are plotted in Fig. 78. The kinetic curves show that the crystallization continually increases from 2 to 12 d with distinct increasing from 12 to 13.75 d.

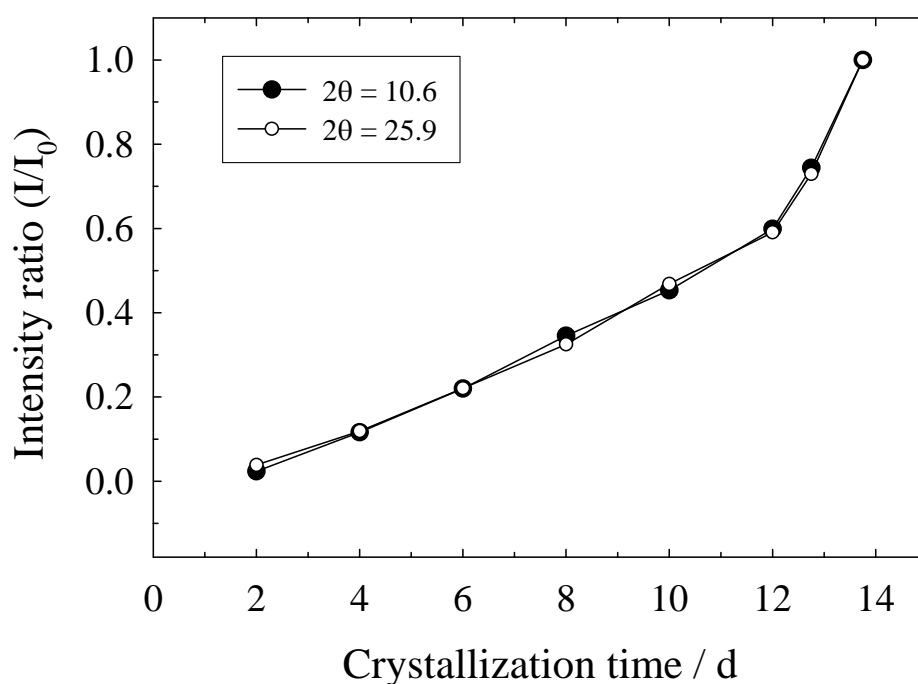


Fig. 78. Kinetic curves of crystallization for MCM-71 referring to the peaks at  $2\theta \approx 10.6$  and  $25.9^\circ$ .

The influence of template amount on the zeolite formation kinetics was investigated by varying the molar ratio of triethanolamine (as template) to  $\text{SiO}_2$  ( $n_{\text{triethanolamine}}/n_{\text{SiO}_2}$ ) in the synthesis gel from 0 to 0.8. Surprisingly, it was observed that the synthesis of MCM-71 is

also possible as main phase in the absence of triethanolamine. However, under these circumstances, the co-crystallization of mordenite is difficult to avoid. The quality of MCM-71 defined as the intensities of the main peaks of  $2\theta \approx 10.6$  and  $25.9^\circ$  exhibits a maximum and a minimum at  $n_{\text{triethanolamine}}/n_{\text{SiO}_2}$  ratios of 0.2 and 0, respectively (Fig. 79). The quality with respect to impurities is also evaluated using the intensity ratio between the mordenite peak at  $2\theta \approx 6.5^\circ$  and the main peak of MCM-71 at  $2\theta \approx 10.6^\circ$  (Fig. 80). It is found that the formation of the impurity is at the minimum when  $n_{\text{triethanolamine}}/n_{\text{SiO}_2} = 0.2$ . Without the template in the synthesis gel, the formation of mordenite is relatively enhanced. Therefore, in terms of the template amount, the ratio of  $n_{\text{triethanolamine}}/n_{\text{SiO}_2} = 0.2$  in the synthesis gel is found to be an optimum value in order to obtain the highest quality of MCM-71.

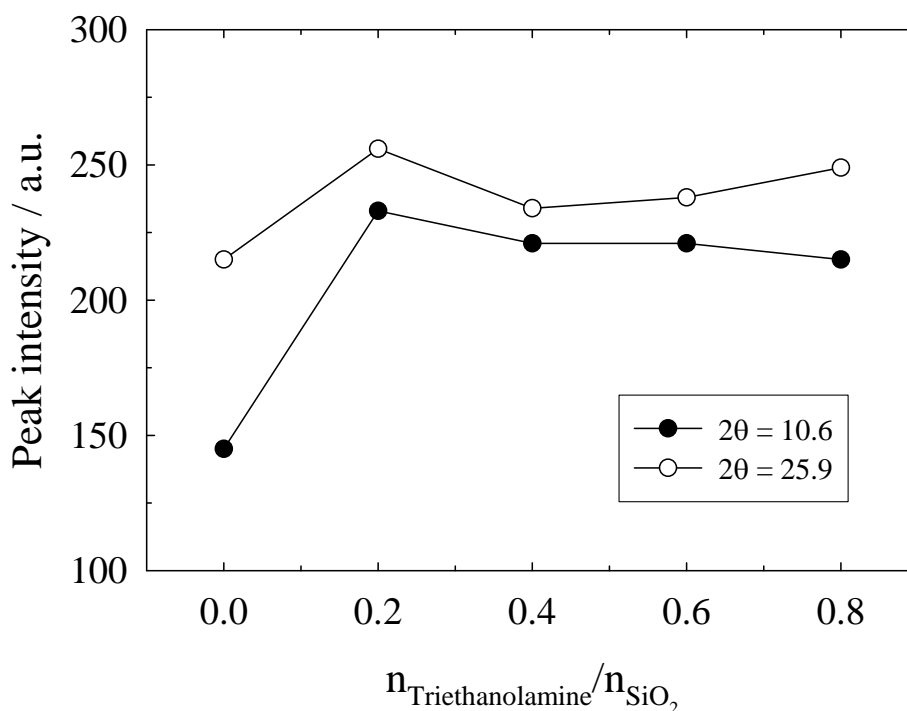


Fig. 79. Intensities of the main peaks at  $2\theta \approx 10.6$  and  $25.9^\circ$  from as-synthesized MCM-71 for different  $n_{\text{triethanolamine}}/n_{\text{SiO}_2}$  ratios.

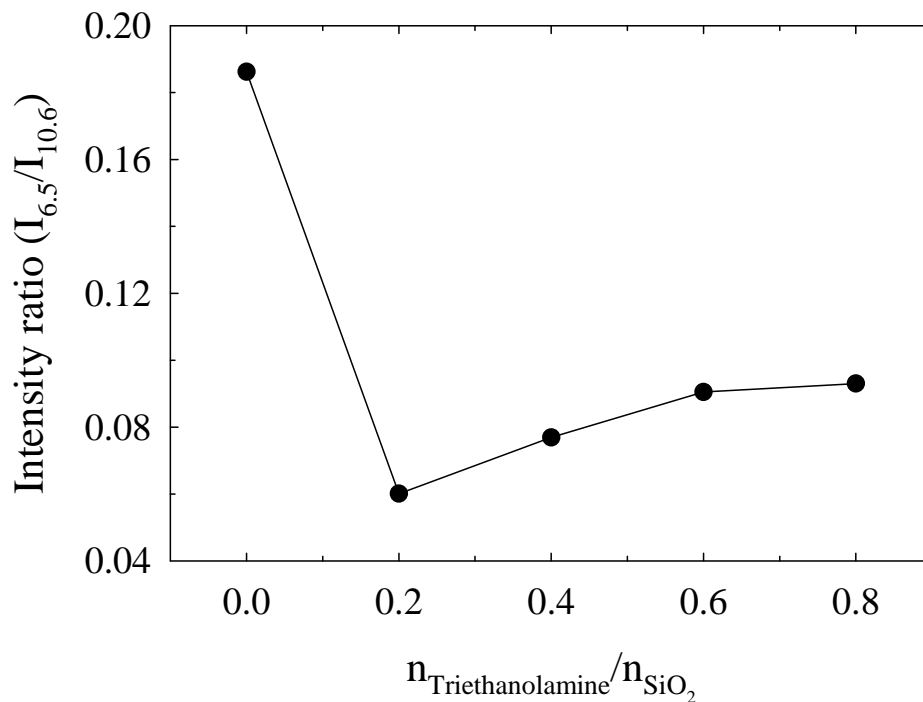


Fig. 80. Intensity ratio of the mordenite peak at  $2\theta \approx 6.5^\circ$  and the main peak of MCM-71 at  $2\theta \approx 10.6^\circ$  depending on the  $n_{\text{triethanolamine}}/n_{\text{SiO}_2}$  ratios in the synthesis mixture.

Fig. 81 shows the results of the thermogravimetric analysis for a treatment of as-synthesized MCM-71 sample in an air or a  $\text{N}_2$  flow. In both media, there is only one distinct weight loss at a temperature below  $300^\circ\text{C}$ . The weight losses amounts to 6.7 wt.-% in air and to 6.2 wt.-% in  $\text{N}_2$  are ascribed to a desorption of water located in the zeolite channels. This was confirmed by mass spectrometry and by the fact that only an endothermal effect was observed. However, no obvious weight loss due to the decomposition of triethanolamine is observed, which shows that it does not act as a genuine template for the formation of zeolite MCM-71. This is further substantiated by CHN-analysis, where a carbon content of only 0.17 wt.-% is detected in the as-synthesized sample. Hence, according to these results, triethanolamine is not incorporated into the intracrystalline pores and cavities during synthesis.

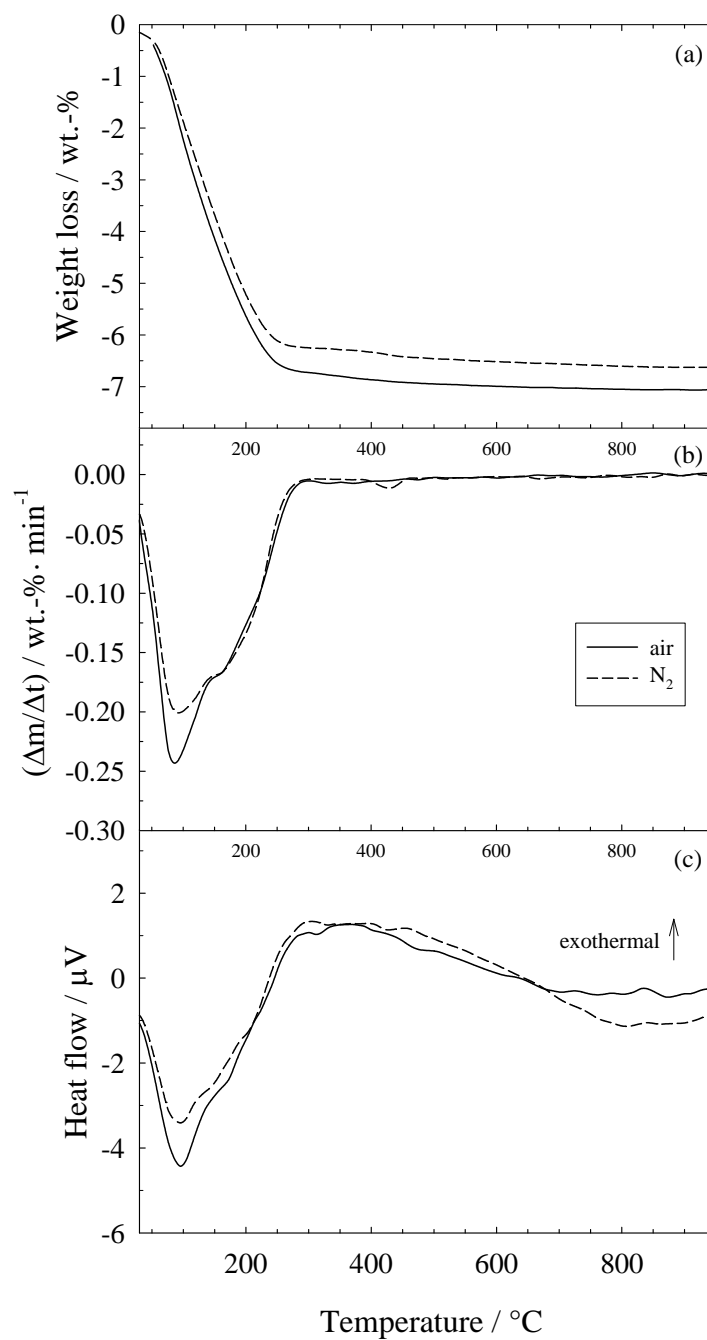


Fig. 81. Thermogravimetric analysis of as-synthesized MCM-71 in an air and in a  $N_2$  flow:

(a) weight loss (b) differential weight loss and (c) heat flow.

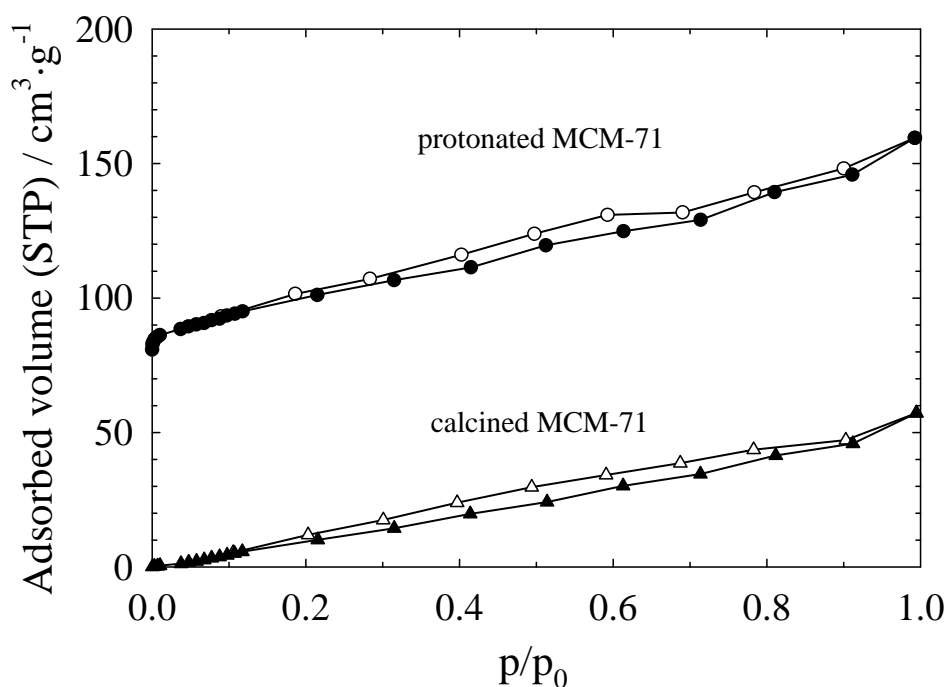


Fig. 82. Nitrogen adsorption isotherms for calcined and protonated MCM-71.

$\text{N}_2$  adsorption and desorption isotherms for calcined MCM-71 and protonated MCM-71 are presented in Fig. 82. For calcined MCM-71, a Henry-type isotherm is found indicating that  $\text{N}_2$  is not (or only to a minor extent) adsorbed in the pores of MCM-71. However, a Langmuir-type isotherm is observed for protonated MCM-71 showing that the pores are now accessible for  $\text{N}_2$ . Hence, the potassium cations are most likely blocking the pore entrances in the calcined form, thus preventing the adsorption of  $\text{N}_2$ . For the protonated form, a specific surface area of  $380 \text{ m}^2/\text{g}$  and specific pore volume of  $0.16 \text{ cm}^3/\text{g}$  are determined.

The  $^{27}\text{Al}$  and  $^{29}\text{Si}$  MAS NMR spectra of as-synthesized and calcined MCM-71 are shown in Fig. 83. In the  $^{27}\text{Al}$  spectra, the major line is centered at a chemical shift of ca. 58 ppm with a low-field shoulder at ca. 56 ppm. The presence of two kinds of tetrahedral aluminium can be explained either by chemical or crystallographic non-equivalence, which may affect both isotropic chemical shift and quadrupolar parameters and, hence, the line position [139].

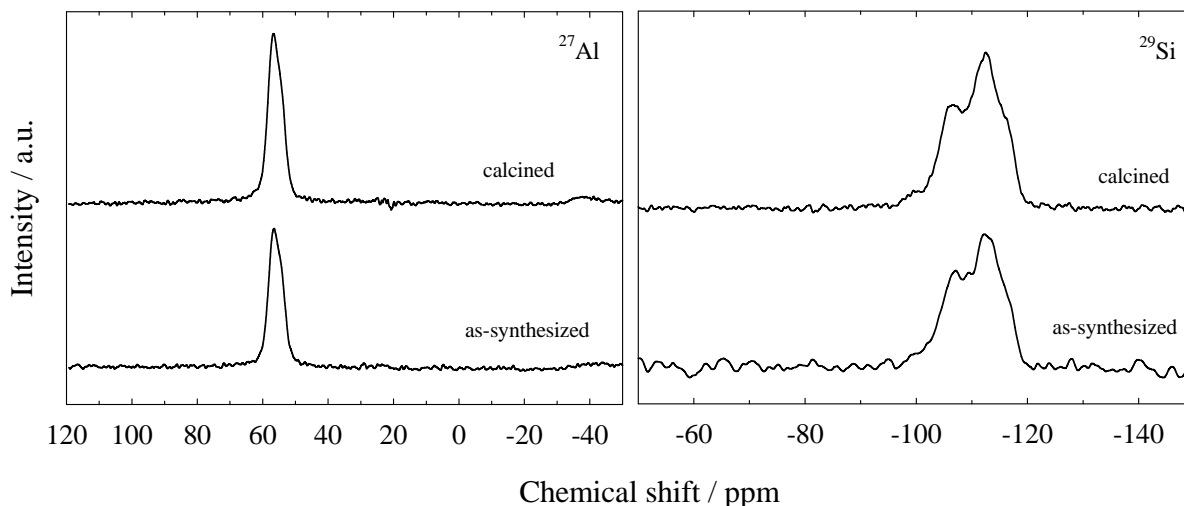


Fig. 83.  $^{27}\text{Al}$  and  $^{29}\text{Si}$  MAS NMR of as-synthesized and calcined MCM-71.

Similar results have been obtained for zeolite MCM-22 [142] where two non-equivalent crystallographic positions are found. The  $^{27}\text{Al}$  NMR spectra reveal that the aluminium is incorporated into the framework of the zeolite (in tetrahedral coordination). The  $^{29}\text{Si}$  NMR spectra of calcined MCM-71 exhibit three distinct lines at ca. -97.8, -104.9 and -112 ppm, while the as-synthesized sample shows an additional signal at -107.9 ppm. The resonance at ca. -112 ppm is assigned to Si(0Al) species of tetrahedrally coordinated silicon atoms with four silicon atoms. The line at ca. -105 ppm is assigned to a superposition of the signal due to Si(1Al) species of silicon tetrahedrally coordinated to one aluminium and three silicon atoms, whereas the signal at -97.8 ppm is ascribed to Si(2Al) species.

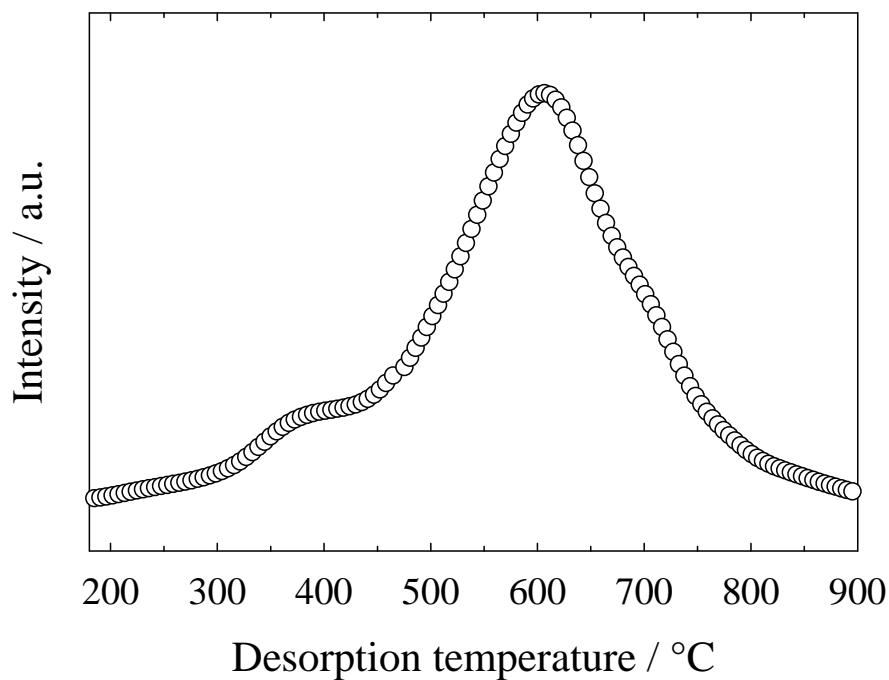


Fig. 84. Temperature programmed desorption of pyridine from protonated MCM-71.

Fig. 84 shows the desorption profile of pyridine from protonated MCM-71. It exhibits two desorption maxima, viz. at 400 °C and 600 °C. The peaks centered at 400 and 600 °C are ascribed to the interaction of pyridine molecules with medium and strong acid sites, respectively, that are most probably located inside the 10-MR channels only.

The major physicochemical properties of the zeolites studied in the present thesis are summarized in Table 28.

Table 28. Major characteristics of the zeolites studied in the present thesis.

Zeolite	$n_{Si}/n_{Al}$ or $n_{Si}/n_B$ in gel	$n_{Si}/n_{Al}$ in $H^+$ form	Crystal morphology	Approximate crystal size ( $\mu m$ )	$S_{BET}$ ( $m^2 g^{-1}$ )	$V_{pore}$ ( $cm^3 g^{-1}$ )
UTD-1	30	28	rod	0.4-1	374	0.18
Si-UTD-1	-	-	thin laths	10 long, 1-2 wide	285	0.13
CIT-5	150	116	thin laths	8-10 long, 0.5 wide	430	0.12
SSZ-53	23	55	needle	1-2	440	0.19
IM-12	-	-	square plate	5x10	490	0.21
ITQ-21	13.7	30	-	-	630	0.14
ITQ-21	23	27	platelet	0.3-0.6	546	0.16
ITQ-21	46	42	-	-	657	0.19
ITQ-21	infinite	>200	-	-	525	0.13
MCM-68	9	9	platelet	0.2	550	0.21
SSZ-35	18	11	platelet	0.2	561	0.24
SSZ-35	36	33	rectangular with round edges	1x2x0.5-2x4x1	546	0.23
SSZ-35	55	42	cubic	1-2	585	0.24
SSZ-35	73	65	cubic	1.5-2	561	0.22
SSZ-35	infinite	>500	cubic	2	525	0.22
MCM-71	10	8	retangular	8x12x4	380*	0.16*

\* This value is taken from the protonated form.

#### 4.4. Characterization of the pore size of zeolites by hydrocarbon adsorption

Adsorption studies with a series of compounds with known molecular size is one method to characterize the pore size of zeolites. Using this method, only mass transfer effects corresponding to reactant and/or product shape selectivity can be explored. For this purpose, a set of hydrocarbon adsorptives with different molecular shapes and sizes, e.g., *n*-alkanes, branched alkanes and cyclic molecules as shown in Table 29 are selected for characterizing the pore sizes of zeolites MCM-68 and MCM-71.

Table 29. Molecular dimensions of hydrocarbon adsorptives approximated using the MOPAC program.

Adsorptive	x-Axis (nm)	y-Axis (nm)	z-Axis (nm)	Spherical diameter (nm)
<i>n</i> -pentane	0.92	0.42	0.46	0.56
<i>n</i> -heptane	1.17	0.42	0.46	0.61
2-methylhexane	1.05	0.62	0.46	0.67
cyclohexane	0.74	0.67	0.51	0.63
benzene	0.74	0.67	0.37	0.57
toluene	0.82	0.68	0.37	0.59

The adsorption isotherms of *n*-pentane, *n*-heptane, 2-methylhexane and cyclohexane on protonated MCM-71 (H-MCM-71) at 30 °C are shown in Fig. 85. The shape of the isotherms of *n*-pentane and *n*-heptane show a BET-type behaviour with high adsorption volumes at low relative pressures. This suggests that the two linear hydrocarbons can enter into the pores of H-MCM-71. This is in agreement with the molecular dimensions of *n*-pentane (ca. 0.46 x 0.42 x 0.92 nm) and *n*-heptane (ca. 0.46 x 0.42 x 1.17 nm) as compared to the pore size of MCM-71 (10-MR: 0.65 x 0.43 nm, 8-MR: 0.47 x 0.36 nm). By contrast, the isotherms for 2-

methylhexane and cyclohexane exhibit a Henry-type behaviour with negligible adsorption volumes at low relative pressures ( $p/p_0 < 0.4$ ). This suggests that the size of 2-methylhexane and cyclohexane are too large to enter the pores of H-MCM-71 (or they enter only in a negligible amount). This is also consistent with the molecular dimensions of 2-methylhexane (ca. 0.62 x 0.46 x 1.05 nm) and cyclohexane (ca. 0.67 x 0.51 x 0.74 nm) which exhibit larger dimension than the pores of MCM-71. Therefore, the pore size of H-MCM-71 lies in the border between the size of *n*-alkanes (head size: ca. 0.46 x 0.42 nm) and branched alkane (head size: ca. 0.62 x 0.46 nm) which is in agreement with its crystallographically determined pore structure (10-MR: 0.65 x 0.43 nm and 8-MR: 0.47 x 0.36 nm).

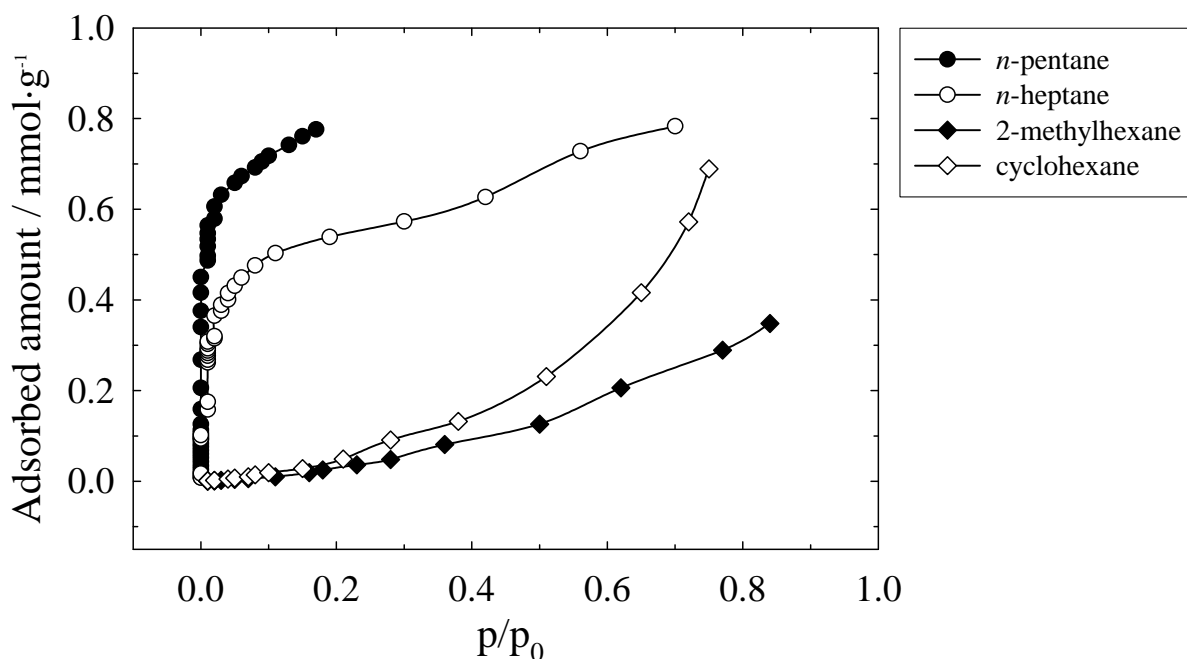


Fig. 85. Adsorption isotherms for various hydrocarbon adsorptives on H-MCM-71 at 30 °C.

Fig. 86 depicts the adsorption isotherms for *n*-pentane, *n*-heptane, 2-methylhexane, cyclohexane, benzene and toluene on H-MCM-68 at 30 °C. The isotherms of *n*-pentane, *n*-heptane, 2-methylhexane and cyclohexane exhibit Langmuir-type behaviour, whereas the isotherms of benzene and toluene are typical for BET-type. The high amount of adsorption at

low relative pressure for all adsorptives suggests that all adsorptives are able to enter the pores of zeolite H-MCM-68 either via 12- or 10-MR or via both channel types.

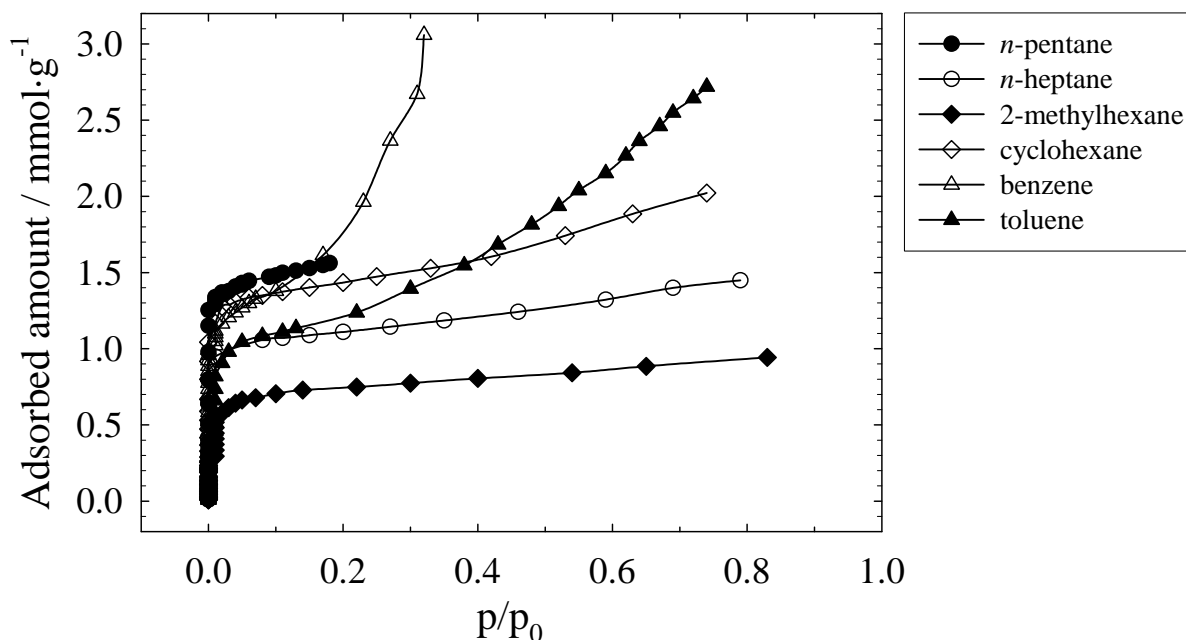


Fig. 86. Adsorption isotherms for various hydrocarbon adsorptives on H-MCM-68 at 30 °C.

The molecular sizes of *n*-pentane (ca. 0.46 x 0.42 x 0.92 nm) and *n*-heptane (ca. 0.46 x 0.42 x 1.17 nm) are smaller than the pore size of MCM-68 (12-MR: 0.68 nm, 10-MR: 0.53 nm), thus they are assumed to enter both, the 12- and the 10-MR pores. By contrast, the sizes of 2-methylhexane (ca. 0.62 x 0.46 x 1.05 nm), cyclohexane (ca. 0.67 x 0.51 x 0.74 nm), benzene (ca. 0.67 x 0.37 x 0.74 nm) and toluene (ca. 0.68 x 0.37 x 0.82 nm), as compared to the pore sizes of MCM-68 suggest that these molecules could enter at least the 12-MR pores. The adsorbed amount of each adsorptives and the calculated volume capacities at the maximum relative pressures are summarized in Table 30. The specific pore volumes of the zeolites were derived from the adsorbed amounts of probe molecules with the assumption that the adsorptives are in the liquid state inside the pores of the zeolite.

Table 30. Adsorbed amount and calculated specific pore volume observed for different adsorptives on H-MCM-71 and H-MCM-68 at 30 °C as compared to the values obtained from N<sub>2</sub> adsorption.

Adsorptive	Adsorbed amount (mmol·g <sup>-1</sup> )		Calculated specific pore volume (cm <sup>3</sup> ·g <sup>-1</sup> )	
	H-MCM-71	H-MCM-68	H-MCM-71	H-MCM-68
N <sub>2</sub>	-	-	0.16	0.27
<i>n</i> -pentane	0.78	1.56	0.09	0.18
<i>n</i> -heptane	0.78	1.45	0.11	0.21
2-methylhexane	-	0.94	-	0.14
cyclohexane	-	2.02	-	0.21
benzene	-	3.06	-	0.27
toluene	-	2.72	-	0.29

## 4.5. Ethylbenzene disproportionation as test reaction

The disproportionation of ethylbenzene is known as a suitable test reaction to characterize acid zeolites [93, 94]. Moreover, shape selective effects of the zeolite can also be investigated by this test reaction [10]. A classification into medium pore (10-MR) and large pore (12-MR) zeolites can be achieved from the characteristic parameters of the conversion profile, the yield ratio of diethylbenzene-to-benzene, the product distribution of diethylbenzenes and the presence of bulky product molecules, as already described in chap. 2.4.1.1. Within the scope of this work, various recent zeolites with different pore sizes and architectures, viz. based on 14-, 12-, and 10-MR pores were selected to investigate both, their catalytic acidities and their pore structures based on the above described parameters.

### 4.5.1. Zeolites based on 14-membered ring pore openings

#### 4.5.1.1. *H-UTD-1*

The time-on-stream behaviour of H-UTD-1 ( $n_{\text{Si}}/n_{\text{Al}} = 28$ ) during ethylbenzene disproportionation is shown in Fig. 87. The reaction was performed at  $T_{\text{R}} = 200$  °C and  $W_{\text{cat}}/F_{\text{E-Bz}} = 290$  g·h/mol. H-UTD-1 exhibits a high conversion (ca. 35 %) at the onset of the experiment, viz. at 0.5 h. The conversion level decreases with time-on-stream and reaches a quasi-stationary state after 22 h with a conversion of 13 %. The decrease of conversion or deactivation is most probably due to coke formation as a result of undesired side reactions. The product from the reaction contains benzene (Bz), 1,3-diethylbenzene (DE-Bz), 1,4-DE-Bz, 1,2-DE-Bz, 1,3,5-triethylbenzene (TE-Bz) and 1,2,4-TE-Bz. The total yield of TE-Bz isomers is ca. 0.95 % at the onset of the experiment but gradually decreases to 0.08 % after 22 h.

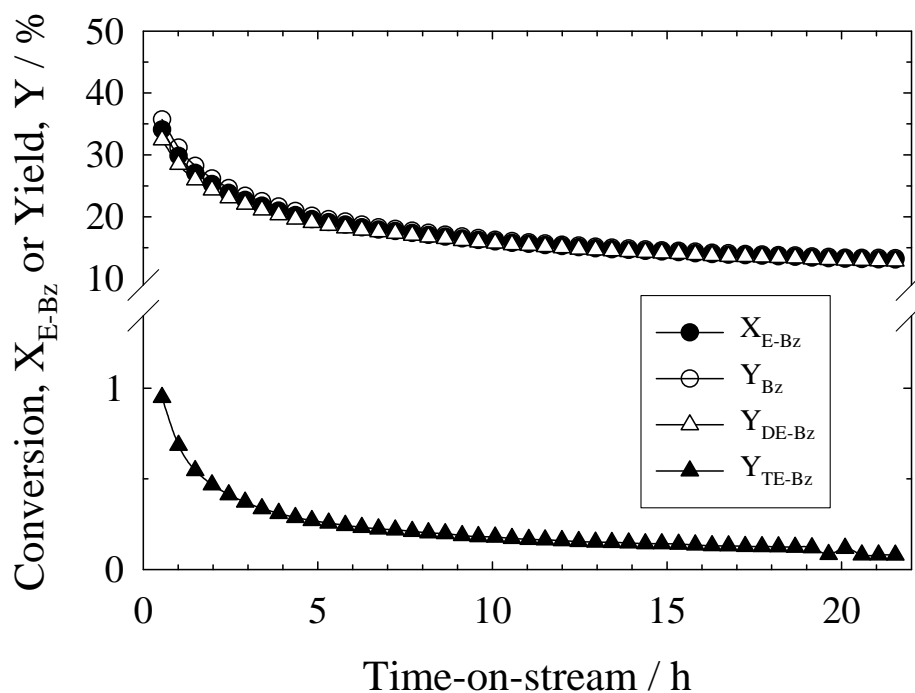


Fig. 87. Conversion and product yields in ethylbenzene disproportionation over H-UTD-1 at  $T_R = 200\text{ }^\circ\text{C}$ ,  $W_{\text{cat}}/F_{E-Bz} = 290\text{ g}\cdot\text{h}/\text{mol}$  and  $W_{\text{cat}} = 290\text{ mg}$ .

Fig. 88 shows the stationary state distribution of the DE-Bz isomers with 64.1 % for the 1,3-(meta), 31.2 % for 1,4-(para) and 4.7 % for 1,2-DE-Bz (ortho) isomer. These isomer distributions correspond to the range of values reported for the reaction in the liquid phase (on catalysts without pore constraints), viz. 69 % meta-, 28 % para- and 3 % ortho-isomers [107] and values reported for E-Bz conversion in large pore zeolite Y (cf. 62 % meta-, 33 % para- and 5 % ortho-isomer [10]). Thus, the formation or diffusion of these isomers is not hindered by the pore size of H-UTD-1. The stationary state distributions of DE-Bz isomers suggest that H-UTD-1 is a large pore zeolite. Moreover, the stationary state distribution of the largest products, viz. 1,3,5- and 1,2,4-TE-Bz isomers at 69 % and 31 %, respectively, are observed as also shown in Fig 88. Besides, the yield ratio between DE-Bz and Bz is close to unity (ca. 0.97) and is also very typical for (very) large pore zeolites [10].

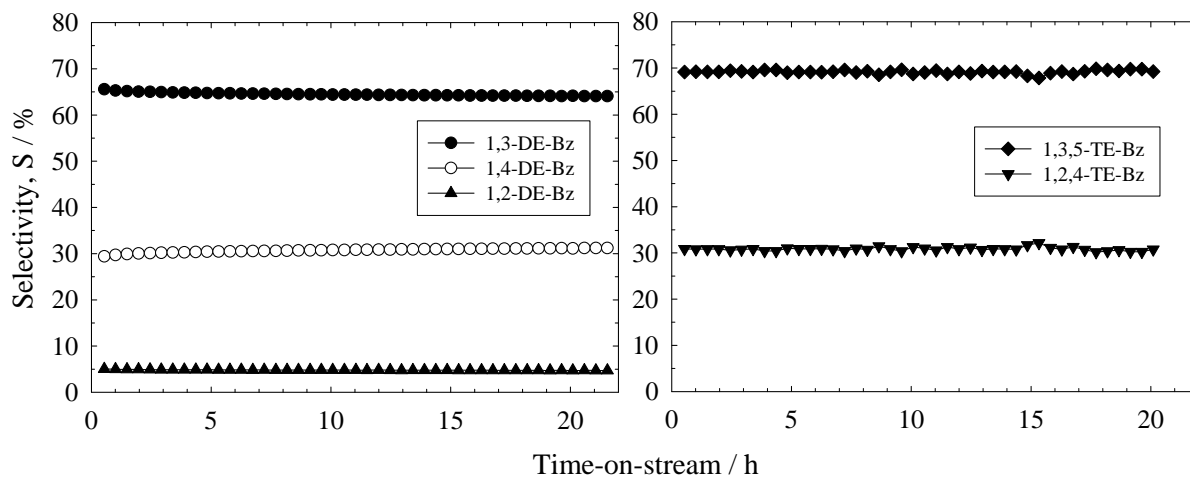


Fig. 88. Selectivities for the diethylbenzene and triethylbenzene isomers (normalized) in ethylbenzene disproportionation over H-UTD-1 at  $T_R = 200\text{ }^\circ\text{C}$ ,  $W_{\text{cat}}/F_{\text{E-Bz}} = 290\text{ g}\cdot\text{h}/\text{mol}$  and  $W_{\text{cat}} = 290\text{ mg}$ .

Finally, (1) the presence of a large amount of TE-Bz isomers, (2) the stationary state distribution of DE-Bz isomers and (3) the yield ratio of DE-Bz to Bz close to unity suggest that H-UTD-1 is a large pore zeolite. This result is in-line with the structure of UTD-1 which possesses unidimensional extra-large pores with 14-membered ring pore openings (1.0 x 0.75 nm) [35, 36].

#### 4.5.1.2. H-CIT-5

Fig. 89 shows the time-on-stream behaviour for ethylbenzene conversion on H-CIT-5 ( $n_{\text{Si}}/n_{\text{Al}} = 116$ ) at  $T_R = 250\text{ }^\circ\text{C}$  and  $W_{\text{cat}}/F_{\text{E-Bz}} = 290\text{ g}\cdot\text{h}/\text{mol}$ . Under these conditions, H-CIT-5 produces Bz as well as 1,3-, 1,4- and 1,2-DE-Bz isomers as reaction products. TE-Bz isomers are not found, even at higher reaction temperatures of  $300\text{ }^\circ\text{C}$  (the results are not shown here). The conversion profile shows a deactivation with time-on-stream with a conversion of 9.2 % at 0.5 h and declining to 6.6 % after 22 h. The stationary state distribution of the DE-Bz isomers is shown in Fig. 90 with 59 % meta-, 36.3 % para- and 4.7 % ortho-DE-Bz. The yield ratio between DE-Bz and Bz at 22 h is close to unity (ca. 0.99).

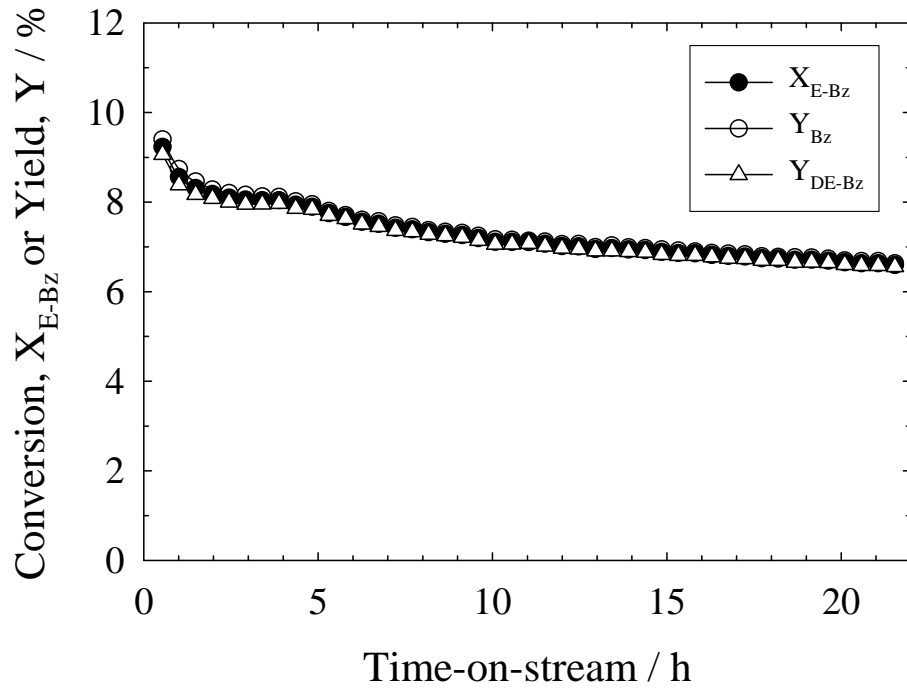


Fig. 89. Conversion and product yields in ethylbenzene disproportionation over H-CIT-5 at

$T_R = 250$  °C,  $W_{cat}/F_{E-Bz} = 290$  g·h/mol and  $W_{cat} = 290$  mg.

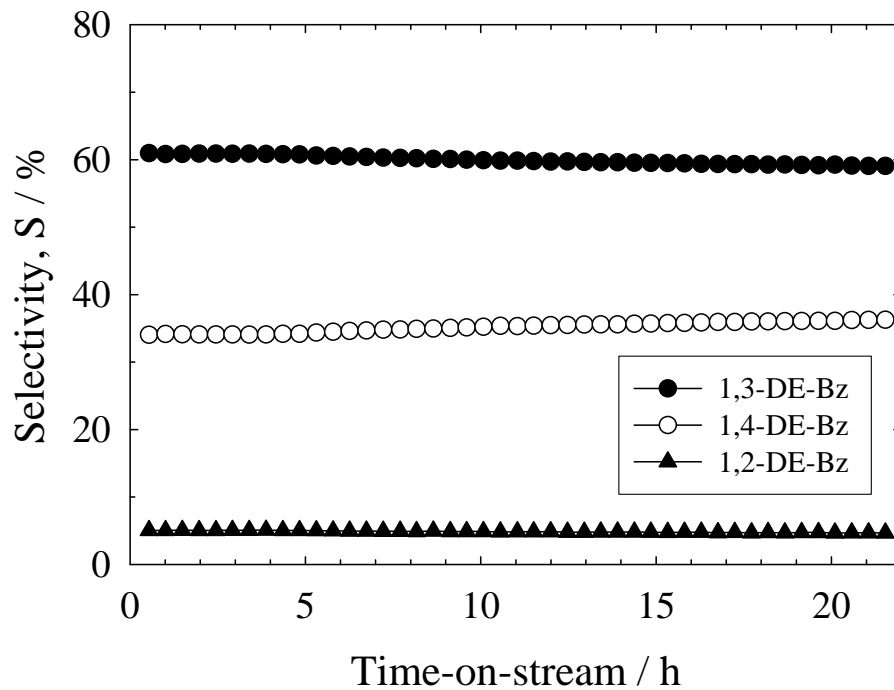


Fig. 90. Selectivities for the diethylbenzene isomers in ethylbenzene disproportionation over

H-CIT-5 at  $T_R = 250$  °C,  $W_{cat}/F_{E-Bz} = 290$  g·h/mol and  $W_{cat} = 290$  mg.

Even though the unexpected result of deactivation and the absence of TE-Bz isomers are observed, (1) the product distribution of DE-Bz isomers reaches the stationary state and (2) the yield ratio of DE-Bz to Bz is close to unity, which suggests the presence of large pores in zeolite H-CIT-5. This is in agreement with its crystallographic structure showing a unidimensional array of extra-large pore 14-MR channels with ca. 0.73 nm in diameter [40, 41].

#### 4.5.1.3. H-SSZ-53

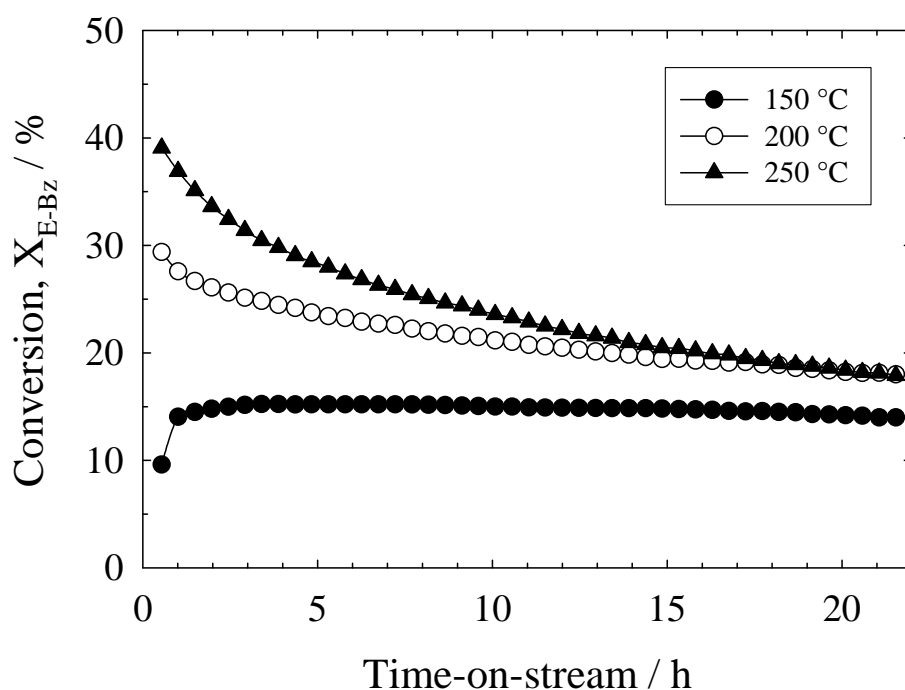


Fig. 91. Conversion profiles for ethylbenzene disproportionation over H-SSZ-53 at different reaction temperatures with  $W_{\text{cat}}/F_{E-Bz} = 290$  g·h/mol and  $W_{\text{cat}} = 290$  mg.

The influence of the reaction temperature on the conversion and the product distribution over H-SSZ-53 ( $n_{\text{Si}}/n_{\text{Al}} = 55$ ) was investigated. The conversion profiles from three reaction temperatures, viz. 150, 200 and 250 °C with  $W_{\text{cat}}/F_{E-Bz} = 290$  g·h/mol are presented in Fig. 91. At  $T_R = 150$  °C, a small induction period, reaching a maximum after ca. 3 h and followed by a stationary state of the conversion profile, is observed. On the other hand, the profiles at

higher reaction temperatures of  $T_R = 200$  and  $250$  °C show a catalyst deactivation. The presence of an induction period at low conversions suggests that zeolite H-SSZ-53 contains large pores or large intracrystalline voids as observed in some other large pore zeolites, e.g., Y and ZSM-12 [10]. At  $T_R = 150$  °C, the conversion level at stationary state is ca. 13.6 %. At higher reaction temperatures, viz. 200 and 250 °C, the conversion starts as high as 30 and 39 %, respectively, before declining to 18 % after 22 h. This shows that the higher the reaction temperature, the faster the catalyst deactivates. The results for different reaction temperatures are summarized in Table 31.

Table 31. Ethylbenzene conversions and yield ratios of diethylbenzene-to-benzene at stationary state over H-SSZ-53.

Reaction temperature (°C)	X at 0.5 h (%)	X at 22 h (%)	$Y_{DE-Bz}/Y_{Bz}$
150	9.6	13.6	0.99
200	29.4	18	0.95
250	39	18	0.91

Bz, all DE-Bz isomers as well as 1,3,5- and 1,2,4-TE-Bz isomers appear as reaction products. The presence of TE-Bz isomers at all three reaction temperatures suggests that H-SSZ-53 is a large pore zeolite. Among the TE-Bz isomers, at  $T_R = 150$  °C, 1,3,5-TE-Bz is first desorbed as product after 1.5 h time-on-stream before 1,2,4-TE-Bz isomer appears after 3.4 h with a total yield at the maximum of ca. 0.2 % (distribution: 72 and 28 % for 1,3,5- and 1,2,4-TE-Bz, respectively). By contrast, at higher temperatures ( $T_R = 200$  and  $250$  °C), both isomers are simultaneously present at the onset of the reaction with a maximum yield of 0.6 and 1.2 %, respectively. The stationary state distribution gives ca. 69 % 1,3,5- and ca. 31 % 1,2,4-TE-Bz as shown in Fig. 92 (shown only for  $T_R = 200$  °C).

At  $T_R = 150$  °C, an induction period for each isomer of DE-Bz and TE-Bz is observed but

not for Bz. As known, the presence of an induction period or a period of increasing conversion could result from the preferential adsorption of DE-Bz inside the zeolite pore system or DE-Bz isomers undergoing consecutive reactions as reported by Weitkamp et al. [10]. The deficiency of DE-Bz in the product stream is also indicated by the pronounced gap in the yield ratio of  $Y_{\text{DE-Bz}}/Y_{\text{Bz}}$  during the induction period.

The yield ratios of DE-Bz and Bz in all cases lies between 0.91-0.99 as summarized in Table 31. These experimentally obtained values fall in the range for large pore zeolite. A decreasing value is observed when the reaction temperature is higher. This is probably due to the occurrence of consecutive reactions, e.g., part of DE-Bz could further disproportionate into E-Bz and TE-Bz.

At  $T_{\text{R}} = 200$  °C, the distribution in the DE-Bz fraction at stationary state is ca. 64 % meta-, ca. 31 % para- and ca. 5 % ortho-DE-Bz as depicted in Fig. 92. A stationary state distribution of the DE-Bz isomers is observed for all three reaction temperatures and this is indicative for the presence of large pore. The distribution data are summarized in Table. 32.

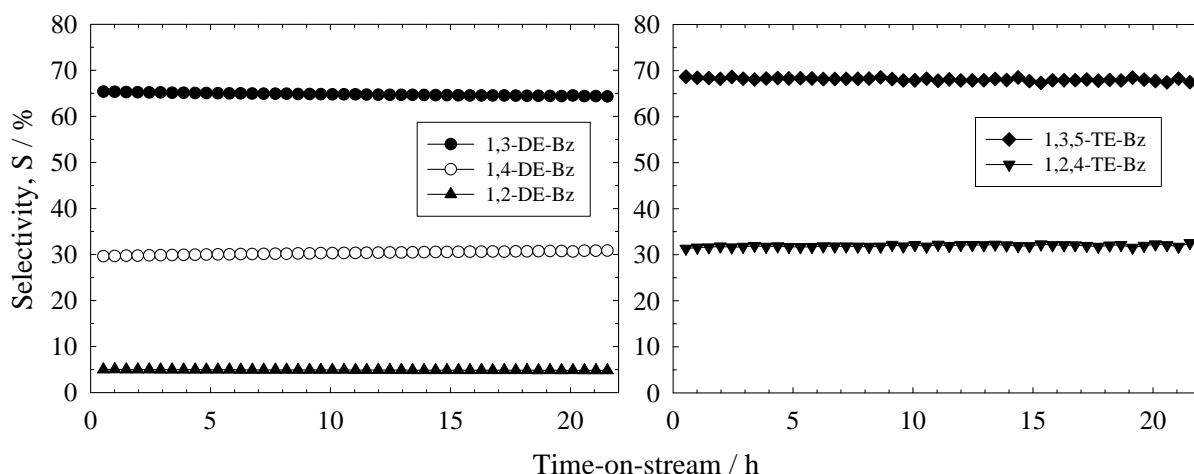


Fig. 92. Selectivities for the diethylbenzene and triethylbenzene isomers (normalized) in ethylbenzene disproportionation over H-SSZ-53 at  $T_{\text{R}} = 200$  °C,  $W_{\text{cat}}/F_{\text{E-Bz}} = 290$  g·h/mol and  $W_{\text{cat}} = 290$  mg.

Table 32. Distribution of the diethylbenzene isomers in ethylbenzene disproportionation over H-SSZ-53 at different reaction temperatures compared to the thermodynamic equilibrium values (Eq.).

Reaction temperature (°C)	S <sub>1,3-DE-Bz</sub> (%)		S <sub>1,4-DE-Bz</sub> (%)		S <sub>1,2-DE-Bz</sub> (%)	
	Test	Eq.	Test	Eq.	Test	Eq.
150	65.3	54.2	30.5	32.6	4.2	13.2
200	64.3	53.7	30.8	31.8	4.8	14.5
250	63.8	53.3	30.8	30.9	5.5	15.8

The distribution values for the DE-Bz isomers observed deviate from the thermodynamic equilibrium values (cf. Fig. 21). The decrease of the distribution of meta-isomer but increase for the ortho-isomer by increasing the reaction temperature are observed in the same trend with the thermodynamic equilibrium values.

In summary, H-SSZ-53 exhibits the typical features of a large pore zeolite in the ethylbenzene disproportionation because (1) the presence of an induction period, (2) the presence of large TE-Bz isomers as products, (3) the stationary state distribution of the DE-Bz isomers and (4) the yield ratios of DE-Bz and Bz are close to unity. This conclusion is in-line with the crystallographic structure of zeolite SSZ-53 with 14-MR unidimensional pores with sizes of ca. 0.85 x 0.65 nm [46].

Comparison of the acid properties of 14-MR zeolites: H-UTD-1, H-CIT-5 and H-SSZ-53

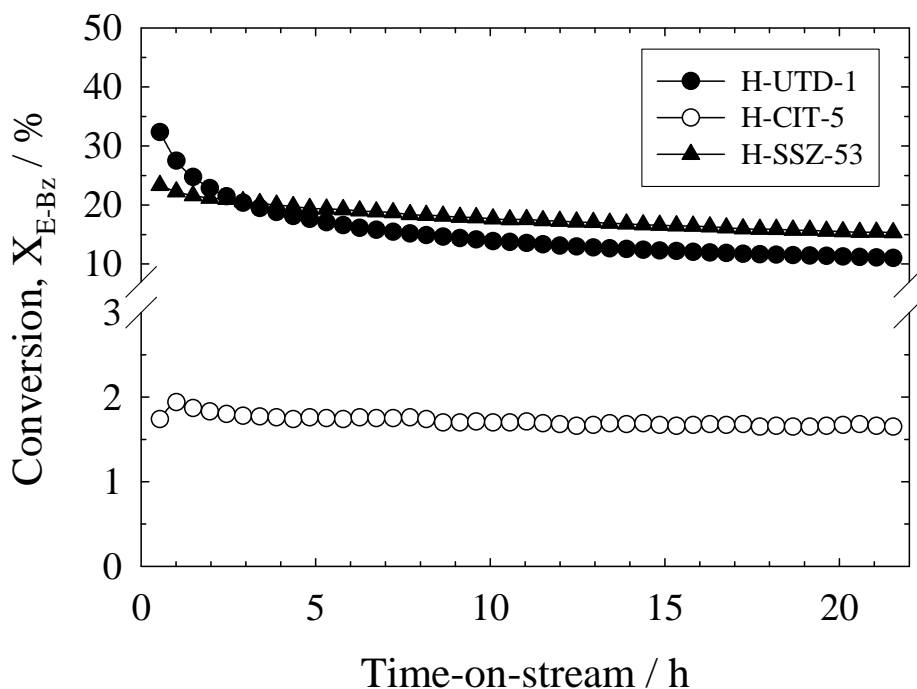


Fig. 93. Conversion profiles for ethylbenzene disproportionation over H-UTD-1, H-CIT-5 and H-SSZ-53 at  $T_R = 200$  °C,  $W_{cat}/F_{E-Bz} = 180$  g·h/mol and  $W_{cat} = 290$  mg.

The tests were carried out at lower conversions by reducing  $W_{cat}/F_{E-Bz}$  to 180 g·h/mol at  $T_R = 200$  °C in order to compare the conversions under stationary state conditions. Three catalysts with unidimensional 14-MR pores, viz. H-UTD-1, H-CIT-5 and H-SSZ-53 have been tested and the conversion profiles are presented in Fig. 93. The conversions in the stationary state after 22 h time-on-stream are ca. 11, 1.7 and 15.3 % for H-UTD-1, H-CIT-5 and H-SSZ-53, respectively. Among these catalysts, H-SSZ-53 and H-UTD-1 exhibit a higher catalytic activity as compared to that of H-CIT-5 and it ranks in this order: H-SSZ-53 > H-UTD-1 > H-CIT-5. This result is in-line with pyridine TPD where the desorption peaks at the maxima  $\geq 550$  °C (strong acid sites) of H-UTD-1 and H-SSZ-53 are larger than that of H-CIT-5 (cf. Fig. 56). The results are summarized in Table 33.

Table 33. Stationary state conversions in ethylbenzene disproportionation over H-UTD-1, H-CIT-5 and H-SSZ-53

Catalyst	$n_{Si}/n_{Al}$	X at 22 h (%)
H-UTD-1	28	11
H-CIT-5	116	1.7
H-SSZ-53	55	15.3

#### 4.5.2. Zeolites based on 12-membered ring pore openings

##### 4.5.2.1. H-MCM-68

The catalytic test was carried out with H-MCM-68 ( $n_{Si}/n_{Al} = 9$ ) at lower modified residence times (viz. at  $W_{cat}/F_{E-Bz} = 145$  g·h/mol at  $T_R = 200$  and  $250$  °C) in order to run the reaction at lower conversion. The conversion profiles are depicted in Fig. 94 and reveal that H-MCM-68 is a very active catalyst. At  $T_R = 250$  °C, the conversion starts at 43 % and slightly decreases to 37 % after 22 h. By contrast, the conversion profile at  $T_R = 200$  °C is virtually constant for the entire reaction time at ca. 25 % conversion. The slow rate of deactivation could probably result, besides the mild reaction conditions, from the three-dimensional pore structure of MCM-68 with intersecting one dimensional 12-MR and two dimensional 10-MR channels. This could minimize diffusion constraints for the reactants or products. The reaction product contains Bz, all possible DE-Bz isomers and 1,3,5- and 1,2,4-TE-Bz isomers for both reaction temperatures. The product yields in dependence of time-on-stream are shown in Fig. 95. TE-Bz isomers are present with a maximum of ca. 0.27 % and ca. 1 % at  $T_R = 200$  and  $250$  °C, respectively, with distributions of ca. 55 % 1,3,5-TE-Bz and ca. 45 % 1,2,4-TE-Bz after 22 h of time-on-stream.

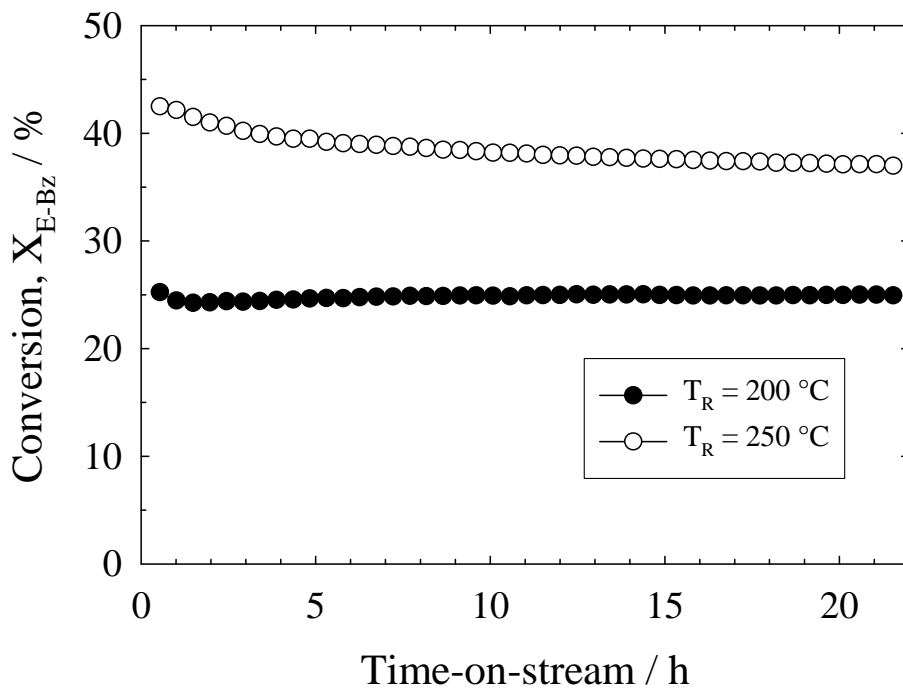


Fig. 94. Conversion profiles for ethylbenzene disproportionation over H-MCM-68 at  $T_R = 200\text{ }^\circ\text{C}$  and  $250\text{ }^\circ\text{C}$ ,  $W_{\text{cat}}/F_{E-Bz} = 145\text{ g}\cdot\text{h}/\text{mol}$  and  $W_{\text{cat}} = 145\text{ mg}$ .

The yield ratios between DE-Bz and Bz after 22 h for  $T_R = 200$  and  $250\text{ }^\circ\text{C}$  are 0.95 and 0.79, respectively. The relatively low value of 0.79 at higher reaction temperature is typically observed when the reaction is performed at high conversion. The distribution of the DE-Bz isomers in both cases are ca. 65 % meta-, ca. 29.5 % para- and ca. 5.5 % of the ortho-isomer.

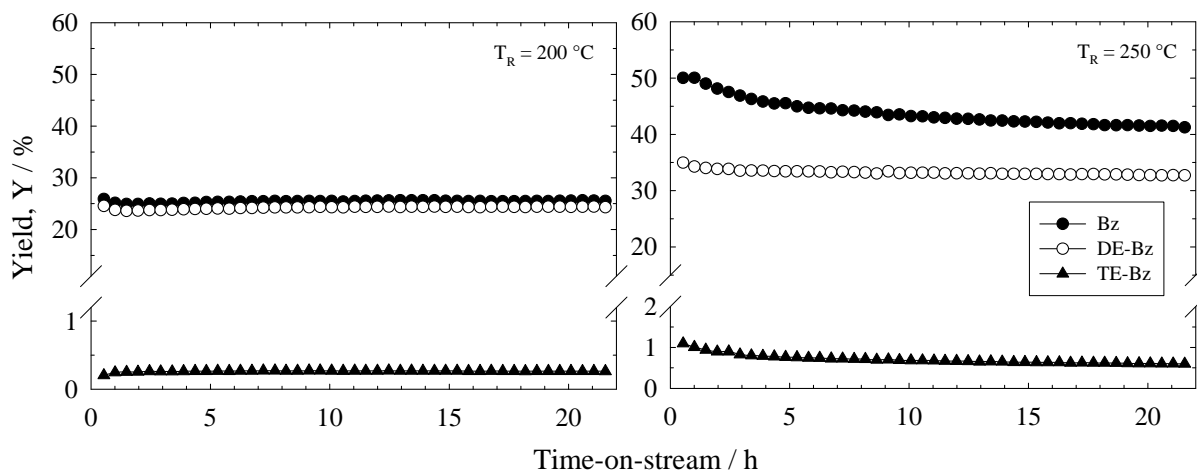


Fig. 95. Product yields in ethylbenzene disproportionation over H-MCM-68 at  $T_R = 200\text{ }^\circ\text{C}$  and  $250\text{ }^\circ\text{C}$ ,  $W_{\text{cat}}/F_{E-Bz} = 145\text{ g}\cdot\text{h}/\text{mol}$  and  $W_{\text{cat}} = 145\text{ mg}$ .

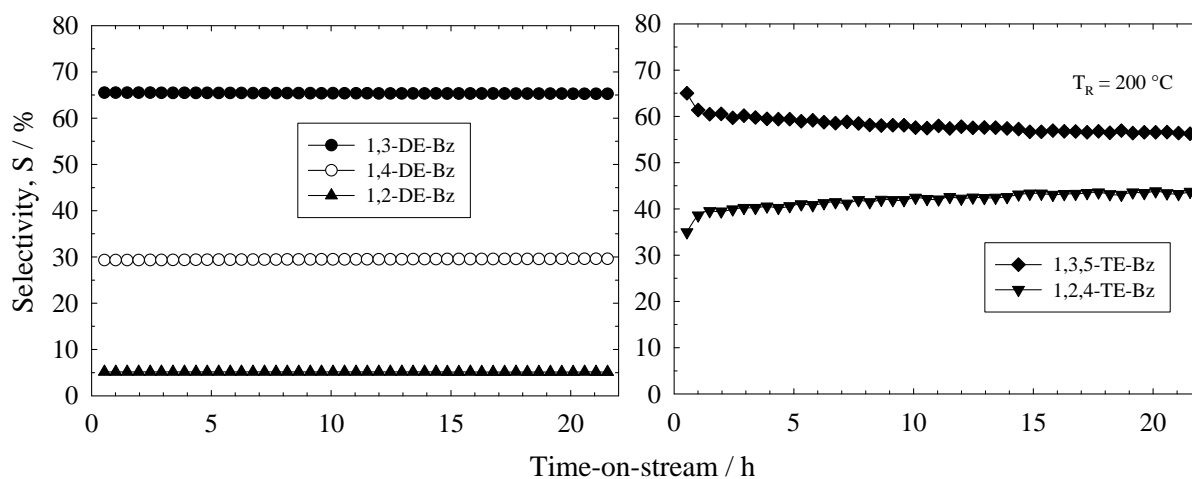


Fig. 96. Selectivities for the diethylbenzene and triethylbenzene isomers (normalized) in ethylbenzene disproportionation over H-MCM-68 at  $T_R = 200\text{ }^\circ\text{C}$ ,  $W_{\text{cat}}/F_{\text{E-Bz}} = 145\text{ g}\cdot\text{h}/\text{mol}$  and  $W_{\text{cat}} = 145\text{ mg}$ .

(1) The presence of the bulky TE-Bz molecules in the product, (2) the almost equal yields of DE-Bz and Bz in the stationary state (at  $T_R = 200\text{ }^\circ\text{C}$ ) and (3) the independence of the DE-Bz isomer distribution on the time-on-stream suggests that MCM-68 contains large pores and/or intersections. This is in-line with its crystallographic structure containing 12-MR pores (0.68 x 0.65 nm) intersecting with the undulating 10-MR pore systems (0.55 x 0.51 nm) [63].

#### 4.5.3. Zeolites based on 10-membered ring pore openings

##### 4.5.3.1. H-SSZ-35

The catalytic experiments were performed on H-SSZ-35 catalysts with different  $n_{\text{Si}}/n_{\text{Al}}$  ratios (11, 33 and 65) at  $W_{\text{cat}}/F_{\text{E-Bz}} = 290\text{ g}\cdot\text{h}/\text{mol}$  in order to investigate the influence of the  $n_{\text{Si}}/n_{\text{Al}}$  ratio (or the Al-content) in the sample. All samples were tested at the same reaction temperature of  $T_R = 200\text{ }^\circ\text{C}$ . Additionally, the sample with  $n_{\text{Si}}/n_{\text{Al}} = 11$  was tested at the higher reaction temperature of  $T_R = 250\text{ }^\circ\text{C}$ . The conversion profiles with time-on-stream are shown in Fig. 97. The profiles of all samples tested at  $T_R = 200\text{ }^\circ\text{C}$  exhibit an induction period at the onset of the experiment for ca. 4 h. While the sample with  $n_{\text{Si}}/n_{\text{Al}} = 11$  tested at

$T_R = 250$  °C shows no induction period and the conversion decreases slowly with time-on-stream. The observed induction period is indicative for the presence of large pores in the structure of SSZ-35. The samples with  $n_{Si}/n_{Al} = 11, 33$  and  $65$  tested at  $T_R = 200$  °C show the conversions in the stationary state at ca. 4.5, ca. 2.8 and ca. 1.4 %, respectively. It was observed that the conversions in this steady state, which correspond to the catalyst activity in terms of Brønsted acidity, decrease with increasing the  $n_{Si}/n_{Al}$  ratio (or reducing the Al-content). The conversion values after 0.5 h and 22 h time-on-stream are presented in Table 34.

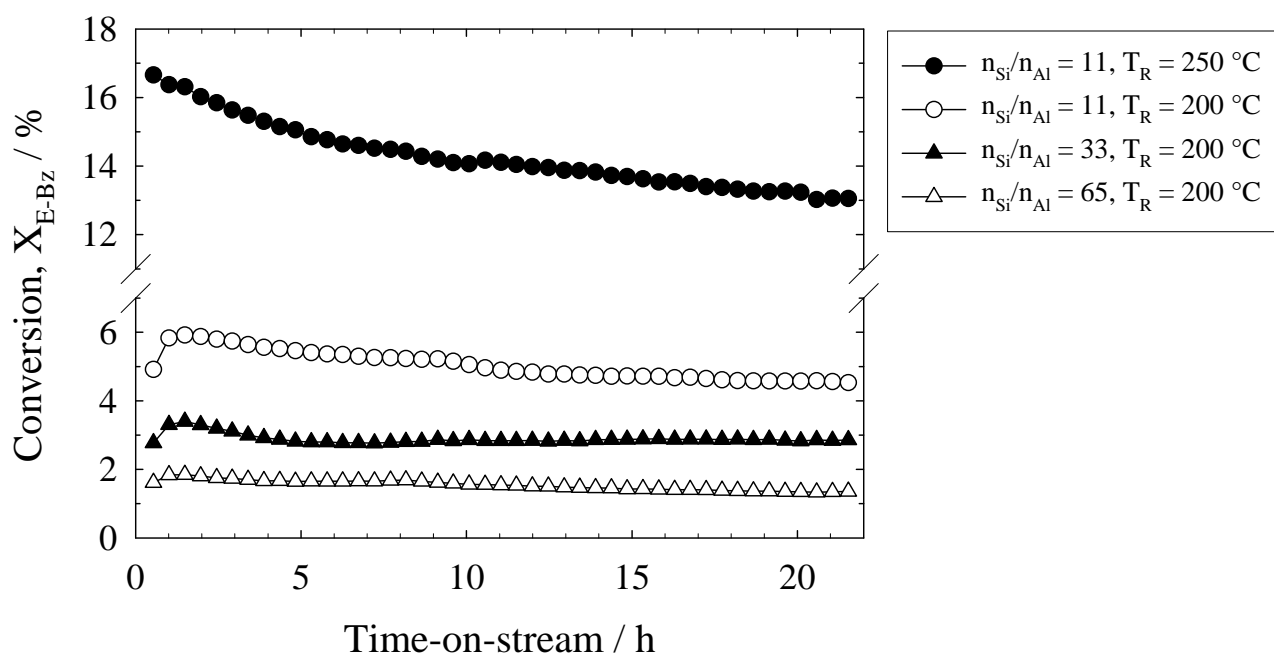


Fig. 97. Conversion profiles for ethylbenzene disproportionation over H-SSZ-35 with different  $n_{Si}/n_{Al}$  ratios at  $T_R = 200$  °C and  $250$  °C,  $W_{cat}/F_{E-Bz} = 290$  g·h/mol and  $W_{cat} = 290$  mg.

The overall product yields are shown in Fig. 98. The product obtained with the sample having  $n_{Si}/n_{Al} = 11$  at  $T_R = 200$  °C is composed of Bz and all three DE-Bz isomers only. However, at the higher reaction temperature of  $T_R = 250$  °C, 1,3,5- and 1,2,4-TE-Bz isomers are observed as additional products with a yield maximum of ca. 0.3 %.

Table 34. Conversions and diethylbenzene-to-benzene yield ratios in the stationary state over different H-SSZ-35 samples.

$n_{Si}/n_{Al}$	$T_R$ (°C)	X at 0.5 h (%)	X at 22 h (%)	$Y_{DE-Bz}/Y_{Bz}$
11	250	16.7	13	0.89
11	200	4.9	4.5	0.96
33	200	2.8	2.8	0.97
65	200	1.6	1.4	0.96

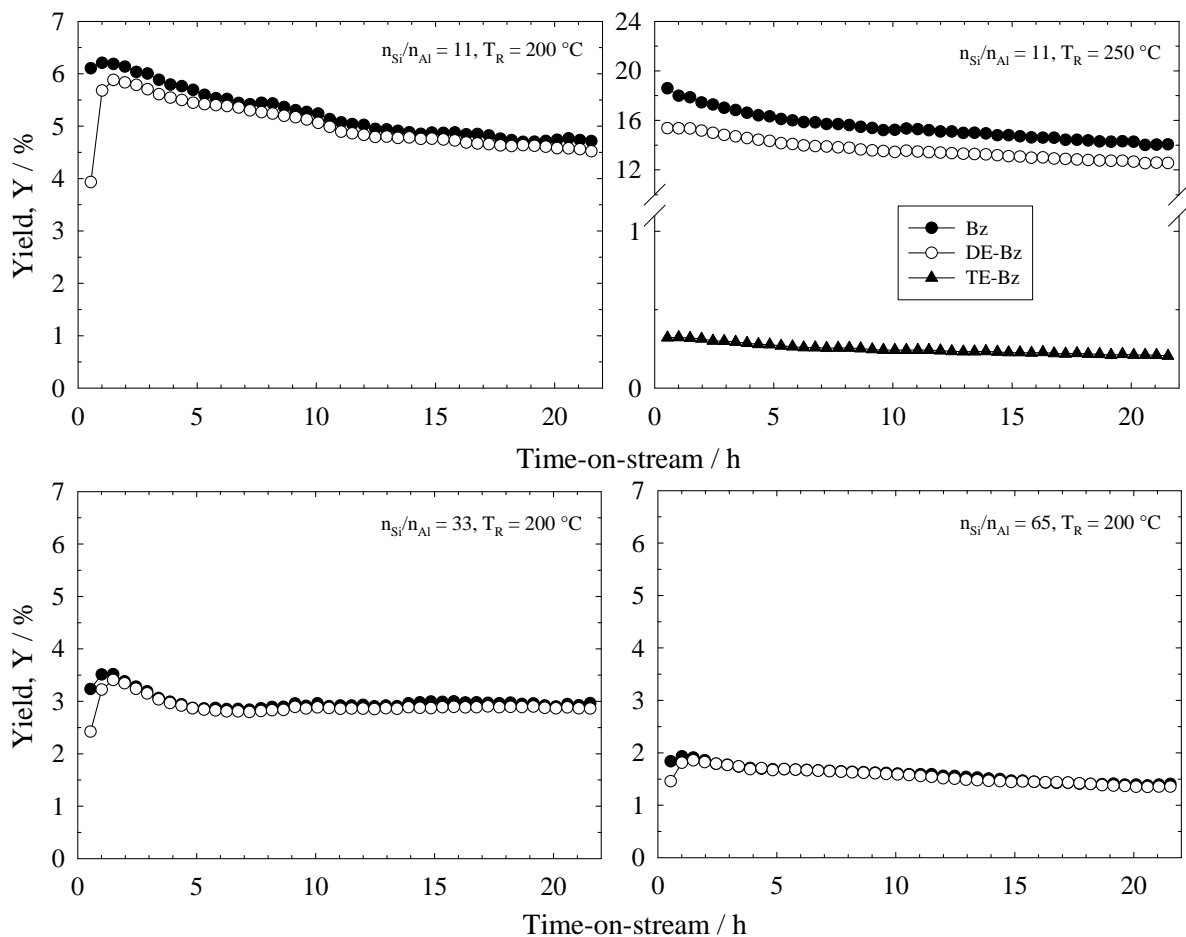


Fig. 98. Product yields in ethylbenzene disproportionation over H-SSZ-35 with different  $n_{Si}/n_{Al}$  ratios at  $T_R = 200$  °C and  $250$  °C,  $W_{cat}/F_{E-Bz} = 290$  g·h/mol and  $W_{cat} = 290$  mg.

By difference, the products over the catalyst samples with  $n_{Si}/n_{Al} = 33$  and  $65$  consist of only Bz, 1,3- and 1,4-DE-Bzs. The presence of 1,2-DE-Bz only on the samples with  $n_{Si}/n_{Al} = 11$

could either be a result from higher conversion or by a preferential formation of this isomer on the external surface since this smallest crystallite size catalyst sample contains a considerably large external surface area (cf. Fig. 70) as compared to the other samples. The preferential formation on the external surface area of the 1,2-DE-Bz was previously observed on H-ZSM-5, on which the formation of 1,2-DE-Bz ceased when the acid sites at the external surface were poisoned with chlorotriphenylsilane [10].

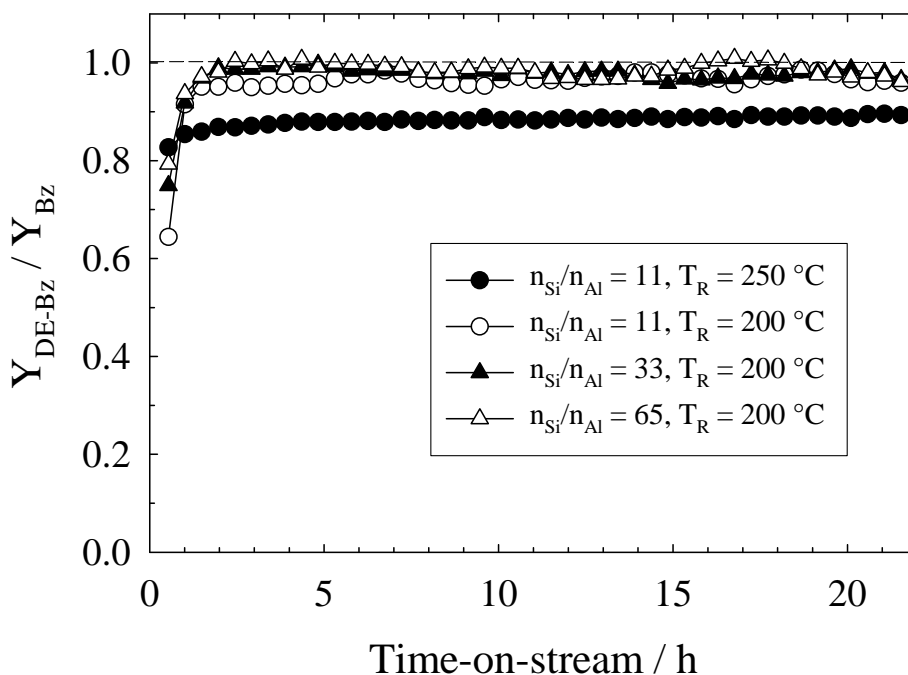


Fig. 99. Yield ratios of the diethylbenzene-to-benzene in ethylbenzene disproportionation over H-SSZ-35 with different  $n_{\text{Si}}/n_{\text{Al}}$  ratios at  $T_{\text{R}} = 200$  °C and 250 °C,  $W_{\text{cat}}/F_{\text{E-Bz}} = 290$  g·h/mol and  $W_{\text{cat}} = 290$  mg.

The time-on-stream behaviour of the yield ratios of DE-Bz and Bz are depicted in Fig. 99. The values at the stationary state are summarized in Table 34. The ratios observed with all samples tested at  $T_{\text{R}} = 200$  °C amount to ca. 0.97, except that for the sample with  $n_{\text{Si}}/n_{\text{Al}} = 11$  tested at  $T_{\text{R}} = 250$  °C which shows a yield ratio of only ca. 0.89. The values at the lower reaction temperature are close to unity which indicates that zeolite SSZ-35 contains large

pores. With medium pore zeolites, e.g., ZSM-5, this value is usually around 0.75 [10]. In case of the sample with  $n_{\text{Si}}/n_{\text{Al}} = 11$  tested at  $T_{\text{R}} = 250$  °C with the yield ratio of ca. 0.89, it is assumed that part of the DE-Bz isomers may further disproportionate into E-Bz and TE-Bz isomers as TE-Bz isomers are observed in the product stream.

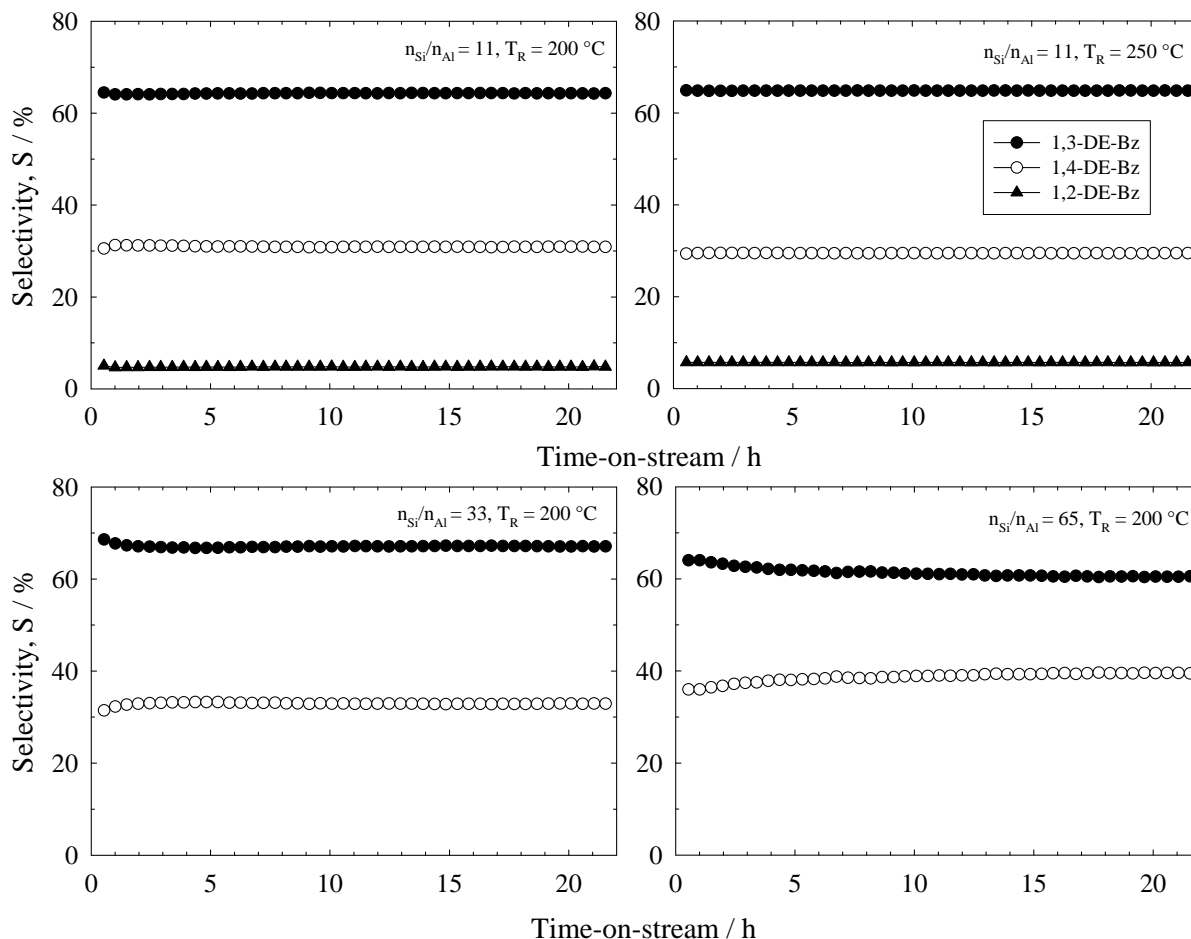


Fig. 100. Selectivities for the diethylbenzene isomers in ethylbenzene disproportionation over H-SSZ-35 with different  $n_{\text{Si}}/n_{\text{Al}}$  ratios at  $T_{\text{R}} = 200$  °C and  $250$  °C,  $W_{\text{cat}}/F_{\text{E-Bz}} = 290$  g·h/mol and  $W_{\text{cat}} = 290$  mg.

The distribution of the DE-Bz isomers are virtually independent of time-on-stream (cf. Fig. 100) which is characteristic for large pore materials. However, a slightly higher ratio of 1,4- to 1,3-DE-Bz (39:61) for the zeolite sample with  $n_{\text{Si}}/n_{\text{Al}} = 65$  as compared to the other samples is observed.

The common findings of three samples with different  $n_{Si}/n_{Al}$  ratios are (1) the presence of an induction period, (2) the independence of the DE-Bz isomers distribution on time-on-stream and (3) the yield ratio of DE-Bz and Bz close to unity at stationary state. This suggests that H-SSZ-35 contains large pores and/or intracrystalline cavities. This result is in-line with its crystallographic structure consisting of large section of 18-MR cages [74].

#### 4.5.3.2. H-MCM-71

The catalytic tests were carried out with different modified residence times, viz. 290 and 580 g·h/mol at  $T_R = 250$  °C over H-MCM-71 ( $n_{Si}/n_{Al} = 8$ ). Fig. 101 illustrates the conversion profiles of E-Bz. Both conversion profiles show a similar behaviour with a more pronounced deactivation of the sample tested at the higher modified residence time. With  $W_{cat}/F_{E-Bz} = 580$  g·h/mol, the conversion starts at 1.5 % at 0.5 h time-on-stream and ends at 0.2 % after 22 h. With  $W_{cat}/F_{E-Bz} = 290$  g·h/mol, the conversion declines from 0.6 to 0.2 %. This behaviour is tentatively ascribed to the pseudo-unidimensional channel system (the 10-MR channels are only connected by 8-MR channels) of MCM-71, where none of the molecules involved in this reaction can enter the 8-MR channels with their narrow pore diameter (0.47 x 0.36 nm). Once the unidimensional 10-MR pores are blocked (either by deposits at the pore mouths or inside the pores), it is no longer accessible for diffusing molecules and, hence, faster deactivation compared to zeolites with two- or multidimensional pore systems (e.g., ZSM-5) occurs [10]. A similar time-on-stream behaviour was also found for other 10-MR zeolites with unidimensional and pseudo unidimensional pores, viz. H-ZSM-22, H-ZSM-48, H-ZSM-35 and H-FER [10].

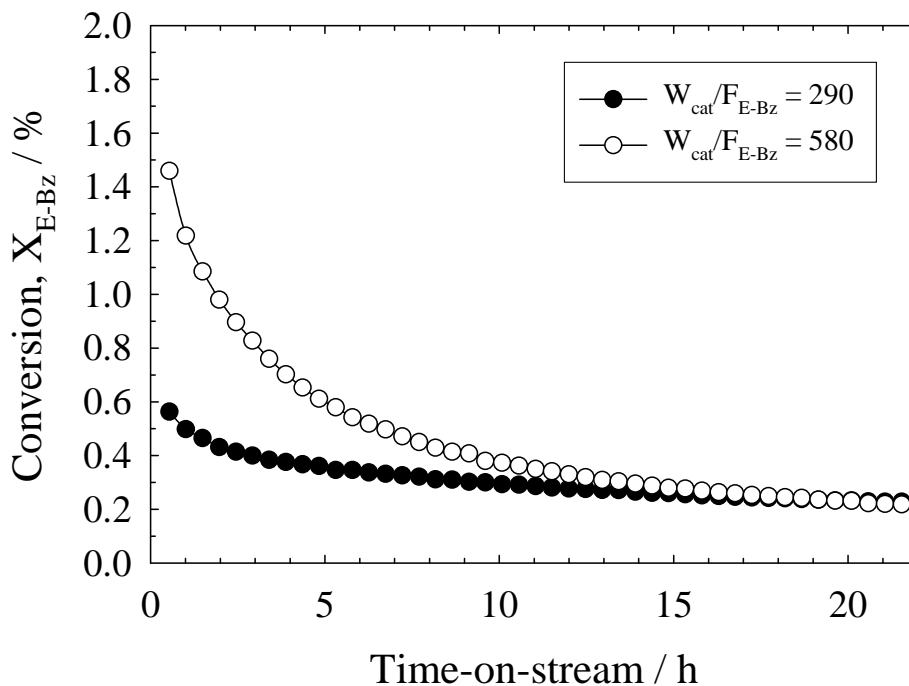


Fig. 101. Conversion profiles for ethylbenzene disproportionation over H-MCM-71 for different modified residence times of  $W_{cat}/F_{E-Bz} = 290$  and  $580$  g·h/mol,  $T_R = 250$  °C and  $W_{cat} = 290$  mg.

For both modified residence times, the products contain only Bz, 1,3- and 1,4-DE-Bz isomers and the yields in dependence of time-on-stream are presented in Fig. 102. The distribution of DE-Bz isomers exhibits a para-selective behaviour as can be seen from Fig. 103. With the term “para-selectivity”, the phenomenon is described where the reaction gives more than twice of the thermodynamic equilibrium amount of the para-isomer in the product [143] (see the comparative values in Table 35). Besides, the DE-Bz isomer distributions on H-MCM-71 are substantially different from those obtained over large pore zeolites, e.g., Y (ca. 62 % meta-, ca. 33 % para- and ca. 5 % ortho-isomer) [10]. At  $W_{cat}/F_{E-Bz} = 290$  and  $580$ , the distributions after 22 h show 40 % meta-, 60 % para-isomer and 37 % meta-, 63 % para-isomer, respectively. The para-isomer is small enough to enter the 10-MR channels of zeolite MCM-71 whereas the formation of the meta-isomer with its larger size tends to be suppressed by the channel size.

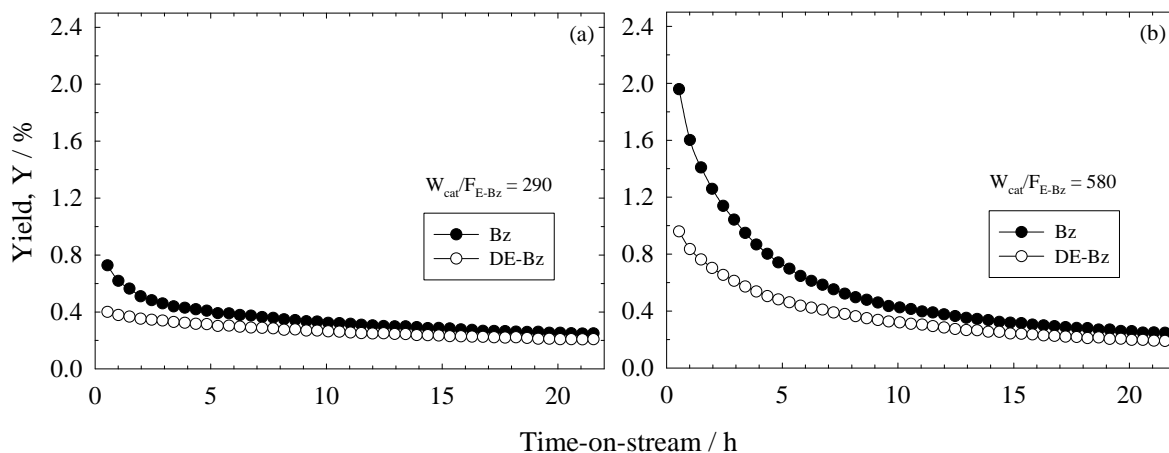


Fig. 102. Product yields in ethylbenzene disproportionation over H-MCM-71 at (a)  $W_{cat}/F_{E-Bz} = 290$  and (b)  $W_{cat}/F_{E-Bz} = 580$  g·h/mol,  $T_R = 250$  °C and  $W_{cat} = 290$  mg.

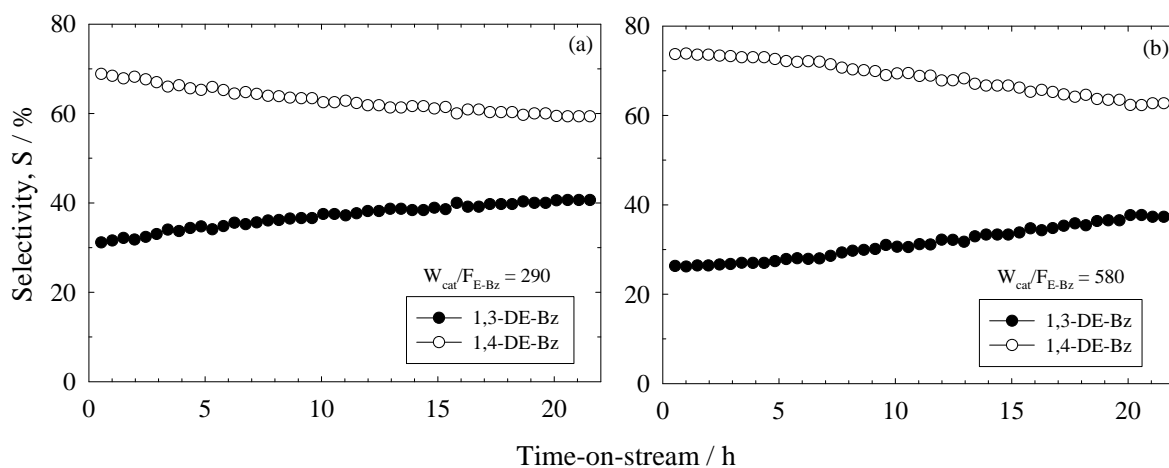


Fig. 103. Selectivities for the diethylbenzene isomers in ethylbenzene disproportionation over H-MCM-71 with (a)  $W_{cat}/F_{E-Bz} = 290$  and (b)  $W_{cat}/F_{E-Bz} = 580$  g·h/mol,  $T_R = 250$  °C and  $W_{cat} = 290$  mg.

Table 35. Distribution of diethylbenzene isomers in ethylbenzene disproportionation over H-MCM-71 at different modified residence times and for thermodynamic equilibrium (Eq.).

Modified residence time (g·h·mol <sup>-1</sup> )	S <sub>1,3-DE-Bz</sub> (%)		S <sub>1,4-DE-Bz</sub> (%)		S <sub>1,2-DE-Bz</sub> (%)	
	Test	Eq.	Test	Eq.	Test	Eq.
290	40	53.3	60	30.9	0	15.8
540	37	53.3	63	30.9	0	15.8

The yield ratios of DE-Bz and Bz under stationary state conditions gives values of ca. 0.84 and ca. 0.77 at  $W_{\text{cat}}/F_{\text{E-Bz}} = 290$  and 580 g·h/mol, respectively, and the corresponding time-on-stream profiles are shown in Fig. 104. In general, these yield ratios fall in the typical range of medium pore zeolite.

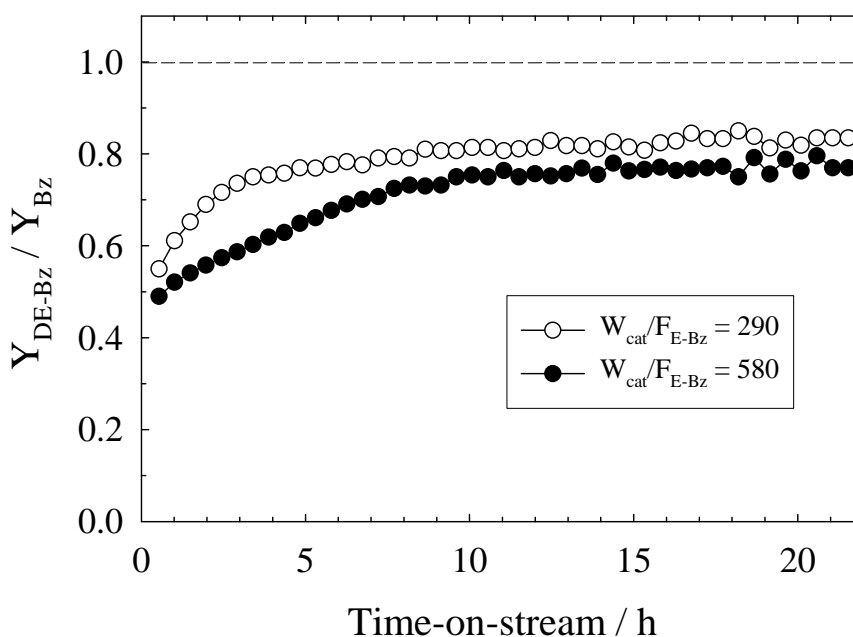


Fig. 104. Yield ratios of diethylbenzene-to-benzene in ethylbenzene disproportionation over H-MCM-71 at  $W_{\text{cat}}/F_{\text{E-Bz}} = 290$  and 580 g·h/mol,  $T_{\text{R}} = 250$  °C and  $W_{\text{cat}} = 290$  mg.

Hence, H-MCM-71 exhibits the typical features of a medium pore zeolite in ethylbenzene disproportionation because (1) there is no induction period, (2) the deactivation is pronounced, (3) a large product, viz. TE-Bz isomer is absent, (4) the ratio of yields of DE-Bz and Bz is low, viz.  $Y_{\text{DE-Bz}}/Y_{\text{Bz}} \leq 0.84$  and (5) para-selective behaviour in the distribution of DE-Bz isomers is observed. The result from the test reaction are in agreement with its determined structure containing 10-MR channels (ca. 0.65 x 0.43 nm) intersecting with 8-MR channels (ca. 0.47 x 0.36 nm) [80].

## 4.6. *n*-Decane hydroconversion as test reaction

*n*-Decane hydroconversion was selected as another test reaction to characterize the pore width and pore architecture of the bifunctional zeolites prepared in this work according to eight criteria [11, 12] already discussed in chap. 2.4.2.1. The advantage of applying a bifunctional reaction is that the deposition of coke on the catalysts is virtually absent [12]. Therefore, this test reaction allows to compare the catalysts under non-deactivating conditions and to obtain steady-state catalytic data. Five criteria, which are derived from the isomerized and hydrocracked products of *n*-decane (viz. 2.4.2.), were selected to characterize the prepared bifunctional zeolites.

All bifunctional samples were prepared via the same method and with the same amount of noble metal, viz. wt.-% palladium contained in the catalysts. The catalytic tests were performed at atmospheric pressure and the reaction conditions were kept constant at  $p_{\text{H}_2} \approx 101.3 \text{ kPa}$ ,  $\dot{n}_{\text{H}_2} / \dot{n}_{n\text{-De}} \approx 100$ ,  $W_{\text{cat}}/F_{n\text{-De}} = 400 \text{ g}\cdot\text{h}/\text{mol}$  and  $W_{\text{cat}} \approx 400 \text{ mg}$ . Two additional bifunctional catalysts, viz. 0.27Pd/HY (modified from NaY,  $n_{\text{Si}}/n_{\text{Al}} = 2.5$ , Degussa) and 0.27Pd/HZSM-5 (modified from H-ZSM-5 (SH-27),  $n_{\text{Si}}/n_{\text{Al}} = 27$ , Süd-Chemie), were tested for comparison.

### 4.6.1. Zeolites based on 14-membered ring pore openings

#### 4.6.1.1. 0.27Pd/HUTD-1

Conversion ( $X_{n\text{-De}}$ ) and yields of isomers ( $Y_{\text{iso.}}$ ) and of hydrocracked ( $Y_{\text{cr.}}$ ) products of *n*-decane in dependence of the reaction temperature over the bifunctional sample of UTD-1 (0.27Pd/HUTD-1) are presented in Fig. 105. The conversion starts at ca. 170 °C and is complete at ca. 300 °C. With increasing conversion, the yield of isomers passes through a maximum at ca. 24 % (at 232 °C), while hydrocracking is observed as a consecutive reaction

starting at ca. 13 % conversion. These are typical profiles of *n*-alkane conversion over bifunctional catalyst in the presence of H<sub>2</sub>, showing skeletal isomerization and hydrocracking (as a consecutive reaction) as the only types of reaction take place [113, 117, 119].

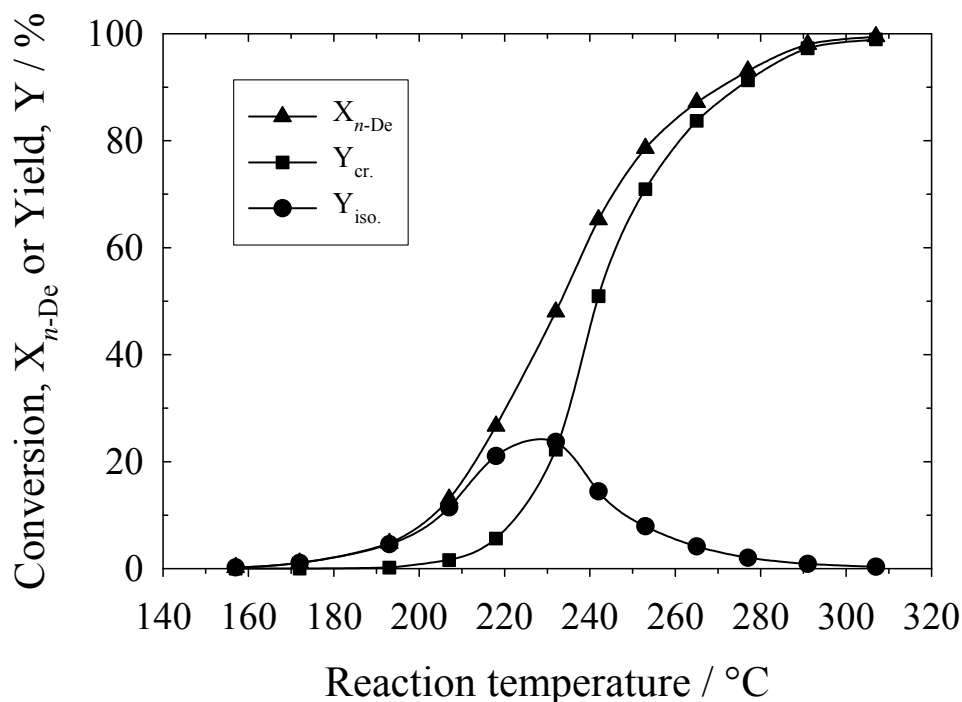


Fig. 105. Conversion and yields of isomers and of hydrocracked products of *n*-decane versus the reaction temperature over 0.27Pd/HUTD-1 ( $n_{Si}/n_{Al} = 28$ ).

Mono-, di- and tribranched isomers are formed over this catalyst and their selectivities are shown in Fig. 106a. The monobranched isomers appear initially in the product at low conversion and are first converted to dibranched isomers and then further to tribranched isomers (in a small amount) with increasing conversion. At low conversion, the predominating species among the monobranched isomers are methylnonanes and among the dibranched isomers are dimethyloctanes. The overall formed products in the fraction of monobranched isomers are comprised of methylnonanes, ethyloctanes and propylheptane whereas the dibranched ones are dimethyloctanes and ethylmethylheptanes.

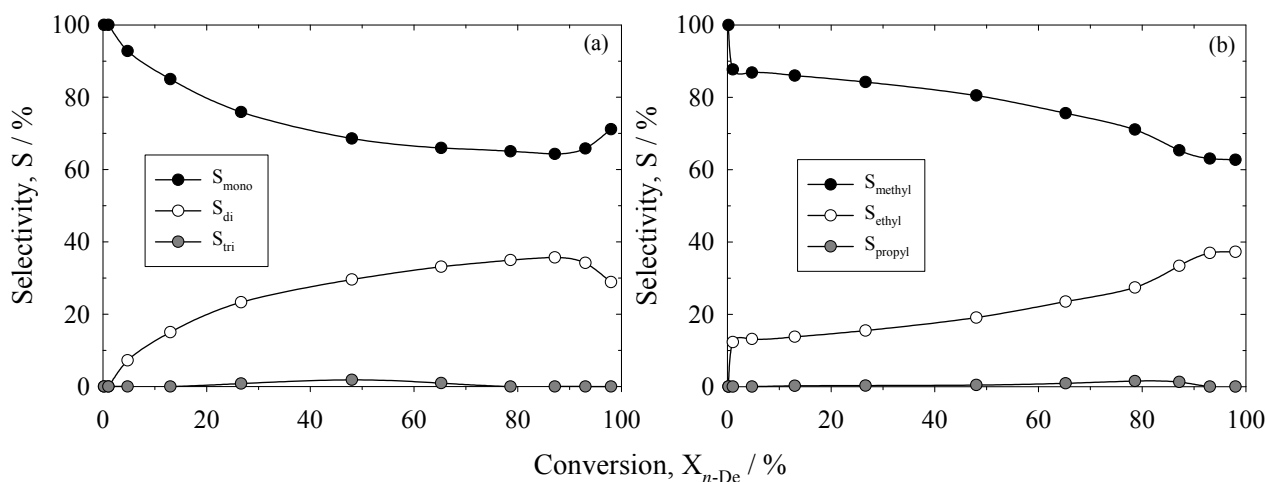


Fig. 106. Selectivities of branched isomers over 0.27Pd/HUTD-1 ( $n_{\text{Si}}/n_{\text{Al}} = 28$ ): (a) for mono-, di- and tribranched isomers and (b) for methyl-, ethyl- and propylbranched isomers.

The selectivity to monobranched isomers gradually decreases from 100 % to ca. 64 % with increasing conversion up to ca. 90 %. While the selectivity to dibranched isomers increases up to a maximum of ca. 36 %. Tribranched isomers occur in a small amount with a maximum selectivity of ca. 1.8 % at ca. 50 % conversion before declining again. The decrease in the selectivity of tribranched isomers after  $X_{n\text{-De}} \approx 50$  % and of dibranched isomers after  $X_{n\text{-De}} \approx 90$  % are ascribed to the occurrence of hydrocracking via  $\beta$ -scission according to the type A- and B-route, respectively [114]. It can be seen that the tribranched isomers are more favourable to be cracked at lower conversion than the dibranched ones.

The first criterion to characterize the pore structure involves the degree of branching of the isomerization products from *n*-decane, quantified as the ratio of mono- to dibranched isomers at the maximum isomer yield. A value of 2.3 is obtained for 0.27Pd/HUTD-1 which is typical for zeolites with large (12-MR) pores ( $< 2.85$  falls in the range of large pore zeolite) [11]. The presence of bulky tribranched isomers also supports this conclusion.

Looking deeper into the distribution of different species among the monobranched isomers as shown in Fig. 106b, methylbranched isomers occur initially at low conversion and are

converted to ethylbranched ones via alkyl-shift rearrangement with increasing conversion. The only possible monobranched isomer (4-propylheptane) is found only in small amounts of 1.5 % at ca. 80 % conversion. The formation of 4-propylheptane is supposed to occur via alkyl-shift from 4-ethyloctane.

The second criterion is based on the relative amounts of ethyl- to methylbranched isomers at ca. 5 % isomer yield. Ethyloctanes have larger kinetic diameters than methylnonanes. Therefore, not only the diffusion of these molecules but also their rate of formation is most probably sterically hindered in smaller pores, e.g., in medium pore (10-MR) channels [11]. A value of 13:87 is obtained for the ratio of ethyl- to methylbranched isomers which ranks UTD-1 as a large pore zeolite (>4:96 falls in the range of large pore zeolite) [11].

The third criterion is the selectivity ratio of 2- to 5-methylnonanes formed at ca. 5 % isomer yield. This ratio is known as the modified constraint index,  $CI^*$  [11]. In large pore zeolites, e.g., zeolite Y, a kinetic limitation for the formation of 2-methylnonane has been observed at low conversion (i.e., in the absence of secondary isomerization), which has been explained by a branching mechanism via PCP (protonated cyclopropanes) structures [117]. The  $CI^*$  has been demonstrated to be a measure for the effective pore size of the zeolite [11]: It increases with decreasing effective pore width. The  $CI^*$  value measured for 0.27Pd/HUTD-1 is 1.7, which is typical result for large pore zeolites [11, 112].

The fourth criterion is the selectivity for the formation of 4-propylheptane among the monobranched isomers at ca. 75 % conversion. 4-Propylheptane is the isomer with the largest kinetic diameter which can be formed from *n*-decane [12]. For 0.27Pd/HUTD-1, a value of 1.5 % at ca. 80 % conversion is obtained, which is comparable to a value of 1.1 % obtained from the Y-type zeolite in our reference and to 1.7 % from ref. [12]. The presence of this

bulkiest isomer suggests that UTD-1 is a large pore zeolite. And this is indeed in accordance with its crystallographic structure.

Fig. 107 shows the distribution of hydrocracked products in terms of carbon numbers at a moderate yield of cracking. It can be seen that  $C_1$  and  $C_2$  as well as  $C_8$  and  $C_9$  hydrocarbons are absent. This suggests that the noble metal is well dispersed in the pores, resulting in the absence of hydrogenolysis on the metal phase. The hydrocracked products exhibit high fractions of branched isomers of  $C_4$  to  $C_6$  (with the maximum at  $C_5$ ). This indicates that hydrocracking starts from highly branched intermediates and this reflects the large space available in the channels of the extra-large pore zeolite UTD-1. The slightly asymmetric distribution of the hydrocracked products indicates a minor contribution of secondary cracking which could proceed via cracking of  $C_6$  to  $C_3+C_3$  and cracking of  $C_7$  to  $C_3+C_4$  fragments.

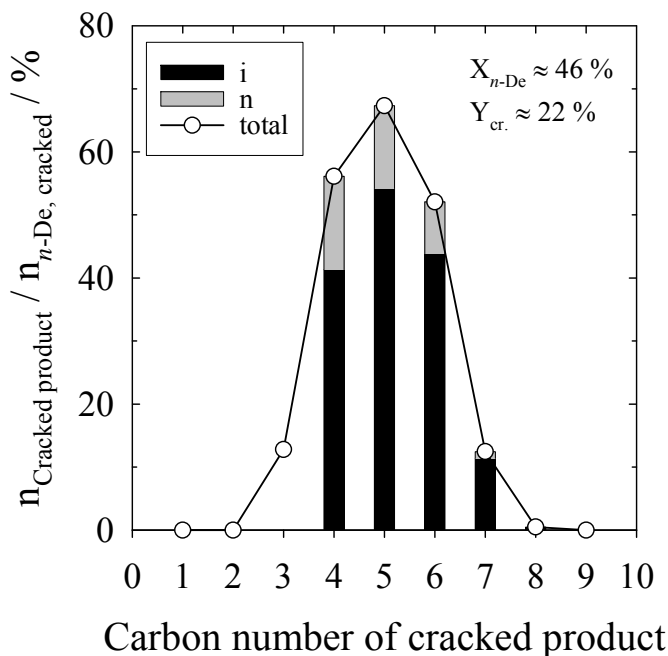


Fig. 107. Distribution of hydrocracked products from *n*-decane over 0.27Pd/HUTD-1 at  $X_{n\text{-De}} \approx 46 \%$  and  $Y_{\text{cr.}} \approx 22 \%$  (i: iso-alkanes; n: *n*-alkanes).

The yield of isopentane observed from *n*-decane hydrocracking at  $Y_{cr.} \approx 35\%$  is applied as the fifth criterion. This parameter, expressed as the molar amount of isopentane formed per 100 moles of *n*-decane hydrocracked, is sensitive to structural effects and insensitive to secondary cracking reactions [11]. In large pores or intracrystalline cavities, a high degree of branching is possible via PCP isomerization before a cracking step via central  $\beta$ -scission occurs. Consequently, a large amount of isopentane will be able to desorb from the active sites and appear in the product [121]. A value of ca. 54% at  $Y_{cr.} \approx 22\%$  is obtained and classifies UTD-1 as a large pore zeolite ( $\geq 37$  is reported for large pore zeolites) [11].

The results of all five criteria are in agreement with the crystallographic structure of zeolite UTD-1 which contains unidimensional extra-large pores (ca.  $1 \times 0.75$  nm) [35].

#### 4.6.1.2. 0.27Pd/HSSZ-53

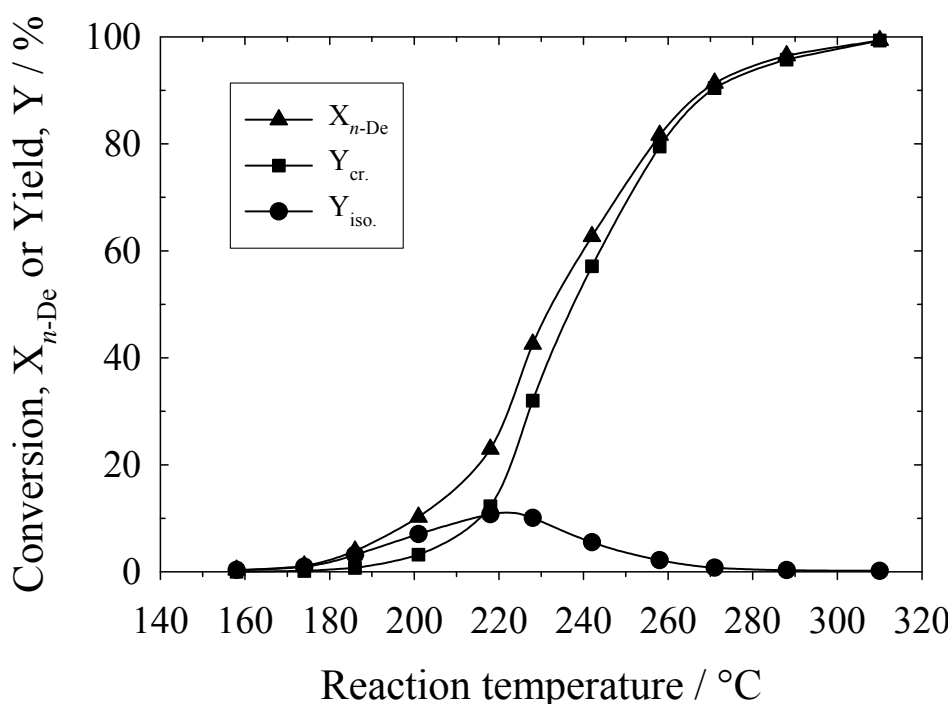


Fig. 108. Conversion and yields of isomers and of hydrocracked products of *n*-decane versus the reaction temperature over 0.27Pd/HSSZ-53 ( $n_{Si}/n_{Al} = 55$ ).

Fig. 108 shows the conversion of *n*-decane and the yields of isomers and of hydrocracked products in dependence of the reaction temperature over 0.27Pd/HSSZ-53. The conversion starts at ca. 170 °C and is complete at ca. 300 °C which is quite similar to the results observed over 0.27Pd/HUTD-1. For conversions up to ca. 5 %, isomerization is the sole reaction. With increasing conversion, hydrocracking occurs as a consecutive reaction in a way typical for bifunctional conversion of long-chain alkanes. A maximum isomer yield of ca. 11 % at a reaction temperature of 220 °C is obtained.

The product selectivities in terms of mono-, di- and tribranched isomers are depicted in Fig. 109a: Mono- and dibranched isomers, but not tribranched ones, could be detected even at high conversion. The monobranched isomers (predominantly consisting of methylnonanes and ethyloctanes) mainly appear in the product at low conversion and are converted to dibranched isomers with increasing conversion. The fast drop of the selectivity of dibranched isomers at higher than 80 % conversion indicates that cracking via  $\beta$ -scission of type B occurs [114], hence, a large amount of hydrocracked products is formed. In contrast with the result from 0.27Pd/HUTD-1 (cf. Fig. 106a), the tribranched isomers are not detected from 0.27Pd/HSSZ-53.

According to the first criterion, the ratio of mono- and dibranched isomers at maximum isomerization of ca. 3.1 is obtained which lies in the typical range of 8-MR zeolites with cage, e.g., chabasite-type zeolites (8-MR: 0.37 x 0.36 nm, cage: 1.10 x 0.65 nm) [11]. However, from the crystallographic structure of SSZ-53 it is known to be a unidimensional extra-large pore zeolite with window diameters of ca. 0.85 x 0.65 nm [46]. This unexpected result could be explained via a fast hydrocracking of the dibranched isomers according to a more favourable pathway of  $\beta$ -scission (type B) comparing to the monobranched isomers (type C) [114].

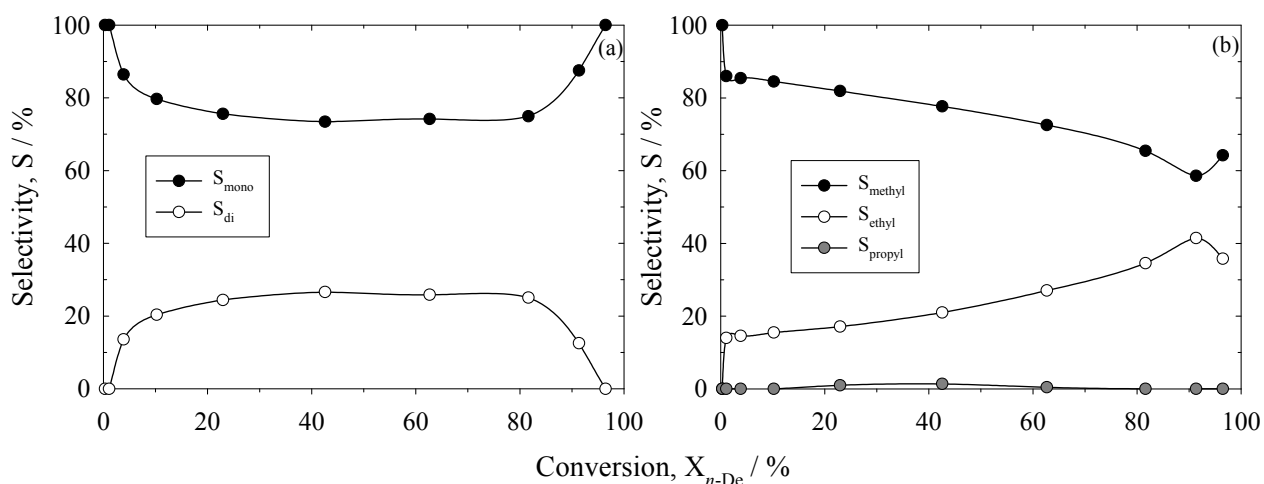


Fig. 109. Selectivities of branched isomers over 0.27Pd/HSSZ-53 ( $n_{Si}/n_{Al} = 55$ ): (a) for mono- and dibranched isomers and (b) for methyl-, ethyl- and propylbranched isomers.

The selectivities of monobranched isomers in terms of methyl-, ethyl- and propylbranched isomers are depicted in Fig. 109b. Again, methylbranched isomers appear initially as the major product and they are then further converted to ethylbranched isomers and then to small amounts of 4-propylheptane with increasing conversion. The second criterion derived from these selectivities, viz. the relative amounts of ethyl- to methylbranched isomers at ca. 5 % isomer yield shows a value of 15:85 which classifies SSZ-53 zeolite as a large pore material [11]. In the third criterion, a ratio of 1.7 between 2- and 5-methylnonane (or CI\*) at ca. 5 % isomer yield indicates the presence of large pores in SSZ-53 [11]. According to Fig. 109b, 4-propylheptane as the bulkiest product isomer is found with a maximum selectivity of ca. 1.3 % at ca. 45 % conversion. Therefore, the fourth criterion again confirms that SSZ-53 is a large pore zeolite [12].

The distribution of hydrocracked products in terms of carbon number distribution at  $Y_{cr} \approx 33$  % is shown in Fig. 110.  $C_1$  and  $C_2$  as well as  $C_8$  and  $C_9$  are absent, which suggests that *n*-decane hydrogenolysis on the metal phase is virtually absent. The distribution of the hydrocracked products exhibits a maximum for  $C_5$  fragments and the major fragments are

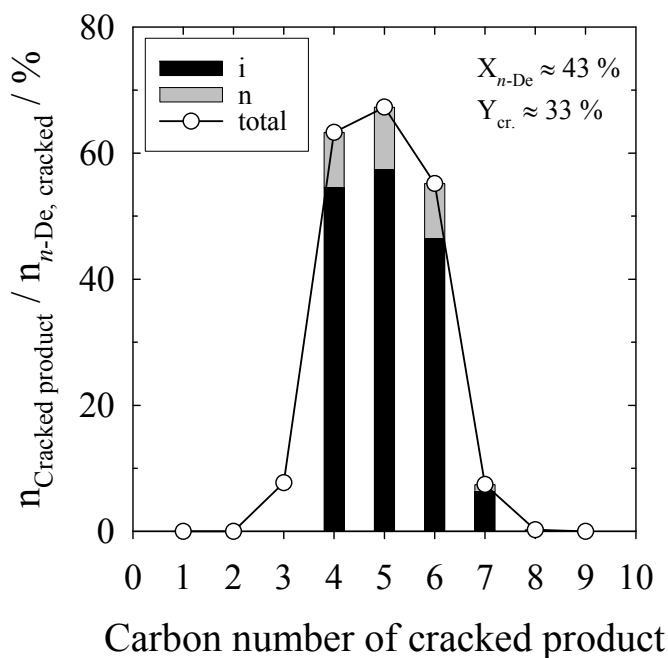


Fig. 110. Distribution of hydrocracked products from *n*-decane over 0.27Pd/HSSZ-53 at  $X_{n\text{-De}} \approx 43\%$  and  $Y_{\text{cr.}} \approx 33\%$  (i: iso-alkanes; n: *n*-alkanes).

branched  $C_4$  to  $C_6$ . A minor asymmetrical product distribution suggests the occurrence of secondary cracking. In the fifth criterion, the yield of isopentane per 100 moles of cracked *n*-decane is as high as 58 which indicates that SSZ-53 possesses much space around the catalytic sites and ranks it as a large pore material [11].

At least four of the five criteria are in agreement with the crystallographic structure of SSZ-53 zeolite which contains unidimensional extra-large pores (ca. 0.85 x 0.65 nm) [46].

#### 4.6.2. Zeolites based on 12-membered ring pore openings

##### 4.6.2.1. 0.27Pd/HMCM-68

The catalytic behaviour of 0.27Pd/HMCM-68 in *n*-decane hydroconversion is depicted in Fig. 111. The conversion starts already at temperatures as low as ca. 80 °C and is complete at ca. 200 °C. Hence, 0.27Pd/HMCM-68 is a very active catalyst in *n*-decane hydroconversion as compared to the bifunctional UTD-1 and SSZ-53 samples. This excellent catalytic activity

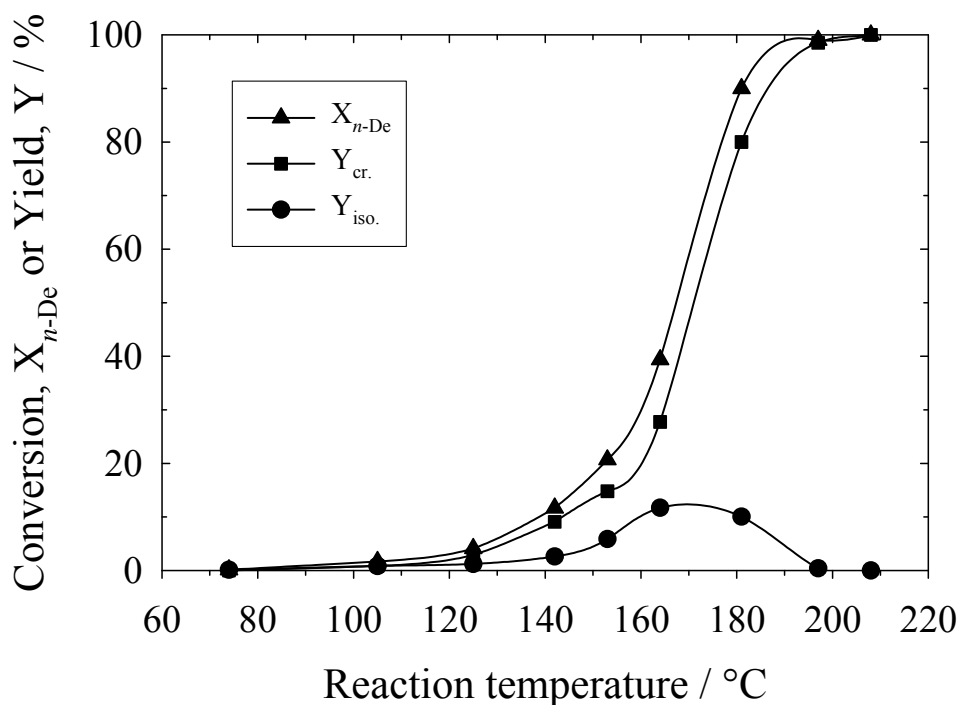


Fig. 111. Conversion and yields of isomers and of hydrocracked products of *n*-decane versus the reaction temperature over 0.27Pd/HMCM-68 ( $n_{Si}/n_{Al} = 9$ ).

is most probably due to the presence of numerous strong acid sites as already revealed by pyridine TPD (cf. chap. 4.2.2.) and by the disproportionation of ethylbenzene (cf. chap. 4.5.2.1.). It can be seen that the essential features are quite similar to the behaviour of the previously reported bifunctional zeolites. With increasing conversion, the isomerization passes through a maximum at ca. 12 % at a reaction temperature of 165 °C. Hydrocracking starts almost simultaneously with isomerization as typical way for bifunctional conversion of long-chain alkanes. The fast cracking could probably result from a large amount of strong acid sites in the catalyst.

The selectivities for mono-, di- and tribranched isomers are shown in Fig. 112a. At low conversions ( $X_{n-De} \approx 2\%$ ), both mono- (methylnonanes) and dibranched (dimethyloctanes) isomers are predominantly formed as products with ca. 40-50 % selectivity. The high selectivity of dibranched isomers at low conversion is ascribed to a fast formation of

dibranched isomers from the monobranched ones. The monobranched isomers start with selectivities of ca. 40 % and increase to ca. 65 % at ca. 20 % conversion before slowly declining at higher conversion with the overall product consisting of methylnonanes and ethyloctanes (Fig. 112b). In the opposite way, dibranched isomers start at ca. 50 %, declining to 35 % before slightly increasing again. Tribranched isomers are found with selectivities below 10 %.

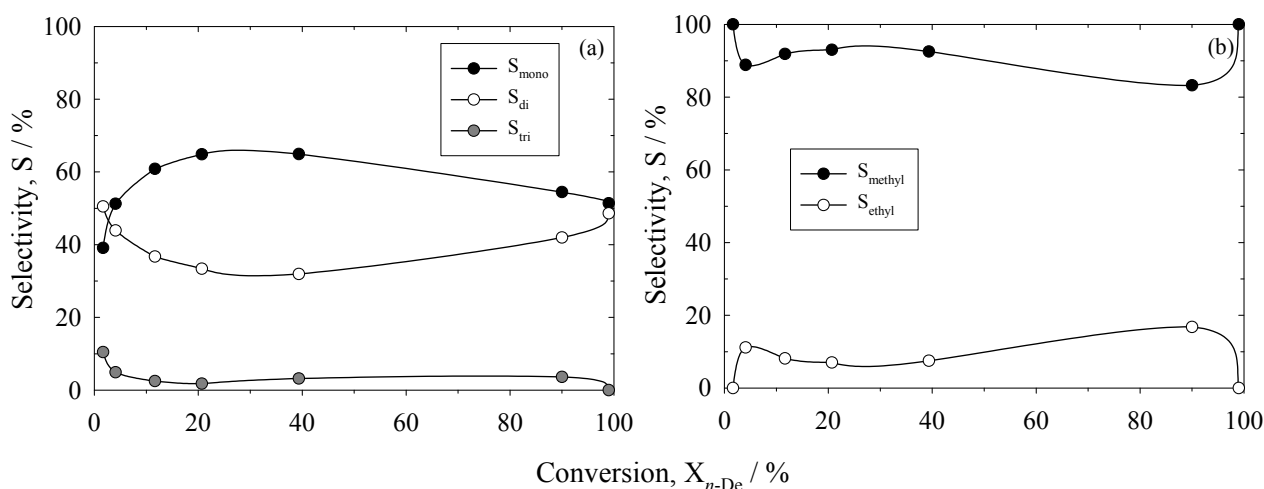


Fig. 112. Selectivities of branched isomers over 0.27Pd/HMCM-68 ( $n_{Si}/n_{Al} = 9$ ): (a) for mono-, di- and tribranched isomers and (b) for methyl- and ethylbranched isomers.

The ratio of mono- to dibranched isomers obtained at maximum isomerization is 2 at ca. 40 % conversion. Therefore, the first criterion suggests that MCM-68 contains large pores [11]. Moreover, the presence of tribranched isomers confirms this assumption. The second criterion based on the ratio of ethyl- to methylbranched isomers formed at ca. 5 % isomer yield reports a value of 11:88 (Fig. 112b), which also ranks MCM-68 as a large pore material [11]. The third criterion (the modified constraint index,  $CI^*$ ) yields a value of 2.9 and classifies MCM-68 as zeolite with 10-MR pore windows or with 8-MR pores with cage structure [11]. The relatively high value of  $CI^*$  most probably corresponds to the small channels also present in the zeolite and these smaller sized pores could suppress the

formation of 5-methylnonane. The fourth criterion, based on the presence of 4-propylheptane, shows there is no formation of this bulky isomer as also found on the medium pore 0.27Pd/HZSM-5 as reference (cf. Table 37). The suppression of this molecule is probably due to the small 10-MR channels (0.55 x 0.51 nm) and the 12-MR (0.68 x 0.65 nm) windows of MCM-68 [63].

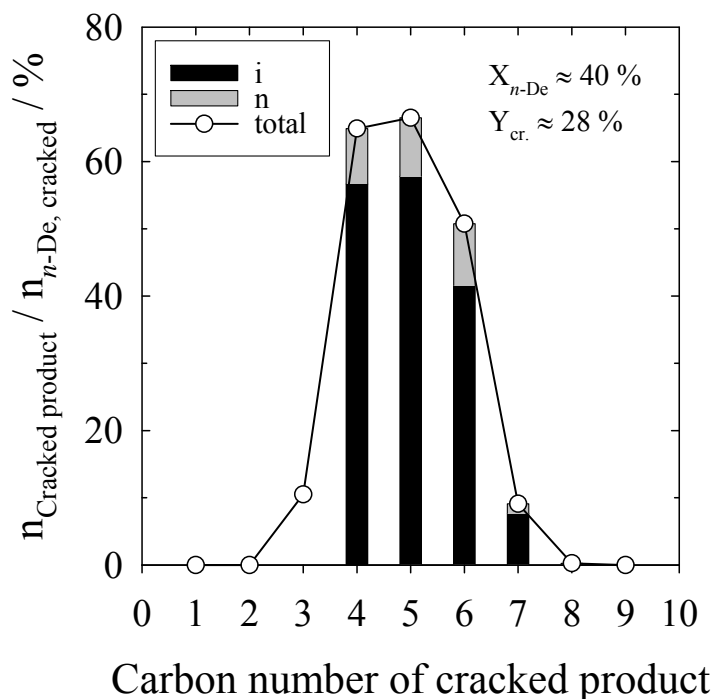


Fig. 113. Distribution of hydrocracked products from *n*-decane over 0.27Pd/HMCM-68 at  $X_{n-De} \approx 40\%$  and  $Y_{cr.} \approx 28\%$  (i: iso-alkanes; n: *n*-alkanes).

Fig. 113 shows the distribution of hydrocracked products in terms of the carbon number. The typical distribution with the maximum centered around C<sub>5</sub> is obtained and the preferred cracked products are branched C<sub>4</sub> to C<sub>6</sub> alkanes. The complete absence of C<sub>1</sub> and C<sub>2</sub> as well as C<sub>8</sub> and C<sub>9</sub> fragments indicates the absence of hydrogenolysis. Even at low conversion, the asymmetrical distribution with a surplus in the formation of light fragments of C<sub>3</sub> and C<sub>4</sub> is found, which indicates the presence of secondary hydrocracking. This observation is in agreement with the presence of large amounts of strong acid sites in MCM-68. From the fifth

criterion, the molar amount of isopentane formed per 100 moles of *n*-decane hydrocracked of 58 at  $Y_{cr.} \approx 28\%$ , suggests MCM-68 is a large pore zeolite [11].

#### 4.6.3. Zeolites based on 10-membered ring pore openings

##### 4.6.3.1. 0.27Pd/HSSZ-35

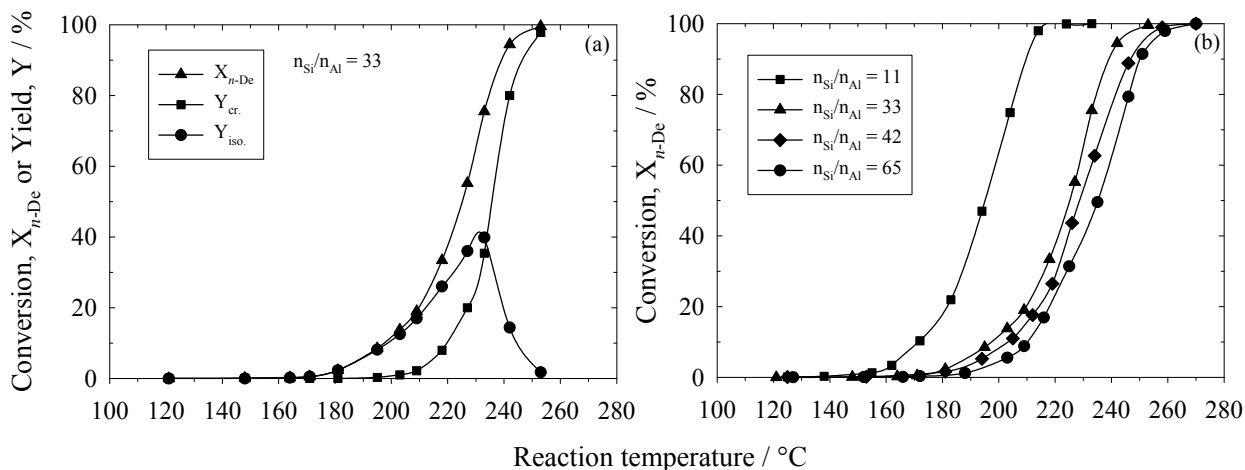


Fig. 114. (a) Conversion and yields of isomers and of hydrocracked products of *n*-decane versus the reaction temperature over 0.27Pd/HSSZ-35 ( $n_{Si}/n_{Al} = 33$ ) and (b) conversion of *n*-decane over 0.27Pd/HSSZ-35 samples with different  $n_{Si}/n_{Al}$  ratios.

The 0.27Pd/HSSZ-35 samples with different  $n_{Si}/n_{Al}$  ratios of 11, 33, 42 and 65 have been tested in order to assess the influence of the aluminium content on the activity and selectivity of the catalysts. The conversion and yields of isomers and of hydrocracked products in dependence of the reaction temperature over 0.27Pd/HSSZ-35 ( $n_{Si}/n_{Al} = 33$ ) as representative are shown in Fig. 114a. As usually observed, isomerization is the sole reaction at low conversion up to ca. 20 % conversion, then hydrocracking starts as consecutive reaction. A maximum isomerization yield of ca. 40 % at a reaction temperature of ca. 230 °C is achieved. High selectivities for branched isodecanes are observed on all samples of 0.27Pd/HSSZ-35 with maximum isomer yields around 40–52 % at reaction temperatures between 205–250 °C. The changes of *n*-decane conversion with reaction temperature for all SSZ-35 catalysts are

presented in Fig. 114b. As expected, the catalytic activity increases with decreasing the  $n_{\text{Si}}/n_{\text{Al}}$  ratios or increasing the aluminium content, respectively. The results of the maximum isomer yields and the conversions at a fixed reaction temperature of 215 °C for all samples are summarized in Table 36.

Table 36. Results of the maximum isomer yields and corresponding reaction temperatures as well as the conversions at reaction temperature of 215 °C over 0.27Pd/SSZ-35 catalysts.

Sample	$Y_{\text{iso.,max}}$ (%)	T at $Y_{\text{iso.,max}}$ (°C)	X at $T_{\text{R}} = 215$ °C (%)
0.27Pd/HSSZ-35 ( $n_{\text{Si}}/n_{\text{Al}} = 11$ )	52	204	100
0.27Pd/HSSZ-35 ( $n_{\text{Si}}/n_{\text{Al}} = 33$ )	40	230	30
0.27Pd/HSSZ-35 ( $n_{\text{Si}}/n_{\text{Al}} = 42$ )	45	234	22
0.27Pd/HSSZ-35 ( $n_{\text{Si}}/n_{\text{Al}} = 65$ )	44	247	16

The products obtained at low conversions are essentially monobranched (mainly monomethylnonanes) and dibranched (dimethyloctanes) isomers. Bulkier isomers with ethyl groups, e.g., ethyloctanes and ethylmethylheptanes appear at higher conversion, viz. for  $X_{n\text{-De}} > 13$  %. Tribranched isomers are formed at even higher conversions from  $X_{n\text{-De}} > 50$  %. 4-Propylheptane as the bulkiest isomer is present only in small amounts of ca. 0.15 % among the monobranched isomers at ca. 75 % conversion and only for 0.27Pd/HSSZ-35 with the lowest  $n_{\text{Si}}/n_{\text{Al}}$  ratio = 11 (smallest crystallite size). In total, with all 0.27Pd/HSSZ-35 catalysts, the formation of bulky tribranched, ethylbranched and propylbranched isomers are sterically suppressed as compared to the products obtained over the 0.27Pd/HY reference sample. To investigate the change of product distribution with conversion for all SSZ-35 samples, the product selectivities in terms of mono-, di- and tribranched isomers are presented in Fig. 115 and the distributions of the monobranched isomers are shown in Fig. 116.

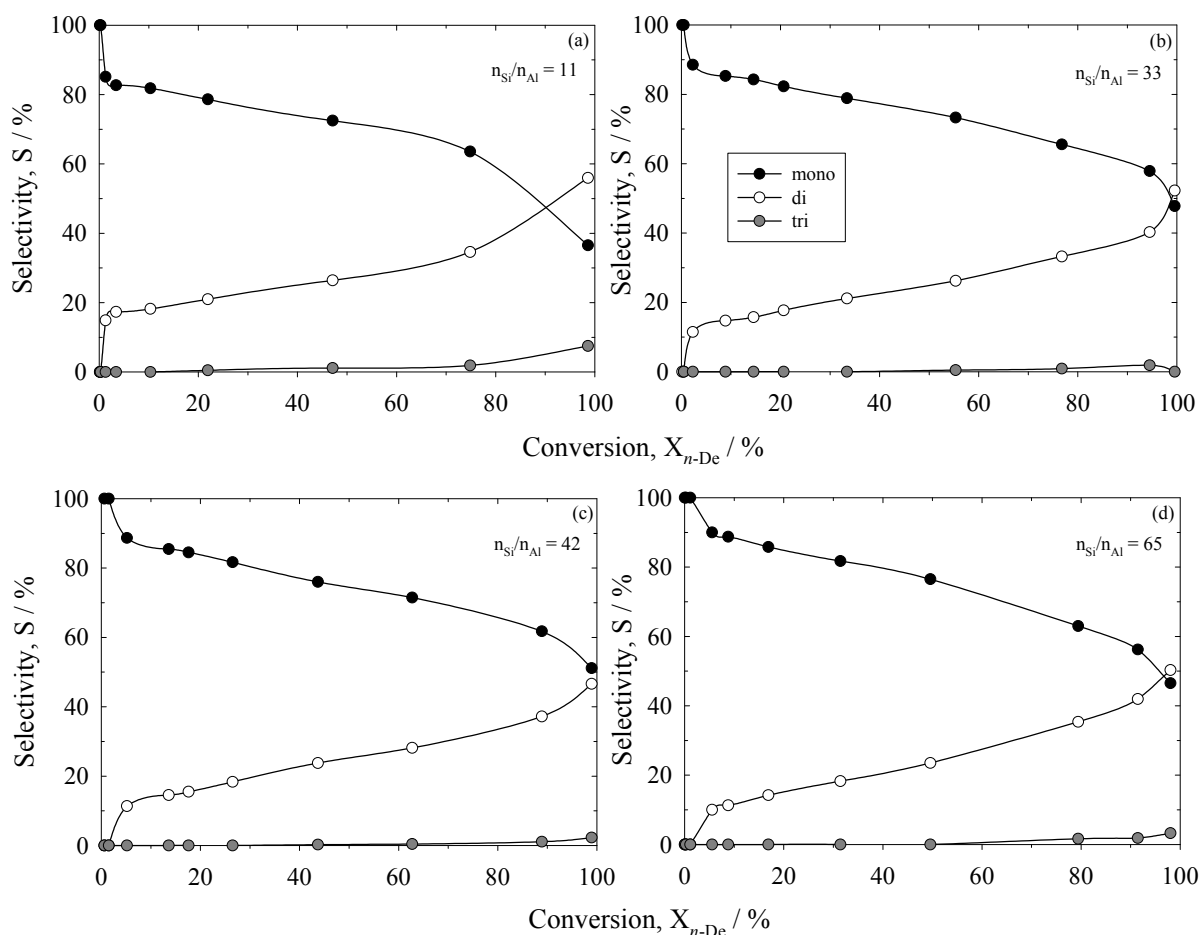


Fig. 115. Selectivities for mono-, di- and tribranched isomers over 0.27Pd/HSSZ-35 with different  $n_{Si}/n_{Al}$  ratios: (a) 11 (b) 33 (c) 42 and (d) 65.

The distributions of the hydrocracked products from *n*-decane at  $Y_{cr.} \approx 18-35$  % over 0.27Pd/HSSZ-35 with different  $n_{Si}/n_{Al}$  ratios are presented in Fig. 117. All catalysts show branched  $C_4$  to  $C_6$  hydrocarbons as major hydrocracked products. As usual, the maximum appears for the pentanes. This suggests the presence of large volumes available around the catalytically active sites where the branching takes place before cracking via  $\beta$ -scission starts. A symmetrical molar distribution of the hydrocracked products is found only for 0.27Pd/HSSZ-35 with  $n_{Si}/n_{Al} = 42$  and 65 (with high  $n_{Si}/n_{Al}$  ratios) as shown in Figs. 117c and d. These samples behave like “ideal bifunctional” catalysts as it has also been found for 0.27Pd/HY. Asymmetrical distributions of the hydrocracked products due to the occurrence

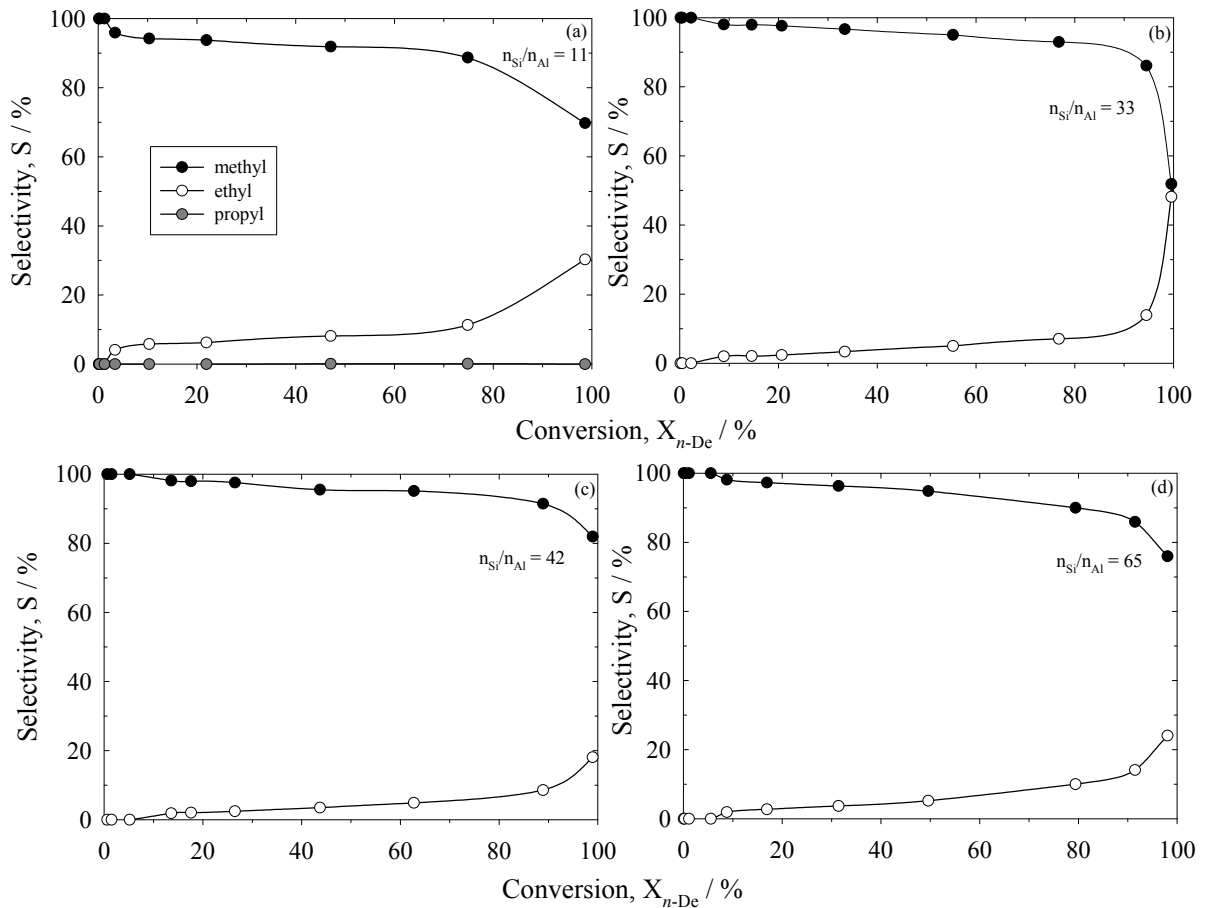


Fig. 116. Selectivities for methyl-, ethyl- and propyl-branched isomers over 0.27Pd/HSSZ-35 with different  $n_{Si}/n_{Al}$  ratios: (a) 11 (b) 33 (c) 42 and (d) 65.

of secondary cracking are detected over SSZ-35 samples with  $n_{Si}/n_{Al} = 11$  and 33 (with low  $n_{Si}/n_{Al}$  ratios) as shown in Figs. 117a and b. Again, the absence of  $C_1/C_2$  and  $C_8/C_9$  suggests that hydrogenolysis is absent.

The known five independent criteria are used to characterize the pore architecture of zeolite SSZ-35. Moreover, data obtained with 0.27Pd/HY are included for comparison. The results are summarized in Table 37. The obtained values around 2 for the first criterion are typical for zeolites with large (12-MR) pores or zeolites with large intracrystalline cavities (12-MR + cage) [11].

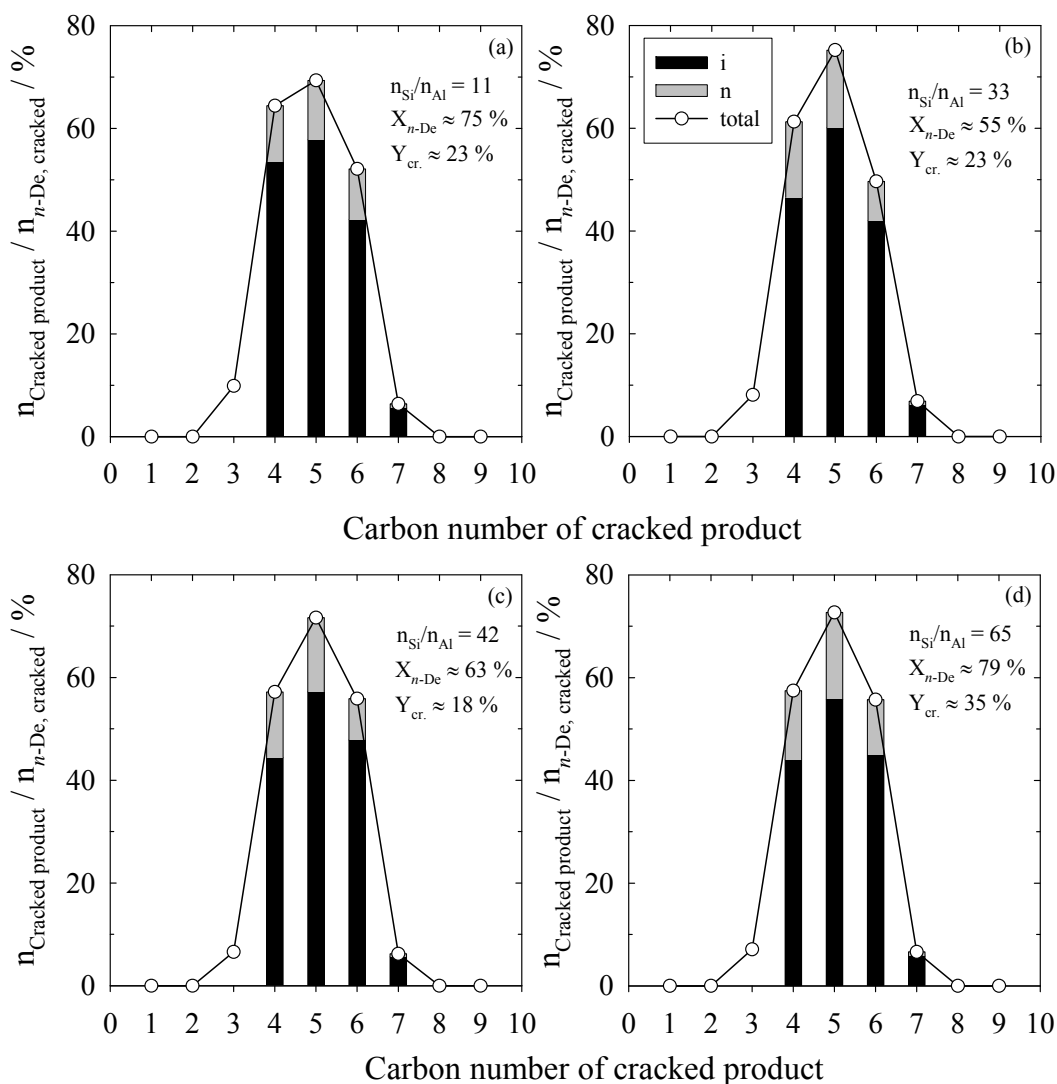


Fig. 117. Distribution of hydrocracked products from *n*-decane over 0.27Pd/HSSZ-35 with different  $n_{Si}/n_{Al}$  ratios: (a) 11 (b) 33 (c) 42 and (d) 65 at  $X_{n-De} \approx 55$ -80 % and  $Y_{cr.} \approx 18$ -35 % (i: iso-alkanes; n: *n*-alkanes).

It can be seen from Fig. 116 and Table 37 that the amounts of ethyloctanes formed (as compared to the methylnonanes, viz. criterion 2) are relatively small or even zero (for the SSZ-35 samples with higher  $n_{Si}/n_{Al}$  ratios). Ethyloctanes have larger kinetic diameters than methylnonanes. Therefore, not only their diffusion but also their rate of formation is most probably sterically hindered in the small pores. This suggests that 10-MR windows are present in the pore system of this zeolite [11, 121], which is in-line with its crystallographic structure containing 10-MR windows (0.61 x 0.55 nm) with large cages (1.25 x 0.9 nm) [74].

The formation of small amounts of ethyloctanes over the samples with higher Al-contents is tentatively attributed to a stronger contribution of the external (and, hence, non-selective) surface of these samples due to the small crystallite size.

The  $CI^*$  values (third criterion) measured for all SSZ-35 samples range from 1.2-2.3 (cf. Table 37), which fall in the range for large pore materials [11, 112]. The low values of  $CI^*$  suggest that SSZ-35 also possesses larger intracrystalline voids. The Y-type zeolite used for reference also shows a typical value of  $CI^* = 1.7$ .

Among the different SSZ-35 catalysts, 4-propylheptane could only be found in the isomer product obtained on 0.27Pd/HSSZ-35 with  $n_{Si}/n_{Al} = 11$  (smallest crystallite size) with a selectivity of 0.15 % (for comparison, 1.1 % were formed over 0.27Pd/HY, fourth criterion). 4-Propylheptane is most probably formed at the external surface of the small crystallites of 0.27Pd/HSSZ-35 with  $n_{Si}/n_{Al} = 11$ . It is absent over the other SSZ-35 samples. This clearly reflects the presence of the 10-MR pore windows in the structure of SSZ-35, which restricts the size of the molecules to escape from the large intracrystalline voids.

Over the 0.27Pd/HSSZ-35 samples, from 56-60 moles of isopentane per 100 moles of *n*-decane hydrocracked (at  $Y_{cr.} \approx 20-35$  %) are formed (cf. Table 37, fifth criterion). These values fall within the range of very large pore zeolites (like zeolite Y, cf. Table 37) and reflect the large intracrystalline voids available around the active sites [11].

The results from hydroconversion of *n*-decane for the selected five criteria for all tested catalysts are summarized in Table 37.

Table 37. Results of the hydroconversion of *n*-decane over bifunctional zeolites.

Criterion	Sample				
	UTD-1 ( $n_{Si}/n_{Al} = 28$ )	CIT-5 ( $n_{Si}/n_{Al} = 116$ )	SSZ-53 ( $n_{Si}/n_{Al} = 55$ )	MCM-68 ( $n_{Si}/n_{Al} = 9$ )	ZSM-5 ( $n_{Si}/n_{Al} = 27$ )
1. Ratio of mono- to dibranched isomers at the maximum isomer yield	2.3	2.8	3.1	2	7.3
2. Ethyloctanes to methylnonanes formed at ca. 5 % isomer yield	13:87	13:87	15:85	11:89	6:94
3. Ratio of 2- to 5-methylnonanes formed at ca. 5 % isomer yield	1.7	2.1	1.7	2.9	5
4. Selectivity to 4-propylheptane among the monobranched isomers at ca. 75 % conversion	1.5	0.8	1.3**	0	0
5. Yield of isopentane in the hydrocracked product at ca. 30 % yield of hydrocracked product ( $Y_{cr.}$ )	54	50	58	58	11

Criterion	Sample				
	SSZ-35 ( $n_{Si}/n_{Al} = 11$ )	SSZ-35 ( $n_{Si}/n_{Al} = 33$ )	SSZ-35 ( $n_{Si}/n_{Al} = 42$ )	SSZ-35 ( $n_{Si}/n_{Al} = 65$ )	Y ( $n_{Si}/n_{Al} = 2.5$ )
1. Ratio of mono- to dibranched isomers at the maximum isomer yield	1.9	2	2.6	1.5	2 (1.86*)
2. Ethyloctanes to methylnonanes formed at ca. 5 % isomer yield	6:94	2:98	0	0	13:87 (11:89*)
3. Ratio of 2- to 5-methylnonanes formed at ca. 5 % isomer yield	2.3	1.6	1.2	1.4	1.7 (1.25*)
4. Selectivity to 4-propylheptane among the monobranched isomers at ca. 75 % conversion	0.15	0	0	0	1.1 (1.7*)
5. Yield of isopentane in the hydrocracked product at ca. 30 % yield of hydrocracked product ( $Y_{cr.}$ )	58	60	58	56	54 (54*)

\* The values are taken from refs. [11, 12].

\*\* The value is taken at the maximum of 4-propylheptane yield at ca. 45 % conversion.

#### 4.7. Competitive hydrogenation of olefins for probing the location of noble metals in zeolites

In order to obtain reliable information on the zeolite pore architecture from *n*-decane hydroconversion, at least a substantial part of the active acid sites or noble metal should be located inside the pores. To probe the latter requirement, competitive hydrogenation of a very slim and a bulky alkene, viz. 1-hexene and 2,4,4-trimethyl-1-pentene, was applied in the assumption that the slim alkene is able to enter the 10-MR pores but the bulky alkene can not. A comparison of the yields of alkanes from the corresponding alkenes suggests either the noble metal is located mainly inside the zeolite pores or at the external surface. Only the 10-MR zeolites SSZ-35 were tested because its 10-MR pores might be too small for the noble metal complex to enter the intracrystalline voids during the preparation of the bifunctional catalyst. This could lead to the result that most of the metal is located on the outer surface of the zeolite. The palladium-containing catalyst 0.27Pd/SSZ-35 used in this test was prepared via a similar procedure as described in chap. 3.1.3.1 and 3.2 with  $n_{\text{Si}}/n_{\text{Al}}$  ratios in the gel = 36 and  $\infty$ , respectively. The obtained  $n_{\text{Si}}/n_{\text{Al}}$  in the final product as revealed by AAS analysis is 37 and >600, respectively.

Fig. 118 shows the time-on-stream behaviour for the yields of the two hydrogenation products, viz. *n*-hexane and 2,2,4-trimethylpentane in the competitive hydrogenation reaction over the Al-containing catalyst 0.27Pd/SSZ-35 ( $n_{\text{Si}}/n_{\text{Al}} = 37$ ) at  $T_{\text{R}} = 75$  and  $100$  °C. At  $T_{\text{R}} = 75$  °C, it was found that there is almost exclusively hydrogenation of 1-hexene ( $Y_{n\text{-hexane}} > 98$  %). Whereas 2,4,4-trimethyl-1-pentene is converted only in a small amount ( $Y_{2,2,4\text{-trimethylpentane}} = 9$  % at 32 min of time-on-stream). At  $T_{\text{R}} = 100$  °C,  $Y_{n\text{-hexane}}$  slightly declines from 99.8 % at 32 min to 95 % after 209 min. While  $Y_{2,2,4\text{-trimethylpentane}}$  starts at 31 % at 32 min and decreases to ca. 10 % after 209 min. It is found that 0.27Pd/SSZ-35 ( $n_{\text{Si}}/n_{\text{Al}} = 37$ ) is highly selective

for the conversion of 1-hexene in the presence of 2,4,4-trimethyl-1-pentene. This indicates that the noble metal is almost exclusively located inside the intracrystalline voids of this zeolite.

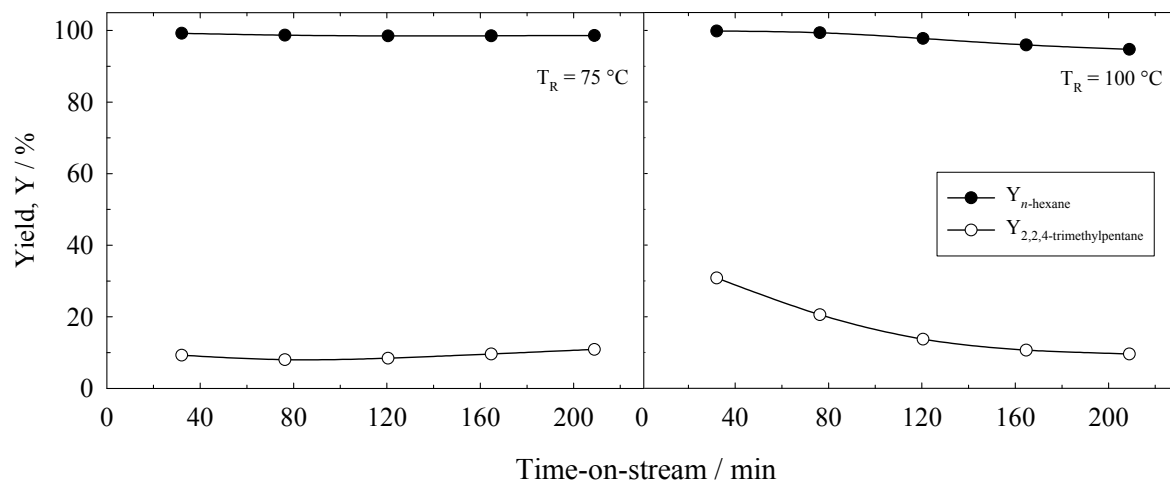


Fig. 118. Yield of *n*-hexane and 2,2,4-trimethylpentane in the competitive hydrogenation of 1-hexene and 2,4,4-trimethyl-1-pentene over 0.27Pd/SSZ-35 ( $n_{\text{Si}}/n_{\text{Al}} = 37$ ) at  $T_{\text{R}} = 75$  °C and 100 °C,  $W_{\text{cat}}/F_{\text{alkenes}} = 10$  g·h/mol and  $W_{\text{cat}} = 200$  mg.

With the other catalyst, 0.27Pd/SSZ-35 ( $n_{\text{Si}}/n_{\text{Al}} > 600$ ) which is essentially Al-free, it is observed that 1-hexene is almost completely hydrogenated to *n*-hexane at both reaction temperatures as shown in Fig. 119. At  $T_{\text{R}} = 75$  °C, 2,4,4-trimethyl-1-pentene is converted moderately to 2,2,4-trimethylpentane with 40-45 %, while at  $T_{\text{R}} = 100$  °C, this bulky reactant is completely converted to 2,2,4-trimethylpentane directly after starting the reaction and declines to 61 % after 209 min. This behaviour suggests that the noble metal is located both, outside and inside the zeolite pores, or exclusively at the external surface. This could be explained by the influence of the aluminium content. The essentially Al-free sample contains insufficient aluminium sites in the intracrystalline void space for an ion-exchange with the noble metal complexes. Hence, at the end of the procedure, the major part of the metal

complex still remains in the solution. After removing the water using a rotary evaporator, the metal complexes could be deposited on the surface of the zeolite crystallites.

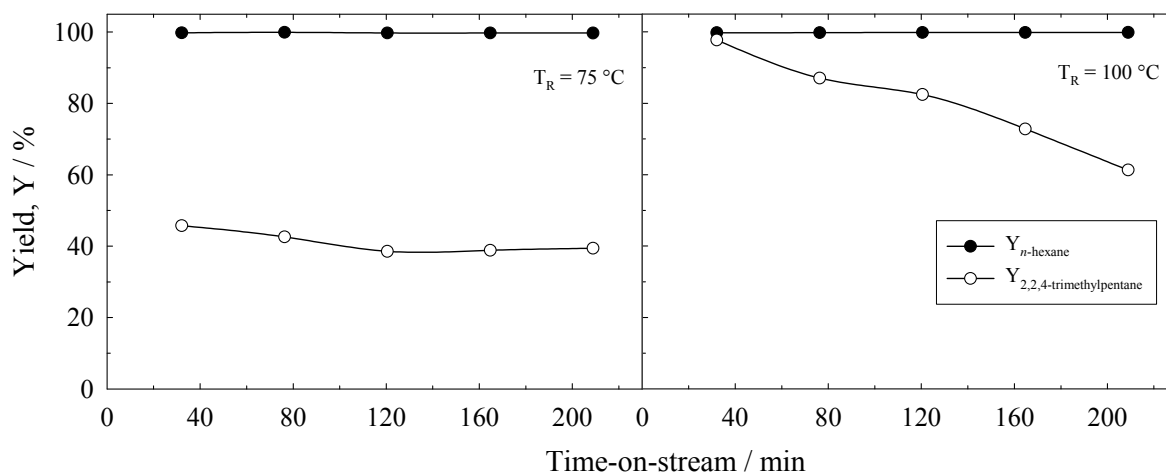


Fig. 119. Yield of *n*-hexane and 2,2,4-trimethylpentane in the competitive hydrogenation of 1-hexene and 2,4,4-trimethyl-1-pentene over 0.27Pd/SSZ-35 ( $n_{\text{Si}}/n_{\text{Al}} > 600$ ) at  $T_{\text{R}} = 75$  °C and 100 °C,  $W_{\text{cat}}/F_{\text{alkenes}} = 10$  g·h/mol and  $W_{\text{cat}} = 200$  mg.

Nevertheless, the results of this catalytic test with the Al-containing sample 0.27Pd/SSZ-35 ( $n_{\text{Si}}/n_{\text{Al}} = 37$ ) suggest that in this material (which was used in the *n*-decane conversion), the noble metal is located mainly inside the pores and intracrystalline voids.

## 5. Conclusions

The synthesis of the following zeolite molecular sieves was successfully performed in the frame of this thesis (they are ranked according to the largest window size in the respective structure):

- 14-MR pores: UTD-1, CIT-5, SSZ-53 and IM-12
- 12-MR pores: ITQ-21 and MCM-68
- 10-MR pores: SSZ-35 and MCM-71

All of them were obtained as pure phase (except zeolite MCM-71 with a minor impurity phase that is hardly to avoid and also present in samples shown in the patent literature). The synthesis conditions are very critical with respect to the formation of the zeolite with a given structure. In this work, the recommended synthesis recipes are included. Among the 14-MR zeolites, the aluminosilicate form of UTD-1 ( $n_{\text{Si}}/n_{\text{Al}} = 28$ ), CIT-5 ( $n_{\text{Si}}/n_{\text{Al}} = 116$ ) and SSZ-53 ( $n_{\text{Si}}/n_{\text{Al}} = 55$ ) have specific pore volumes of 0.18, 0.12 and 0.19 cm<sup>3</sup>/g, respectively. They exhibit promising catalytic properties with high thermal stability and they possess strong Brønsted-acid sites, especially UTD-1 and SSZ-53 (thermal stability:  $\geq 800$  °C). The Brønsted-acid activity as observed by the disproportionation of ethylbenzene with the protonated aluminium-treated forms can be ranked in the order: H-SSZ-53 > H-UTD-1 > H-CIT-5. The germanosilicate IM-12, with its structure containing 14-MR channels (0.95 x 0.71 nm) intersecting with 12-MR channels (0.85 x 0.55 nm), possesses a high specific pore volume of 0.21 cm<sup>3</sup>/g. Although it is thermally stable upon calcination, its calcined form is unstable toward moisture. To explore the pore size and architecture of the prepared zeolites, the acid catalyzed disproportionation of ethylbenzene (using criteria suggested by Weitkamp et al. [10]) and the bifunctional hydroconversion of *n*-decane (selected five criteria suggested by Martens et al. [11, 12]) were applied as test reactions. Both reactions suggest that UTD-1

and SSZ-53 zeolites possess an open pore system (12-MR or larger pore systems): For ethylbenzene disproportionation, this is indicated by the stationary state distribution of the DE-Bz isomers, the yield ratios of DE-Bz to Bz close to unity and the formation of large TE-Bz isomers as products. By contrast, an induction period was found only for zeolite H-SSZ-53 at low reaction temperatures. For H-CIT-5, although TE-Bz isomers are not observed in the product, the other criteria are fulfilled to classify H-CIT-5 as large pore material. The *n*-decane hydroconversion, applied for 0.27Pd/HUTD-1 and 0.27Pd/HSSZ-53, suggests the presence of large pores in both zeolites. All possible product isomers ranging from small size to the bulkiest ones are present in the isomer mixture, very similar to a product mixture obtained in Y-type zeolites. One exception is the lack of tribranched isomers on 0.27Pd/HSSZ-53 catalyst. The low values of  $CI^*$  of 1.7 and the high isopentane yields of ca. 54 % and 58 % in the hydrocracked product suggest the presence of large pores in the structures of UTD-1 and SSZ-53. The catalytic results are in complete agreement with their crystallographic structures containing unidimensional 14-MR pores (UTD-1: ca. 1 x 0.75 nm, SSZ-53: ca. 0.85 x 0.65 nm, CIT-5: ca. 0.73 nm).

The 12-MR pore zeolites ITQ-21 and MCM-68 are relatively new large pore materials. ITQ-21, a germanoaluminosilicate zeolite with three-dimensional spherical cages (ca. 1.18 nm) accessible via six 12-MR windows (ca. 0.74 nm), can be synthesized with  $n_{Si}/n_{Al}$  ratios between 27 and >200 and specific pore volumes between 0.13-0.19 cm<sup>3</sup>/g. It is not possible to prepare the protonated form via the standard ammonium ion-exchange route without structural damage. However, its calcined form already contains a sufficiently large amount of acid sites.

The aluminosilicate zeolite MCM-68 ( $n_{Si}/n_{Al} = 9$ ) possesses a high specific pore volume of 0.27 cm<sup>3</sup>/g and it is an extremely active catalyst in the disproportionation of ethylbenzene and in the *n*-decane hydroconversion. This is due to the presence of numerous strong Brønsted-

acid sites in its structure. Ethylbenzene disproportionation as catalytic test classifies MCM-68 as a large pore zeolite because of the independence of the DE-Bz isomer distribution on time-on-stream, almost equal yields of DE-Bz and Bz in the stationary state and the presence of bulky TE-Bz molecules in the product. In the hydroconversion of *n*-decane, the formation of ethyloctanes and a high isopentane yield of 58 % suggest that this material contains large pores. By contrast, a relatively high value for  $CI^*$  of 2.9 suggests the presence of medium pores in its structure. As a whole, the results from the catalytic tests are in-line with the crystallographic structure determined structure of MCM-68, viz. a three-dimensional pore system of 12-MR channels (ca. 0.68 x 0.65 nm) intersecting with two orthogonal undulating 10-MR channels (ca. 0.55 x 0.51 nm).

As 10-MR pore zeolites, SSZ-35 and MCM-71 were studied. Both are thermally stable up to 1000 °C. SSZ-35 can be synthesized in a broad range of  $n_{Si}/n_{Al}$  ratios between 11 and >500 and possesses a high pore volume of ca. 0.23 cm<sup>3</sup>/g. The size and shape of the zeolite crystallites depend on the  $n_{Si}/n_{Al}$  ratio. The smallest crystallite size is found with the lowest  $n_{Si}/n_{Al}$  ratio. This zeolite is interesting in terms of shape selectivity due to its unusual pore system consisting of unidimensional channels alternating between 10-MR windows (ca. 0.61 x 0.55 nm) and large 18-MR cages (ca. 1.25 x 0.9 nm). SSZ-35 contains both strong Brønsted- and strong Lewis-acid sites. The disproportionation of ethylbenzene classifies SSZ-35 as a large pore zeolite because of the presence of an induction period, the independence of the DE-Bz isomer distribution on time-on-stream and a yield ratio of DE-Bz to Bz close to unity. The difference in the  $n_{Si}/n_{Al}$  ratio of different H-SSZ-35 samples influences its product selectivities: The sample with the lowest  $n_{Si}/n_{Al}$  ratio (and, hence, the smallest crystallite size) produces the relatively bulky products 1,2-DE-Bz and TE-Bz isomers, while the catalysts with higher  $n_{Si}/n_{Al}$  ratios (and larger crystallites) do not give these products. The presence of these isomers with the former catalyst probably results from

the higher conversion or they are preferentially formed on the external surface area of the catalyst. In the hydroconversion of *n*-decane, the suppression of bulky product isomers, viz. ethyloctanes and propylheptane clearly suggests the presence of medium pore windows. This is in-line with the crystallographic structure of SSZ-35. Moreover, the low  $CI^*$  values of 1.2-2.3 and the yields of isopentane of 56-60 % suggest that SSZ-35 also possesses larger intracrystalline voids. Only the sample with the smallest crystallite size ( $n_{Si}/n_{Al} = 11$ ) produces the bulkiest product from *n*-decane, viz. 4-propylheptane, which probably is formed at the external surface area. In addition, it is observed that the catalytic activity increases with decreasing the  $n_{Si}/n_{Al}$  ratio (or increasing the Al-content).

Zeolite MCM-71 ( $n_{Si}/n_{Al} = 8$ ) is a relatively new medium pore zeolite. It can be synthesized using triethanolamine as template or even in the absence of it. It exhibits an extremely high thermal stability and possesses a specific pore volume of 0.16 cm<sup>3</sup>/g. Its medium pore topology with a high concentration of Brønsted-acid sites suggests MCM-71 to be useful in shape-selective acid catalyzed reactions. Moreover, its structure allows the separation of *n*-alkane mixtures with branched alkanes by selective adsorption. MCM-71 exhibits unique shape-selective properties in ethylbenzene disproportionation. The reaction parameters definitely classify MCM-71 as medium pore zeolite due to a pronounced deactivation, a low value of  $Y_{DE-Bz}/Y_{Bz} \approx 0.8$ , para-selective behaviour in the formation of DE-Bz isomers and the absence of bulky product molecules, viz. TE-Bz isomers. This is in good agreement with its reported structure consisting of 10-MR channels (ca. 0.65 x 0.43 nm) intersecting with sinusoidal 8-MR channels (ca. 0.47 x 0.36 nm).

An additional test, viz. the competitive hydrogenation of 1-hexene and 2,4,4-trimethyl-1-pentene was exploited as an analytical tool to probe the location of the noble metal on palladium-containing medium pore zeolites, i.e., 0.27Pd/SSZ-35 ( $n_{Si}/n_{Al} = 37$ ). It was found that this catalyst is highly selective for the hydrogenation of 1-hexene. This indicates that the

noble metal is almost exclusively located inside the intracrystalline void volume of this zeolite where it is available for shape-selective catalysis.

## 6. Appendices

### 6.1. Appendix A: List of symbols and indices

#### Symbols in latin letters

$a_i$	corrected values of area under the peak of component i corresponding to the molar amount from the gas chromatogram (-)
$A_i$	area under the peak of component i from the gas chromatogram (-)
$C$	gas chromatographic constant (-)
$f$	flame ionization detector factor (-)
$F_{E-Bz}$	molar flow of ethylbenzene at the reactor inlet ( $\text{mol}\cdot\text{h}^{-1}$ )
$K$	equilibrium constant (-)
$\dot{m}_i$	mass flow ( $\text{g}\cdot\text{h}^{-1}$ )
$M$	molecular weight ( $\text{g}\cdot\text{mol}^{-1}$ )
$\dot{n}$	molar flow ( $\text{mol}\cdot\text{h}^{-1}$ )
$n_{Si}/n_{Al}$	molar ratio of silicon to aluminium (-)
$P$	pressure (kPa)
$p$	partial pressure (kPa)
$R$	ideal gas constant ( $\text{J}\cdot\text{mol}^{-1}\cdot\text{K}^{-1}$ )
$S$	selectivity (-)
$S_{BET}$	specific surface area derived from BET measurements ( $\text{m}^2\cdot\text{g}^{-1}$ )
$T$ or $T_R$	temperature or reaction temperature ( $^{\circ}\text{C}$ )
$U$	extent of reaction (-)
$V_{\text{pore}}$	specific total pore volume ( $\text{cm}^3\cdot\text{g}^{-1}$ )
$V$	volumetric flow ( $\text{ml}\cdot\text{min}^{-1}$ )
$W$	weight (mg)

x	molar fraction (-)
X	conversion (-)
Y	yield (-)
Z	carbon number (-)

### Symbols in greek letters

$\Delta G_{f,T}^0$	change of standard Gibbs free enthalpy of formation at temperature T (J·mol <sup>-1</sup> )
$\Delta m/\Delta t$	differential weight loss (wt.-%·min <sup>-1</sup> )
$\theta$	angle of the incident X-ray beam (degree)
$\lambda$	wavelength of the incident X-ray beam (nm)
$\nu$	stoichiometric coefficient (-)
$\tau_{\text{mod}}$	modified residence time (g·h·mol <sup>-1</sup> )

### Indices

0	state at the inlet of the reactor
Bz	benzene
cat	catalyst
cr.	hydrocracked products
DE-Bz	diethylbenzene
di	dibranched isomers
E-Bz	ethylbenzene
eq	equilibrium
ethyl	ethylbranched isomers
i	compound i

iso.	isomer products
k	reactant
max	maximum
methyl	methylbranched isomers
mono	monobranched isomers
<i>n</i> -De	<i>n</i> -decane
propyl	propylbranched isomers
s	saturation
tri	tribranched isomers
TE-Bz	triethylbenzene

## 6.2. Appendix B: List of abbreviations

AAS	atomic absorption spectroscopy
a.u.	arbitrary units
BET	Brunauer-Emmett-Teller
Bz	benzene
CHN	carbon-hydrogen-nitrogen
CI	constraint index
CI*	modified constraint index
CIT-5	California Institute of Technology No. 5
Cp* <sub>2</sub> CoCl	bis(pentamethylcyclopentadienyl) cobalt(III) chloride
Cp* <sub>2</sub> CoOH	bis(pentamethylcyclopentadienyl) cobalt(III) hydroxide
Cp* <sub>2</sub> CoPF <sub>6</sub>	bis(pentamethylcyclopentadienyl) cobalt(III) hexafluorophosphate
D4R	double four ring
DE-Bz	diethylbenzene

---

DRIFT	diffuse reflectance Fourier transform infrared spectroscopy
DTA	differential thermal analysis
DTGS	deuterated triglycine sulfate
E-Bz	ethylbenzene
FCC	fluid catalytic cracking
FID	flame ionization detector
FT-IR	Fourier transform infrared spectroscopy
GC	gas chromatograph
i	iso-alkanes
I	intensity
IM-12	Institut Français du Pétrole and University of Mulhouse No. 12
IR	infrared
ITQ-21	Instituto de Tecnologia Quimica Valencia No. 21
IUPAC	International Union of Pure & Applied Chemistry
IZA	International Zeolite Association
MAS NMR	magic angle spinning nuclear magnetic resonance
MCM-68	Mobil Composition of Matter No. 68
MCM-71	Mobil Composition of Matter No. 71
<i>m</i> -DE-Bz	meta-diethylbenzene
MR or MRs	membered ring or membered rings
MS	mass spectroscopy
MSPTOH	(-)-N(16)-methylsparteinium hydroxide
MTG	methanol to gasoline
n	<i>n</i> -alkane
<i>n</i> -De	<i>n</i> -decane

---

<i>o</i> -DE-Bz	ortho-diethylbenzene
PCP	protonated cyclopropane
<i>p</i> -DE-Bz	para-diethylbenzene
PyH <sup>+</sup>	pyridinium ions
RT	room temperature
SBU	secondary building unit
SDA	structure-directing agent
SEM	scanning electron microscopy
SI	spaciousness index
SSZ-35	Socaf Synthetic Zeolite No. 35
SSZ-53	Socaf Synthetic Zeolite No. 53
STP	standard temperature and pressure
TCD	thermal conductivity detector
TE-Bz	triethylbenzene
TGA	thermogravimetric analysis
TPD	temperature-programmed desorption
TPR	temperature-programmed reduction
USY	ultrastable Y zeolite
UTD-1	University of Texas at Dallas No. 1
UV-Vis	ultraviolet-visible spectroscopy
XRD	X-ray diffraction
ZnSe	zinc selenide
ZSM-5	Zeolite Socony Mobil No. 5

## 7. References

- [1] D.W. Breck, *Zeolite Molecular Sieves: Structure, Chemistry and Use*, Wiley, New York, 1974.
- [2] G.A. Ozin, *Adv. Mater.* 4 (1992) 613.
- [3] P.B. Weisz and V.J. Frilette, *J. Phys. Chem.* 64 (1960) 382.
- [4] S.M. Csicsery, *Zeolites* 4 (1984) 202.
- [5] P.M.M. Blauwhoff, J.W. Gosselink, E.P. Kieffer, S.T. Sie, W.H.T. Stork, in: J. Weitkamp and L. Puppe (Eds.): *Catalysis and Zeolites Fundamentals and Applications*, Springer, Berlin, Heidelberg, 1999, p. 437.
- [6] Th.L.M. Maesen and B. Marcus, in: H. van Bekkum, E.M. Flanigen, P.A. Jacobs, J.C. Jansen (Eds.): *Introduction to Zeolite Science and Practice, Studies in Surface Science and Catalysis*, Vol. 137, Elsevier, Amsterdam, 2001, p. 3.
- [7] Website: <http://www.iza-structure.org> in the news.
- [8] V.J. Frilette, W.O. Haag, R.M. Lago, *J. Catal.* 67 (1981) 218.
- [9] J. Dewing, *J. Mol. Catal.* 27 (1984) 25.
- [10] J. Weitkamp, S. Ernst, P.A. Jacobs, H.G. Karge, *Erdöl und Kohle, Erdgas, Petrochem.* 39 (1986) 13.
- [11] J.A. Martens, M. Tielen, P.A. Jacobs, J. Weitkamp, *Zeolites* 4 (1984) 98.
- [12] J.A. Martens and P.A. Jacobs, *Zeolites* 6 (1986) 334.
- [13] J. Weitkamp, S. Ernst, R. Kumar, *Appl. Catal.* 27 (1986) 207.
- [14] A.F. Cronstedt, *Akad. Handl.*, Stockholm, 17 (1756) 120, translated by J. Schlenker and G.H. Köhl, in: R. von Ballmoos, J.B. Higgins, M.M.J. Treacy (Eds.), *Proceedings of the 9<sup>th</sup> International Zeolite Conference, Montreal, Canada, Vol. 1*, Butterworth-Heinemann, Boston, MA, 1992, p. 3-9.
- [15] W. Löwenstein, *Am. Mineral.* 39 (1954) 92.

- [16] R.E. Morris, *J. Mater. Chem.* 15 (2005) 931.
- [17] M.E. Davis, P.E. Hathaway, C. Montes, *Zeolites* 9 (1989) 436.
- [18] E.M. Flanigen, in: H. van Bekkum, E.M. Flanigen, P.A. Jacobs, J.C. Jansen (Eds.): *Introduction to Zeolite Science and Practice, Studies in Surface Science and Catalysis*, Vol. 137, Elsevier, Amsterdam, 2001, p. 13.
- [19] L.B. McCusker, F. Liebau, G. Engelhardt, *Pure Appl. Chem.* 73 (2001) 381.
- [20] C.H. Baerlocher, W.M. Meier, D.H. Olson, *Atlas of Zeolite Framework Types*, 5<sup>th</sup> Ed., Elsevier, Amsterdam, 2001.
- [21] Website: <http://www.iza-structure.org/databases/>.
- [22] M.A. Martin-Luengo and M. Yates, *J. Mater. Sci.* 30 (1995) 4483.
- [23] J.B. Uytterhoeven, L.G. Christner, W.K. Hall, *J. Phys. Chem.* 69 (1965) 2117.
- [24] W.J. Mortier, J. Sauer, J.A. Lercher, H. Noller, *J. Phys. Chem.* 88 (1984) 905.
- [25] D.N. Stamires and J. Turkevich, *J. Am. Chem. Soc.* 86 (1964) 749.
- [26] R.D. Shannon, K.H. Gardner, R.H. Staley, G. Bergeret, P. Gallezot, A. Auroux, *J. Phys. Chem.* 89 (1985) 4778.
- [27] M.J. Remy, D. Stanica, G. Poncelet, E.J.P. Feijen, P.J. Grobet, J.A. Martens, P.A. Jacobs, *J. Phys. Chem.* 100 (1996) 12440.
- [28] A. Pöppl, T. Rudolf, D. Michel, *J. Am. Chem. Soc.* 120 (1998) 4879.
- [29] T. Barzetti, E. Selli, D. Moscotti, L. Forni, *J. Chem. Soc., Faraday Trans.* 92 (1996) 1401.
- [30] K.J. Balkus, Jr., A.G. Gabrielov, N. Sandler, in: E. Iglesia, P.W. Lednor, D.A. Nagaki, L.T. Thompson (Eds.): *Synthesis and Properties of Advanced Catalytic Materials, Material Research Society Symposium Proceeding*, Vol. 368, Materials Research Society, Warrendale, PA, 1995, p. 369.

- [31] K.J. Balkus, Jr., A.G. Gabrielov, S.I. Zones: Synthesis of Zeolites, Layered Compounds and Other Microporous Solids, Preprints for the Division of Petroleum Chemistry, Vol. 40, American Chemical Society, 1995, p. 296.
- [32] K.J. Balkus, Jr., A.G. Gabrielov, S.I. Zones, in: L. Bonneviot and S. Kaliaguine (Eds.): Zeolites: A Refined Tool for Designing Catalytic Sites, Studies in Surface Science and Catalysis, Vol. 97, Elsevier, Amsterdam, 1995, p. 519.
- [33] K.J. Balkus, Jr. and A.G. Gabrielov, US Patent 5,489,424, 1996, assigned to University of Texas, Austin.
- [34] K.J. Balkus, Jr., M. Biscotto, A.G. Gabrielov, in: H. Chon, S.-K. Ihm, Y.S. Uh (Eds.): Progress in Zeolite and Microporous Materials, Studies in Surface Science and Catalysis, Vol. 105, Elsevier, Amsterdam, 1997, p. 415.
- [35] C.C. Freyhardt, M. Tsapatsis, R.F. Lobo, K.J. Balkus, Jr., M.E. Davis, Nature 381 (1996) 295.
- [36] R.F. Lobo, M. Tsapatsis, C.C. Freyhardt, S. Khodabandeh, P. Wagner, C.-Y. Chen, K.J. Balkus, Jr., S.I. Zones, M.E. Davis, J. Am. Chem. Soc. 119 (1997) 8474.
- [37] T. Muñoz, Jr. And K.J. Balkus, Jr., J. Am. Chem. Soc. 121 (1999) 139.
- [38] K.J. Balkus, Jr., A.K. Khanmanedova, A. Scott, J. Höfelmeyer, in: M.M.J. Treacy, B.K. Marcus, M.E. Bisher, J.B. Higgins (Eds.): Proceedings of the 12<sup>th</sup> International Zeolite Conference, Baltimore, MD, Vol. 3, Materials Research Society, Warrendale, PA, 1999, p. 1403.
- [39] Z. Deng, A. Dalton, O. Terasaki, K.J. Balkus, Jr., in: E. van Steen, L.H. Callanan, M. Claeys (Eds.): Recent Advances in the Science and Technology of Zeolites and Related Materials, Studies in Surface Science and Catalysis, Vol. 154, Elsevier, Amsterdam, 2004, p. 903.

- [40] P. Wagner, M. Yoshikawa, M. Lovallo, K. Tsuji, M. Taspatsis, M.E. Davis, *Chem. Commun.* (1997) 2179.
- [41] M. Yoshikawa, P. Wagner, M. Lovallo, K. Tsuji, T. Takawaki, C.-Y. Chen, L.W. Beck, C. Jones, M. Tsapatsis, S.I. Zones, M.E. Davis, *J. Phys. Chem. B* 102 (1998) 7139.
- [42] M. Yoshikawa and M.E. Davis, US Patent 6,040,258 A, 2000, assigned to California Institute of Technology.
- [43] P.A. Barrett, M.J. Díaz-Cabañas, M.A. Cambor, R.H. Jones, *J. Chem. Soc., Faraday Trans. 94* (1998) 2475.
- [44] K. Tsuji, P. Wagner, M.E. Davis, *Microporous Mesoporous Mater.* 28 (1999) 461.
- [45] S. Elomari, WO Patent 01/92155 A1, 2001, assigned to Chevron.
- [46] A. Burton, S. Elomari, C.-Y. Chen, R.C. Medrud, I.Y. Chan, L.M. Bull, C. Kibby, T.V. Harris, S.I. Zones, E.S. Vittoratos, *Chem. Eur. J.* 9 (2003) 5737.
- [47] S.A. Elomari and S.I. Zones, in: A. Galarneau, F. Di Renzo, F. Fajula, J. Vedrine (Eds.): *Zeolites and Mesoporous Materials at the Dawn of the 21<sup>st</sup> Century*, Studies in Surface Science and Catalysis, Vol. 135, Elsevier, Amsterdam, 2001, p. 479.
- [48] S. Elomari, US Patent 0020828 A1, 2004, assigned to Chevron Texaco Corporation.
- [49] S. Elomari, US Patent 0106511 A1, 2004, assigned to Chevron Texaco Corporation.
- [50] J.-L. Paillaud, B. Harbuzaru, J. Patarin, N. Bats, *Science* 304 (2004) 990.
- [51] B. Harbuzaru, J.-L. Paillaud, J. Patarin, N. Bats, US Patent 0067604 A1, 2005.
- [52] A. Corma Canos, F. Rey Garcia, M.J. Díaz-Cabañas, WO Patent 02/092511 A1, 2002, assigned to Consejo Superior de Investigaciones Cientificas and Universidad Politecnica de Valencia.
- [53] A. Corma, M.J. Díaz-Cabañas, J. Martínez-Triguero, F. Rey, J. Rius, *Nature* 418 (2002) 514.

- [54] A. Corma, M.J. Díaz-Cabañas, F. Rey, *Chem. Commun.* (2003) 1050.
- [55] A. Corma, M.T. Navarrows, F. Rey, S. Valencia, *Chem. Commun.* (2001) 1486.
- [56] A. Corma, M.T. Navarro, F. Rey, J. Rius, S. Valencia, *Angew. Chem., Int. Ed.* 40 (2001) 2277.
- [57] T. Blasco, A. Corma, M.J. Díaz-Cabañas, F. Rey, J. Rius, G. Sastre, J.A. Vidal-Moya, *J. Am. Chem. Soc.* 126 (2004) 13414.
- [58] M.A. Camblor, L.A. Villaescusa, M.J. Díaz-Cabañas, *Top. Catal.* 9 (1999) 59.
- [59] A.S. Kuperman, S. Oliver, G.A. Ozin, J.M. Garces, M.M. Olken, *Nature* 365 (1993) 239.
- [60] P.A. Barrett, M.A. Camblor, A. Corma, R.H. Jones, L.A. Villaescusa, *J. Phys. Chem. B* 102 (1998) 4147.
- [61] A. Corma, M.J. Díaz-Cabañas, C. López, A. Martínez, in: E. van Steen, L.H. Callanan, M. Claeys (Eds.): *Recent Advances in the Science and Technology of Zeolites and Related Materials, Studies in Surface Science and Catalysis, Vol. 154*, Elsevier, Amsterdam, 2004, p. 2380.
- [62] D.C. Calabro, J.C. Cheng, R.A. Crane, Jr., C.T. Kresge, S.S. Dhingra, M.A. Steckel, D.L. Stern, S.C. Weston, US Patent 6,049,018, 2000, assigned to Mobil Oil Corporation.
- [63] D.L. Dorset, S.C. Weston, S.S. Dhingra, *J. Phys. Chem. B* 110 (2006) 2045.
- [64] A.W. Chester, L.A. Green, S.S. Dhingra, T. Mason, H.K.C. Timken, WO Patent 00/43466, 2000, assigned to Mobil Oil Corporation.
- [65] A.W. Chester, D.C. Calabro, S.S. Dhingra, J.W. Beeckman, T.J. Fiebig, G.R. Sweeten, T.E. Helton, C.T. Kresge, R.F. Socha, S.C. Weston, US Patent 6,310,265 B1, 2001, assigned to ExxonMobil.

- [66] J.C. Cheng, A.B. Dandekar, M.A. Steckel, H.K.C. Timken, WO Patent 01/53236, 2001, assigned to Mobil Oil Corporation.
- [67] S.-S. Chen, S.-Y. Hwang, WO Patent 02/062734 A1, 2002, assigned to ExxonMobil.
- [68] M.M. Wu, P. Trotto, S. Luo, J.G. Santiesteban, H.K.C. Timken, S.S. Dhingra, S.C. Weston, R.T. Spissel, US Patent 0137971 A1, 2002, assigned to ExxonMobil.
- [69] W.A. Weber, W.R. Cade, F.S. Bryan, J.G. Santiesteban, WO Patent 02/088052, 2002, assigned to ExxonMobil.
- [70] S. Ernst, S.P. Elangovan, M. Gerstner, M. Hartmann, T. Hecht, S. Sauerbeck, in: E. van Steen, L.H. Callanan, M. Claeys (Eds.): *Recent Advances in the Science and Technology of Zeolites and Related Materials*, Studies in Surface Science and Catalysis, Vol. 154, Elsevier, Amsterdam, 2004, p. 2861.
- [71] S.P. Elangovan, M. Ogura, S. Ernst, M. Hartmann, S. Tontisirin, M.E. Davis, T. Okubo, *Microporous Mesoporous Mater.* 96 (2006) 210.
- [72] Y. Nakagawa, US Patent 5,316,753 A, 1994, assigned to Chevron.
- [73] Y. Nakagawa, in: L. Bonneviot, S. Kaliaguine (Eds.): *Zeolites: A Refined Tool for Designing Catalyst Sites*, Studies in Surface Science and Catalysis, Vol. 97, Elsevier, Amsterdam, 1995, p. 53.
- [74] P. Wagner, S.I. Zones, M.E. Davis, R.C. Medrud, *Angew. Chem., Int. Ed.* 38 (1999) 1269.
- [75] L.A. Villaescusa, P.A. Barrett, M.A. Cambor, *Chem. Commun.* 21 (1998) 2329.
- [76] B. Harbuzaru, M. Roux, J.-L. Paillaud, F. Porcher, C. Marichal, J.-M. Chézeau, J. Patarin, *Chem. Lett.* 6 (2002) 616.
- [77] P. Wagner, Y. Nakagawa, G.S. Lee, M.E. Davis, S. Elomari, R.C. Medrud, S.I. Zones, *J. Am. Chem. Soc.* 122 (2000) 263.

- [78] Y. Kurata, T. Hanaoka, H. Hamada, in: A. Galarneau, F. Di Renzo, F. Fajula, J. Vedrine (Eds.): *Zeolites and Mesoporous Materials at the Dawn of the 21st Century*, Studies in Surface Science and Catalysis, Vol. 135, Elsevier, Amsterdam, 2001, p. 366.
- [79] S.S. Dhingra, WO Patent 02/42207 A2, 2002, assigned to ExxonMobil.
- [80] D.L. Dorset, W.J. Roth, G.J. Kennedy, S.S. Dhingra, *Z. Kristallogr.* 223 (2008) 456.
- [81] D.M. Millar, G.E. Lewis, J.M. Garcés, US Patent 5,397,560, 1995, assigned to Dow Chemical.
- [82] I.A. Cody, W.J. Murphy, S.S. Hantzer, WO Patent 033590 A2, 2004, assigned to ExxonMobil.
- [83] A.R. Bishop, W.B. Genetti, J.W. Johnson, L.L. Ansell, N.M. Page, US Patent 0072676 A1, 2004, assigned to ExxonMobil.
- [84] I.A. Cody, W.J. Murphy, S.S. Hantzer, WO Patent 033094 A1, 2004, assigned to ExxonMobil.
- [85] E.P. Parry, *J. Catal.* 2 (1963) 371.
- [86] M.R. Basila, T.R. Kantner, K.H. Rhee, *J. Phys. Chem.* 68 (1964) 3197.
- [87] T.R. Hughes and H.M. White, *J. Phys. Chem.* 71 (1967) 2192.
- [88] L.H. Little, *Infrared Spectra of Adsorbed Species*, Academic Press, London, New York, 1966, p. 193.
- [89] J.W. Niemantsverdriet, *Spectroscopy in Catalysis: An Introduction*, VCH, Weinheim, New York, Basel, Cambridge, Tokyo, 1995, p. 207.
- [90] P.A. Jacobs and R. von Ballmoos, *J. Phys. Chem.* 86 (1982) 3050.
- [91] V.L. Zholobenko, M.A. Makarova, J. Dwyer, *J. Phys. Chem.* 97 (1993) 5962.

- [92] H.G. Karge, J. Ladebeck, Z. Sarbak, in: T. Seiyama and K. Tanabe (Eds.): *New Horizons in Catalysis, Studies in Surface Science and Catalysis*, Vol. 7, Elsevier, Amsterdam, New York, 1981, p. 1408.
- [93] H.G. Karge, J. Ladebeck, Z. Sarbak, K. Hatada, *Zeolite* 2 (1982) 94.
- [94] H.G. Karge, K. Hatada, Y. Zhang, R. Fiedorow, *Zeolites* 3 (1983) 13.
- [95] H.A. Benesi, *J. Phys. Chem.* 61 (1957) 970.
- [96] H.G. Karge, Y. Wada, J. Weitkamp, S. Ernst, U. Girkbach, H.K. Beyer, in: S. Kaliaguine and A. Mahay (Eds.): *Catalysis on the Energy Scene, Studies in Surface Science and Catalysis*, Vol. 19, Elsevier, Amsterdam, 1984, p. 101.
- [97] D.E. De Vos, S. Ernst, C. Perego, C.T. O'Connor, M. Stöcker, *Microporous Mesoporous Mater.* 56 (2002) 185.
- [98] D.A. McCaulay and A.P. Lien, *J. Am. Chem. Soc.* 75 (1953) 2411.
- [99] H.C. Brown and C.R. Smoot, *J. Am. Chem. Soc.* 78 (1956) 2176.
- [100] A. Streitwieser, Jr. and L. Reif, *J. Am. Chem. Soc.* 82 (1960) 5003.
- [101] J.A. Amelse, in: J.W. Ward (Ed.): *Catalysis 1987, Studies in Surface Science and Catalysis*, Vol. 38, Elsevier, Amsterdam, 1988, p. 165.
- [102] D.S. Santilli, *J. Catal.* 99 (1986) 327.
- [103] J. Das, Y.S. Bhat, A.B. Halgeri, *Ind. Eng. Chem. Res.* 32 (1993) 2525.
- [104] J.M. Silva, M.F. Ribeiro, F.R. Ribeiro, E. Benazzi, M. Guisnet, *Appl. Catal. A: General* 125 (1995) 15.
- [105] A. Philippou and M.W. Anderson, *J. Catal.* 167(1997) 266.
- [106] N. Arsenova-Härtel, H. Bludau, W.O. Haag, H.G. Karge, *Microporous Mesoporous Mater.* 35-36 (2000) 113.
- [107] G.A. Olah, M.W. Meyer, N.A. Overchuk, *J. Org. Chem.* 29 (1964) 2313.
- [108] A.P. Bolton, M.A. Lanewala, P.E. Pickert, *J. Org. Chem.* 33 (1968) 1513.

- [109] S.M. Csicsery, *J. Org. Chem.* 34 (1969) 3338.
- [110] G. Emig and E. Klemm, *Technische Chemie: Einführung in die Chemische Reaktionstechnik*, 5<sup>th</sup> Edn., Springer, Berlin, Heidelberg, 2005, p. 117-135.
- [111] D.R. Stull, E.F. Westrum, Jr., G.C. Sinke, *The Chemical Thermodynamics of Organic Compounds*, John Wiley & Sons, New York, London, Sidney, Toronto, 1969.
- [112] P.A. Jacobs and J.A. Martens, *Pure Appl. Chem.* 58 (1986) 1329.
- [113] H.L. Coonradt and W.E. Garwood, *Ind. Eng. Chem., Process Des. Develop.* 3 (1964) 38.
- [114] J. Weitkamp and S. Ernst, in: J.W. Ward (Ed.): *Catalysis 1987, Studies in Surface Science and Catalysis*, Vol. 38, Elsevier, Amsterdam, 1988, p. 367.
- [115] D.M. Brouwer and H. Hogeveen, in: A. Streitwieser, Jr. and R.W. Taft (Eds.): *Progress in Physical Organic Chemistry*, Vol. 9, Interscience, New York, London, Sydney, Toronto, 1972, p. 179.
- [116] J. Weitkamp and H. Farag, *Acta Phys. Chem.* 24 (1978) 327.
- [117] J. Weitkamp, *Ind. Eng. Chem., Prod. Res. Develop.* 21 (1982) 550.
- [118] P.A. Jacobs, J.A. Martens, H.K. Beyer, in: B. Imelik, C. Naccache, G. Coudurier, Y. Ben Taarit, J.C. Vedrine (Eds.): *Catalysis by Acids and Bases, Studies in Surface Science and Catalysis*, Vol. 20, Elsevier, Amsterdam, 1985, p. 399.
- [119] J. Weitkamp, P.A. Jacobs, J.A. Martens, *Appl. Catal.* 8 (1983) 123.
- [120] P.A. Jacobs, J.B. Uytterhoeven, M. Steyns, G. Froment, J. Weitkamp, in: L.V.C. Rees (Ed.): *Proceedings of the 5<sup>th</sup> International Conference On Zeolites*, Naples, Italy, Heyden, London, 1980, p. 607.
- [121] P.A. Jacobs, J.A. Martens, J. Weitkamp, H.K. Beyer, *Faraday Discuss. Chem. Soc.* 72 (1982) 353.
- [122] R.M. Dessau, *J. Catal.* 77 (1982) 304.

- [123] R.M. Dessau, *J. Catal.* 89 (1984) 520.
- [124] J. Weitkamp, T. Kromminga, S. Ernst, *Chem. Ing. Tech.* 64 (1992) 1112.
- [125] S. Altwasser, R. Gläser, A.S. Lo, P. Liu, K. Chao, J. Weitkamp, *Microporous Mesoporous Mater.* 89 (2006) 109.
- [126] J. Weitkamp, S. Ernst, T. Bock, A. Kiss, P. Kleinschmit, in: H.K. Beyer, H.G. Karge, I. Kiricsi, J.B. Nagy (Eds.): *Catalysis by Microporous Materials, Studies in Surface Science and Catalysis, Vol. 94*, Elsevier, Amsterdam, 1995, p. 278.
- [127] C.M. van Ballegoy, A.G. Gabrielov, T.L.M. Maesen, WO Patent 98/56718, 1998, assigned to Shell.
- [128] S.I. Zones, D.L. Holtermann, L.W. Jossens, D.S. Santilli, A. Rainis, J.N. Ziemer, WO patent 91/00777, 1991, assigned to Chevron.
- [129] Y. Nakagawa, US Patent 5,271,922, 1993, assigned to Chevron.
- [130] V. Sascha, Diplomarbeit, Technische Universität Kaiserslautern, 2002.
- [131] S. Ernst, Ph.D. Dissertation, Universität Karlsruhe, 1987, p. 31.
- [132] C.N.R. Rao, *Ultra-Violet and Visible Spectroscopy, Chemical Application*, 3<sup>rd</sup> Edn., Butterworths, London, 1975, p. 183-192.
- [133] R. de Ruiter, J.C. Jansen, H. van Bekkum, *Zeolites* 12 (1992) 56.
- [134] R. de Ruiter, A.P.M. Kentgens, J. Grootendrost, J.C. Jansen, H. van Bekkum, *Zeolites* 13 (1993) 128.
- [135] R.F. Lobo and M.E. Davis, *Microporous Mater.* 3 (1994) 61.
- [136] I. Kiricsi, C. Flego, G. Pazzuconi, W.O. Parker, Jr., R. Millini, C. Perego, G. Bellussi, *J. Phys. Chem.* 98 (1994) 4627.
- [137] M. Trombetta, G. Busca, L. Storaro, M. Lenarda, M. Casagrande, A. Zambon, *Phys. Chem. Chem. Phys.* 2 (2000) 3529.

- [138] P. Behrens, M. Hartl, R. Jäger, R. Wartchow, A. Schneider, Poster at the 14<sup>th</sup> International Zeolite Conference, Cape Town, South Africa, 2004.
- [139] G. Engelhardt and D. Michel, High-Resolution Solid-State NMR of Silicates and Zeolites, John Wiley & Sons, Chichester, New York, Brisbane, Toronto, Singapore, 1987, p. 211-218.
- [140] C.A. Fyfe, Y. Feng, H. Grondy, G.T. Kokotailo, H. Gies, Chem. Rev. 91(1991) 1525.
- [141] H.S. Jacobsen, P. Norby, H. Bildsøe, H.J. Jakobsen, Zeolites 9 (1989), 491.
- [142] M. Hunger, S. Ernst, J. Weitkamp, Zeolites 15 (1995) 188.
- [143] W.W. Kaeding, J. Catal. 95 (1985) 512.

# Curriculum Vitae

Name: Supak Tontisirin  
Birth: 2 August 1974  
Birth place: Rayong, Thailand  
Nationality: Thai  
Marital Status: Married (1 daughter)

## Education

08/03-07/10 **Ph.D., Institute of Technical Chemistry,**  
University of Kaiserslautern, Kaiserslautern, Germany

10/00-06/03 **Master of Science, International Program, Chemical Engineering,**  
University of Erlangen-Nürnberg, Erlangen, Germany

09/98-04/00 **Master of Science in Engineering, International Program,**  
**Management of Production,**  
Chalmers University of Technology, Gothenburg, Sweden

06/92-03/96 **Bachelor of Engineering, Chemical Engineering,**  
Chulalongkorn University, Bangkok, Thailand

06/90-03-92 **High School,**  
Triam Udom Suksa School, Bangkok, Thailand

## Career

08/03-03/07 **Research Assistant at Institute of Technical Chemistry,**  
University of Kaiserslautern, Kaiserslautern, Germany

04/96-03/98 **Process Engineer, Dow Chemical Thailand,**  
Map-Ta-Phut Industrial Estate, Rayong, Thailand

## Publications

S. Ernst, M. Hartmann, S. Tontisirin and W. Böhlmann

**"Characterization and catalytic evaluation of zeolite MCM-71"**

Studies in Surface Science and Catalysis 158B (2005) 1287-1294.

Proceedings of the 3<sup>rd</sup> International Zeolite Symposium (3<sup>rd</sup> FEZA), Prague, Czech Republic, 23-26<sup>th</sup> August 2005

S.P. Elangovan, M. Ogura, S. Ernst, M. Hartmann, S. Tontisirin, M.E. Davis, T. Okubo

**"A comparative study of zeolites SSZ-33 and MCM-68 for hydrocarbon trap applications"**

Microporous and Mesoporous Material 96 (2006) 210-215

Supak Tontisirin and Stefan Ernst

**"Zeolite SSZ-53: An Extra-Large-Pore Zeolite with Interesting Catalytic Properties"**

Angew. Chem. Int. Ed. 46 (2007) 7304-7306

Supak Tontisirin and Stefan Ernst

**"Zeolith SSZ-53: ein superweitporiger Zeolith mit interessanten katalytischen Eigenschaften"**

Angew. Chem. 119 (2007) 7443-7446

S. Tontisirin and S. Ernst

**"Characterization of zeolite SSZ-35 by catalytic hydrocarbon conversion"**

Studies in Surface Science and Catalysis 170 (2007) 1351-1356.

Proceedings of the 15<sup>th</sup> International Zeolite Conference, Beijing, P.R. China 12-17<sup>th</sup> August 2007

## Conferences

S. Tontisirin, M. Hartmann, S. Ernst

**"Characterization and catalytic evaluation of zeolite MCM-71"**

17<sup>th</sup> German Zeolite Conference, Giessen, Germany, 2<sup>nd</sup>-4<sup>th</sup> March 2005

S. Ernst, M. Hartmann, S. Tontisirin and W. Böhlmann

**"Characterization and catalytic evaluation of zeolite MCM-71"**

3<sup>rd</sup> International Federation of European Zeolite Associations (FEZA) Conference, Prague, Czech Republic, 23-26<sup>th</sup> August 2005

S. Ernst, S. Tontisirin, M. Hartmann

**"Synthesis, Characterization and Catalytic Properties of Zeolite SSZ-35"**

40<sup>th</sup> German Catalyst Conference, Weimar, Germany, 24-26<sup>th</sup> March 2007

S. Tontisirin and S. Ernst

**"Characterization of zeolite SSZ-35 by catalytic hydrocarbon conversion"**

15<sup>th</sup> International Zeolite Conference, Beijing, P.R. China, 12-17<sup>th</sup> August 2007